

AD-A142 209

RESEARCH INVESTIGATION DIRECTED TOWARD EXTENDING THE
USEFUL RANGE OF THE ELECTROMAGNETIC SPECTRUM(U)

1/ 3

UNCLASSIFIED

COLUMBIA RADIATION LAB NEW YORK G W FLYNN 31 MAY 84

DAAG29-82-K-0080

F/G 20/3

NL





MICROCOPY RESOLUTION TEST CHART
NATIONAL BUREAU OF STANDARDS-1963-A



COLUMBIA UNIVERSITY

DEPARTMENTS OF PHYSICS,
CHEMISTRY, ELECTRICAL ENGINEERING

12

★ PROGRESS REPORT NO. 34

April 1, 1983 - March 31, 1984

CONTRACT DAAG29-82-K-0080

APPROVED FOR PUBLIC RELEASE: DISTRIBUTION UNLIMITED

AD-A142 209

TO:

THE JOINT SERVICES TECHNICAL ADVISORY COMMITTEE

REPRESENTING: THE U.S. ARMY RESEARCH OFFICE
THE OFFICE OF NAVAL RESEARCH
THE AIR FORCE OFFICE OF SCIENTIFIC RESEARCH

DTIC
ELECTE
JUN 15 1984
S D

COLUMBIA RADIATION LABORATORY, NEW YORK, NEW YORK 10027

★ May 31, 1984

DTIC FILE COPY

84 06 15 079

COLUMBIA RADIATION LABORATORY

RESEARCH INVESTIGATION DIRECTED TOWARD
EXTENDING THE USEFUL RANGE OF THE
ELECTROMAGNETIC SPECTRUM

Progress Report No. 34

April 1, 1983 through March 31, 1984

Contract DAAG29-82-K-0080

Object of the Research:

Basic research in the fields of quantum electronics; electromagnetic propagation, detection and sensing; and solid state electronics.

The research reported in this document was made possible through support extended the Columbia Radiation Laboratory, Columbia University, by the Joint Services Electronics Program (U.S. Army Research Office, Office of Naval Research, and the Air Force Office of Scientific Research) under Contract DAAG29-82-K-0080.

Submitted by: George W. Flynn, Director

Coordinated by: Vicki J. Zell, Administrative Assistant

COLUMBIA UNIVERSITY
Columbia Radiation Laboratory
Department of Physics
New York, New York 10027

May 31, 1984

Approved for public release; distribution unlimited

Accession For	
NTIS GRA&I	<input checked="checked" type="checkbox"/>
DTIC TAB	<input type="checkbox"/>
Unannounced	<input type="checkbox"/>
Justification	
By	
Distribution/	
Availability Codes	
Dist	Avail and/or Special
Al	



The research reported in this document was made possible through support extended to the Columbia Radiation Laboratory, Columbia University by the Joint Services Electronics Program (U.S. Army Research Office, Office of Naval Research, and the Air Force Office of Scientific Research) under Contract DAAG29-82-K-0080.

Portions of this work were also supported by:

Air Force Office of Scientific Research

AFOSR-84-0013

AFOSR/DARPA

F-49620-82-K-0008

Army Research Office

Contract DAAG29-82-K-0089

National Science Foundation

Grant NSF-DMR 80-06966
Grant NSF-CHE 80-23747
Grant NSF-BNS 80-21140
Grant NSF-ECS 82-11593
Grant NSF-ECS 82-09218
Grant NSF-ECS 82-17677
Grant NSF-ECS 82-19636

Office of Naval Research

Contract N00014-78-C-0517

Department of Energy

Contract DE-AC02-78-ER-04940

National Institutes of Health

NIH-2-RO1-NS03654

The support of these agencies is acknowledged in footnotes in the text.

Unclassified

SECURITY CLASSIFICATION OF THIS PAGE (When Data Entered)

REPORT DOCUMENTATION PAGE		READ INSTRUCTIONS BEFORE COMPLETING FORM
1. REPORT NUMBER Progress Report No. 34	2. GOVT ACCESSION NO. A142 209	3. RECIPIENT'S CATALOG NUMBER
4. TITLE (and Subtitle) RESEARCH INVESTIGATION DIRECTED TOWARD EXTENDING THE USEFUL RANGE OF THE ELECTRO- MAGNETIC SPECTRUM		5. TYPE OF REPORT & PERIOD COVERED 1 April 1983 - 31 March 1984
		6. PERFORMING ORG. REPORT NUMBER 34
7. AUTHOR(s) George W. Flynn		8. CONTRACT OR GRANT NUMBER(s) DAAG29-82-K-0080
9. PERFORMING ORGANIZATION NAME AND ADDRESS Columbia Radiation Laboratory Columbia University New York, New York 10027		10. PROGRAM ELEMENT, PROJECT, TASK AREA & WORK UNIT NUMBERS
11. CONTROLLING OFFICE NAME AND ADDRESS Department of the Army U. S. Army Research Office Research Triangle Park, NC 27709		12. REPORT DATE 31 May 1984
		13. NUMBER OF PAGES 257
14. MONITORING AGENCY NAME & ADDRESS (if different from Controlling Office)		15. SECURITY CLASS. (of this report) Unclassified
		15a. DECLASSIFICATION/DOWNGRADING SCHEDULE
16. DISTRIBUTION STATEMENT (of this Report) Approved for public release; distribution unlimited		
17. DISTRIBUTION STATEMENT (of the abstract entered in Block 20, if different from Report)		
18. SUPPLEMENTARY NOTES Portions of this work were also supported by the Air Force Office of Scientific Research, the Army Research Office, the National Science Foundation, the Office of Naval Research, the Department of Energy, AFOSR/DARPA, and NIH.		
19. KEY WORDS (Continue on reverse side if necessary and identify by block number) Fiber-optic communications Coherence Photon statistics Sub-Poisson light (continued)		
20. ABSTRACT (Continue on reverse side if necessary and identify by block number) ▶ We have been studying the characteristics of light generated by distinctly non-Poisson processes. We are particularly interested in sub-Poisson light (light whose fluctuations are lower than those of lasers). The use of such quiet light can be beneficial, e.g., it can increase the distance between repeaters in a fiber-optic communications system.		

DD FORM 1 JAN 73 1473

EDITION OF 1 NOV 65 IS OBSOLETE

1

Unclassified

SECURITY CLASSIFICATION OF THIS PAGE (When Data Entered)

Block 20 continued - Abstract

As an example of a mechanism for producing such light, we have begun studying a Franck-Hertz apparatus excited by a space-charge-limited electron beam. We have carried out extensive theoretical calculations of the properties of such a source of light and demonstrated that under suitable conditions it can indeed lead to antibunched and sub-Poisson photon emissions. We have also proved a quantum analog of the Burgess variance theorem. This confirmed that the sub-Poisson nature of a light beam is conserved in the presence of absorptive media and additive (Poisson) background light. Thus the sub-Poisson light can be used in a real detection system once it is generated. 47

The performance of orthogonal and nonorthogonal modulation formats has been compared for fiber-optic communications with avalanche photodiode detectors. Shot noise was found to play an important role in determining the reduction in the minimum detectable energy using orthogonal modulation. In the ideal quantum limit, the detection threshold is equal to one photon, and the performance of orthogonal and nonorthogonal modulation is the same. In a thermal noise dominated system, orthogonal modulation provides a 1.5 dB decrease in minimum detectable energy, compared to nonorthogonal modulation. For a practical shot noise dominated system, orthogonal modulation shows a 6 dB improvement. A series of experiments was carried out comparing orthogonal modulation (e.g., frequency shift keying or FSK, pulse position modulation) to nonorthogonal modulation (e.g., amplitude shift keying), and the effects of crosstalk and suboptimal threshold were studied. Approximately 4dB improvement was observed using FSK in a 100 Mbit/sec fiber system.

A design for an ultra-small metal-oxide-semiconductor field effect transistor (MOSFET) is presented. MOSFETs with one-quarter micrometer and sub-quarter micrometer channel lengths that operate with controlled punchthrough current are analyzed by two-dimensional numerical modeling. Current-voltage characteristics for subthreshold, nonsaturated and saturated regions of operation were obtained at various temperatures for devices of different channel length. The results clearly indicate that device current is due to barrier-limited, space-charge-limited and surface-inversion conduction processes.

Block 20 continued - Abstract

A model has been developed to characterize the photovoltaic properties of a thin-film polycrystalline semiconductor device with a metal-insulator-semiconductor (MIS) structure and an accumulated back contact which forms a back surface field. Semiconductor doping density, thickness, grain size, and grain boundary trap density are the parameters used to characterize the semiconductor. Collection velocity, diode ideality factor, effective junction barrier height, and light transmittance are the parameters used to characterize the MIS interfacial region. The three-dimensional grain size and grain boundary problem is simplified by transforming it to an equivalent one-dimensional single-level bulk trap problem. The majority-carrier density and the built-in potential are assumed to be affected by light intensity, doping and trap densities. The effects of deep-level grain boundary traps and of surface passivation on the short-circuit current, open-circuit voltage, fill factor, collection and conversion efficiencies of these devices are calculated based on the potential distribution in the thin-film semiconductor. Recombination current and series and shunt resistance are not included and the superposition principle is not used in the calculation. Sample calculations are included for the specific case of electrodeposited n-type CdTe MIS devices. Methods to improve the conversion efficiency and the application of modeling are discussed.

A theory has been proposed to quantify the collection efficiency of a thin-film metal-insulator-semiconductor (MIS) device with back-surface field. The model incorporates two loss mechanisms: first, the image force effect producing an electron potential maximum located at x_m near the surface within which all photogenerated electrons as well as holes are collected and thus do not contribute to the photocurrent; and second, the collection of the majority carriers, photogenerated in the depletion region, which diffuse against the electric field to x_m and, thus, reduce the photocurrent. In addition to being affected by doping density, majority carrier mobility, minority carrier diffusion length, and effective surface collection velocity, the collection efficiency is shown to be thickness dependent when the semiconductor is fully depleted. Calculations are included for the specific case of electrodeposited n-type CdTe MIS devices. Methods to improve the collection efficiency

Block 20 continued - Abstract

include: designing a high-low doping profile, reducing the surface collection velocity, and optimizing the thickness and doping for the semiconductor.

We have developed a thermal nitridation process which is used to produce nitroxide films ranging between 15 and 50 Å in thickness. Fabricated MIS-Schottky barrier diodes, with varying turn-on voltages, show an improvement in breakdown voltage.

We have fabricated a new type of metal-semiconductor thin-film diode with an I-V characteristic similar to that of a p-n junction. Its forward-bias current is dominated by majority carrier tunneling, and its reverse breakdown voltage is over 50 V. The fabrication process, the I-V curves and the Auger depth profile of the interfacial layer are presented.

UV radiation from an ArF laser has been used to perform large-area, rapid etching of single-crystal GaAs. The process is based on the photochemical production of reactive radicals from methyl bromide, trifluoromethyl bromide or hydrogen bromide. The etching is crystallographically selective, rapid ($>8 \mu\text{m}/\text{min}$) and produces features below $1 \mu\text{m}$.

The basic physics of laser-surface interactions have been explored. This research provides the first clear understanding of the photodissociation of metal-alkyl molecules, the first observation of surface enhanced photochemistry with coherent metal arrays, and the first observation of UV-enhanced semiconductor etching at liquid solid interfaces.

Submicrometer optical gratings have been produced in GaAs surfaces by a visible-laser-enhanced, wet-etching process which permits the fabrication of different gratings profiles. The etch process was investigated by in situ optical measurements of the diffracted beams and electron microscopy. In addition, we report the first use of deep-ultraviolet light for grating fabrication.

Block 20 continued - Abstract

Laser-enhanced etching of Si in a CF_4/O_2 plasma is described. Both p- and n-type Si were investigated for different dopant concentrations at laser intensities from 0-2 Watts. Etch-rate enhancement due to both thermal and nonthermal effects was observed and is discussed.

Directly written patterns of $\text{TiO}_2/\text{SiO}_2$ on glass cover slides were produced to demonstrate the ability to directly write a waveguiding material ($n = 1.9$) on silicon dioxide ($n = 1.45$). The technique used, a localized laser heating of an organosilicate, is to be published in the Journal of Vacuum Science and Technology B. To demonstrate waveguiding for electro-optical structures on silicon substrates, a thick ($\sim 1 \mu\text{m}$) silicon dioxide layer is needed to prevent coupling of the evanescent wave to the underlying substrate.

The clean room, a new facility of our Microelectronics Laboratory, was tested and put into functional operation during the last year. This facility provides the controllable environment which is necessary in microelectronic processing. A number of different electro-optical devices have been fabricated using this facility.

We have used a supersonic gas expansion coupled with a simple discharge source (capillaritron) to produce beams of translationally cold, metastable OH radicals. All neutrals produced by this source are found to have a narrow translational energy distribution but ions, having an average energy of about 25 eV, are produced with an energy width of 2-5 eV.

The vibrational energy distribution of CH_3 radicals, produced by excimer laser photolysis of $\text{Cd}(\text{CH}_3)_2$ and $\text{Zn}(\text{CH}_3)_2$, has been determined. Both the ν_2 out of plane bending vibrational mode and the ν_3 C-H stretch mode of CH_3 are created with substantial vibrational excitation as a result of photofragmentation. The ratio of the number of bend to stretch quanta produced by photodissociation decreases as the photolysis wavelength is varied from 193 nm to 248 nm.

Block 20 continued - Abstract

A new, extraordinarily powerful diode laser probe technique has been used to study the vibrational excitation of CO_2 molecules produced by collisions with hyperthermal hydrogen atoms having a translational energy of approximately 2 eV. These hot atoms are made by excimer laser photolysis of HBr , H_2S , and HI . Hot atom/ CO_2 collisions produce an excess of CO_2 ν_2 bending vibrational excitation compared to ν_3 stretching excitation. Almost no pure antisymmetric stretching vibration (00^01 level) is produced during collisions, although significant amounts of bend/stretch combination vibrational states are excited during such collisions.

The collisional energy transfer rates which couple the 10^00 , 02^20 , 02^00 and 01^10 "lower laser levels" in CO_2 have been determined in pure CO_2 for the first time. The new diode laser probe technique has been used to determine these rates. The 02^20 level was found to be most strongly coupled to 02^00 and 10^00 . The doorway state which couples the overtone levels 10^00 , 02^20 , and 02^00 to the bending fundamental 01^10 was found to be 02^20 .

Our new diode laser technique has been used to probe the CO_2 vibrational states produced as a result of the excimer laser photodissociation of pyruvic acid (CH_3COCOOH) vapor. Approximately 3% of the CO_2 molecules are found in the ν_2 , 01^10 bending state and less than 0.1% are found in the ν_3 00^01 antisymmetric stretching state. This vibrational state distribution follows that expected from the geometry changes undergone by the CO_2 fragment which rearranges from a non-linear configuration in pyruvic acid to a linear configuration in CO_2 .

We have obtained a preliminary distribution for the rotational states of OH radical produced when high energy hydrogen atoms react with N_2O . Laser induced UV fluorescence was used to detect the OH and excimer laser photolysis of H_2S was employed to make hot hydrogen atoms. Some of the OH observed in these reactions comes from reaction between ^1D oxygen atoms and H_2S molecules since the excimer laser slightly dissociates N_2O giving N_2 and O.

Block 20 continued - Abstract

We have observed clusters of SF_6 molecules in a supersonic molecular beam expansion. The clusters, which cannot be detected mass spectrometrically, were observed by exciting the beam with a CO_2 laser and measuring the loss of molecules from the beam with a low temperature germanium bolometer. Clustering is observed to set in at a nozzle backing pressure of 150 Torr. The CO_2 laser absorption of the clusters is red shifted from that of SF_6 monomer. Similar clustering was observed for C_4F_8 expansions at low backing pressures (less than 150 Torr), but for CO_2 , clusters could only be detected at pressures above one atmosphere.

We have established from our picosecond laser studies that the solvent environment has a large effect on the intramolecular dynamics of excited singlet to ground triplet transformation in the chemical intermediate diphenylcarbene, $\text{C}_6\text{H}_5-\ddot{\text{C}}-\text{C}_6\text{H}_5$. We have carried out the first studies of the photochemistry of a carbene, i.e. the excited state properties of this reactive and short-lived species.

We have successfully extended our studies of twisted internal charge transfer phenomena, an important mechanism of energy decay and structural change for excited molecules in condensed media. In the aprotic nitrile solvents we have found that the rate of formation of the twisted molecular form depends exponentially on the solvent polarity as measured by an empirical solvent parameter. Solvent viscosity in the neat nitriles is not a factor indicating that the structural change does not involve a significant change in volume or shape which would experience a frictional resistance.

The photofragmentation of two isomeric precursors of singlet oxygen was found to follow different kinetics and wavelength dependence. These results indicate that the photodissociation is a state selective process dependent on the structural differences between the two isomeric precursors studied.

Unexpected satellite photon echoes have been observed on the $^3\text{P}_0 - ^3\text{H}_4$ transition in $\text{LaF}_3:\text{Pr}^{3+}$, a potential solid-state laser system. We have also observed a four-wave mixing signal on the $^3\text{P}_0 - ^3\text{H}_6$ excited state transition

Block 20 continued - Abstract

in $\text{LaF}_3:\text{Pr}^{3+}$ as a preliminary to a tri-level echo experiment coupling the $^3\text{H}_4$, $^3\text{P}_0$ and $^3\text{H}_6$ levels.

Two-pulse angled-beam photon echoes have been generated on the $3^2\text{S}_{1/2} - 3^2\text{P}_{3/2}$ transition of atomic sodium. Echo intensity was measured as a function of the time separation between the first excitation pulse and the echo signal over a dynamic range exceeding 10^{11} . This allowed us to observe signals from sodium atoms that had been in their excited state for more than 23 lifetimes.

We have also generated photon echoes using incoherent (thermal) excitations on the $3^2\text{S}_{1/2} - 3^2\text{P}_{3/2}$ transition of atomic sodium. These echoes were generally the same size as, and displayed the same modulation with pulse separation as, those generated using coherent laser excitations. An instantaneous four-wave-mixed signal was generated using an incoherent source (giving 7-nsec-long pulses) on the same sodium transition. This signal showed a fast turn on time on the order of 100 psec suggesting that echo experiments using incoherent excitations can be performed with a time resolution on this order.

In another experiment, measurements of the collisional broadening cross sections for the $2\text{S}-n\text{S}$ and $2\text{S}-n\text{D}$ superposition states of lithium with He, Ne, Ar, Kr, and Xe have been completed. An anomaly has been observed in the Li-Ne cross sections which we are continuing to investigate.

Block 19 continued - Key Words

Antibunched light	NO
Fiber-optics	H ₂ S
Frequency-shift-keying	Excimer laser
Orthogonal modulation	Diode laser
Pulse-position modulation	Ions
Photovoltaic effects	OH
Collection efficiency	SF ₆
Thin-films	Clusters
Metal-insulator-semiconductor (MIS) devices	CO ₂ laser
Grain boundaries	Photodissociation
Traps	C ₄ F ₈
Carrier transport	Pyruvic acid
Ultra-small	N ₂ O
Punchthrough	Dye laser
Barrier-limited current	Chemical reactions
Space-charge-limited current	Capillaritron
Surface-inversion current	Radicals
Subquartermicron	Supersonic expansion
Quartermicron channel length	Energy transfer
MOSFET	Rotational relaxation
Schottky barrier	Picosecond lasers
Tunneling rectifier	Intramolecular energy relaxation
Amorphous silicon	Singlet oxygen
Interface states	Wavelength dependence of photodissociation
GaAs	Photochemistry of chemical intermediates
Dry-etching	Excited state structural change
Photon-assisted dry etching	Solvent effects
Laser processing	Carbenes
Organometallics	Photon echoes
Silicon	Dynamic range
SiO ₂	Incoherent excitations
Waveguides	Collisionally induced coherences
Integrated optics	Tri-level echo in solids
Wet etching	Collisional line broadening
Clean Room	Four-wave mixing
Photolithography	Broadband information storage and retrieval
Hot atoms	
CO ₂	
Hydrogen	

TABLE OF CONTENTS

PUBLICATIONS AND REPORTS	xiii
------------------------------------	------

FACTUAL DATA, CONCLUSIONS, AND PROGRAM FOR THE NEXT INTERVAL

I.	QUANTUM DETECTION AND SENSING OF RADIATION	1
	A. Noise in the Generation, Partition, and Detection of Light . .	1
	B. Frequency-Shift-Key Modulation for Fiber-Optic Communications .	9
II.	PHYSICAL AND PHOTOCHEMICAL PROPERTIES OF ELECTRONIC MATERIALS . .	17
	A. Conduction Mechanisms in Ultra-Small Punchthrough MOSFET . . .	17
	B. Collection Efficiency of Thin-Film Metal-Insulator-Semiconductor Photovoltaic Devices	23
	C. Photoconductance Transient Response in Polycrystalline Silicon .	32
	D. Modeling of Grain Boundary Effects on the Performance of Metal-Insulator - Thin Film Polycrystalline Semiconductor Photovoltaic Device	38
	E. Fabrication of MIS-Schottky Diodes with Thermal Nitroxide Film .	49
	F. A Metal-Amorphous Silicon-Silicon Tunnel Rectifier	54
	G. Photon-Assisted Dry Etching of GaAs	61
	H. Physics of Laser Surface Interactions	79
	I. Photochemical Recording of Phase Diffraction Gratings on Semiconductor Surfaces	88
	J. Laser Controlled Plasma Etching	96
	K. Laser Processing for Electro-Optical Components	105
	L. Microelectronics Fabrication Instrumentation	108

III. GENERATION AND DYNAMIC PROPERTIES OF METASTABLE SPECIES FOR QUANTUM ELECTRONICS.	110
A. Translational Energy Characteristics of Radicals and Ions in a Capillaritron Supersonic Nozzle Discharge	110
B. Infrared Emission Studies of Vibrational Excitation in CH_3 Fragments Produced from ArF and KrF Laser Photolysis of $\text{Cd}(\text{CH}_3)_2$ and $\text{Zn}(\text{CH}_3)_2$	115
C. Diode Laser Probes of Bending and Stretching Excitation in CO_2 Caused by Collisions with Hot Atoms from Excimer Laser Photolysis	128
D. Vibrational Energy Transfer Between the Symmetric Stretching and Bending Modes of CO_2 : A Diode Laser Double Resonance Study	150
E. Diode Laser Probes of Photofragmentation Products	153
F. Laser-Induced Fluorescence of OH Radicals Produced in Reactions of Laser-Generated Hot Hydrogen Atoms	159
G. Vibrational Predissociation of SF_6 Clusters in a Supersonic Molecular Beam	169
H. A Molecular Beam Study of C_4F_8	184
IV. PICOSECOND ENERGY TRANSFER AND PHOTOFRAGMENTATION SPECTROSCOPY	196
A. Twisted Internal Charge Transfer Phenomena	196
B. Kinetics and Wavelength Dependence of the Photofragmentation of Singlet Oxygen Precursors	207
C. Photophysics and Photochemistry of a Divalent Carbon Chemical Intermediate - Diphenylcarbene	214
V. GENERATION AND CONTROL OF RADIATION	223
A. Optical Coherent Transient Spectroscopy.	223
SIGNIFICANT ACCOMPLISHMENTS AND TECHNOLOGY TRANSITION REPORTS	247
PERSONNEL	252
JSEP REPORTS DISTRIBUTION LIST	254

PUBLICATIONS AND REPORTS

Publications

B. E. A. Saleh, D. Stoler, M. C. Teich, "Coherence and Photon Statistics for Optical Fields Generated by Poisson Random Emissions," Phys. Rev. A 27, 360 (1983). (JSEP and NSF)

K. Matsuo, M. C. Teich, and B. E. A. Saleh, "Thomas Point Process in Pulse, Particle, and Photon Detection," Applied Optics 22, 1898 (1983). (JSEP)

M. C. Teich, B. E. A. Saleh, and D. Stoler, "Antibunching in the Franck-Hertz Experiment," Optics Comm. 46, 244 (1983). (JSEP)

J. Perina, B. E. A. Saleh, and M. C. Teich, "Independent Photon Deletions from Quantized Boson Fields: The Quantum Analog of the Burgess Variance Theorem," Opt. Comm. 48, 212 (1983). (JSEP)

B. E. A. Saleh and M. C. Teich, "Statistical Properties of a Nonstationary Neyman-Scott Cluster Process," IEEE Trans. Inform. Theory IT-29, 939 (1983). (JSEP and NSF)

M. C. Teich and G. L. Lachs, "A Neural Counting Model Incorporating Refractoriness and Spread of Excitation: III. Application to Intensity Discrimination and Loudness Estimation for Variable-Bandwidth Noise Stimuli," Acustica, 53, 225 (1983). (NSF)

G. Lachs, R. A. Saia, and M. C. Teich, "A Neural-Counting Model Based on Physiological Characteristics of the Peripheral Auditory System: IV. Application to Response of Individual Neural Fibers," IEEE Trans., Syst., Man, Cybern. SMC-13, 964 (1983). (NSF)

M. C. Teich, "Statistics of Primary Excitations as a Determinant of the Character of Generated Photons," in Proc. NSF Grantee-User Meeting, edited by D. J. Epstein, H. A. Haus, and J. H. Shapiro (Massachusetts Institute of Technology, Cambridge, 1983), Optical Communication Systems, pp. 77-78. (NSF and JSEP)

M. C. Teich and B. E. A. Saleh, "Antibunched and Sub-Poisson Light from the Franck-Hertz Effect," J. Opt. Soc. Am. 73, 1876 (1983). (JSEP)

B. E. A. Saleh and M. C. Teich, "ROC Curves for Multiplied-Poisson Counting Processes," J. Opt. Soc. Am. 73, 1957 (1983). (NSF)

M. C. Teich and S. M. Khanna, "Behavior of the Pulse-Number Distribution for the Neural Spike Train in the Cat's Auditory Nerve," J. Acoust. Soc. Am. 74, S7 (1983). (NIH)

G. Lachs, R. Al-Shaikh, Q. Bi, and M. C. Teich, "A Neural-Counting Model Based on Physiological Characteristics of the Peripheral Auditory System: Application of Loudness Estimation and Intensity Discrimination," J. Acoust. Soc. Am. 74, S41 (1983). (NSF)

P. R. Prucnal, "Wideband FSK Fiber-Optic Communication Experiment," J. Opt. Comm. 4, 99 (1983). (JSEP and NSF)

P. R. Prucnal and M. C. Teich, "Refractory Effects in Neural Counting Processes with Exponentially Decaying Rates," IEEE Trans. on Sys., Man, and Cybern., SMC-13, 1028 (1983). (NSF)

Q. Hua, D. K. Yang, and E. S. Yang, "Fabrication of MIS-Schottky Diodes with Thermal Nitroxide Film," Materials Lett. 2, 147 (1983). (NSF and JSEP)

E. Poon, H. L. Evans, W. Hwang, R. M. Osgood, Jr., and E. S. Yang, "Measurement of Grain Boundary Parameters by Laser-Spot Photoconductivity," in Laser Diagnostics and Photochemical Processing for Semiconductor Devices, R. M. Osgood, S. R. J. Brueck, and H. Schlossberg, Eds., Elsevier, New York p. 103-108 (1983). (NSF, JSEP and DOE/SERI)

E. Poon, E. S. Yang, H. L. Evans, W. Hwang, and R. M. Osgood, Jr., "Determination of Grain Boundary Barrier Height and Interface States by a Focused Laser Beam," Appl. Phys. Lett. 42, 285 (1983). (NSF, JSEP and DOE/SERI)

W. Hwang, E. Poon, E. S. Yang, H. L. Evans, J. S. Song, and R. M. Osgood, Jr., "Electrical Characterization of Grain Boundary Parameters by Laser-Spot Photoconductivity Techniques," 1983 Symposium on VLSI Technology, Systems and Applications, 275-278 (1983). (NSF, JSEP and DOE/SERI)

E. S. Yang, E. Poon, H. L. Evans, W. Hwang, J. S. Song, and C. M. Wu, "Electronic Properties of Grain Boundaries in Polycrystalline Silicons," SPIE Proceedings 385, 59 (1983). (NSF, JSEP and DOE/SERI)

W. Hwang, E. Poon, and H. C. Card, "Carrier Recombination at Grain Boundaries and Effective Recombination Velocity," Solid State Electronics, 26, 599 (1983). (JSEP and DOE/SERI)

E. S. Yang and W. Hwang, "Fundamental Studies of MIS and MS Solar Cells on Polycrystalline Silicon," Quarterly Report No. 1, Jan. 1983, No. 2 April, 1983; No. 3, June 1983. Final Report Sept. 1983. (DOE/SERI)

L. M. Chen, H. Y. Li, K. B. Sarachik, W. Hwang, and E. S. Yang, "Spray Deposition Process Study of S_nO_n Solar Cells Using Orthogonal Experimental Design," Proceeding Fifth European Community Photovoltaic Solar Energy Conference, Athens, Greece, October (1983). (DOE/SERI)

A. M. Hawryluk, H. I. Smith, R. M. Osgood, and D. J. Ehrlich, "Deep UV Spatial Period Division Using Excimer Laser Sources," Opt. Lett. 7, 402 (1983). (ARO and JSEP)

C. J. Chen and R. M. Osgood, "Measurement of the Electronic Spectra of Physisorbed Molecular Layers," Chem. Phys. Lett. 98, 363 (1983). (ARO and JSEP)

V. Daneu, D. J. Ehrlich, R. M. Osgood, A. Sanchez, "Reflectometric Spectroscopy of Adsorbed Molecular Layers," Opt. Lett. 8, 151 (1983). (ARO)

D. J. Ehrlich, T. F. Deutsch, R. M. Osgood, Jr., and D. J. Silversmith, "Laser Photochemical Processing for Microelectronics," Proceedings of the 14th International Conference on Solid State Devices, March 1983, Japanese J. of Applied Physics, 22, 161 (1983). (DARPA/AFOSR and ARO)

D. Podlesnik, H. H. Gilgen, R. M. Osgood, A. Sanchez, "Maskless Chemical Etching of Submicrometer Gratings in Single-Crystalline GaAs," Appl. Phys. Lett. 43, 1083 (1983). (DARPA/AFOSR)

C. J. Chen and R. M. Osgood, "Direct Observation of the Local-Field-Enhanced Surface Photochemical Reactions," Phys. Rev. Letts. 50, 1705 (1983). (ARO and JSEP)

C. J. Chen and R. M. Osgood, "Surface-Catalyzed Photochemical Readings of Physisorbed Molecules," Appl. Phys. 31, 171 (1983). (JSEP and ARO)

R. M. Osgood, Jr., "Material Deposition and Removal Using Laser-Initiated Chemistry," Journal of De Physique, p. C5-133, 1983. (DARPA/AFOSR, ARO, and JSEP)

R. M. Osgood, Jr., "Laser Microchemistry and its Application to Electron Device Fabrication," Am. Rev. Phys. Chem. 34, 77 (1983). (DARPA/AFOSR, ARO and JSEP)

C. J. Chen, H. H. Gilgen, and R. M. Osgood, Jr., "Microstructure of Photodeposited Thin Films," Microscope Semiconductor Material Conference, Oxford, 21-23, 1983. (ARO)

C. J. Chen and R. M. Osgood, Jr., "Spectroscopy and Photoreactions of Organometallic Molecules on Surfaces," in Laser Diagnostics and Photochemical Processing for Semiconductor Devices, R. M. Osgood, S. R. J. Brueck, and H. Schlossberg, Eds., Elsevier, New York (1983). (JSEP)

P. Brewer, W. Holber, G. Reksten, and R. M. Osgood, Jr., "Laser-assisted Dry Etching of Semiconducting Materials," SPIE - Laser Processing of Semiconductor Devices, 1983. (JSEP, DARPA/AFOSR, and NSF)

Jack Chu, George W. Flynn, and Ralph E. Weston, Jr., "Spectral Distribution of CO₂ Vibrational States Produced by Collisions with Fast Hydrogen Atoms from Laser Photolysis of HBr," J. Chem. Phys. 78, 2990 (1983). (DOE, NSF, and JSEP)

J. L. Ahl, and G. W. Flynn, "Temperature Dependent Studies of Vibrational Energy Transfer in S¹⁸O₂ and S¹⁸O₂ Rare Gas Mixtures," J. Phys. Chem. 87, 2172 (1983). (DOE, NSF, and JSEP)

Paul B. Beeken, Eric A. Hanson, and George W. Flynn, "Spectroscopy and Energy Transfer in Electronically Excited States of I₂ Trapped in a Rare Gas Matrix Cage," J. Chem. Phys. 78, 5892 (1983). (DOE, NSF, and JSEP)

E. V. Sitzmann, R. Wang, and K. B. Eisenthal, "Picosecond Laser Studies on the Reaction of Excited Triplet Diphenylcarbene with Alcohols," J. Phys. Chem. 87, 2283 (1983). (AFOSR, NSF, and JSEP)

- K. B. Eisenthal, "Intermolecular and Intramolecular Excited State Charge Transfer," in Photochemistry and Photobiology (Proceedings of the International Conference, January 5-10, 1983, University of Alexandria, Egypt), Vol. I & II, Ahmed Zewail, ed. Harwood Academic Publishers, Chur, Switzerland: 1983. (AFOSR, NSF, and JSEP)
- E. V. Sitzmann, J. Langan, and K. B. Eisenthal, "Picosecond Laser Studies of the Charge-Transfer Reaction of Excited Triplet Diphenylcarbene with Electron Donors," Chem. Phys. Letters, 102, 446 (1983). (AFOSR, NSF, and JSEP)
- R. Beach, B. Brody, and S. R. Hartmann, "Photon Echoes Made Simple," International Conf. on Photochemistry and Photobiology, Alexandria, Egypt Jan. 1983. (ONR and JSEP)
- R. Beach, B. Brody, and S. R. Hartmann, "Photon Echoes in Lithium Vapor with the use of Angled Excitation Beams," Phys. Rev. A 27, 2925 (1983). (ONR and JSEP)
- R. Beach, B. Brody, and S. R. Hartmann, "Elliptical Billiard-ball Echo Model," Phys. Rev. A 27, 2537 (1983). (ONR and JSEP)
- R. Beach, B. Brody, and S. R. Hartmann, "Angled Beam Photon Echoes," Submitted to Journal of Optical Society of America. (1983). (ONR and JSEP)
- S. R. Hartmann, "Application of the Billiard Ball Model to Problems in Atomic Physics," Proceeding of the Third Symposium on Laser and Applications, Kanpur, India, December 17-21, 1983. (ONR and JSEP)
- R. Beach, B. Brody, and S. R. Hartmann, "Photon Echoes with Angled Beams," Laser Spectroscopy VI, Proceeding of the Sixth International Conference, Interlaken, Switzerland, 1983, ed., H. P. Weber and W. Lüthy (Springer-Verlag, Berlin, 1983), Vol. 40, p. 48. (ONR and JSEP)
- R. Beach, B. Brody, and S. R. Hartmann, "Photon Echoes Made Simple," Laser Chem. 2, 3 (1983). (ONR and JSEP)
- K. Matsuo, M. C. Teich, and B. E. A. Saleh, "Poisson Branching Point Processes," J. Math. Phys. 24, (1984). (JSEP)
- M. C. Teich, B. E. A. Saleh, and J. Perina, "Role of Primary Excitation Statistics in the Generation of Antibunched and Sub-Poisson Light," J. Opt. Soc. Am. B 1, (1984). (JSEP)
- P. R. Prucnal and T. R. Fan, "Orthogonal Modulation Formats for Fiber-Optic Communications," J. Opt. Soc. Am., in press. (JSEP)
- P. R. Prucnal, R. E. Crochiere, and L. E. Rabiner, "Multirate Digital Signal Processing," American Scientist, (submitted for publication).
- E. S. Yang, Q. Hua, D. K. Yang, G. S. Yang, and P. S. Ho, "A Metal-Amorphous Silicon-Silicon Tunnel Rectifier," Applied Phys. Lett. June 15, 1984. (NSF and JSEP)

P. H. Siegel, A. K. Kerr, and W. Hwang, "Topics in the Optimization of Millimeter-wave Mixers," NASA Technical Paper 2287, March (1984). (JSEP)

S. M. So, W. Hwang, P. V. Meyers, and C. H. Liu, "Collection Efficiency of Thin-film MIS Solar Cells," J. Appl. Phys. 55, 253 (1984). (JSEP and AMETEK)

F. Shoucair, W. Hwang, and P. Jain, "Electrical Characteristics of Large Scale Integration (LSI) MOSFETs at Very High Temperatures: Part I - Theory," Microelectronics and Reliability, 1984 (accepted for publication). (Schlumberger)

F. Shoucair, W. Hwang, and P. Jain, "Electrical Characteristics of Large Scale Integration (LSI) MOSFETs at Very High Temperatures: Part II - Experiment," Microelectronics and Reliability, 1984 (accepted for publication). (Schlumberger)

F. Shoucair, W. Hwang, and P. Jain, "Electrical Characteristics of Large Scale Integration (LSI) MOSFETs at Very High Temperatures: Part III - Modeling and Circuit Behavior," IEEE Trans. on Components, Hybrids and Manufacturing Technology, 1984 (accepted for publication). (Schlumberger)

S. M. So, W. Hwang, P. V. Meyers, and C. H. Liu, "Modeling of Grain Boundary Effects on Photovoltaic Properties of Metal-Insulator Thin Film Polycrystalline Semiconductor Solar Cells," IEEE Trans. on Electron Devices, 1984 (to be published). (JSEP and AMETEK)

B. H. Grossman, W. Hwang, and F. F. Fang, "Ultra-small Punchthrough MOSFET," Solid State Electronics, 1984 (accepted for publication). (IBM)

D. Podlesnik, H. H. Gilgen, R. M. Osgood, A. Sanchez, V. Daneu, "High Resolution Etching of GaAs and CdS Crystals," in Laser Diagnostics and Photochemical Processing for Semiconductor Devices, R. M. Osgood, S. R. J. Brueck, and H. Schlossberg, eds., Elsevier, New York, NY., 1984 (to be published). (DARPA/AFOSR)

C. J. Chen and R. M. Osgood, "Spectroscopy and Photoreactions of Organometallic Molecules on Surfaces," Published in Laser Diagnostics and Photochemical Processing for Semiconductor Devices, Elsevier, New York, NY., 1984 (to be published). (ARO)

R. M. Osgood, "Excimer Laser Interface Chemistry for Microelectronic Processing," Excimer Lasers, eds. C. K. Rhodes, H. Egger, and H. Pummer, AIP, NY., 1984 (to be published). (JSEP)

R. M. Osgood, D. J. Ehrlich, T. F. Deutsch, D. J. Silversmith, and A. Sanchez, "Direct-Write Laser Fabrication: Customization, Correction, and Repair," to be published in Microelectronics-Structures and Complexity, 1984. (DARPA, AFOSR and ARO)

C. J. Chen and R. M. Osgood, "A Spectroscopic Study of the Excited States of Dimethylcadmium, Dimethylzinc, and Dimethylmercury," J. Chem. Phys., June (1984). (ARO and JSEP)

C. J. Chen and R. M. Osgood, "An Analytic Theory of Photodissociation of Linear Symmetric Polyatomic Molecules," J. Chem. Phys., June (1984). (ARO and JSEP)

R. Krchnavek, H. Gilgen, and R. M. Osgood, "Maskless Laser Writing of Silicon Dioxide," to be published in J. Vac. Sci. Tech. (DARPA/AFOSR and JSEP)

P. Brewer, S. Halle, and R. M. Osgood, "Photon-Assisted Dry Etching of GaAs," to be published in Appl. Phys. Lett. (JSEP)

D. Podlesnik, H. H. Gilgen, and R. M. Osgood, Jr., "GaAs Wet Etching with Deep-UV Light," submitted to Appl. Phys. Lett. (DARPA/AFOSR and ARO)

R. M. Osgood, Jr., D. J. Ehrlich, T. F. Deutsch, D. J. Silversmith, A. Sanchez, "Laser Microchemistry for Direct Writing of Microstructures," SPIE vol. 385 - Laser Processing of Semiconductor Devices, 1984. (DARPA/AFOSR and ARO)

P. Brewer, S. Halle, and R. M. Osgood, "Excimer-Laser-Initiated, Dry Etching of Single Crystal GaAs," Material Research Society Symposium Proceedings, 1984. (JSEP)

H. H. Gilgen, D. Podlesnik, C. J. Chen, and R. M. Osgood, Jr., "Direct Holographic Proceeding Using Laser Chemistry," Material Research Society Symposium Proceedings, 1984. (DARPA/AFOSR and ARO)

D. V. Podlesnik, H. H. Gilgen, R. M. Osgood, "Deep-UV, Light-Assisted, Wet Etching of Compound Semiconductors," Material Research Society, Laser-Controlled Chemical Processing of Surfaces, A. W. Johnson and D. Ehrlich, eds. 1984. (DARPA/AFOSR)

M. I. Lester, L. M. Casson, G. B. Spector, G. W. Flynn, and R. B. Bernstein, "Collisional Effects on the Internal and Translational Energy Distributions of Laser Excited and Thermally-Heated SF₆ Supersonic Beams," J. Chem. Phys. 80, 1490 (1984). (DOE, NSF, and JSEP)

J. O. Chu, C. F. Wood, G. W. Flynn, and R. E. Weston, Jr., "Diode Laser Probes of Vibrational Excitation in CO₂ Caused by Hot Atoms from Excimer Laser Photolysis," J. Chem. Phys. 80, 1703 (1984). (DOE, NSF, and JSEP)

S. Datta, R. E. Weston, Jr., and G. W. Flynn, "Vibrational Excitation of CH₃F Excited by Collisions with "Hot" Hydrogen Atoms," J. Chem. Phys. 80, 0000 (1984). (DOE)

J. O. Chu, C. F. Wood, G. W. Flynn, and R. E. Weston, Jr., "Counting Vibrational Quanta with a Diode Laser Probe: Bending and Stretching Excitation in CO₂ Caused by Collisions with Hot Atoms from Excimer Laser Photolysis," submitted for publication. (DOE, NSF, and JSEP)

T. H. Allik, B. B. Brady, G. W. Flynn, and G. B. Spector, "Translational Energy Characteristics of Radicals and Ions in a Capillaritron Supersonic Nozzle Discharge," J. Phys. Chem. 88, 0000 (1984). (DOE, NSF, and JSEP)

C. F. Wood, J. A. O'Neill, and G. W. Flynn, "Infrared Diode Laser Probes of Photofragmentation Products: Bending Excitation in CO₂ Produced by Excimer Laser Photolysis of Pyruvic Acid," Chem. Phys. Lett., submitted for publication. (DOE, NSF, and JSEP)

E. V. Sitzmann and K. B. Eiseenthal, "Studies of the Chemical Intermediate Diphenylcarbene," in Applications of Picosecond Spectroscopy to Chemistry, K. B. Eiseenthal, ed., D. Reidel Publishing Co., Dordrecht, Holland: 1984. (AFOSR, NSF, and JSEP)

E. V. Sitzmann, J. Langan, and K. B. Eiseenthal, "Intermolecular Effects on Intersystem Crossing Studied on the Picosecond Time Scale," JACS, 10, 1868 (1984). (AFOSR, NSF, and JSEP)

K. B. Eiseenthal, R. A. Moss, and N. J. Turro, "Divalent Carbon (Carbene) Chemistry, Time Resolved Laser Photolysis and Spectroscopy in the Investigation of Reactive Organic Intermediates," Science, 0000 (1984). (AFOSR, NSF, and JSEP)

K. B. Eiseenthal, N. J. Turro, E. V. Sitzmann, I. R. Gould, G. Hefferon, J. Langan, and Y. Cha, "Singlet-Triplet Interconversion of Diphenylmethylen. Energetics, Dynamics and Reactivities of Different Spin States," Tetrahedron, 40, 0000 (1984). (AFOSR, NSF, and JSEP)

K. P. Leung, T. W. Mossberg, and S. R. Hartmann, "Switching of Photon Echo Polarization and Direction by Coherent Optical Fields," Phys. Rev. A 29, 225 (1984). (ONR and JSEP)

R. Beach and S. R. Hartmann, "Incoherent Photon Echoes," submitted to Phys. Rev. Lett. (1984). (ONR and JSEP)

Lectures and Presentations

- M. C. Teich, "Statistics of Primary Excitations as a Determinant of the Character of Generated Photons," Meeting of the NSF Grantee-User Group in Optical Communication Systems, Cambridge, Mass., June 1983.
- M. C. Teich, "Role of Statistics of Primary Excitations in Optical Coherence," with B. E. A. Saleh, and J. Perina, Invited Lecture, Fifth Rochester Conference on Coherence and Quantum Optics, Rochester, New York, June 1983.
- M. C. Teich, "Antibunched and Sub-Poisson Light from the Franck-Hertz Experiment," with B.E.A. Saleh, Annual Meeting of the Optical Society of America, New Orleans, Louisiana, October 1983.
- M. C. Teich, "ROC Curves for Multiplied-Poisson Counting Processes," with B.E.A. Saleh, Annual Meeting of the Optical Society of America, New Orleans, Louisiana, October 1983.
- M. C. Teich, "Behavior of the Pulse-Number Distribution for the Neural Spike Train in the Cat's Auditory Nerve," with S.M. Khanna, Annual Meeting of the Acoustical Society of America, San Diego, California, November 1983.
- M. C. Teich, "A Neural-Counting Model Based on Physiological Characteristics of the Peripheral Auditory System: Application to Loudness Estimation and Intensity Discrimination," with G. Lachs, R. Al-Shaikh, and Q. Bi, Annual Meeting of the Acoustical Society of America, San Diego, California, November 1983.
- M. C. Teich, "Photon Statistics in Vision and Communication," Guest Lecture, The Technion Department of Electrical Engineering, Haifa, Israel, December 1983.
- M. C. Teich, "Cascaded/Branching Poisson Point Processes," with K. Matsuo, and B.E.A. Saleh, Invited Lecture, University of California Conference on Statistical Mechanics, Davis, California, March 1984.
- P. R. Prucnal, "Orthogonal Modulation Formats for Fiber-Optic Communications," Optical Society of America Annual Meeting, New Orleans, Louisiana, October 1983.
- P. R. Prucnal, "Channel Codes for Fiber-Optic Communications," Optical Information Systems, Elmsford, New York, June 1983.
- P. R. Prucnal, "Orthogonal Modulation Formats for Fiber-Optic Communications," GTE Labs, Waltham, Mass., August 1983.
- W. Hwang, "Electronic Properties of Polycrystalline Silicon," Philips Laboratories, Briarcliff Manor, New York, December 1983.
- R. M. Osgood, "Microstructure of Photodeposited Thin Films," Conference on Microscopy of Semiconducting Compounds, Oxford, England, April 1983.

- R. M. Osgood, "Recent Advances in Photochemical Deposition," CLEO '82, Baltimore, Maryland, May 1983.
- B. Krchnavek, "Laser-Formed Oxide Layers on Silicon," CLEO '82, Baltimore, Maryland, May 1983.
- R. M. Osgood, "Laser Chemistry for Deposition and Etching," IBM Laboratory, Yorktown Heights, New York, May 1983.
- R. M. Osgood, "Material Deposition and Removal Using Laser-Initiated Chemistry", MRS, Strassbourg, France, May 1983.
- R. M. Osgood, "Laser Direct Writing for Microelectronics," N. Y. Regional A.V.S. Meeting, Rochester, New York, June 1983.
- H. Gilgen, "Ultraviolet Laser Deposition of Thin Metal Films," N. Y. Regional A.V.S. Meeting, Rochester, New York, June 1983.
- P. Brewer, "Photochemical Etching of Semiconductor Materials," N. E. Regional American Chem. Society Meeting, Hartford, Conn., June 1983.
- H. Gilgen, "Progress of Laser Photochemical Processing," Riken Symposium, High Efficiency Gas Lasers, Tokyo, Japan, June 1983.
- R. M. Osgood, "Microfabrication Using Laser Induced Chemistry," American Vacuum Society, Boston, Mass., November 1983.
- R. M. Osgood, "Holographic Applications of Laser-Photochemical Processing," Materials Research Symposium, Boston, Mass., November 1983.
- W. Holber, "Laser-Controlled Plasma Etching," American Vacuum Society Symposium, Boston, Mass., November 1983.
- P. Brewer, "UV-Laser Initiated Photochemical Dry Etching of Single Crystal GaAs Substrates," Materials Research Symposium, Boston, Mass., November 1983.
- W. Holber, "Effects of Laser Radiation in Plasma Etching of Si," Materials Research Symposium, Boston, Mass., November 1983.
- D. Podlesnik, "Deep-UV, Light-Assisted, Wet Etching of Compound Semiconductors," Materials Research Symposium, Boston, Mass., November 1983.
- R. M. Osgood, "Laser Interface Chemistry for Microelectronics," Stanford Industrial Program on Irradiated Thin Film Technology, Stanford, California, December 1983.
- H. Gilgen, "Ultraviolet Laser Deposition of Thin Metal Films," University of Berne, Berne, Switzerland, December 1983.
- R. M. Osgood, "Laser Interface Chemistry," Symposium on the Future of Lightwave Technology, Los Angeles, California, January 1984.

- R. M. Osgood, "Laser Assisted Dry Etching of Semiconducting Compounds", SPIE Meeting, Los Angeles, California, January 1984.
- R. M. Osgood, "Laser Metallization for Packaging," Symposium - Raychem. Inc., San Francisco, California, January 1984.
- R. M. Osgood, "Microelectronics Research at Columbia," Symposium ITT, Sheldon, Conn., February 1984.
- R. M. Osgood, "The Physics of Laser Metallization," APS Meeting, Detroit, Michigan, March 1984.
- G. W. Flynn, "A Decade of Progress in the Study of Vibrational Energy Transfer," Reilly Lecturer, University of Notre Dame, South Bend, Indiana, April 1983.
- G. W. Flynn, "Infrared Fluorescence Probes of Vibrational Excitation by Hot Hydrogen Atoms," Rutgers University, New Brunswick, New Jersey, May 1983.
- G. W. Flynn, "High Resolution Diode Laser Probes of Vibrational Excitation by Hot H Atoms from Excimer Laser Photolysis," Cornell University, Ithaca, New York, September 1983.
- G. W. Flynn, "High Resolution Diode Laser Probes of Vibrational Excitation by Hot H Atoms from Excimer Laser Photolysis," Princeton University, Princeton, New Jersey, September 1983.
- G. W. Flynn, "High Resolution Diode Laser Probes of Vibrational Excitation by Hot H Atoms from Excimer Laser Photolysis," University of California, Berkeley, California, September 1983.
- G. W. Flynn, "High Resolution Diode Laser Probes of Vibrational Excitation by Hot H Atoms from Excimer Laser Photolysis," University of Ottawa, Ottawa, Canada, October 1983.
- G. W. Flynn, "High Resolution Diode Laser Probes of Vibrational Excitation by Hot H Atoms from Excimer Laser Photolysis," Massachusetts Institute of Technology, Cambridge, Mass., October 1983.
- G. W. Flynn, "High Resolution Diode Laser Probes of Vibrational Excitation by Hot H Atoms from Excimer Laser Photolysis," General Motors Research Laboratories, Warren, Michigan, November 1983.
- G. W. Flynn, "High Resolution Diode Laser Probes of Vibrational Excitation by Hot H Atoms from Excimer Laser Photolysis," University of Pennsylvania, Philadelphia, Pennsylvania, November 1983.
- G. W. Flynn, "High Resolution Diode Laser Probes of Vibrational Excitation by Hot H Atoms from Excimer Laser Photolysis," Georgetown University, Washington, D.C., November 1983.

- G. W. Flynn, "High Resolution Diode Laser Probes of Vibrational Excitation by Hot H Atoms from Excimer Laser Photolysis," Columbia University, Department of Chemistry, New York, N.Y., December 1983.
- G. W. Flynn, "High Resolution Diode Laser Probes of Vibrational Excitation by Hot H Atoms from Excimer Laser Photolysis," Bell Telephone Laboratories, Murray Hill, N.J., February 1984.
- G. W. Flynn, "Diode Laser Probes of Hot Atom Vibrational Excitation of CO₂," Austin Symposium on Molecular Structure, Austin, Texas, February 1984.
- G. Spector, "Collisional Effects on the Internal and Translational Energy Distributions of Laser- and Thermal-Excited SF₆ Supersonic Beams," Conference on the Dynamics of Molecular Collisions, Gull Lake, Minnesota, June 1983.
- G. Spector, "The Case of the Missing Energy - Is the First Law Really Valid?," Chemical Physics Evening Seminar, Department of Chemistry, Columbia University, February 1984.
- K. B. Eisenthal, "Intermolecular and Intramolecular Excited State Charge Transfer," Internal Conference on Photochemistry and Photobiology, Alexandria, Egypt, January 1983.
- K. B. Eisenthal, "Picosecond Laser Studies of Intramolecular Motions in Liquids," Structure and Dynamics in Liquids Symposium, A.C.S. Meeting, Seattle, Washington, March 1983.
- K. B. Eisenthal, "Picosecond Laser Studies of Energy and Spin Relaxation in Diphenylcarbene," Chemical Physics of Free Radicals Symposium, A.C.S. Meeting, Seattle, Washington, March 1983.
- K. B. Eisenthal, "Chemistry on the Picosecond Time Scale," Laser Spectroscopy and Photochemistry Symposium, A.C.S. Meeting, Hershey Resort, Pennsylvania, April 1983.
- K. B. Eisenthal, "Chemistry on the Picosecond Time Scale," University of Toronto Laser Seminar, Toronto, Canada, April 1983.
- K. B. Eisenthal, "Picosecond Laser Studies of Chemical Intermediates," NATO Workshop on Application of Picosecond Spectroscopy to Chemistry, Acquafredda Di Maratea, Italy, June 1983.
- E. V. Sitzmann and K. B. Eisenthal, "Studies of the Chemical Intermediate Diphenylcarbene," NATO Workshop on Application of Picosecond Spectroscopy to Chemistry, Acquafredda Di Maratea, Italy, June 1983.
- K. B. Eisenthal, "Picosecond Laser Studies on Intramolecular Motions in Liquids," Gordon Research Conference on Liquids, Plymouth, New Hampshire, August 1983.
- K. B. Eisenthal, "Picosecond Laser Studies of Chemical Intermediates," Princeton University, Princeton, New Jersey, November 1983.

- K. B. Eisenthal, "Chemistry on the Picosecond Time Scale," Radiationless Transitions Conference, Newport Beach, California, January 1984.
- K. B. Eisenthal, "Chemistry on the Picosecond Time Scale," University of South Florida, Tampa, Florida, February 1984.
- K. B. Eisenthal, "Chemistry on the Picosecond Time Scale," University of Miami, Miami, Florida, February 1984.
- K. B. Eisenthal, "Chemistry on the Picosecond Time Scale," Rutgers University, New Brunswick, New Brunswick, New Jersey, April 1984.
- K. B. Eisenthal, "Chemistry on the Picosecond Time Scale-Ground and Excited State Dynamics of Carbenes," New York University, New York, New York, April 1984.
- S. R. Hartmann, "Applications of the Billiard Ball Model to Problems in Atomic Physics," First Binational Workshop and Third Symposium on Lasers and Applications, Kanpur, India, December 1983.
- R. J. Beach, "Angled Beam Photon Echoes," Symposium on Atomic Spectroscopy, Berkeley, California, September 1983.
- S. R. Hartmann, "Photon Echoes with Angled Beams," Laser Spectroscopy VI, Interlaken, Switzerland, September 1983.
- S. R. Hartmann, "Photon Echoes Made Simple," Internal Conference on Photochemistry and Photobiology, Alexandria, Egypt, January 1984.

Resonance Seminars

Meetings are held periodically at Columbia University, New York, New York during the academic year and are open to all members of the New York scientific community. Guest speakers are invited to discuss work in the general area of the research in the Columbia Radiation Laboratory.

Walter Faust, Naval Research Laboratory, "Fragmentation Kinetics of Electronically Excited Nitriles," October 5, 1983.

Kumar Patel, Bell Laboratories, "The New Optical Spectroscopy of Overtone Absorption in Solid Hydrogens," October 12, 1983.

Steve Brueck, MIT, "Microstructure Electromagnetic Effects in Laser-Material Interactions," October 26, 1983.

Gerard Mourou, University of Rochester, "Time Resolved Structural and Electrical Transience in the Picosecond Time Scale," November 16, 1983.

John Muentner, University of Rochester, "Vibrational Predissociation in Hydrogen Fluoride Dimer," November 18, 1983.

Jack Feinberg, University of Southern California, "Photorefractive Effect and It's Applications: Mirrors that Reflect Time Reversed Waves," November 21, 1983.

Kenneth Janda, California Institute of Technology, "Vibrational Predissociation of Van-der-Waal's Molecules - Do Energy Gap Laws Apply?," November 29, 1983.

Fedrico Capasso, Bell Laboratories, "Band Structure Engineering via Graded Gap and Multilayer Structures: A New Approach to Semiconductor Devices," November 30, 1983.

George Flynn, Columbia University, "Diode Laser Probes of Molecular Excitation by Hot Atoms," December 15, 1983.

Douglas Worsnap, Albert Ludwigs University, Germany, "Minimal Values for Solvating Electrons in H_2O and NH_3 ," February 29, 1984.

Stephen R. Forrest, Martin L. Kaplan, and Paul H. Schmidt, AT&T Bell Laboratories, "Unique Properties of Pristine and Irradiated Organic Thin Films," March 28, 1984.

Michael Littman, Princeton University, "Atoms in Crossed Electric and Magnetic Fields: A Penning for Your Thoughts," April 11, 1984.

Richard Hall, Exxon Research and Engineering Corporate Research Labs., "Pulsed Laser Induced Surface Reactions Via Surface Excitation: Kinetic Limits and Opportunities," April 25, 1984.

David H. Auston, AT&T Bell Laboratories, "Hertz, Cerenkov, and Sub-picosecond Pulses," May 2, 1984.

I. QUANTUM DETECTION AND SENSING OF RADIATION

A. NOISE IN THE GENERATION, PARTITION, AND DETECTION OF LIGHT*

(M. Teich, P. Prucnal, B. Saleh, D. Stoler, K. Matsuo)
(JSEP work unit 1, 1982-1985)
(Principal Investigator: M. C. Teich (212) 280-3117)

We have recently explored the generation of quiet light and the low-noise multiplication of carriers in avalanche photodiodes (APDs). Our earlier work⁽¹⁾ permitted us to understand the origins of noise in the generation of light⁽²⁾ and in the avalanche process.⁽³⁾ We present our progress below.

A. Progress in the Generation of Low-noise Light

We have shown theoretically that it is possible to produce light less noisy than the LED or laser by regulating the atomic excitations rather than the atoms themselves.⁽⁴⁾ In particular, when atoms are excited by electrons, Coulomb repulsion is useful in regulating the electrons by means of space-charge effects.

More specifically, for light generated by a two-step process of excitation and emission, there are two key effects that regulate its antibunching and sub-Poisson possibilities: (i) the statistical properties of the excitations themselves; and (ii) the statistical properties of the individual emission.⁽⁵⁾ This is most simply illustrated in terms of the schematic representation provided in Fig. 1. In Fig. 1(a), we show an excitation process that is Poisson. Consider each excitation as generating photons independently. Now if each excitation instantaneously produces a single photon, and if we ignore the effects of interference, the outcome is a Poisson stream of photons, which is neither antibunched nor, obviously, sub-Poisson. This is the least random situation that we could hope to produce, given the Poisson excitation statistics. Interference will

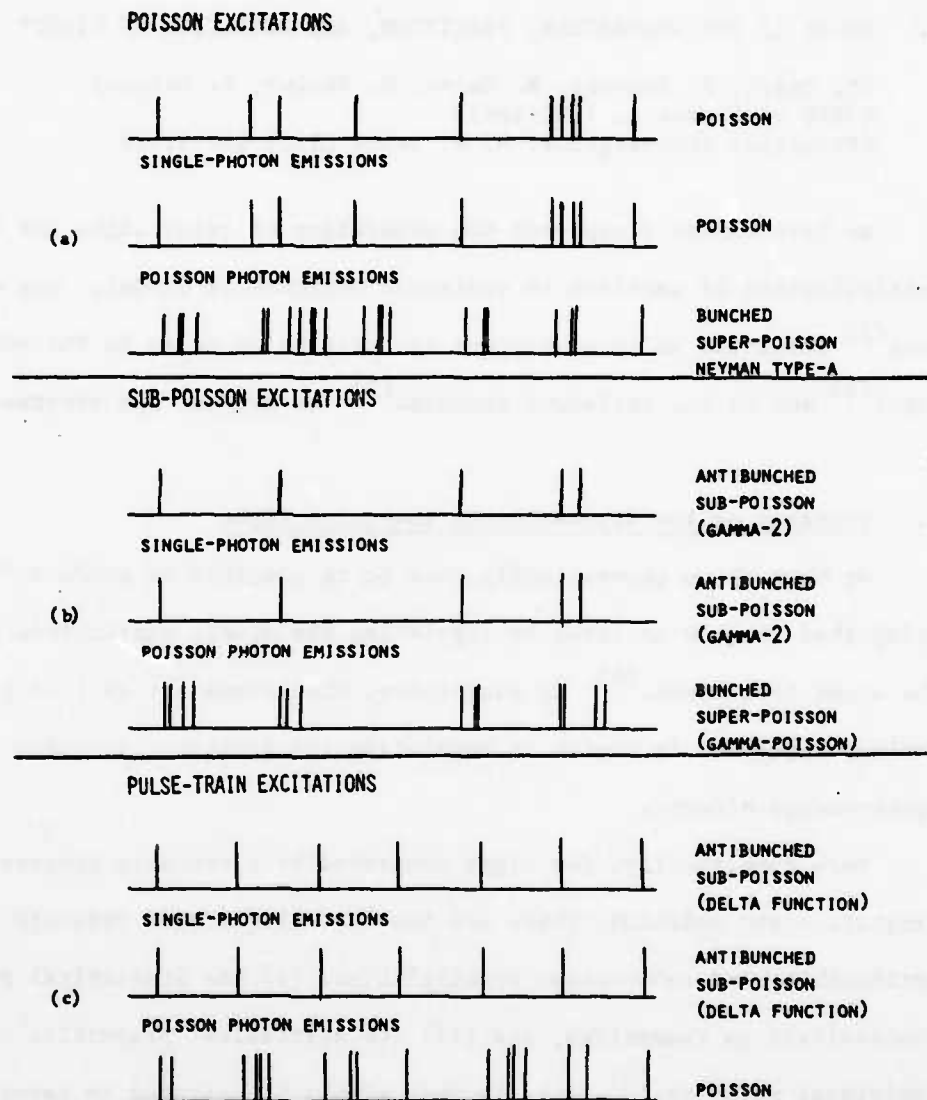


Figure 1. Schematic representation of a two-step process for the generation of light, illustrating stochastic excitations (first line) with either instantaneous single-photon emissions (second line) or Poisson multiple-photon emissions (third line). Interference effects are ignored in this simple representation. (a) Poisson excitations. (b) Antibunched, sub-Poisson excitations ($\gamma-2$). (c) Pulse-train excitations (random phase).

redistribute the photon occurrences, leading us to the results for chaotic light (which is both bunched and super-Poisson).⁽²⁾ On the other hand, the individual nonstationary emissions may consist of multiple photons or random numbers of photons. In this case, we encounter two sources of randomness: one associated with the excitations and another associated with the emissions, so that the outcome will be both bunched and super-Poisson. In particular, if the emissions are also described by Poisson statistics, and the counting time is sufficiently long, we recover the Neyman Type-A counting distribution, as we have discussed in detail elsewhere.⁽⁶⁾⁻⁽⁸⁾ Even if the individual emissions are comprised of deterministic numbers of photons, the end result is the fixed-multiplicative Poisson distribution,⁽⁶⁾ which is super-Poisson. Related results have been obtained when interference is permitted.⁽²⁾ It is quite clear, therefore, that if the excitations themselves are Poisson (or super-Poisson), there is little hope of generating antibunched or sub-Poisson light by such a two-step process.

In Fig. 1(b) we consider a situation in which the excitations are more regular than those for the Poisson. For the purposes of illustration and concreteness, we choose the excitation process to be produced by deleting every other event of a Poisson pulse train. The outcome is the gamma-2 (or Erlang-2) renewal process, whose analytical properties are well understood.⁽⁹⁾ Single-photon emissions, in the absence of interference, result in antibunched, sub-Poisson photon statistics. Poisson emissions, on the other hand, result in super-Poisson light statistics. Of course, the presence of interference introduces additional bunching. Clearly, a broad variety of excitation processes can be invoked for generating many different kinds of light. A process that is similar to the gamma-2, and for which many analytical results are available, is the nonparalyzable dead-time-modified

Poisson process.^{(9),(10)} Resonance fluorescence radiation from a single atom will be described by a process of this type since, after emitting a single photon, the atom decays to the ground state where it cannot radiate. However, the superposition of light from a number of such atoms will wash out the sub-Poisson behavior of the individual emissions.

Finally, in Fig. 1(c), we consider the case of pulse-train excitations (with random phase). This is the limiting result for both the gamma family of processes and for the dead-time-modified Poisson process. In the absence of interference, single-photon emissions in this case yield antibunched, ideally sub-Poisson photon statistics. Interference causes the antibunching to disappear, but the sub-Poisson nature remains in the long counting-time limit. Poisson emissions give rise to Poisson photon statistics.

The illustration in Fig. 1 is intended to emphasize the importance of the excitation statistics as a determinant of the character of the generated light. To produce antibunched and/or sub-Poisson photons, we have shown that both sub-Poisson excitations and sub-Poisson emissions are required.⁽⁵⁾ The production of sub-Poisson light by means of the nonlinear optical processes, as suggested by many researchers, has been difficult because they all involve a struggle, in one way or another, to reduce the Poisson fluctuations of the exciting optical beam (which is usually derived from a laser).

This discussion provides the rationale underlying our recent suggestion⁽⁴⁾ for producing antibunched and sub-Poisson light using the Franck-Hertz effect. Space charge is used to produce sub-Poisson electron excitations. Since the individual emissions are single photons, the generated light can be antibunched and sub-Poisson (see Fig. 2 for schematic representation). This light can be strong if interference effects are minimized.

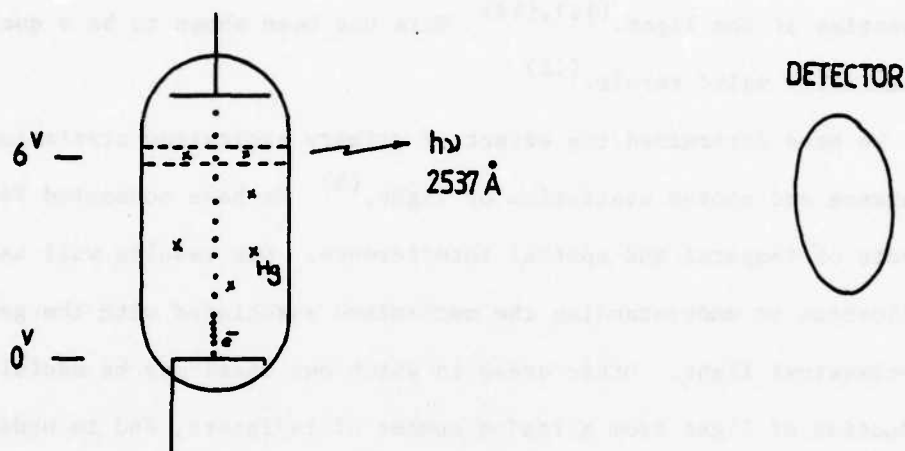


Figure 2. Schematic representation of an experiment for generating antibunched and sub-Poisson Franck-Hertz light from the $6^1P_1 \rightarrow 6^1S_0$ atomic transition in Hg. The wavelength of the radiation is 2537 Å ($h\nu = 4.88$ eV), in the near ultraviolet (see Ref. 4).

Of course, once such light is produced by whatever means, there are obstacles to maintaining its character. These include optical absorption (random deletion), and the addition of spontaneous emission, both of which dilute (but fortunately do not destroy) the antibunching and sub-Poisson properties of the light.^{(11),(12)} This has been shown to be a quantum mechanically valid result.⁽¹²⁾

We have determined the effect of primary excitation statistics on the coherence and photon statistics of light.⁽⁵⁾ We have accounted for the effects of temporal and spatial interference. Our results will have application in understanding the mechanisms associated with the generation of non-classical light. Other areas in which our model may be useful are the production of light from a random number of radiators, and in understanding non-Gaussian scattered light.

B. Progress in the Analysis of Low-Noise APDs

In the course of studying the noise in APDs, we examined a special generalized branching process in which the multiplication of each event is Poisson and a random time delay is introduced at every stage. The first model that we analyzed⁽⁶⁾⁻⁽⁸⁾ is the two-stage cascaded Poisson, in which each event of a primary Poisson point process produces a virtual inhomogeneous rate function which, in turn, generates a secondary Poisson point process. These secondary point processes are superimposed to form the final point process. In that model, primary events themselves are excluded from the final point process. The description turns out to be that of a doubly stochastic Poisson point process (DSPP), which we refer to as the shot-noise-driven process (SNDP).⁽⁷⁾ The SNDP is also a special case of the Neyman-Scott cluster process. Because of the great body of theoretical results available for the

DSPP, our calculations for the statistical properties of the process turned out to be relatively straightforward. In another version of this two-stage model, primary events are carried forward to the final process.⁽¹³⁾

The second system which we analyzed⁽¹⁴⁾ is an m -stage cascade of Poisson processes buffered by linear filters. Each filtered point process forms the input to the following stage, acting as a rate for a DSPP. This is equivalent to a cascaded SNDP. We obtained the counting and time statistics, as well as the autocovariance function. The results of that study are likely to find use in problems where a series of multiplicative effects occur. Examples are the behavior of photon and charged-particle detectors, the production of cosmic rays, and the transfer of neural information.

More recently (and directly pertinent to APD noise), we considered⁽³⁾ a cascade model in which primary events are carried forward together with secondary events, to form the point process at the input to each successive stage. Since the primary and secondary events comprising the union process at each stage are not independent,⁽¹³⁾ the solution is somewhat more difficult than for the cascaded Poisson case considered previously.⁽¹⁴⁾ The initial point process is assumed to be a homogeneous Poisson process (HPP). The final process is itself homogeneous (stationary). This treatment allows us to model a wide variety of physical phenomena in which particles produce more particles, and so on, with the original particles remaining. Our process may also be regarded as a special generalized branching process, in which each event of the HPP produces an age-dependent point process. However, our interest is in the union of the branching point processes rather than in the statistics of the number of events at a certain time (or place), which is the customary quantity of interest in age-dependent branching processes.

Branching processes with properties such as age-dependence, random walk,

and diffusion have been studied extensively from a general theoretical point of view.⁽¹⁵⁾ Few of the statistical properties are obtained in a form amenable to numerical solution, however. We examined a relatively simple process that describes branching with time delay. Thanks to the simplicity offered by the Poisson assumption, we can obtain explicit formulas for useful statistical properties that may be experimentally measured. Examples are the counting distribution, moments, and power spectral density.

This early work on APD multiplication statistics has permitted us to understand some of the origins of APD noise.

*This research was also supported by the National Science Foundation under Grant NSF ECS-82-19636.

- (1) M. C. Teich, CRL Prog. Rept. No. 33, March 31, 1983, pp. 1-10.
- (2) B. E. A. Saleh, D. Stoler, and M. C. Teich, *Phys. Rev. A* 27, 360 (1983).
- (3) K. Matsuo, M. C. Teich, and B. E. A. Saleh, *J. Math. Phys.* 24, xxx (1984).
- (4) M. C. Teich, B. E. A. Saleh, and D. Stoler, *Opt. Commun.* 46, 244 (1983).
- (5) M. C. Teich, B. E. A. Saleh, and J. Perina, *J. Opt. Soc. Am.* B1, xxx (1984).
- (6) M. C. Teich, *Appl. Opt.* 20, 2457 (1981).
- (7) B. E. A. Saleh and M. C. Teich, *Proc. IEEE* 70, 229 (1982).
- (8) B. E. A. Saleh and M. C. Teich, *IEEE Trans. Inform. Th.* IT-29, 939 (1983).
- (9) D. R. Cox, Renewal Theory (Methuen, London, 1962).
- (10) B. I. Cantor and M. C. Teich, *J. Opt. Soc. Am.* 65, 786 (1975).
- (11) M. C. Teich and B. E. A. Saleh, *Opt. Lett.* 7, 365 (1982).
- (12) J. Perina, B. E. A. Saleh, and M. C. Teich, *Opt. Commun.* 48, 212 (1983).
- (13) K. Matsuo, M. C. Teich, and B. E. A. Saleh, *Appl. Opt.* 22, 1898 (1983).
- (14) K. Matsuo, B. E. A. Saleh, and M. C. Teich, *J. Math. Phys.* 23, 2353 (1982).
- (15) T. E. Harris, The Theory of Branching Processes (Springer-Verlag, New York, 1963).

B. FREQUENCY-SHIFT-KEY MODULATION FOR FIBER-OPTIC COMMUNICATIONS

(P. Prucnal, M. Teich)

(JSEP work unit 1, 1982-1985)

(Principal Investigator: M. C. Teich (212) 280-3117)

The performance of orthogonal and nonorthogonal modulation formats was compared for fiber-optic communications with avalanche photodiode detectors. Shot noise was found to play an important role in determining the reduction in minimum detectable energy (6 dB) using orthogonal modulation. These results were extended to power-law signal dependent noise. A series of experiments was carried out comparing orthogonal (e.g., frequency-shift-keying, pulse position modulation) to nonorthogonal modulation (amplitude shift keying), and the effects of crosstalk and suboptimal threshold were studied.

1. Minimum Detectable Energy for Power-Law Noise

The quantity n is observed at a detector output. The variance of n is assumed to be the sum of a power-law signal dependence noise component plus thermal noise:

$$\text{var } n = F\langle n \rangle^{2p} + Z^2/M^2. \quad (1)$$

Here Z is the detector noise figure. For the case of an avalanche photodetector, p is $1/2$, F is the excess noise factor, and M is the average avalanche gain. The minimum detectable energy for orthogonal modulation and symmetric channels is specified by the solution to the equation

$$\langle n \rangle^2 - Q^2 F \langle n \rangle^{2p} - Q^2 Z^4/M^4 = 0, \quad (2)$$

where Q is the signal-to-noise ratio. The minimum detectable energy for nonorthogonal modulation with a threshold $\theta_{\text{mid}} = \langle n \rangle/2$ is specified approximately by the solution to the equation

$$\langle n \rangle^2 - 4Q^2 F \langle n \rangle^{2p} - 4Q^2 Z^4/M^4 = 0. \quad (3)$$

With a threshold θ_{eq} that yields equal false alarm and miss probabilities the minimum detectable energy is specified by the solution to the equation

$$\langle n \rangle - Q^2 F \langle n \rangle^{2p-1} - 2QZ/M = 0. \quad (4)$$

For the case of thermal noise domination, (2), (3) and (4) indicate that the reduction of minimum detectable energy using orthogonal modulation is $D = 1.5$ dB. For the case of power-law noise domination, D is shown in figure 1. For a combination of thermal and shot noise ($p = 1/2$), D is shown in figure 2. Note that θ_{mid} is the threshold used in most practical receivers, and for this case D approaches 6 dB as M increases.

2. FSK Experiment

To compare orthogonal and nonorthogonal modulation, a series of four experiments was carried out with a multimode fiber-optic system:

- (1) FSK and ASK; 6 nm wavelength deviation; suboptimal ASK threshold; 10 M bits/sec;
- (2) same as (1) with optimal ASK threshold (see ref. 1);
- (3) FSK and ASK; 2.5 nm deviation; θ_{mid} ; 100 M bits/sec; receiver with AGC, cosine rolloff equalization, phase locked loop timing recovery;
- (4) PPM; 100 M bits/sec; high-Q tank circuit for clock recovery.

In case (1), D ranged from 3 to 15 dB. In case (2) D ranged from 2.5 to 3.25 dB, and increased with greater shot-noise domination. In case (3), which represents a more realistic receiver, the data (crosses) and theoretical bit-error rate (curves) are shown in figure 3. The effect of interwavelength crosstalk on D is shown in figure 4. The crosstalk in this experiment was about 10%, as shown in the figure. In case (4), PPM modulation was used, and sample waveforms are shown in figure 4. The top waveform is the transmitter clock, followed by the encoded data, the recovered 200 MHz clock, and the received data. Since PPM requires twice the bandwidth of ASK for the same information rate, a higher noise figure results. Therefore, PPM provides no

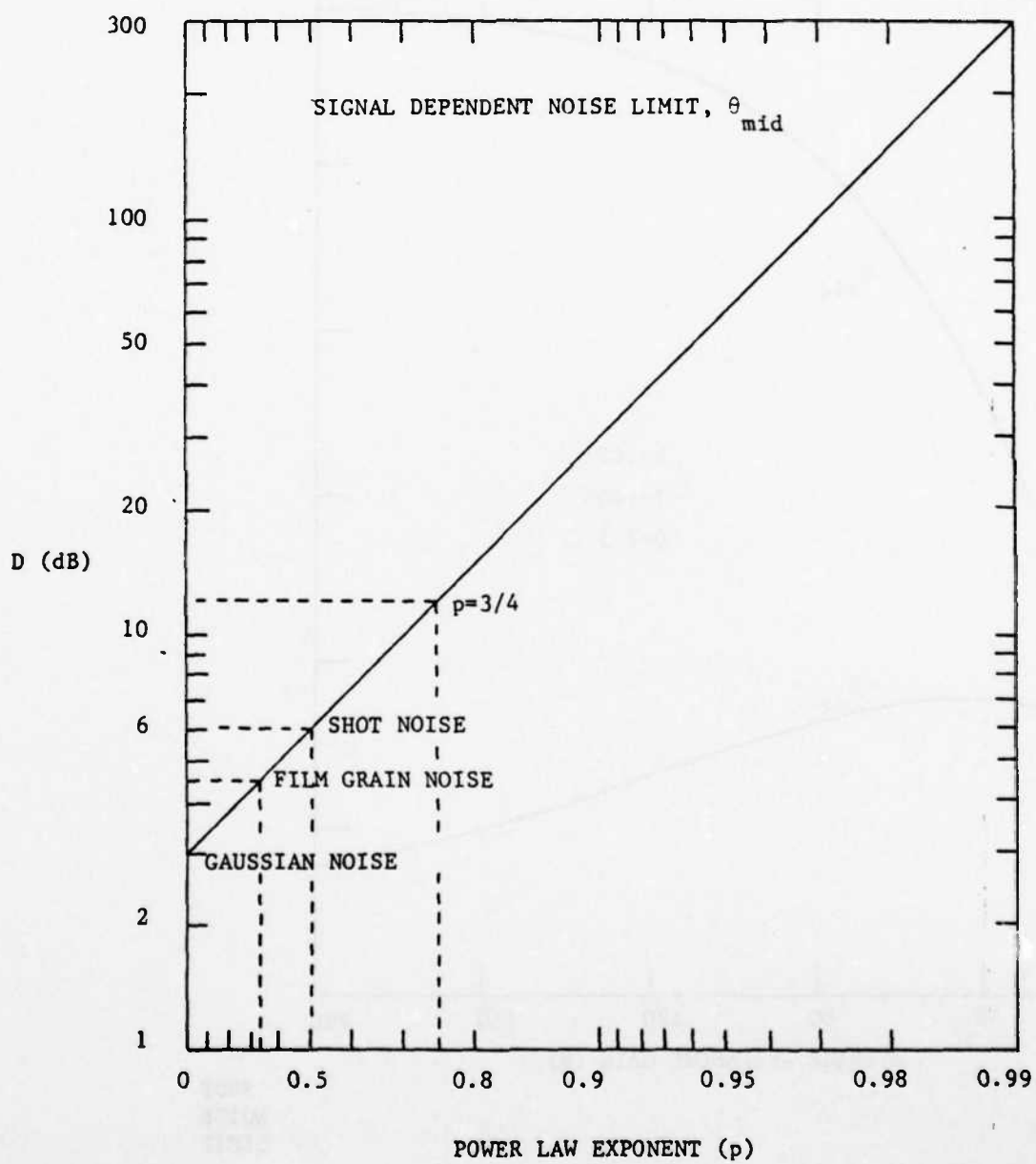


Figure 1

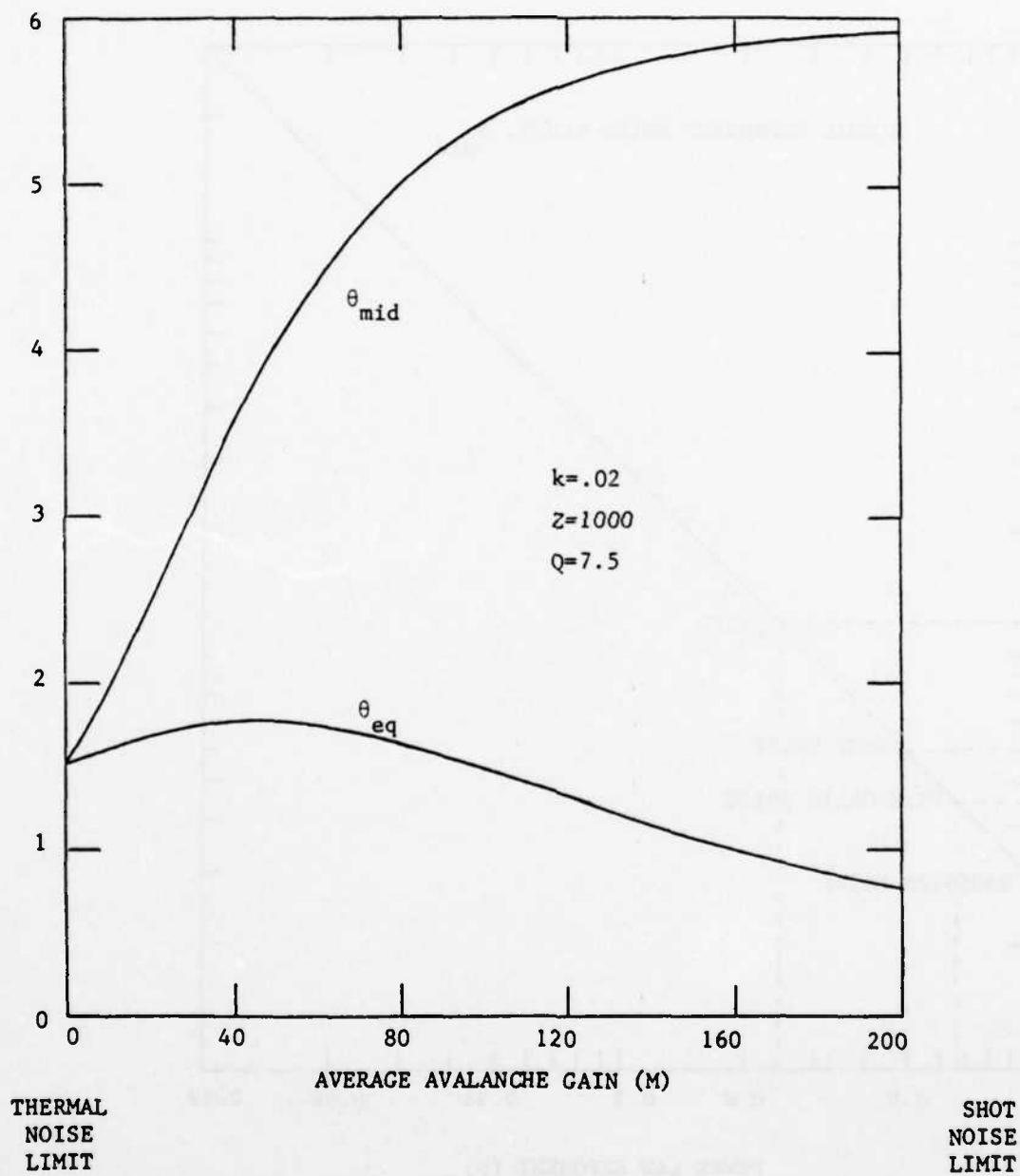


Figure 2

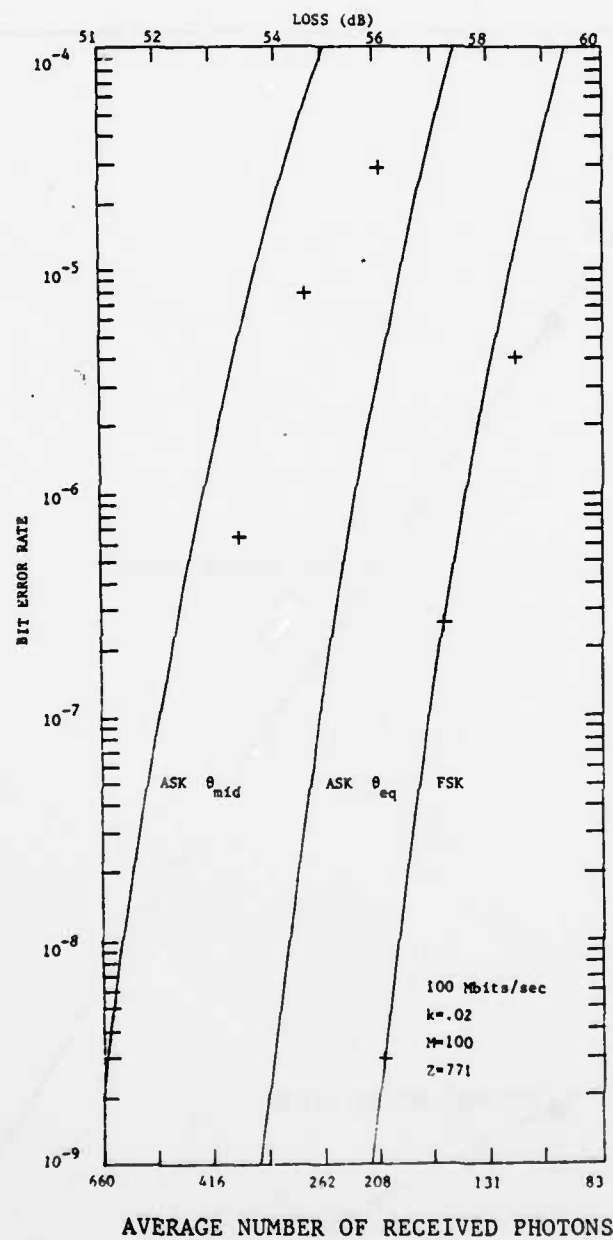


Figure 3

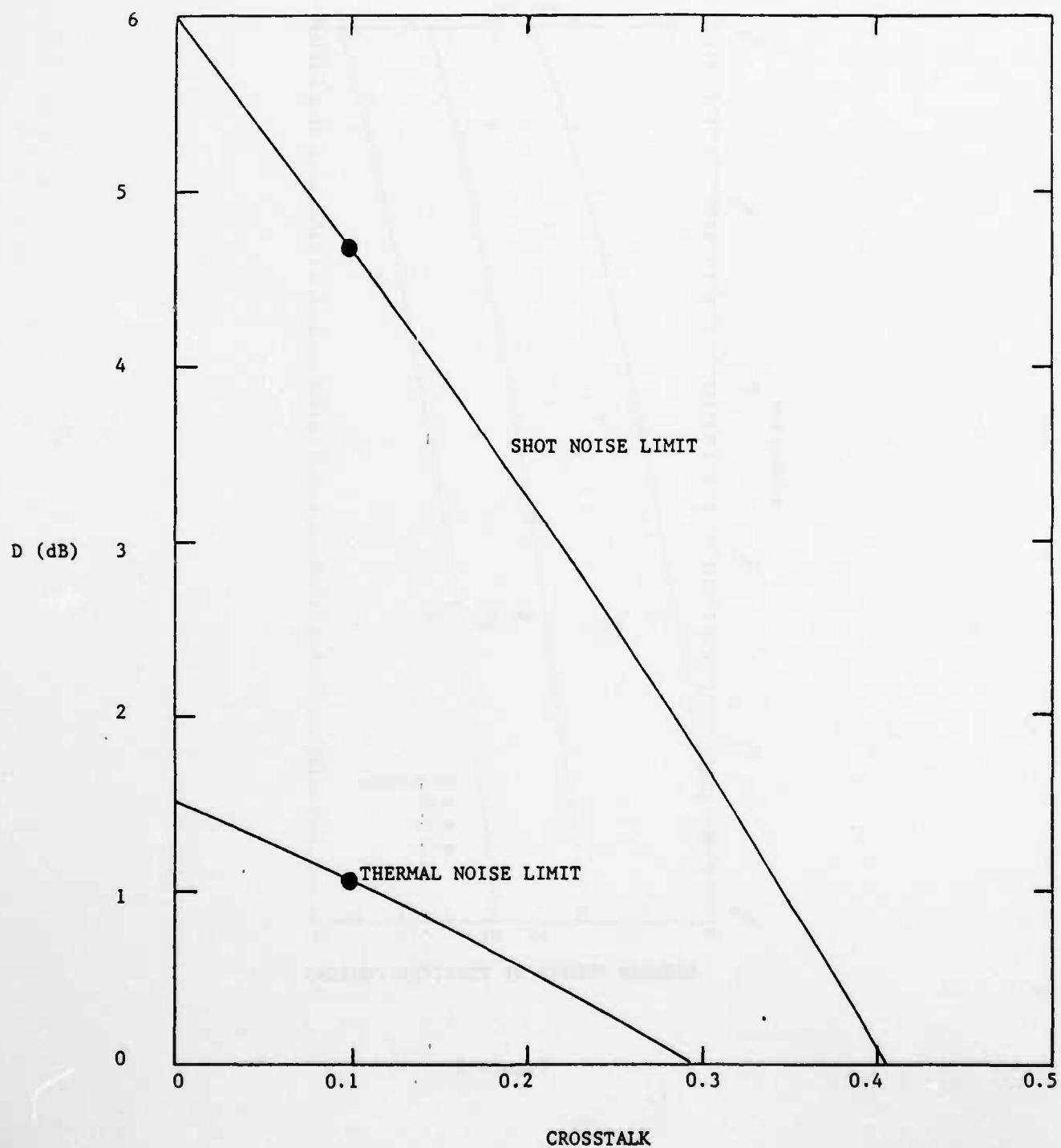


Figure 4

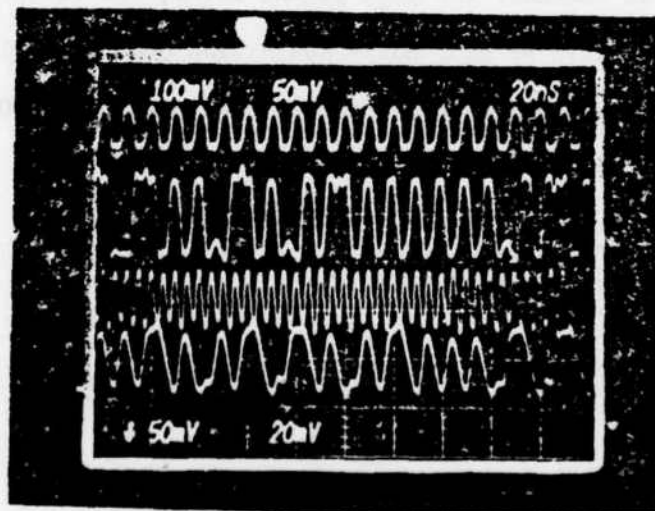


Figure 5

reduction in minimum detectable energy over ASK.

3. Conclusion

In the ideal quantum limit (photon noise only), the detection threshold is equal to one photon, and the performance of orthogonal and nonorthogonal modulation is the same. In a thermal noise dominated system, orthogonal modulation (FSK) provides a 1.5 dB decrease in minimum detectable energy, compared to nonorthogonal modulation (ASK). For a practical ASK receiver, the threshold is set at one-half the peak signal level, and FSK provides a 6 dB improvement in the limit of shot noise domination over thermal noise. Approximately 4 dB improvement was observed using FSK in a 100 M bit/sec fiber system.

- (1) P. R. Prucnal, "Wideband FSK optical fiber communication experiment," J. Opt. Communic., Issue #2 (1983).

II. PHYSICAL AND PHOTOCHEMICAL PROPERTIES OF ELECTRONIC MATERIALS

A. CONDUCTION MECHANISMS IN ULTRA-SMALL PUNCHTHROUGH MOSFET*

(B. M. Grossman, W. Hwang, F. F. Fang)

(JSEP work unit 4, 1982-1985)

(Principal Investigators: W. Hwang (212) 280-3115

E. Yang (212) 280-3120)

Designers of semiconductor devices usually regard punchthrough as a limiting regime which is to be avoided by all available means. However, when carefully controlled, the punchthrough current in a short-channel MOSFET may be used to advantage. An approach to FET design based on controlled punchthrough current offers a possible alternative to scaling methods⁽¹⁾⁻⁽³⁾ commonly used for down-sizing MOSFETs to submicron dimensions.

The scaling methods avoid punchthrough and maintain the shape of the electric-field patterns within a device and by increasing the channel doping as device geometries shrink. However, increasing the impurity concentration in the channel will introduce some undesirable effects. In order to invert the semiconductor surface, a large gate field must be applied. This places an increasing demand on the dielectric strength of the gate insulator. In addition, a larger electric field in the normal direction to the semiconductor surface, resulting from the more sharply bent surface-to-substrate energy bands in the more heavily doped channel, will lower the carrier mobility at the surface^{(4),(5)} and increase the likelihood of the injection of hot electrons into the gate insulator.⁽⁶⁾ These and other problems ultimately prevent the adherence to scaling principles with respect to channel doping in the design of ultra-small devices^{(7),(8)} and point to the need for some alternative approach. One possibility is to permit and control punchthrough current.

In this work, we show that the operating range of submicron punchthrough MOSFETs can be extended by introducing a significant and controllable barrier-limited component of current through the placement of a heavily

doped layer underneath the conducting channel.⁽⁹⁾ The heavily doped layer is placed deep enough so that the conducting channel near the surface remains punched through. A simple analytic calculation of punchthrough current in MOS transistors is not possible because of the two-dimensional (and sometimes three-dimensional) nature of the punchthrough effect.^{(9),(10)} In this paper, the conduction processes in punchthrough MOSFETs were analyzed in two-dimensions by the FIELDAY program.⁽¹¹⁾

Along a particular streamline of drain-to-source current, the mechanism for the transport of electrons is determined by the height and position of the potential-energy barrier presented to the flow of electrons and the distribution of charge in the stream. The height of the barrier and the charge distribution depend on the values of all the applied biases. The position of the peak of the barrier is mainly determined by the value of the drain-to-source voltage. In the punchthrough MOSFETs investigated in here, the doping in the conducting channel is sufficiently low and the channel length sufficiently short that the source and drain depletion regions overlap at all values of V_{DS} , creating a source-to-drain potential-energy profile with a well defined peak. At equilibrium, the peak of the barrier is located midway between the source and drain. With the application of a positive drain-to-source voltage, the barrier decreases in height and moves toward the source. The resulting total current consists of either

- (i) barrier-limited current (BLC),
- (ii) space-charge-limited current (SCLC), or
- (iii) ordinary surface-inversion current (SIC).

Along each current streamline the three conduction mechanisms effectively operate in series. Current is controlled or limited by whichever mechanism imposes the greatest restriction on the flow of carriers. When the flow of

carriers is impeded by a high energy barrier the conduction process is referred to as "barrier limited." When the major impediment to the flow of current is the retarding electric-field created by the space charge of other injected carriers, we say that the current is "space-charge limited." And, when the controlling process is due to the amount of mobile carriers induced along the entire length of the channel by a gate bias, drain-to-source current flow consists of the usual surface-inversion found in conventional MOSFETs.

Streamlines of drain-to-source current may be bundled together to form channels of BLC, SCLC, and SIC at different depths below the semiconductor surface. Then, the total current flowing into the drain consists of a mixture of BLC, SCLC, and SIC components with the relative amount of each current component determined by the applied bias. Under certain operating conditions one of the three component mechanisms may dominate. BLC at the drain will be sensitive to changes in temperature, while the temperature dependencies of SCLC and SIC are through the carrier mobility which is relatively less temperature sensitive.⁽⁵⁾ SIC and BLC will be sensitive to changes in gate bias while SCLC is nearly independent of gate bias.

Both the SCLC and ordinary SIC mechanisms share the characteristic of a high carrier concentration in the region between the source and the peak of the energy barrier, or injection region. However, they can be differentiated by their carrier-density profiles in the region between the injection point at the peak of the barrier and the drain. For the SCLC case, the space charge in the channel region mainly consists of electrons that were injected from the source. For SIC, the space charge in the region between the injection point and the drain consists of injected electrons and a much larger concentration of electrons that were induced by a positive gate potential.

To a first order approximation, charge inversion along the semiconductor

surface is controlled by gate bias while the parallel electric field between the injection point and the drain is mainly due to drain-to-source bias. However, in ultra-small MOSFETs, the parallel component of the drain-to-gate electric field may comprise a significant part of the total electric field in the parallel direction. A more positive gate bias decreases the strength of the drain-to-gate electric field and increases the strength of the gate-to-source energy bands and energy barrier. The energy bands become flatter near the drain and more steep on the drain side of the barrier peak. For the devices operating with either SIC or BLC, increasing the gate bias moves the peak of the energy barrier toward the source.

For some ranges of applied bias, current at the drain terminal may exhibit the distinguishing characteristics of one of the three mechanisms listed above. However, over most of the operating range of the device, drain current is due to a combination of these mechanisms which blurs the distinctive features of any particular conduction process. The transition from BLC to SCLC to SIC occurs in a continuous and smooth manner with changing gate and drain biases. The observations made from the data obtained from the numerical experiments are for the purpose of determining general trends toward particular conduction mechanisms. The distinct features of a particular mechanism will only appear in the limiting cases of high or low gate and drain-to-source bias. (12)

In conclusion, as devices are made smaller, transport mechanisms other than surface-inversion conduction become important and merit attention. Small geometries favor high-field drift mechanisms. The current-voltage characteristics and transport mechanisms for an ultra-small n-channel MOSFET that operates in the punchthrough mode were deduced from two-dimensional numerical simulations. Current flow in this device was controlled by

barrier-limited, space-charge limited or surface-inversion conduction mechanisms. The presence of these conduction processes was determined by varying temperature, channel length and applied biases. Although the thickness of the gate insulator was not varied in the present study, increasing the thickness of the insulator would have raised the threshold voltage for surface-inversion conduction and extended the range of barrier-limited control by the gate. Space-charge limited current is relatively unaffected by the thickness of the gate insulator.⁽¹²⁾

A punchthrough MOSFET is less susceptible to the undesirable effects caused by the higher normal electric field found in scaled-down devices of the same size. The degradation of performance caused by the injection of hot carriers into the gate insulator and reduction of carrier mobility at the semiconductor surface is partially relieved in the proposed device. The relatively large activation energy at the onset of drain-to-source conductance warrants careful design consideration so that the device remains "off" even at elevated temperatures. An obvious remedy for this problem is to increase the acceptor impurity concentration in the channel at the expense of reducing the large-signal transconductance.⁽¹²⁾

*This research was also supported by IBM.

- (1) R. H. Dennard, F. H. Gaensslen, H. N. Yu, V. L. Rideout, E. Bassous, and A. R. LeBlanc, IEEE J. Solid-State Circuits, SC-9, 256 (1974).
- (2) J. R. Brews, W. Fichtner, E. H. Nicollian, and S. M. Sze, IEEE Electron Device Letters, EDL-1, 2 (1980).
- (3) W. Fichtner, E. N. Fuls, R. L. Johnson, R. K. Watts, and W. W. Weick, IEDM, Technical Digest, 384 (1983).
- (4) F. F. Fang and A. B. Fowler, Physical Review, 169, 619 (1968).
- (5) S. C. Sun and J. D. Plummer, IEEE Trans. Electron Devices, ED-27, 1497 (1980).

- (6) P. E. Cottrell, R. R. Troutman, and T. H. Ning, IEEE J. Solid-State Circuits, SC-14, 442 (1979).
- (7) R. H. Dennard, J. Vac. Sci. Technol. 19, 537 (1981).
- (8) Y. El-Mansy, IEEE Trans. Electron Devices, ED-29, 567 (1982).
- (9) L. M. Dang and M. Konaka, IEEE Trans. on Electron Dev. ED-27, 1533 (1980).
- (10) J. J. Barnes, K. Shimohigashi, and R. W. Dutton, IEEE J. Solid-State Circuits, SC-14, 368 (1979).
- (11) E. M. Buturla, P. E. Cottrell, B. M. Grossman, and K. A. Salsburg, IBM, J. Res. Develop. 25, 218 (1981).
- (12) B. M. Grossman, W. Hwang, and F. F. Fang, Solid State Electronics, to be published.

B. COLLECTION EFFICIENCY OF THIN-FILM METAL-INSULATOR-SEMICONDUCTOR PHOTOVOLTAIC DEVICES*

(S. M. So, W. Hwang)

(JSEP work unit 4, 1982-1985)

(Principal Investigators: W. Hwang (212) 280-3115

E. Yang (212) 280-3120)

When a metal-insulator-semiconductor (MIS) photovoltaic device is illuminated with light of energy larger than the bandgap of the semiconductor, the collection efficiency or the internal quantum efficiency η of the device is customarily calculated using the Gartner model.⁽¹⁾ This model assumes a complete collection of photogenerated minority carriers in the depletion region and predicts η increases monotonically with increasing absorption coefficient. However, experimental data often indicate that η exhibits a peak at some value of absorption coefficient and falls with larger values.

A theory is proposed to calculate η of a thin-film MIS photovoltaic device with back-surface field.⁽²⁾ The model incorporates two loss mechanisms to account for the falloff in the short wavelength response. First, due to the image force effect which produces a majority carrier potential maximum located at x_m near the illuminated surface, all carriers photogenerated between the surface and x_m are swept to the surface and do not contribute to the photocurrent. Second, the photogenerated majority carriers which are generated in the depletion region and diffuse against the electric field to x_m may be collected at the metal surface and thus reduces the photocurrent.

The net collection efficiency is calculated as the difference between the minority and majority carrier collection efficiencies at the metal surface. It is assumed that recombination inside the space-charge region is negligible. This is a reasonable assumption for thin-film semiconductors which normally have wide bandgaps and low intrinsic carrier concentrations. The number of minority carriers that are photogenerated in the space-charge region and

diffuse against the electric field away from the surface is found to be small.⁽³⁾ Therefore, all the minority carriers photogenerated in the space-charge region can be considered as being swept out of that region. Consequently, when the semiconductor is thin enough and the entire device is totally depleted, the photogenerated minority carrier current density is determined by the generation rate. In the case when the device is not totally depleted and a neutral region exists in the semiconductor, the minority carrier current collected at the metal surface is the sum of the drift current due to the minority carriers photogenerated in the depletion region and the diffusion current of the photogenerated minority carriers diffusing into the depletion region from the bulk and from the back injection region. This diffusion current is limited by the minority carrier diffusion length. Some of the majority carriers photogenerated in the depletion region can diffuse against the electric field towards the interface, thus reducing the net photocurrent. This diffusion loss can be accounted for by evaluating the majority carrier current density flowing towards the interface in terms of an effective collection velocity v_c at the potential maximum.⁽⁴⁾ In MIS devices, v_c depends upon the concentration of interface states, being high when there are many states, but much lower when the interface is passivated. For an intimate Schottky barrier device, v_c is on the order of the electron thermal velocity, about 10^7 cm/sec. This diffusion current of the photogenerated majority carriers is calculated from the transport and continuity equations, the solution of which requires the knowledge of the potential distribution in the depletion region. The potential distribution is calculated from Poisson's equation for a homogeneous and uniformly doped semiconductor with the modification due to the image force lowering effect.

Detailed derivation of the equations and sample calculations for a MIS

n-type CdTe photovoltaic device have been reported in Ref. (2). Part of the results are represented here by Figs. 1 through 4. The net collection efficiency is computed at zero bias as a function of wavelength of low level illumination varying from 300 to 900 nm for different semiconductor thickness, doping density, electron mobility, and effective collection velocity. The following parameters for n-type CdTe are used in the computation: hole (minority carrier) diffusion length = 0.25 μm , CdTe relative dielectric constant = 9.6, temperature = 300 $^{\circ}\text{K}$, insulating layer thickness = 25 \AA , Schottky barrier height = 0.82 V, and the effective density of states in the conduction band = $9.155 \times 10^7 \text{ cm}^{-3}$.

Figure 1 shows that the net collection efficiency is strongly dependent on v_c . When v_c is large, meaning high interface state density, the short wavelength falloff is also large. On the contrary, when v_c is low, meaning the interface is well passivated, the short wavelength response is relatively better.

In Figure 2, the net collection efficiency is calculated as a function of doping density which affects the electric field in the depletion region. For high doping density, the depletion width is narrow and the electric field near the surface is high. The short wavelength falloff is small because losses due to the diffusion and the image force effects which are electric field dependent are less. However, the long wavelength response is poor because of the short depletion width and the short minority carrier diffusion length. For lower doping density, the spectral response changes in accordance with the variations in depletion width and electric field.

Figure 3 shows the effect of the semiconductor thickness on the net collection efficiency. When thickness is thin, illumination of longer wavelength cannot be totally absorbed, and therefore, the long wavelength

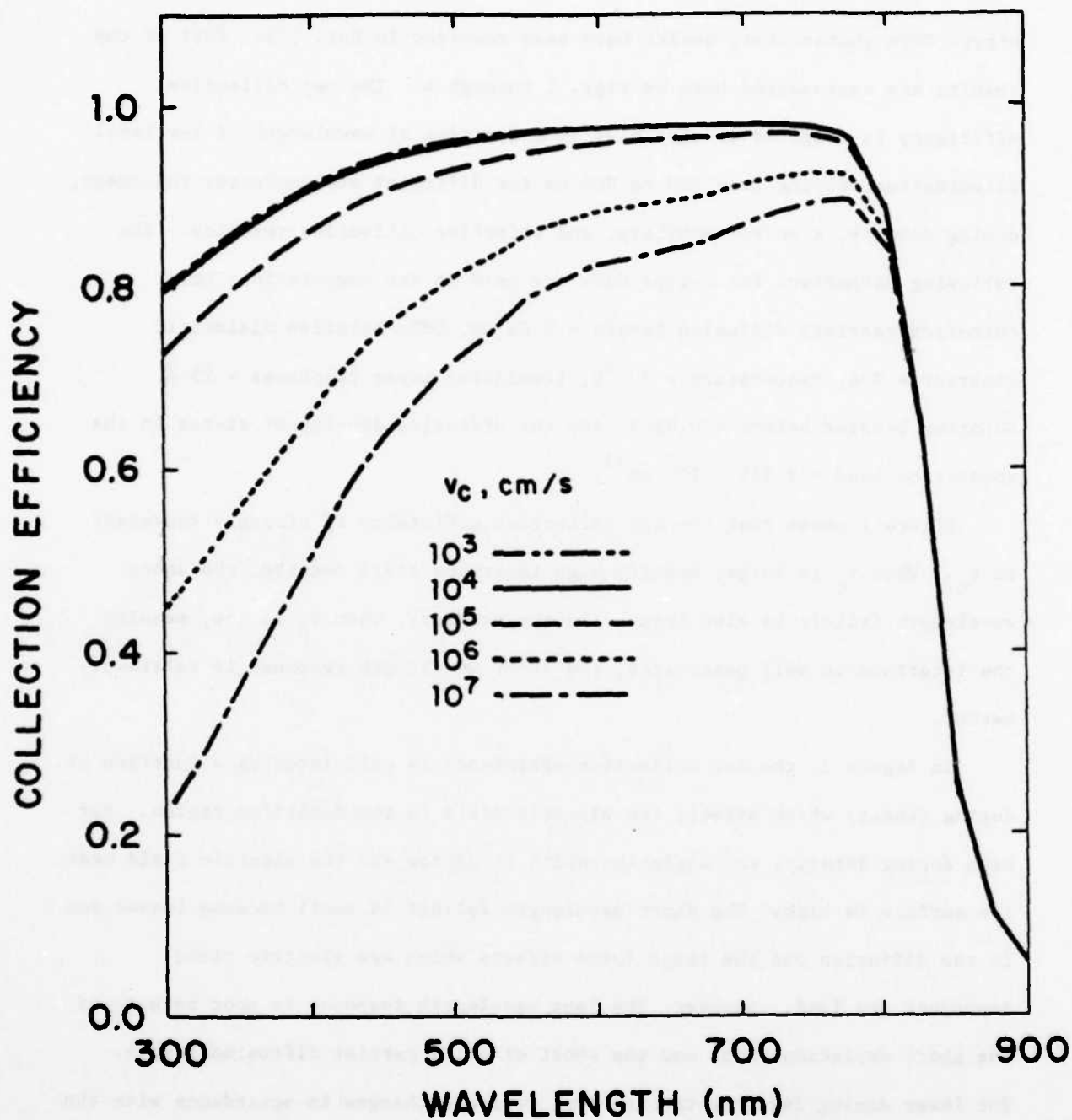


Figure 1. Calculated net collection efficiency vs wavelength with $v_c = 10^3, 10^4, 10^5, 10^6$, and 10^7 cm/sec, electron mobility = $100 \text{ cm}^2/\text{V sec}$, semiconductor thickness = $2 \text{ }\mu\text{m}$, and doping density = 10^{14} cm^{-3} .

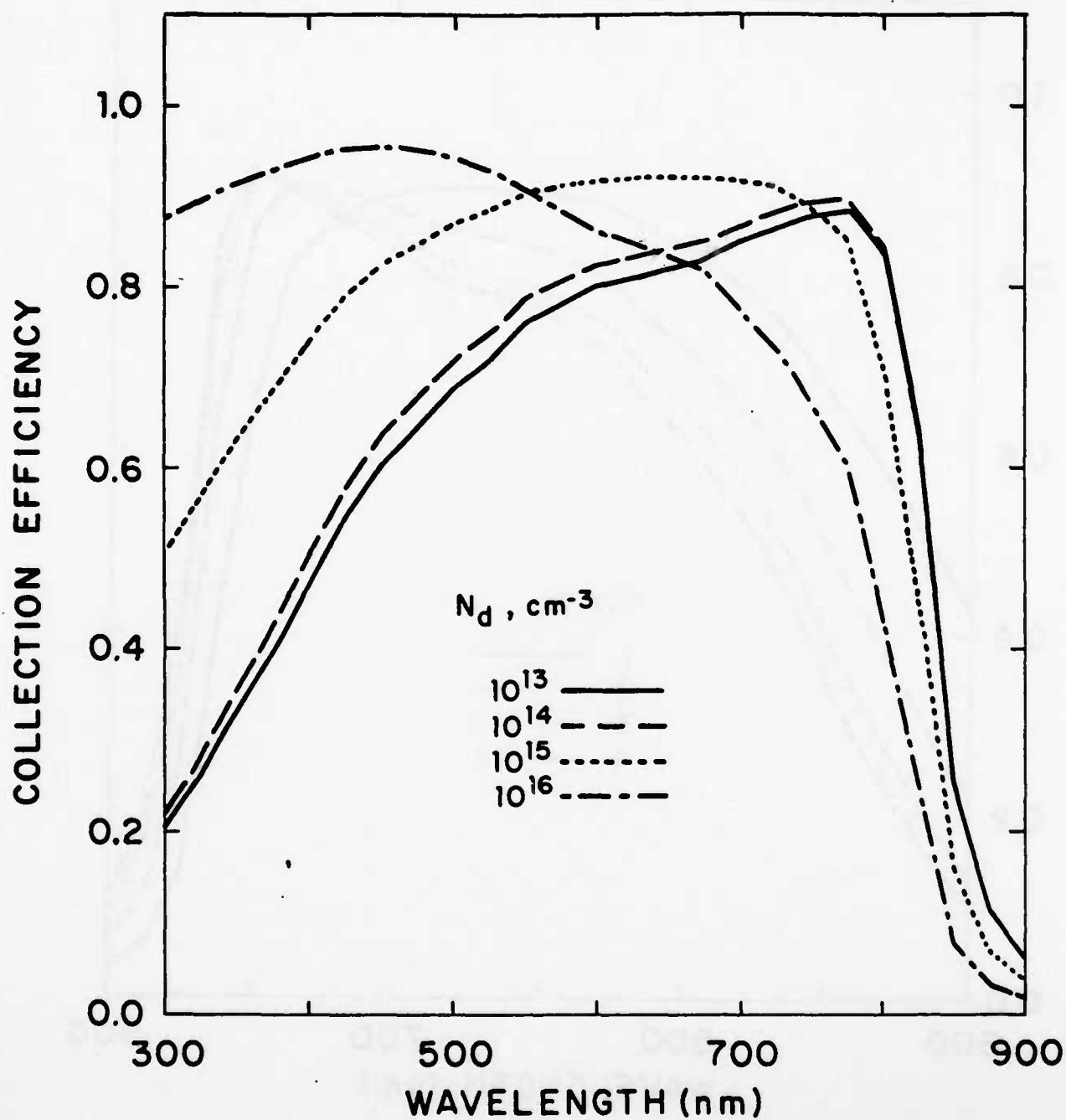


Figure 2. Calculated net collection efficiency vs wavelength with doping density $N_d = 10^{13}$, 10^{14} , 10^{15} , and 10^{16} cm^{-3} , electron mobility = $100 \text{ cm}^2/\text{V sec}$, semiconductor thickness = $2 \mu\text{m}$, and $v_c = 10^7 \text{ cm/sec}$.

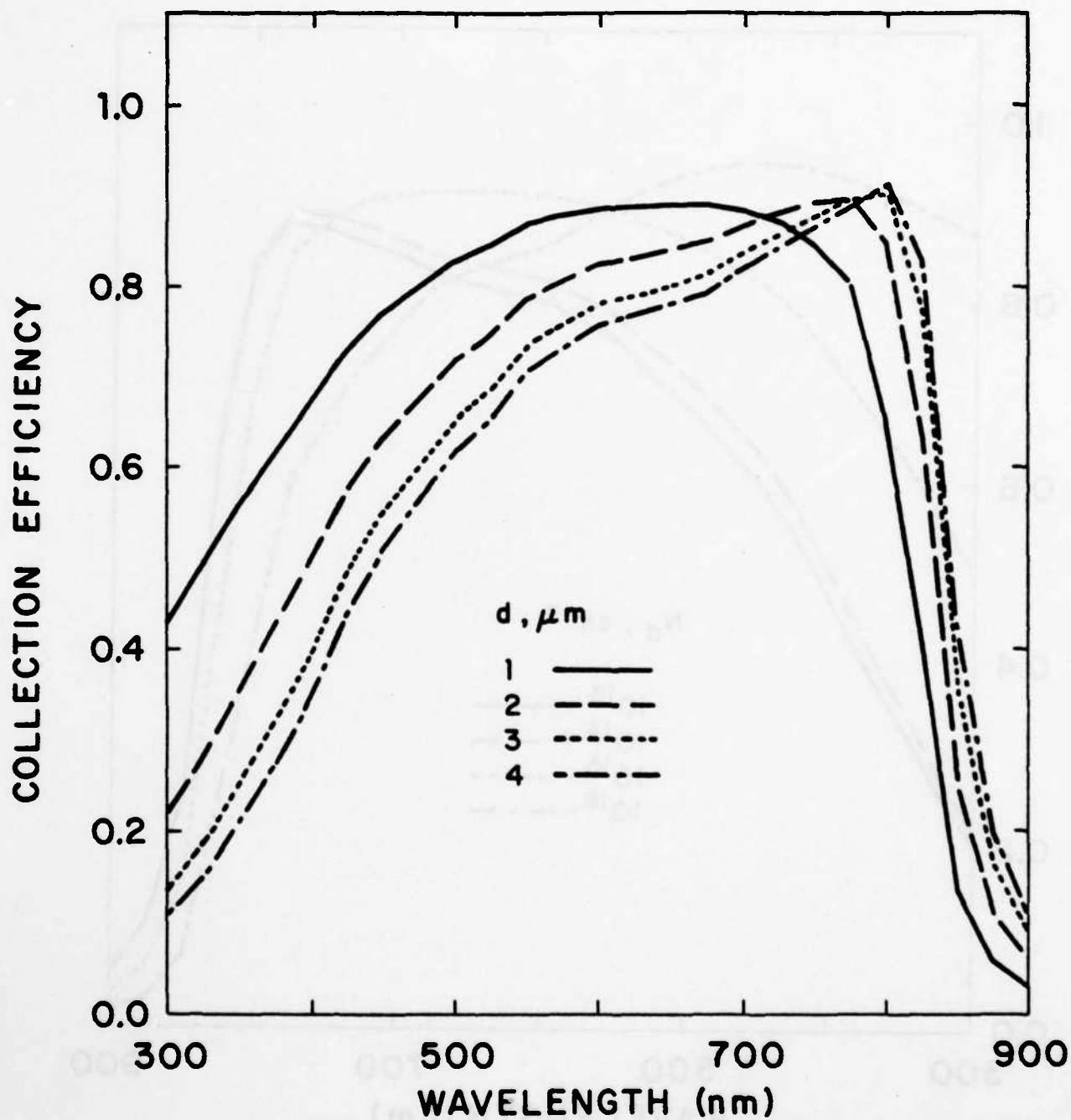


Figure 3. Calculated net collection efficiency vs wavelength with semiconductor thickness $d = 1, 2, 3, \text{ and } 4 \mu\text{m}$, electron mobility $= 100 \text{ cm}^2/\text{V sec}$, doping density $= 10^{14} \text{ cm}^{-3}$, and $v_c = 10^7 \text{ cm/sec}$.

response is poor. However, in this case when the thickness is thinner resulting that the device becomes totally depleted, the surface potential gradient is increased as the thickness is decreased. Hence, the short wavelength falloff is decreased as thickness decreases. Therefore, the thickness and the doping density can be designed to meet the desired spectral response requirement.

Figure 4 compares the efficiency as predicted separately by the diffusion and the combined diffusion and the image force effects models. When v_c is large, the dominant loss mechanism is due to the diffusion of the photogenerated majority carriers to the metal surface, and the difference between the two models is small. When v_c is small, the difference between the two models is large, especially in the short wavelength region, which indicates that the collection losses due to the image force effect are significant.

In conclusion, for any semiconductor with large absorption coefficient and a doping density below 10^{15} cm^{-3} , the calculated results indicate that the loss in collection efficiency due to the image force effect is significant. For MIS photovoltaic devices with an effective surface collection velocity less than 10^6 cm/sec , the collection losses due to the image force effect and the diffusion of the photogenerated majority carriers are comparable. As a result, the combined theory incorporating both the image force and the diffusion loss mechanisms is able to model quantitatively the collection efficiency of a thin-film MIS photovoltaic device more accurately than either model alone. When the whole semiconductor is a space-charge region, the potential distribution, the location of the potential maximum, and consequently the collection efficiency are shown to depend on the thickness of the semiconductor. The collection efficiency can be increased by reducing the

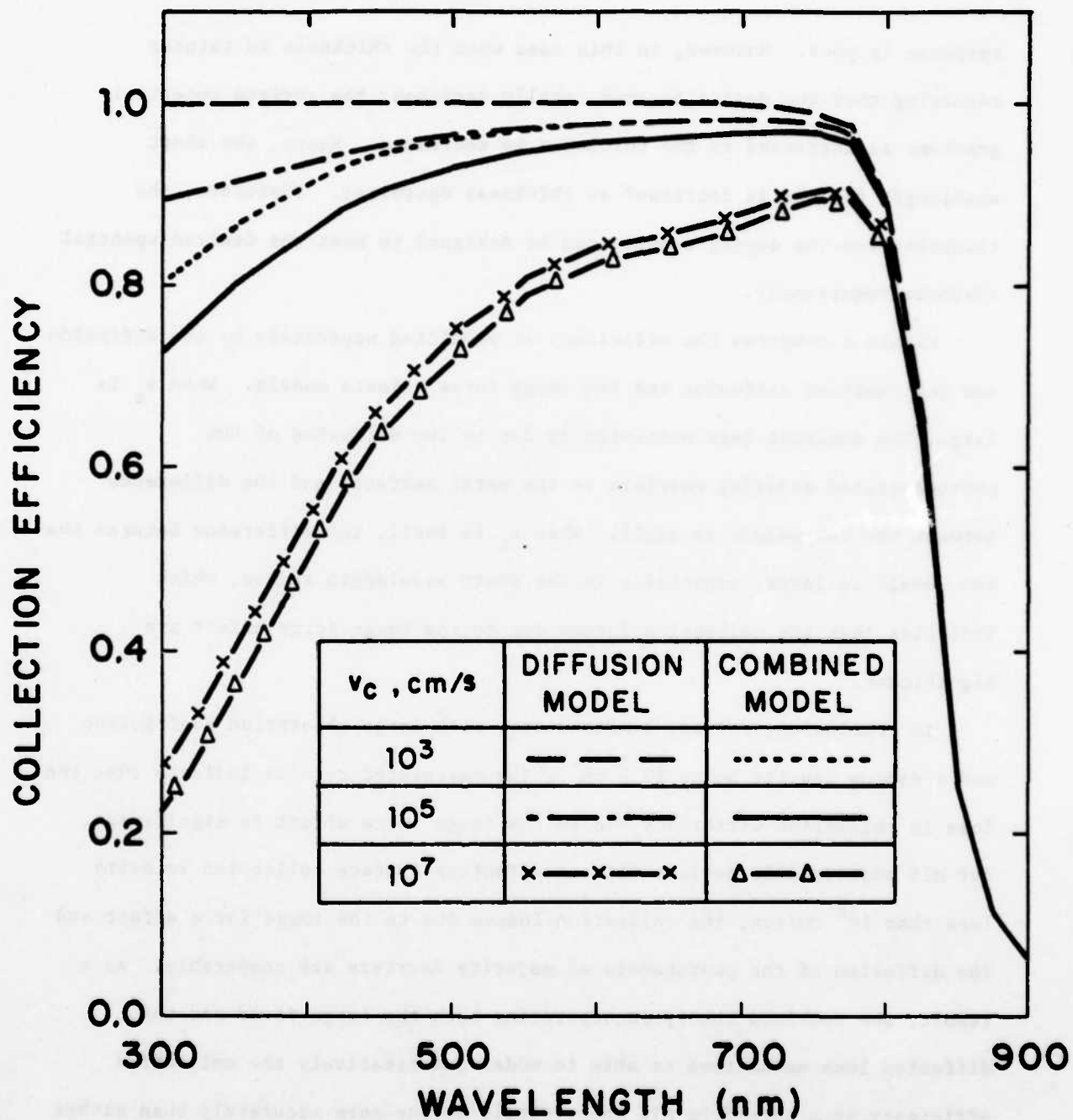


Figure 4. Calculated net collection efficiency vs wavelength with $v_c = 10^3$, 10^5 , and 10^7 cm/sec, doping density = 10^{14} cm $^{-3}$, semiconductor thickness = 2 μ m, and electron mobility = 100 cm 2 /V sec for the diffusion and the combined diffusion and image force models.

surface collection velocity and optimizing the thickness and doping of the semiconductor, or by designing a high-low doping profile such that the collection losses for the entire spectrum are minimized.

*This work is supported by the National Science Foundation under the contract NSF-ECS-82-17677.

- (1) W. W. Gartner, Phys. Rev. 116, 84 (1959).
- (2) S. M. So, W. Hwang, P. V. Meyers, and C. H. Liu, J. Appl. Phys. 55(1), 253 (1984).
- (3) J. Reichman, Appl. Phys. Lett. 38, 251 (1981).
- (4) C. R. Crowell and S. M. Sze, Solid-State Electron. 9, 1035 (1966).

C. PHOTOCONDUCTANCE TRANSIENT RESPONSE IN POLYCRYSTALLINE SILICON*

(E. Poon, W. Hwang, E. Yang, H. Evans)

(JSEP work unit 4, 1982-1985)

(Principal Investigators: W. Hwang (212) 280-3115

E. Yang (212) 280-3120)

When under illumination, the transport of excess carriers in polycrystalline silicon is obstructed by the grain boundaries (GBs) in two ways. The electric fields in the depletion regions around the GBs tend to pin down the majority carriers at the depletion edges and minority carriers at the GBs, and the trapping and recombination process at the GBs reduce the minority carrier lifetime and diffusion length. The former is well demonstrated by the photovoltaic effect experiment^{(1),(2)} and the latter by the photoconductance spatial scanning experiment.⁽³⁾ When the GB is under direct illumination, the former one also gives rise to a seemingly barrier height lowering as in the latter one. The fundamental difference, however, is in the transient time involved. Carrier separation takes place in picoseconds and is not too temperature sensitive, whereas carrier trapping and emission require a time ranging from μ s to ms and are extremely temperature sensitive. Since the photoconductance change is a result of direct interaction between charge carriers and the GB traps, the measurement of the photoconductance should provide valuable information on various GB parameters.

Last year we reported⁽⁴⁾ a GB trap energy 0.5 eV below the conduction band with an associated electron thermal capture cross-section of $2 \times 10^{-16} \text{ cm}^2$. The interpretation of the data is based on the assumption that the measured photoconductance voltage decay time is the time constant of the trap. Theoretical support of this interpretation was not given at that time.

In this report, the photoconductance transient response in polycrystalline silicon is studied theoretically. The conventional

Shockly-Read-Hall statistics^{(5),(6)} are used to describe the carrier emission and trapping processes at the GB traps. The results show that, under appropriate conditions, the minority carrier capture and emission time constants can be obtained directly from the photoconductance transient response. The theory not only supports the previous interpretation, it further shows that other GB parameters, such as the trap density, the minority carrier lifetime and photo-capture cross-section of the traps can also be deduced. The photoconductance measurement is therefore useful in studying GB deep level states.

As shown in Fig. 1, a constant d.c. bias (V_B) is applied across a large grain p-type silicon bicrystal which is in series with a load resistor R_L . GB traps are assumed to be donor-like. When under illumination, the photoconductance voltage change across R_L is given by:⁽⁴⁾

$$\Delta V_L = V_m [1 - \exp(-\phi_{bo} - \phi_b)kT)] \quad (1)$$

where

$$V_m = (f_{sp} V_B k / R_L A A^* q T) \exp(\phi_{bo} / kT) \quad (2)$$

f_{sp} is included to account for the effect of the spot-size. As will be seen below, under the appropriate condition, Eq. (1) allows deduction of GB barrier height, rise time and fall time of the traps.

A. Steady State Photoconductance

If the intensity of the light source is high enough to reach the flatband condition, from Eq. (1), the maximum magnitude of the signal is given by:

$$(\Delta V_L)_{f.b.} = V_m \quad (3)$$

If the pre-exponential factor in Eq. (2) is relatively insensitive to the temperature in logarithmic scale, the slope of the plot of $\ln(\Delta V_L)_{f.b.}$ versus

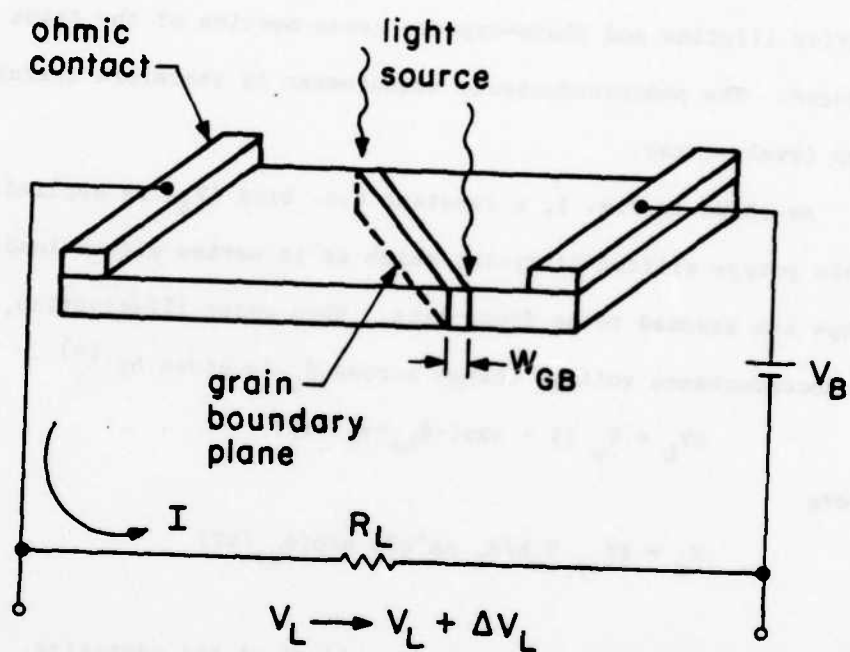


Figure 1. Schematic diagram of photoconductance measurement.

$1/T$ then gives the barrier height in the dark, ϕ_{bo} . Experimental results reported previously⁽⁴⁾ indicate that f_{sp} does not depend strongly on T , at least in logarithmic scale.

B. Transient Photoconductance

Assuming injection is not too high such that there is no significant change in majority carrier (hole) concentration in the bulk. Then

$$(\phi_{bo} - \phi_b)/q = V_{do} - V_d \quad (4)$$

Using depletion approximation,⁽⁷⁾ the diffusion potential V_d is given by:

$$V_d = (q/8\epsilon N_a) N_T^2 \quad (5)$$

where N_T is the total empty donor-like traps per unit area, ϵ is the permittivity and N_a is the doping concentration. For a general distribution,

$$N_T(t) = \int_{E_f}^{E_c} N_t(E, t) dE \quad (6)$$

where N_t is the empty trap concentration with energy E_t .

The detailed derivation of the transient response will not be presented here and the readers are merely referred to reference (8). In brief, the change of the GB charge state can be described by the equation:

$$N_t(t) = N_t(\infty) - [N_t(\infty) - N_t(0)] \exp(-t/\tau) \quad (7)$$

For the rise,

$$1/\tau_T = e_n + C_n (n_0 + \Delta n) + I\sigma_{ph} \quad (8)$$

$$N_t(\infty) = \tau_r N_{to} (e_n + I\sigma_{ph}) \quad (9)$$

where N_{to} is the total trap concentration with energy E_t , n_0 is the electron concentration at the GB in the dark and Δn is the excess electron concentration. In the region near the end of the decay,

$$1/\tau_d = e_n + C_n n_0 \approx e_n \quad (10)$$

$$N_t(\infty) = \tau_d N_{to} e_n \quad (11)$$

From Eqs. (8) and (10),

$$\begin{aligned} 1/\tau_r - 1/\tau_d &= C_n \Delta n + I \sigma_{ph} \\ &= C_n (\gamma \tau_n / \lambda) I + I \sigma_{ph} \end{aligned} \quad (12)$$

where τ_n is the effective electron lifetime, λ is the absorption depth, σ_{ph} is the photo-capture cross-section of the trap and γ is the loss of electrons due to non-ideal quantum conversion and diffusion to the bulk areas. In the region where

$$V_{do} - V_d \ll kT/q \equiv V_T \quad (13)$$

it can be shown that for the rise transient,

$$(\Delta V_L)_r = \int_{E_f}^{E_c} \alpha(E) N_{to}(E) [1 - \exp(-t/\tau_r)] dE \quad (14)$$

with

$$\alpha(E) = (V_m/V_T) (qV_{do}/2\epsilon N_a)^{1/2} [N_t(E,0)/N_{to} - \tau_r (e_n + I \sigma_{ph})] \quad (15)$$

For the decay,

$$(\Delta V_L)_d = \int_{E_f}^{E_c} \beta(E) N_{to}(E) \exp(-t/\tau_d) dE \quad (16)$$

with

$$\beta(E) = (V_m/V_T) (qV_{do}/2\epsilon N_a)^{1/2} [1 - f(E, E_f) - N_t(E,0)/N_{to}(E)]_d \quad (17)$$

If the trap distribution is discrete, Eqs. (14) and (16) reduce to the familiar forms:

$$(\Delta V_L)_r^{\text{discrete}} = \sum_i \alpha(E_i) N_{to}(E_i) [1 - \exp(-t/\tau_r(E_i))] \quad (18)$$

$$(\Delta V_L)_d^{\text{discrete}} = \sum_i \beta(E_i) N_{to}(E_i) \exp(-t/\tau_d(E_i)) \quad (19)$$

Eq. (19) therefore supports our previous interpretation of the experimental data.

*This work is supported by the National Science Foundation under the contract NSF-ECS-82-17677.

- (1) Y. Matukura, Jpn. J. Appl. Phys. 2, 91 (1963).
- (2) L. Sosnowski, J. Phys. Chem. Solids 8, 142 (1959).
- (3) P. Panayotatos, E. S. Yang, and W. Hwang, Solid-State Electron. 25, 417 (1972).
- (4) E. Poon, E. S. Yang, H. L. Evans, W. Hwang, and R. M. Osgood, Jr., Appl. Phys. Lett. 42, 285 (1983); also Progress Report No. 33, Columbia Radiation Lab., Columbia Univ., p. 63 (1983).
- (5) W. Shockley and W. T. Read, Jr., Phys. Rev. 87, 835 (1952).
- (6) R. N. Hall, Phys. Rev. 87, 387 (1952).
- (7) E. S. Yang, Fundamentals of Semiconductor Devices (McGraw-Hill, 1978), Ch. 4-2.
- (8) E. K. Poon, Chapter 5, Ph.D. Dissertation, Dept. of Electrical Engineering, Columbia Univ., 1984 (to be published).

D. MODELING OF GRAIN BOUNDARY EFFECTS ON THE PERFORMANCE OF
METAL-INSULATOR - THIN FILM POLYCRYSTALLINE SEMICONDUCTOR
PHOTOVOLTAIC DEVICES*

(S. M. So, W. Hwang)

(JSEP work unit 4, 1982-1985)

(Principal Investigators: W. Hwang (212) 280-3115

E. Yang (212) 280-3120)

The photovoltaic conversion efficiency of a single-crystal silicon device can be calculated by the superposition principle.⁽¹⁾ Due to the higher absorption coefficient, lower carrier mobilities, and lower free carrier concentrations, typical of thin-film polycrystalline semiconductor photovoltaic devices, however, the photogenerated majority carrier current in these devices is a strong function of light level.^{(2),(3)} Thus, the superposition principle does not apply for this type of devices, and the efficiency calculated by this principle may be seriously over-estimated.⁽⁴⁾

We have developed a model based on experimental observations of thin-film polycrystalline metal-insulator-semiconductor (MIS) photovoltaic device with back surface field.⁽⁵⁾ Photocapacitance measurements, showing that the depletion width and the free majority carrier density are modulated by light intensity, suggest the presence of traps. The grain sizes of thin-film polycrystalline semiconductors are small - typically about one micron. With grain-boundary interface state density about 10^{10} to $10^{13} \text{ cm}^{-2} \text{ eV}^{-1}$, the equivalent bulk trap density due to the grain-boundary interface states is significant compared to the doping density of interest. The analysis based on the experimental data indicates that there is a dominant majority-carrier trap level around the mid-gap. The experimental and theoretical studies on polysilicon show that the energy distribution of grain-boundary interface states is well approximated by a discrete level located near the center of forbidden gap.⁽⁶⁾ Therefore, we can assume that the dominant trap originates

from the grain-boundary interface states.

Under steady-state illumination, grain-boundary interface states trap majority carriers which subsequently recombine with photogenerated minority carriers. The trap density affects the minority carrier lifetime and diffusion length which determine the collection efficiency of the photogenerated minority carrier current in the bulk. In the neutral region of the semiconductor, the trap occupancy under steady-state illumination is governed by Shockley-Read-Hall statistics.⁽⁷⁾ By equating the generation and trap recombination rates and assuming charge neutrality in the bulk neutral region, the steady-state majority carrier density, minority carrier lifetime, and trap occupancy can be solved numerically. The free majority carrier density is found to be less than the doping density and is modulated by the trap density. As the trap density is increased, free majority carrier density is decreased and the bulk Fermi level moves closer towards the mid-gap, and accordingly the built-in potential is decreased. The depletion width, location of the potential maximum, and the electric field in the depletion region are all affected by the changes in the built-in potential and the free majority carrier density.

The net photocurrent is the algebraic sum of the photogenerated minority carrier current, the junction majority and minority carrier currents due to bias, and the photogenerated majority carrier current collected at the metal surface, which arises principally from two sources: first, the diffusion against the electric field of majority carriers photogenerated in the depletion region to the surface; and second, the collection of majority carriers which are photogenerated between the interface and the potential maximum created by the image force and swept to the surface by the high electric field there.⁽⁸⁾ The performance of a photovoltaic device is usually

evaluated by its short-circuit current, open-circuit voltage, and photovoltaic conversion efficiency. Detailed derivation of the equations and calculated results are reported in Ref. (5). Some sample calculations are shown here for the specific case of thin-film polycrystalline n-type CdTe MIS photovoltaic devices.

Figure 1 shows the difference between the majority carrier current density in the dark and under AM1 illumination for a MIS device with diode ideality factor $A = 1.3$, effective collection velocity $v_c = 10^5$ cm/sec, semiconductor thickness $d = 1$ micron, grain size $g = 0.5$ micron, and grain-boundary interface state density $N_{is} = 10^{12}$ cm⁻² eV⁻¹. The photogenerated majority carrier current is very sensitive to the electric field in the depletion region, being small when the field is high and large when it is low. It is the dominant opposing current under low bias and is larger for device of lower doping density, higher trap density, and higher collection velocity.

The photovoltaic conversion efficiency of a MIS device with $A = 1.3$, $d = 1$ micron, and $v_c = 10^5$ cm/sec is compared for different doping density and trap density, as shown in Fig. 2. When doping density is high, the depletion width is narrow and the minority carrier diffusion length is important. When doping density is low, however, the depletion width is wide and the photogenerated majority carrier current is critical. Only when the trap density can be very low, meaning longer minority carrier diffusion length, the devices will perform better if they are made of higher doping density, as indicated by curves a and b. Otherwise there will be an optimum doping density or depletion width.

In Fig. 3, the efficiency is examined as a function of the effective collection velocity for a 1 micron thick device with $A = 1.3$. In general

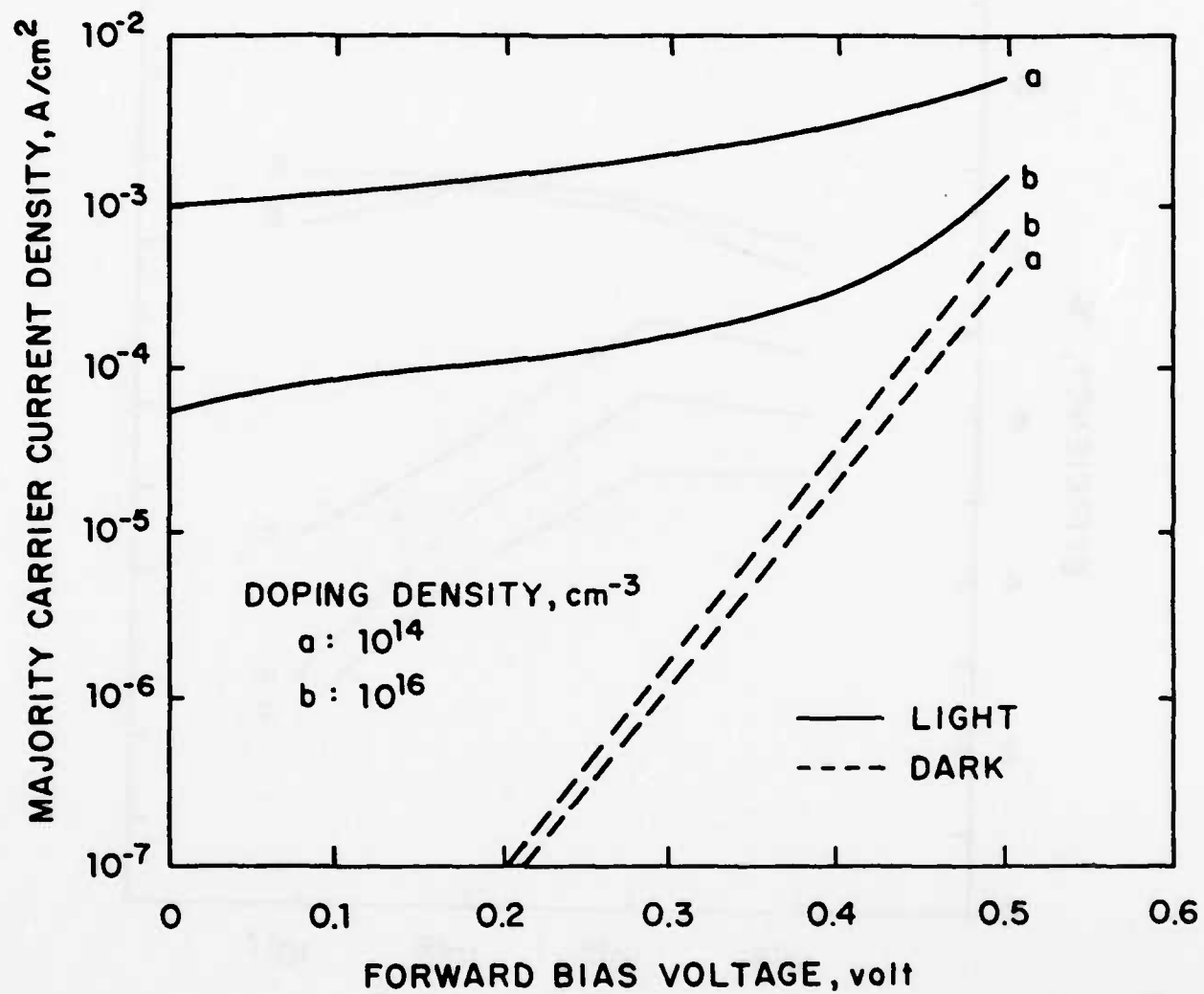


Figure 1. Calculated majority carrier current density in the dark and under AM1 illumination of a MIS photovoltaic device.

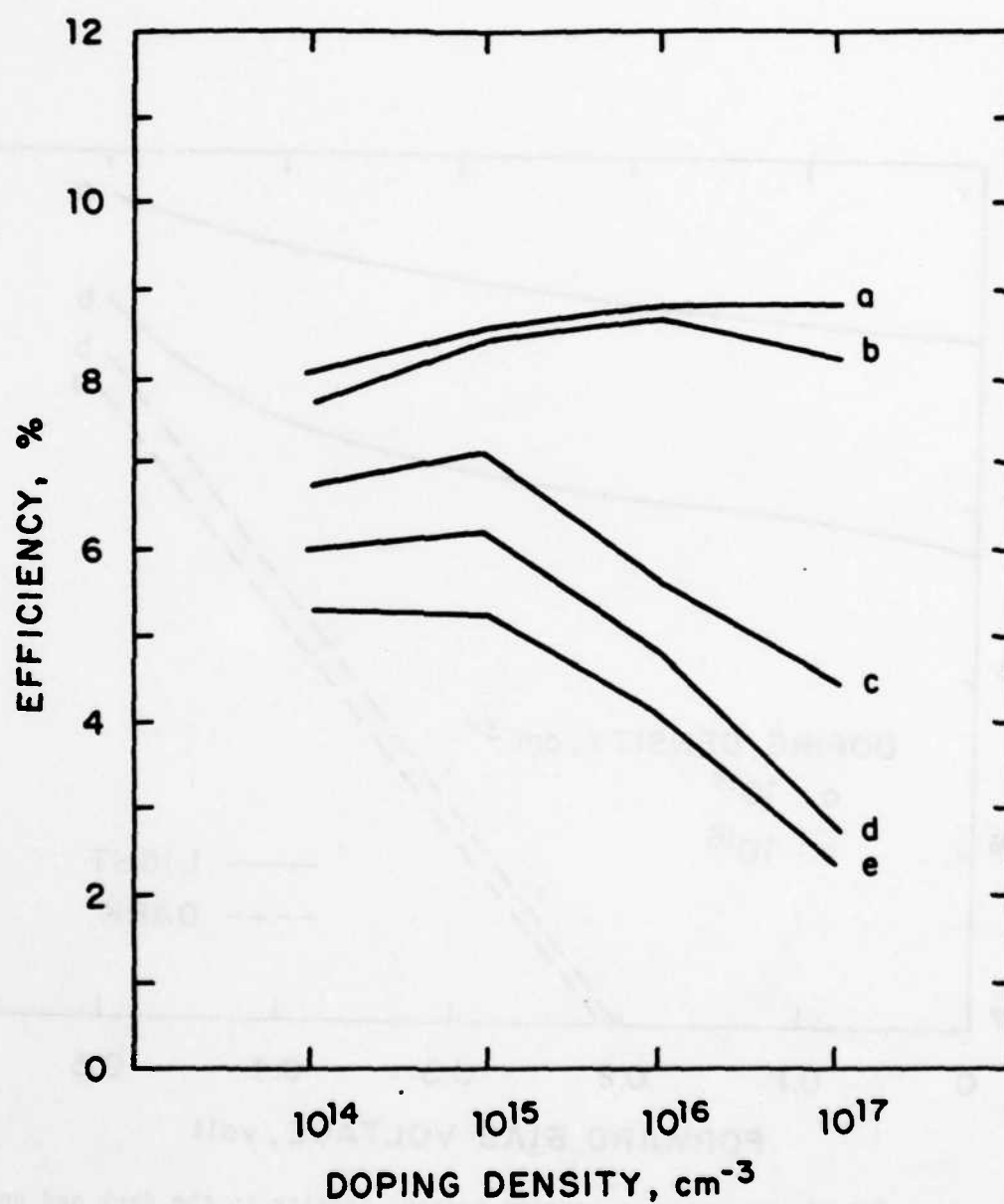


Figure 2. Calculated photovoltaic conversion efficiency vs. doping density of a MIS photovoltaic device under AM1 illumination,
 (a) $g = 10 \mu\text{m}$, $N_{is} = 10^{10} \text{ cm}^{-2} \text{ eV}^{-1}$,
 (b) $g = 1 \mu\text{m}$, $N_{is} = 10^{10} \text{ cm}^{-2} \text{ eV}^{-1}$,
 (c) $g = 1 \mu\text{m}$, $N_{is} = 10^{12} \text{ cm}^{-2} \text{ eV}^{-1}$,
 (d) $g = 0.5 \mu\text{m}$, $N_{is} = 10^{13} \text{ cm}^{-2} \text{ eV}^{-1}$,
 (e) $g = 500 \text{ \AA}$, $N_{is} = 10^{13} \text{ cm}^{-2} \text{ eV}^{-1}$.

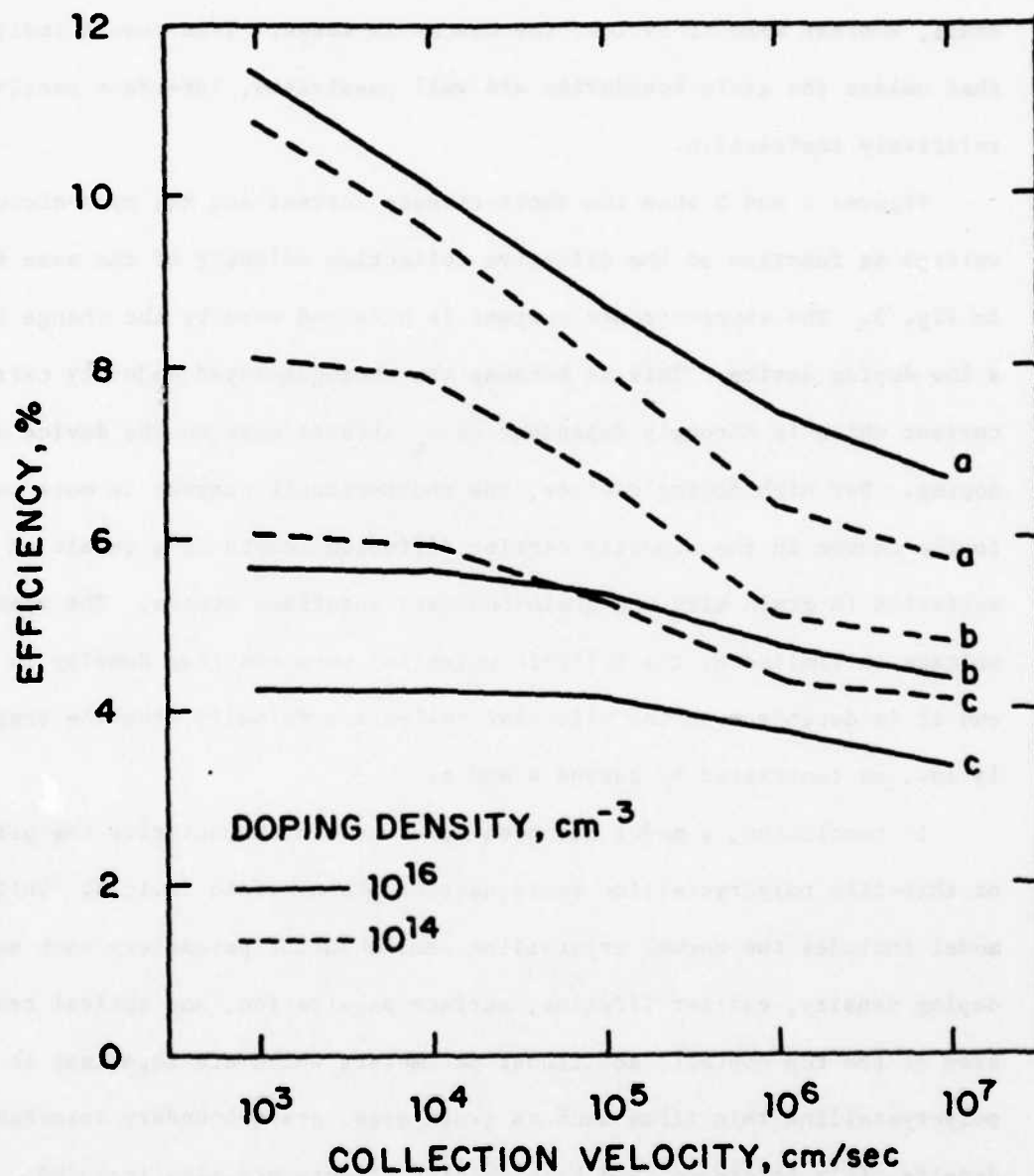


Figure 3. Calculated photovoltaic conversion efficiency vs. collection velocity of a MIS photovoltaic device under AM1 illumination,
 (a) $g = 10 \text{ } \mu\text{m}$, $N_{is} = 10^{10} \text{ cm}^{-2} \text{ eV}^{-1}$,
 (b) $g = 0.5 \text{ } \mu\text{m}$, $N_{is} = 10^{12} \text{ cm}^{-2} \text{ eV}^{-1}$,
 (c) $g = 500 \text{ } \text{\AA}$, $N_{is} = 10^{13} \text{ cm}^{-2} \text{ eV}^{-1}$.

efficiency is high when v_c is low and it is decreased as v_c is increased. When trap density is high, the change in efficiency as a function of v_c is small, whereas when it is low, the change is large. This result indicates that unless the grain boundaries are well passivated, interface passivation is relatively ineffective.

Figures 4 and 5 show the short-circuit current and the open-circuit voltage as function of the effective collection velocity of the same device as in Fig. 3. The short-circuit current is affected more by the change in v_c for a low doping device. This is because the photogenerated majority carrier current which is strongly dependent on v_c affects more on the device of low doping. For high doping devices, the short-circuit current is more sensitive to the change in the minority carrier diffusion length as a result of the variation in grain size and grain-boundary interface states. The open-circuit voltage is limited by the built-in potential when the trap density is high, and it is dependent on the effective collection velocity when the trap density is low, as contrasted by curves a and c.

In conclusion, a model has been developed to characterize the performance of thin-film polycrystalline semiconductor photovoltaic devices. While this model includes the normal crystalline semiconductor parameters such as doping density, carrier lifetime, surface passivation, and optical transmission of the top contact, additional parameters which are important in polycrystalline thin films such as grain size, grain-boundary interface state density, film thickness, and back contact effects are also included. In addition, light induced changes in the majority carrier current and free majority carrier density are shown to dramatically affect the photovoltaic properties of these devices. In particular the effective collection velocity significantly affects the photovoltaic properties when the doping density is

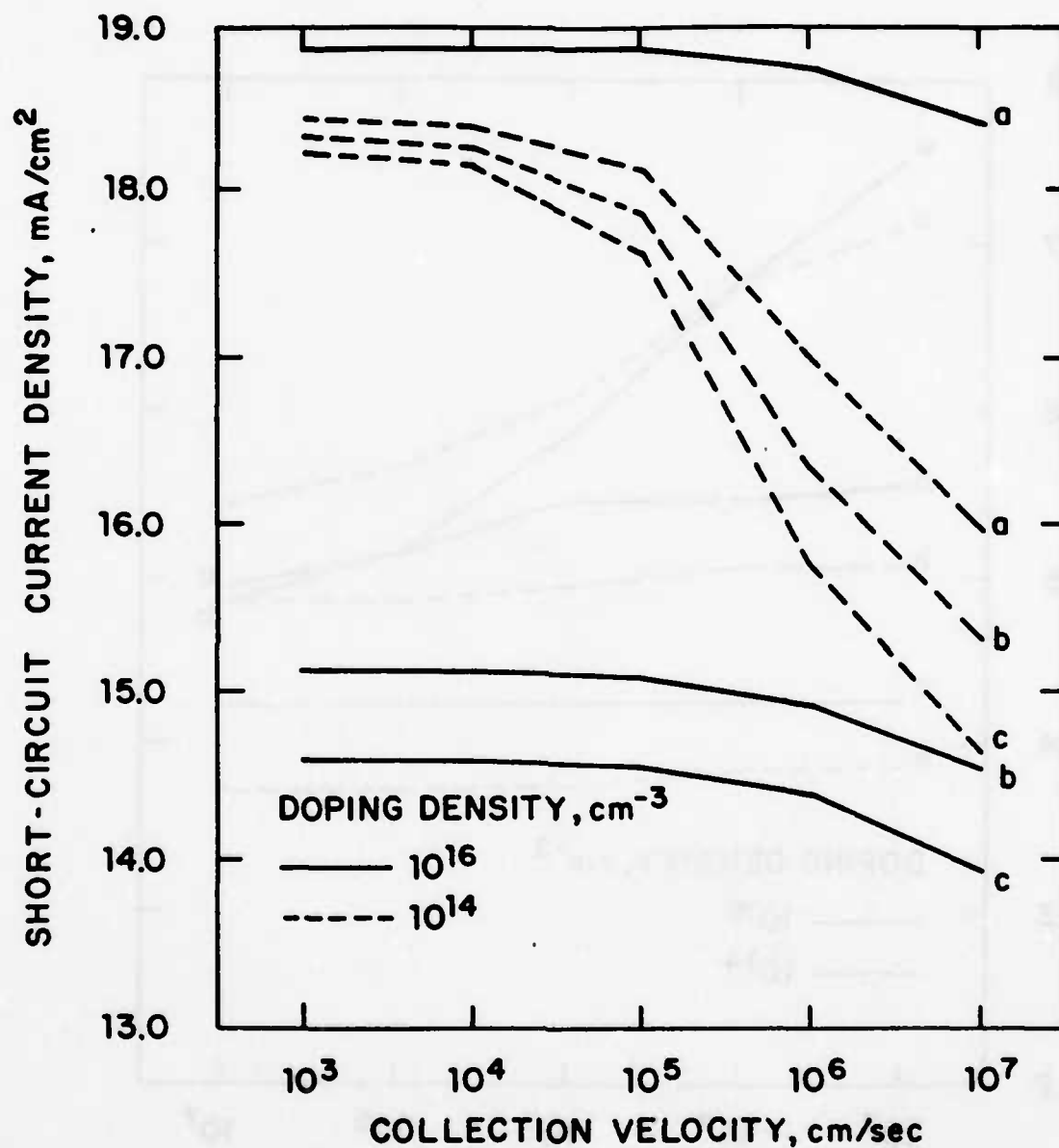


Figure 4. Calculated short-circuit current density vs. collection velocity of the same device as in Figure 3.

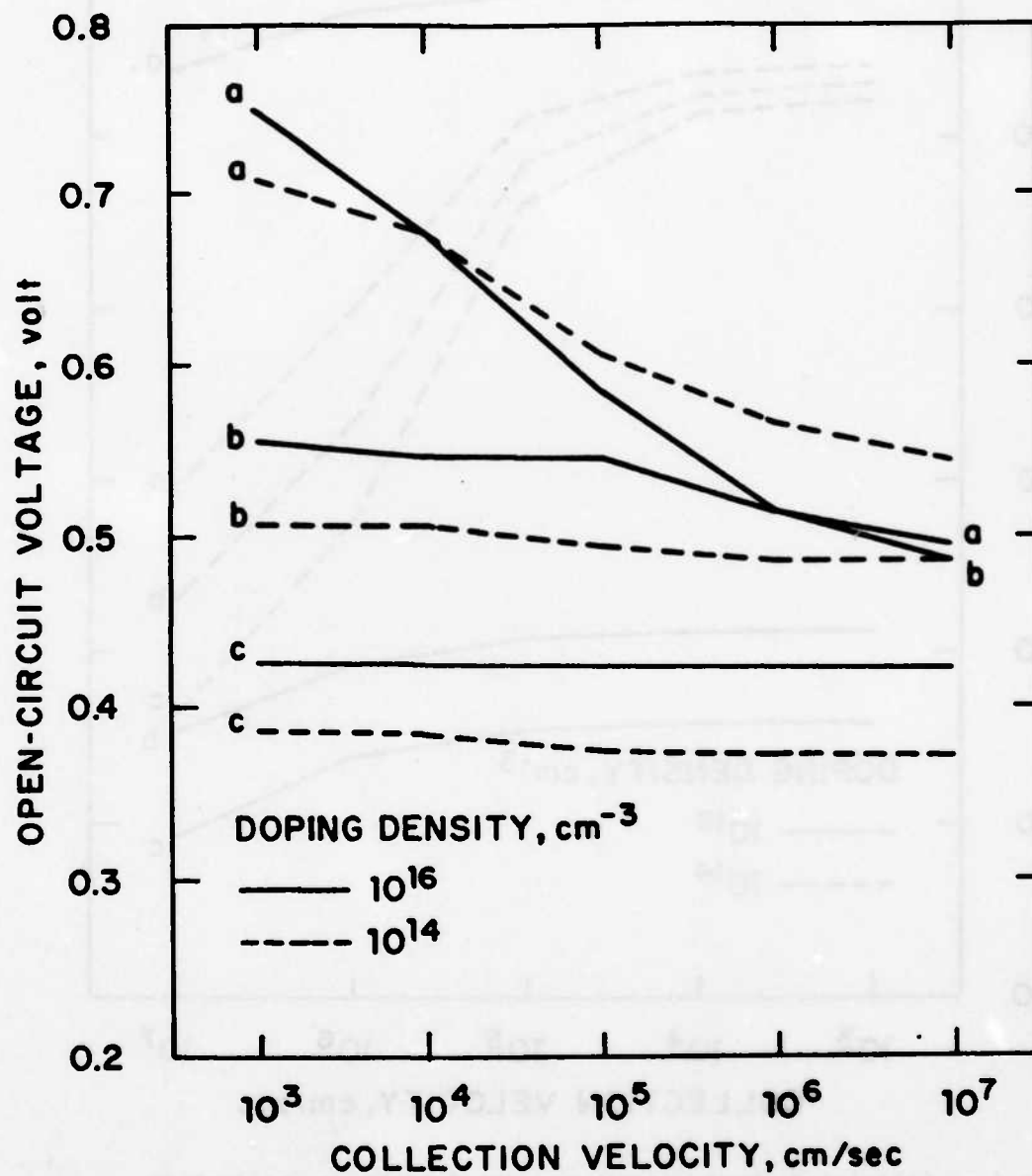


Figure 5. Calculated open-circuit voltage vs. collection velocity of the same device as in Figure 3.

low. The trap density, which is computed from the grain size and grain-boundary interface state density, is the most important feature in determining photovoltaic properties. In addition to its effect on minority carrier lifetime, these traps enhance the light-induced changes in the free majority carrier density which in turn affect the built-in potential, depletion width, open-circuit voltage, fill factor and short-circuit current. In general, it is shown that grain boundaries must first be passivated in order to achieve high efficiency. Interface passivation, as it affects the effective collection velocity, will then further improve the efficiency. The influence of the grain boundaries can be reduced, however, by designing the photovoltaic device with lower doping density and a thickness such that the whole semiconductor becomes a space-charge region. As the doping density is lowered, however, the band bending in the junction depletion region will be reduced due to the accumulated back contact, resulting in higher majority carrier current and lower conversion efficiency. Therefore, an optimum doping density and thickness exist for specific semiconductor material and device structure. Modeling together with photovoltaic parameter measurements can help identify the major loss mechanisms so that processing can be modified and efficiency optimized.

*This work is supported by the National Science Foundation under the contract NSF-ECS-82-17677.

- (1) S. M. Sze, Physics of Semiconductor Devices, ch. 14, Wiley - Interscience, New York, 1981.
- (2) G. Fulop, M. Doty, P. Meyers, J. Betz, and C. H. Liu, Appl. Phys. Lett. 40, 327 (1982).
- (3) J. Reichman, Appl. Phys. Lett. 38, 251 (1981).
- (4) N. G. Tarr and D. L. Pulfrey, IEEE Trans. Electron. Devices ED-27, 771 (1980).

- (5) S. M. So, W. Hwang, P. V. Meyers, and C. H. Liu, IEEE Trans. Electron. Devices ED-31, May (1984).
- (6) G. Baccarani, B. Ricco, and G. Spadini, J. Appl. Phys. 49, 5565 (1978).
- (7) W. Shockley and W. T. Read, Jr., Phys. Rev. 87, 835 (1952).
- (8) S. M. So, W. Hwang, P. V. Meyers, and C. H. Liu, J. Appl. Phys. 55(1), 253 (1984).

E. FABRICATION OF MIS-SCHOTTKY DIODES WITH THERMAL NITROXIDE FILM*

(D. K. Yang, Q. Hua, E. S. Yang)

(JSEP work unit 4, 1982-1985)

(Principal Investigators: E. Yang (212) 280-3120

W. Hwang (212) 280-3115)

In the development of ultra-small electronic devices, it has been found that thin gate oxide less than 200 Å often deteriorates after silicide-gate, ion-beam or plasma-assisted processing. Yet, because of scaling, future generations of megabit RAMs will require a film thickness of 100 Å or less.^{(1),(2)} The integrity of such thin insulator films is most important in achieving highly reliable device structures. Recently, thermal nitridation of thin oxide films has been found to improve MOS characteristics.⁽³⁾ Incorporation of nitrogen in an oxide produces a dense, uniform and pinhole-free film known as oxynitride or nitroxide. We have used this technique to fabricate MIS rectifiers whose forward turn-on voltage can be controlled by varying the thickness of the oxynitride film. This section reports the results of the process when a closed tube moving furnace is used. I-V characteristics of MIS-Schottky diodes fabricated by this process are also presented.

Thermal nitridation of a silicon wafer is achieved by reaction with ammonia in the system illustrated in Fig. 1. The substrates are (111) n/n⁺ polished Si. The surface cleaning procedure consists of: (1) degreasing in organic solvents in an ultra-sonic bath; (2) dipping in H₂SO₄ at 80°C for 5 min. to remove heavy ions; (3) immersion in HNO₃ at 80°C for 5 min. to form a thin native oxide; and (4) etching in buffered HF for 30 sec. to remove the oxide. After these steps the silicon surface should be hydrophobic. In order to obtain a thin nitroxide film on Si, we dip the wafer in HNO₃ at 80°C for 5 min. to form a controlled SiO₂ about 15-20 Å. Then we load the wafer into the quartz reaction tube and purge the tube with pure N₂ for 30 min. after sealing

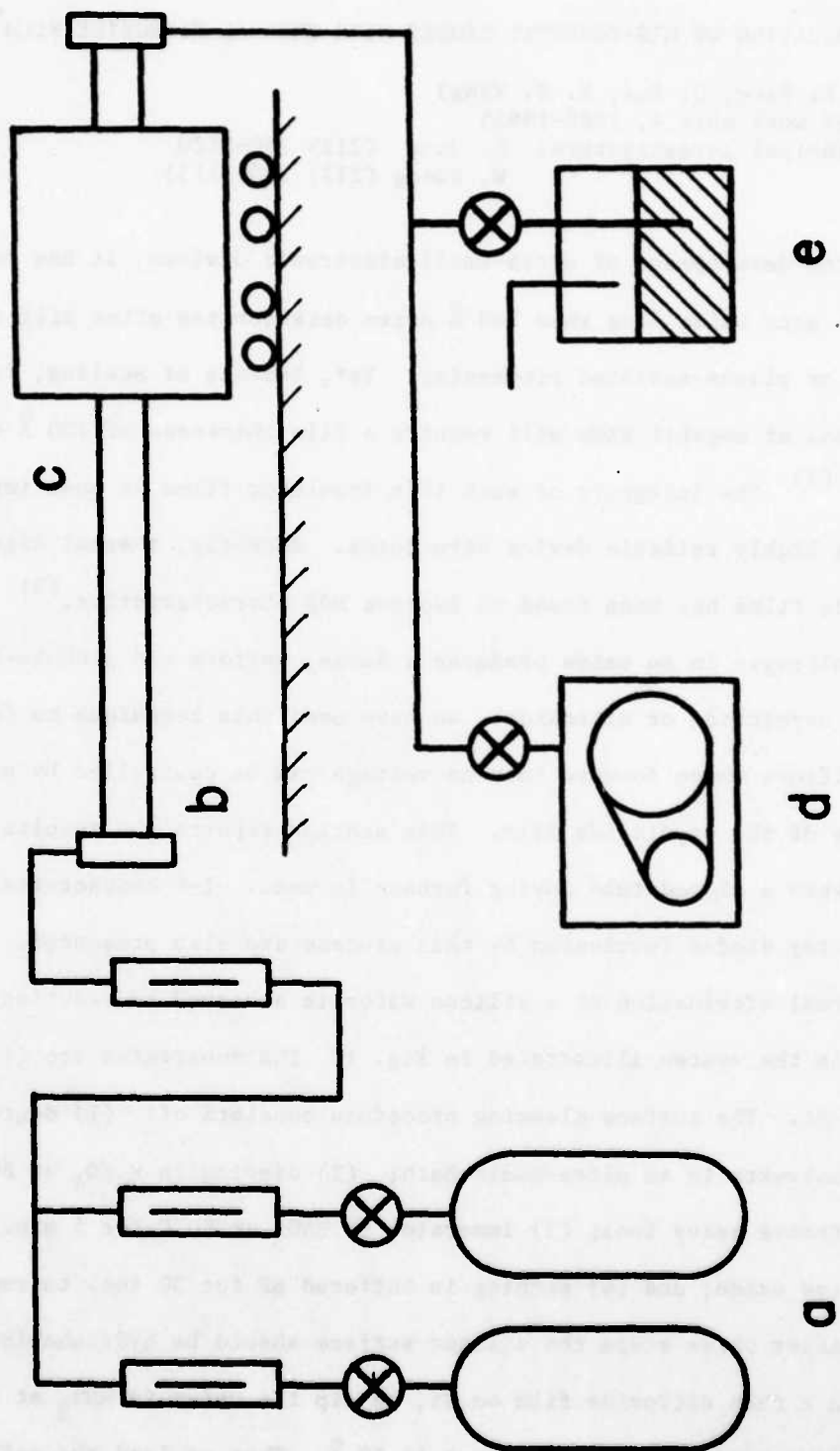


Figure 1

and evacuating the tube to 0.1 Torr. Subsequently, NH_3 is introduced into the quartz tube and the preheated furnace is moved to encompass the wafers. The insulator-film will become a nitroxide whose thickness depends on the growth time and temperature. In our experience, the thickness of the film depends slightly on the growth time, but strongly depends on the temperature. In some cases, in order to avoid using high temperature, we can grow thicker nitroxide on Si by preheating the wafer in an oxygen environment for several minutes, purging the oxygen with N_2 , and heating the wafer in NH_3 . After the desired film thickness is achieved, the furnace is removed, and the wafers are allowed to cool down to room temperature. The tube is then purged with N_2 before unloading the wafers. Aluminum is evaporated on the back side of the wafer to form an ohmic contact and aluminum dots are deposited on the front surface to produce MIS-Schottky diodes.

The film thickness is measured by ellipsometry, and its dependence on growth time is shown in Fig. 2. The refractive index is found to be between 1.9 and 2.2. At 920°C , the film thickness remains to be essentially constant beyond a heating period of 40 minutes. Therefore, a higher temperature (960°C) is used to obtain a thicker film. Our experience shows that the thickness can be controlled easily by fixing the temperature, whereas the growth time is relatively unimportant after the initial growth. This indicates that the mechanism is likely to be limited by the diffusion of the nitriding species through the insulator.

In Fig. 3, the forward current-voltage characteristics are shown for diodes fabricated on the same substrate with different insulator film thickness. The turn-on voltage increases with the film thickness as expected from known theory.⁽⁴⁾ The dashed line represents a diode with SiO_2 insulator which is used as a reference. It is interesting to note that the behavior of

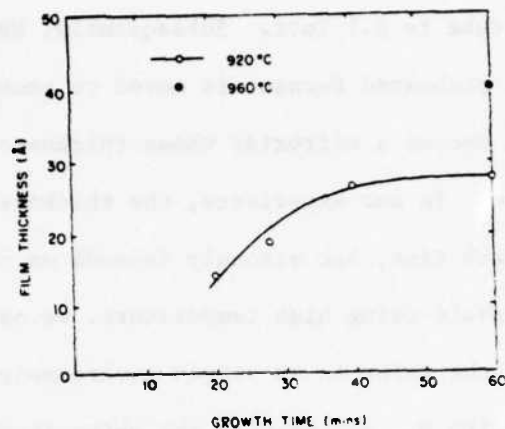


Fig. 2. Dependence of nitroxide film thickness on growth time.

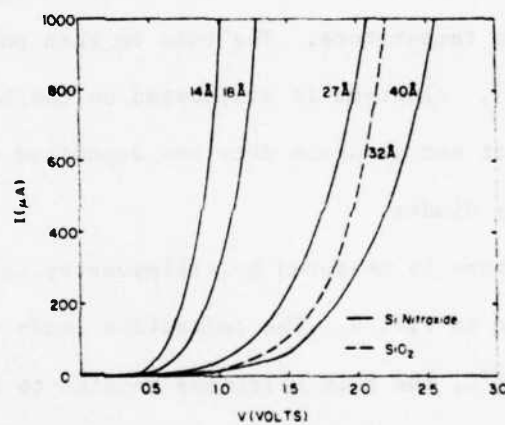


Fig. 3. Forward current-voltage characteristic of MIS-Schottky diodes.

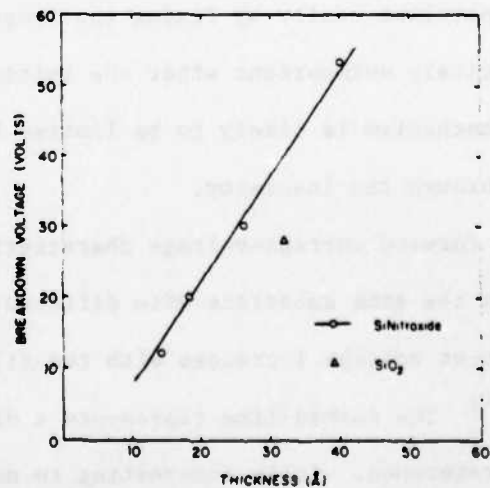


Fig. 4. Reverse breakdown voltage as a function of nitroxide film thickness.

these MIS-Schottky diodes is not sensitive to the band-gap value of different dielectrics and that the turn-on voltage follows the insulator thickness. Similar results have been noted by Card and Rhoderick in their work.⁽⁴⁾ On the other hand, the reverse-biased breakdown voltage shown in Fig. 4 indicates that the nitroxide films are better. More important is the fact that the devices with the nitroxide film do not seem to degrade after months, whereas diodes with SiO_2 insulator degrade in days. It appears that the MIS-Schottky structure may also be useful in evaluating the stability of the insulator films less than 50 Å in thickness.⁽⁵⁾ In conclusion, we have fabricated aluminum-nitroxide-silicon Schottky diodes and found that their electrical characteristics are similar to MIS-Schottky junctions with SiO_2 insulator. However, the better breakdown and degradation characteristics indicates that the integrity of nitroxide films is significantly better than pure oxide films.

*This research was also supported by the National Science Foundation under Grant ECS-82-17677.

- (1) J. D. Meindl, K. H. Ratnakumar, L. Gerzbert and K. C. Saraswat, ISSCC Digest Tech. Papers, p. 36 (1981).
- (2) H. H. Chao, R. H. Dennard, M. Y. Tsai, M. R. Wordeman and A. Cramer, ISSC Digest Tech. Papers, p. 152 (1981).
- (3) T. Ito, T. Nakamura and H. Ishikawa, IEEE Trans. Electron Devices ED-29, 498 (1982).
- (4) H. C. Card and E. H. Rhoderick, J. Phys. D. 4, 1589 (1971).
- (5) L. C. Olsen, D. L. Barton and W. Miller, J. Appl. Phys. 51, 6393 (1980).

F. A METAL-AMORPHOUS SILICON-SILICON TUNNEL RECTIFIER*

(Q. Hua, D. Yang, E. Yang)

(JSEP work unit 4, 1982-1985)

(Principal Investigators: E. Yang (212) 280-3120

W. Hwang (212) 280-3115)

Ever since the discovery of the tunneling phenomenon in a p-n junction by Esaki,⁽¹⁾ design engineers have attempted to make use of this ultra-fast switching device. Yet, with the exception of some microwave circuits, the applications have been limited. The tunneling mechanism has also been shown to be important in thin-oxide MOS structures.^{(2),(3)} The carrier transport in these devices is, however, not pure tunneling since it is thermionic emission modified by tunneling.⁽⁴⁾ In this section, we report the successful fabrication of a nearly ideal tunnel diode with excellent rectifying properties. It will be shown that while the majority carrier current of this new structure is distinctly dominated by tunneling, its current-voltage characteristics conform to those of a typical p-n junction diode. The device is produced at room temperature without a high temperature annealing cycle.

To fabricate the device, a 30 Å layer of amorphous silicon was deposited on an n/n^+ silicon wafer by electron-beam evaporation at a pressure less than 2×10^{-6} Torr. Aluminum dots, 1000 Å thick and 1.20 mm in diameter, were evaporated on the front of the wafer, and a 1000 Å layer of aluminum was evaporated on the back to provide ohmic contact (see insert of Fig. 2). A control sample fabricated without the amorphous silicon layer showed the characteristic of an ohmic contact. The current-voltage (I-V) characteristic was then measured at different temperatures, and the capacitance-voltage (C-V) characteristic was measured at room temperature.

Fig. 1 shows a typical I-V characteristic at room temperature. The vertical scale is 500 uA per division; the horizontal scale is 500 mV per

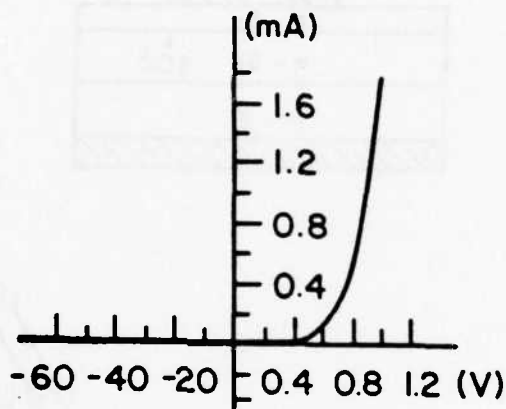


Figure 1. A typical current-voltage characteristic of Metal-a-Si-Si rectifier. Horizontal scales: 0.2 V/Div in forward bias and 20 V/Div in reverse bias.

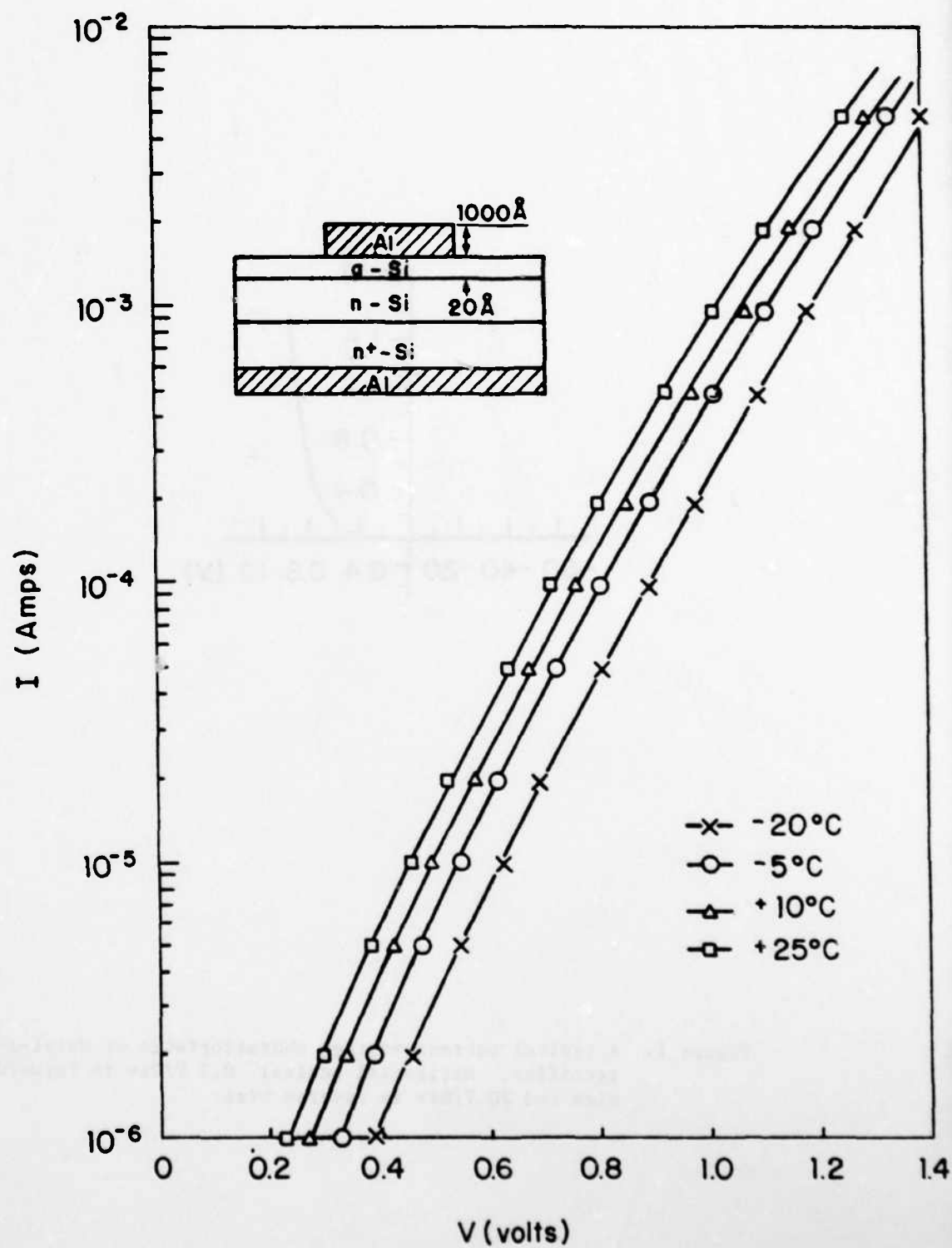


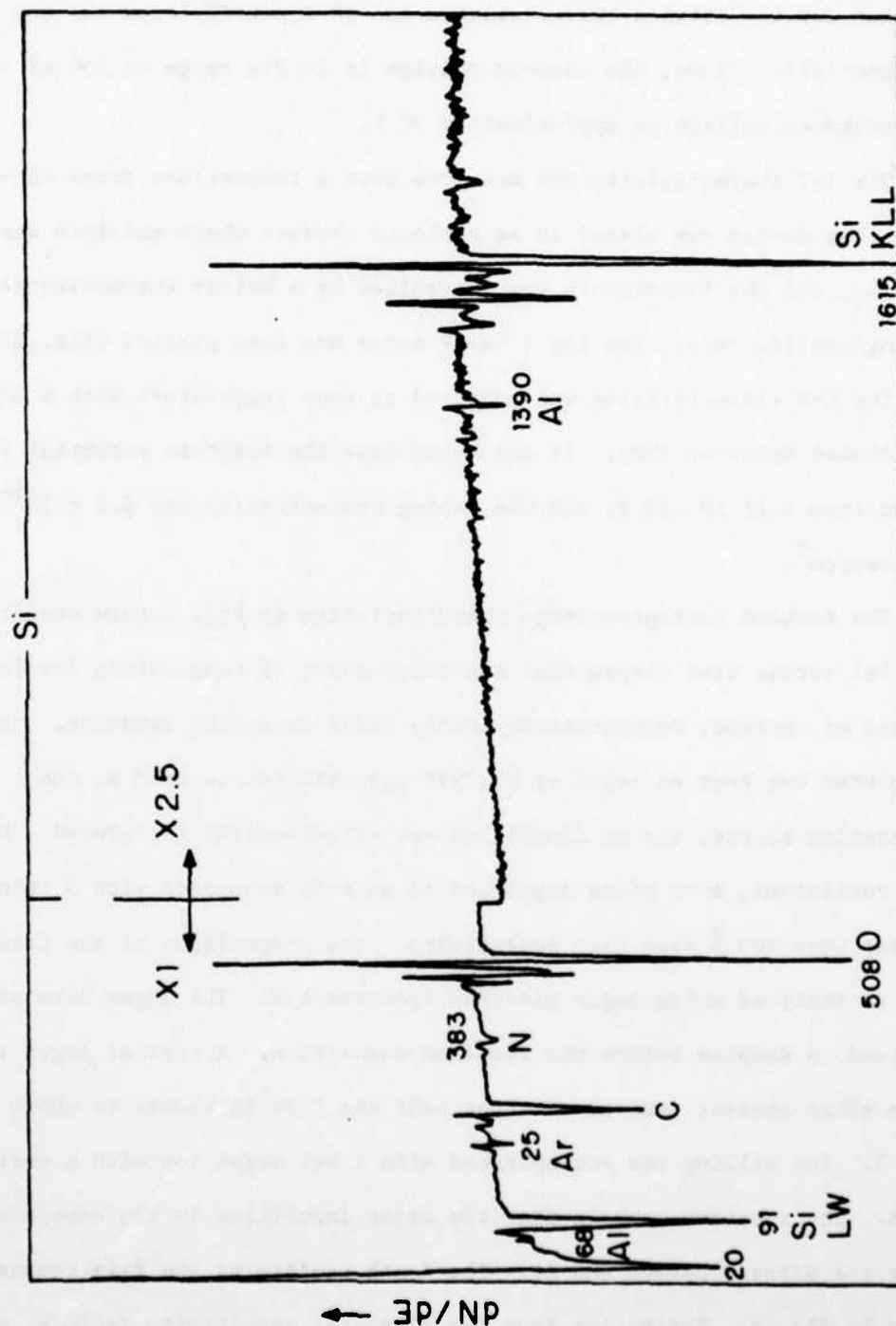
Figure 2. Temperature dependence of the forward biased I-V characteristics.

division for the forward characteristic and 20 V per division for the reverse characteristic. Thus, the turn-on voltage is in the range of 700 mV - 1V, and the breakdown voltage is approximately 50 V.

The I-V characteristic was measured over a temperature range of -20°C to 25°C . The device was placed in an enclosed chamber where moisture was removed by CaCl_2 , and the temperature was controlled by a Melcor thermoelectric heating/cooling chip. The $\log I$ vs. V curve was then plotted (Fig. 2).

The C-V characteristic was measured at room temperature with a Boonton capacitance meter at 1MHz. It was found that the built-in potential (V_D) ranged from $\sim .15$ to $.13$ V, and the doping concentration was 5.5×10^{14} carriers/ cm^3 .

The forward current-voltage characteristics in Fig. 2 form essentially parallel curves with slopes that are independent of temperature for four decades of current, demonstrating nearly ideal tunneling behavior. It should be pointed out that an ingot of 99.999% pure silicon is used as the evaporation source, and no impurities are intentionally introduced. Under the same conditions, a-Si films deposited on an n-Si substrate with a thickness greater than 300 \AA show high resistivity. The composition of the interfacial a-Si is analyzed using Auger electron spectroscopy. The Auger data were obtained on samples before the aluminum deposition. A typical Auger spectrum taken after sputter removal of about half the film thickness is shown in Fig. 3. Ion milling was accomplished with 2 KeV argon ion with a current of 25 mA. The spectrum reveals that the major impurities in the amorphous Si layer are oxygen, carbon and Al. The depth profile of the film composition is shown in Fig. 4. Estimating from the elemental sensitivity factors, we find that the amorphous layer contains almost equal amounts of carbon and oxygen (about 20 at %). At the present, it is not clear to what extent that carbon



KINETIC ENERGY, eV

Figure 3. An Auger spectrum after sputtering for 5 seconds.

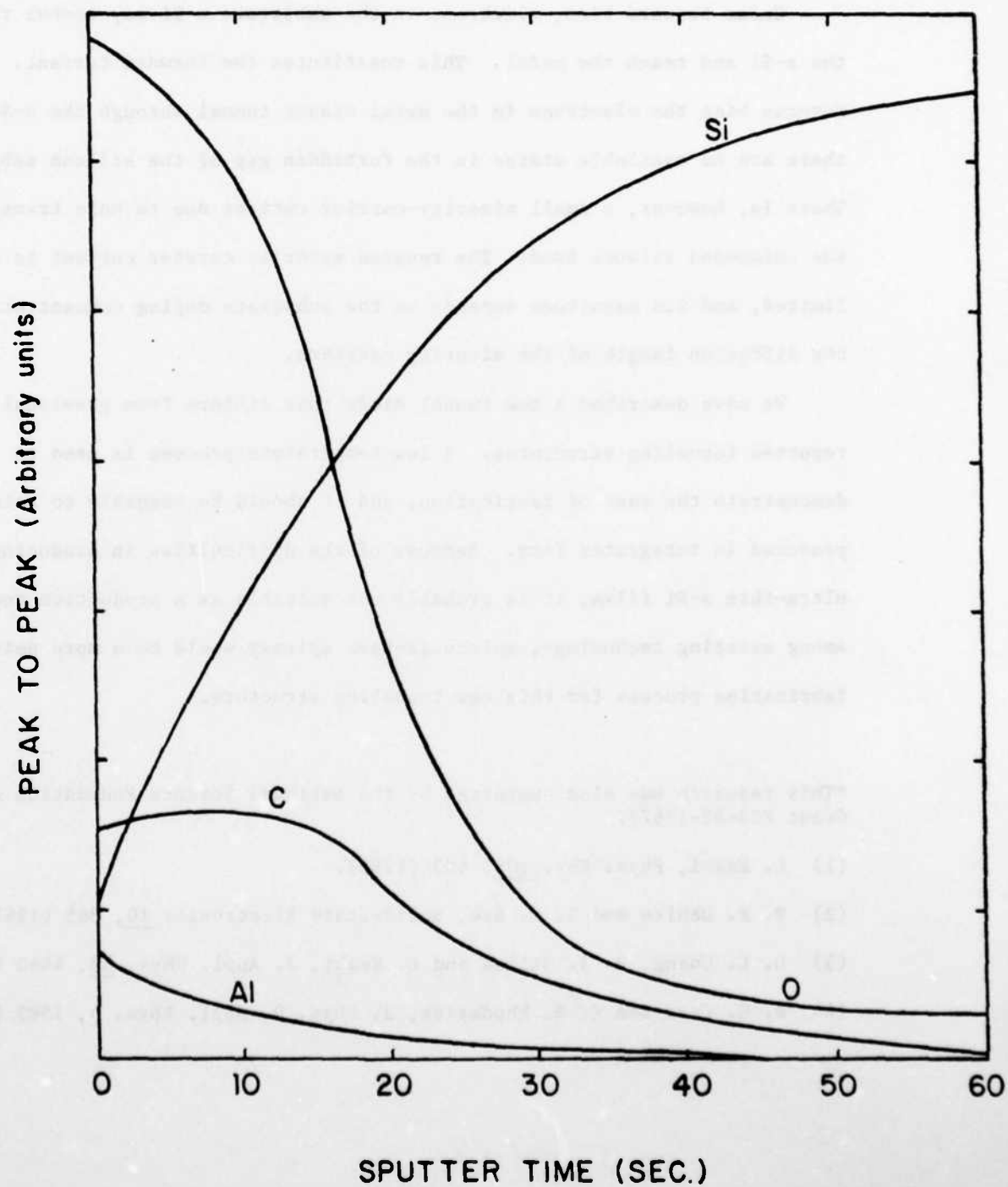


Figure 4. Depth profile of the interfacial a-Si layer.

oxygen or aluminum affecting the electronic properties of the amorphous silicon layer.

Under forward bias, electrons in the substrate n-Si may tunnel through the a-Si and reach the metal. This constitutes the forward current. Under reverse bias the electrons in the metal cannot tunnel through the a-Si since there are no available states in the forbidden gap of the silicon substrate. There is, however, a small minority-carrier current due to hole transport in the unimpeded valence band. The reverse minority carrier current is diffusion limited, and its magnitude depends on the substrate doping concentration and the diffusion length of the minority carriers.

We have described a new tunnel diode that differs from previously reported tunneling structures. A low-temperature process is used to demonstrate the ease of fabrication, and it should be amenable to being produced in integrated form. Because of the difficulties in producing ultra-thin a-Si films, it is probably not suitable as a production technique. Among existing technology, molecular-beam epitaxy would be a more suitable fabrication process for this new tunneling structure.

*This research was also supported by the National Science Foundation under Grant ECS-82-17677.

- (1) L. Esaki, Phys. Rev. 109, 603 (1958).
- (2) W. E. Dahlke and S. M. Sze, Solid-State Electronics 10, 865 (1967).
- (3) L. L. Chang, P. J. Stiles and L. Esaki, J. Appl. Phys. 38, 4440 (1967).
- (4) H. C. Card and E. H. Rhoderick, J. Phys. D. Appl. Phys. 4, 1589 (1971).

G. PHOTON-ASSISTED DRY ETCHING OF GaAs

(Peter Brewer, R. M. Osgood, Jr.)

(JSEP work unit 5, 1982-1985)

(Principal Investigator: R. M. Osgood, Jr. (212) 280-4462)

Pulsed, laser-initiated chemistry is being used for a number of new approaches to planar, dry processing of thin films. These include etching, deposition, and doping. Each of these techniques is generally based on gas-phase reactants and some combination of photon or thermally driven chemistry.⁽¹⁾ The advantages of laser-initiated dry processing over conventional techniques are that material processing is typically performed under lower temperatures, with no electrical damage due to ions and in a well defined chemical environment. In the first experiments on pulsed laser etching, CO₂ infrared lasers were used to effect multiphoton dissociation of freons and halide-bearing gases to etch SiO₂ and Si.⁽²⁾ Due to the adoption of conventional dry processing techniques as standard by the industry for Si and SiO₂, the greatest impact of these studies will be in the understanding of the mechanism of dry etching reactions. In the case of newer materials, such as GaAs, InP and other more novel semiconductors, dry-laser-processing has a better potential of implementation by the industry because no one technique is employed. In this report, we describe the use of a pulsed excimer laser,⁽³⁾ ArF at 193 nm, for the gas-phase etching of both masked and maskless GaAs substrates. One advantage of the excimer laser source lies in the fact that with the use of UV irradiation only a single photon is required to dissociate many molecular species. It can, therefore, in principle, produce a single set of reactants in specific electronic states, thus simplifying the etching chemistry. Previously, UV-laser-assisted etching of GaAs has been done with a

low-power, cw UV-laser,⁽⁴⁾ an approach which is suitable for direct-writing micrometer-scale surface features. The excimer laser allows for large-area etching due to its relatively high pulse energies and high average powers.

Experimental

The experimental set-up used a repetitively-pulsed (10-50 Hz) ArF laser at 193 nm and XeF laser at 351 nm. The laser output is focused with a 200-mm-focal-length lens into a stainless-steel, 4-window cross cell which houses the GaAs substrates. The cell is positioned on a precision swivel mount which allows for different substrate-laser beam configurations. The GaAs substrates are fixed to a nickel-plated, copper holder which can be resistively heated from 23° - 150°C. Ga and As populations were detected in the gas phase by laser-induced fluorescence filtered through a 3/4 meter monochromator. The GaAs substrates were commercially polished and had etch pit densities $< 900/\text{cm}^2$. Several orientations were explored: n-GaAs (100), n-GaAs(111) A and B, and p-GaAs (100). The samples were cleaned by a standard chemical washing procedure⁽⁵⁾ and dried with nitrogen before each experiment. Etch depths and etch rates were measured by means of a mechanical stylus and the etching morphology was studied by scanning electron microscopy.

Two types of experiments were performed with respect to the laser-substrate configuration, positioning in the parallel (indirect) and the perpendicular (direct) orientations. These orientations give rise to interactions involving purely photochemical gas-phase photodissociation and combined surface- and gas-phase UV-initiated chemistry, respectively. In general, the etching reactions initiated by the direct laser-substrate orientation proved to be more useful in measuring etching rates because of the localized etched features which could be obtained. The indirect orientation

was employed mostly for chemical mechanistic studies because the laser then serves only to produce reactive gas-phase radicals. In both cases, the GaAs substrates were heated to aid in removal of gas-surface products. The gases used in these studies were CF_3Br , CH_3Br and HBr . In the cases of CF_3Br , and CH_3Br questions of etch rate, anisotropic etching, temperature effects and chemical reaction mechanisms are addressed. For HBr , mainly etching rate and etching anisotropy will be discussed.

Dry Laser-Etching: CF_3Br and CH_3Br Results

As shown in Table I, both methyl and trifluoromethyl bromides were used as parent gases; the most studied gas was CF_3Br . The interaction of a 193 nm photon with a CF_3Br or CH_3Br molecule leads to fragmentation into CF_3 or CH_3 , and Br radicals in specific quantum states as noted in Table I.^{(6),(7)} The Br atoms in the photodissociation of CF_3Br are formed in nearly equal populations in the spin-orbit excited $^2\text{P}_{1/2}$ and the ground $^2\text{P}_{3/2}$ states.⁽⁶⁾ Whereas in the case of CH_3Br , the Br radicals are all produced in the ground $^2\text{P}_{3/2}$ state.⁽⁶⁾ The CF_3 and the CH_3 radicals are produced in excited vibrational states. Based on recently measured vibrational relaxation times the radicals produced within ~ 0.5 mm from the surface remain activated until they collide with the GaAs surface.

Direct illumination of the GaAs substrates in the presence of several Torr of CF_3Br produces an etching reaction confined to the spot illuminated on the surface. In this orientation, a weakly focused beam is positioned so as to illuminate only a portion of the GaAs substrate, with typical energy densities $< 35 \text{ mJ/cm}^2$. The localized etching is due to several sources including laser-initiated surface reactions, and laser-enhanced desorption of gas-surface products. The etch rate for CF_3Br as a function of laser energy

TABLE I

A. Parent gases used in UV-laser initiated dry etching of GaAs and parent gas photochemistry at 193 nm.

<u>Parent Gas</u>	<u>Photofragments</u>	<u>E(AVL)</u>
$\text{CF}_3\text{Br} \xrightarrow{193 \text{ nm}}$	$\text{CF}_3(\text{v}) + \text{Br}$	79.3 kCal/mole
	$\text{CF}_3(\text{v}) + \text{Br}^*$	68.8 kCal/mole
$\text{CH}_3\text{Br} \xrightarrow{193 \text{ nm}}$	$\text{CH}_3(\text{v}) + \text{Br}$	79.5 kCal/mole

B. Physical properties of etching reaction products of GaAs with CF_3Br and CH_3Br .

<u>Etching Gas: CH_3Br</u>		<u>Etching Gas: CH_3Br</u>	
Arsenic Products	M.P./B.P.	Gallium Products	M.P./B.P.
$\text{As}(\text{CH}_3)_3$	-70°C	$\text{Ga}(\text{CH}_3)_3$	-55.7°C
$\text{As}(\text{CH}_3)_2\text{Br}$	-51°C	$\text{Ga}(\text{CH}_3)_2\text{Br}$	-58.5°C
$\text{As}(\text{CH}_3)\text{Br}_2$	-89°C	$\text{Ga}(\text{CH}_3)\text{Br}_2$	-/-
AsBr_3	32/221°C	GaBr_3	121/278°C
<u>Etching Gas: CF_3Br</u>		<u>Etching Gas: CF_3Br</u>	
Arsenic Products	M.P./B.P.	Gallium Products	M.P./B.P.
$\text{As}(\text{CF}_3)_3$	-33°C	$\text{Ga}(\text{CF}_3)_3$	-/-
$\text{As}(\text{CF}_3)_2\text{Br}$	-59.5°C	$\text{Ga}(\text{CF}_3)_2\text{Br}$	-/-
$\text{As}(\text{CF}_3)\text{Br}_2$	-118°C	$\text{Ga}(\text{CF}_3)\text{Br}_2$	-/-
AsBr_3	32/221°C	GaBr_3	121/278°C

density, which is shown in Fig. 1, can be separated into two regions. At high energy densities $> 35 \text{ mJ/cm}^2$, physical ablation and laser-enhanced desorption due to local heating are the primary mechanisms of etching. In this region, the surface morphology is rough and the material damaged as earlier reported for ablative etching.^{(8),(9)} For intermediate energy densities, $\sim 35 \text{ mJ/cm}^2$, the etching rate in the presence of 5 Torr of CF_3Br was found to be at least 100 times the ablation rate, obtained with no CF_3Br in the sample cell. In the low-energy density region, the etching is driven by laser-photochemically initiated reactions.

In the experiments with direct illumination, patterning was demonstrated both by exposing a masked substrate to the photofragments and by projecting a masked excimer beam on the substrate. The first patterning technique employed the writing of an SiO_2 pattern from a spin-on liquid organosilicate with a focused, Ar^+ , cw laser.⁽¹⁰⁾ The surface morphology of the unmasked portion after etching is smooth and flat for the case of (100) crystal surface orientation (Fig. 2a); the (111) crystal surface (Fig. 2b) is also flat with minor surface roughness, apparently due to anisotropic etching. The resolution of the etching with GaAs (111)B substrates, see Fig. 2b, is below 200 nm with edge definition on the order of $\pm 100 \text{ \AA}$. The resolution observed is clearly limited by the masking resolution. The sidewalls of the etched microstructures are nearly vertical $\sim 80^\circ$ and follow the submicrometer roughness in the mask pattern exactly.

The second patterning technique used projection of a masked excimer laser beam. The mask was a pinhole grid with a hole width of 10 μm . Features down to the resolution of the pinholes were obtained with good image reproduction.

By measuring the etch rate for different GaAs orientations with CF_3Br , it was found that the etching process was preferential. For the three crystal

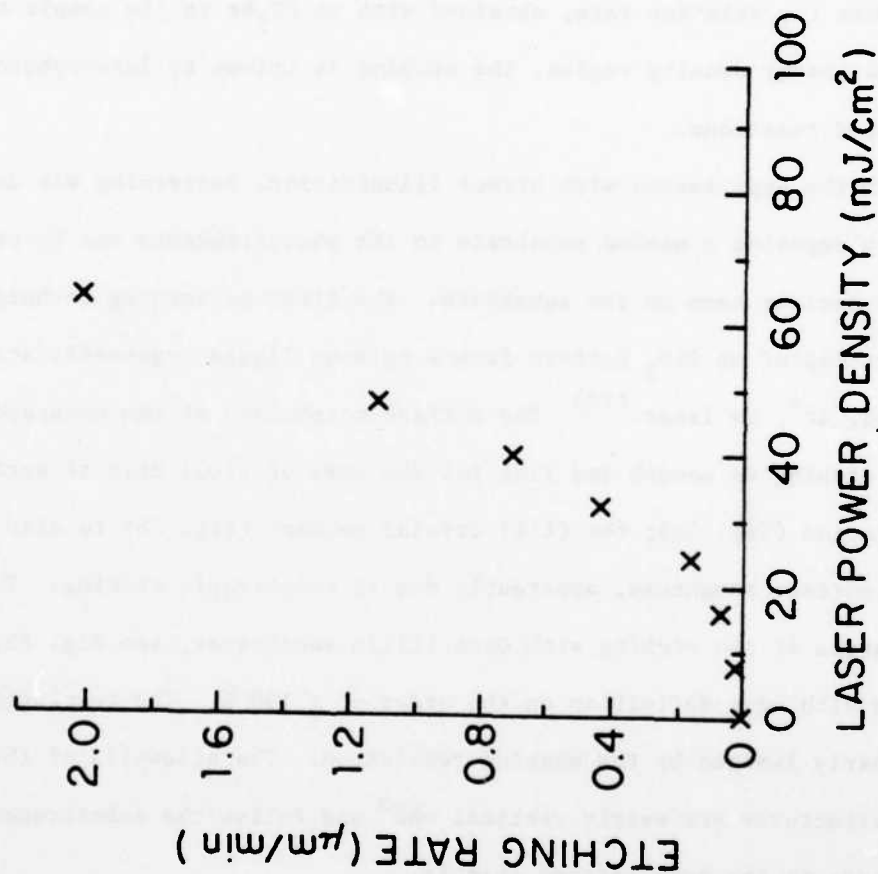


Figure 1. The etching rate of GaAs (100) by CF_3Br as a function of laser power density (50 Hz) is plotted with the substrate heated to 60 C.

Figure 2' (a)

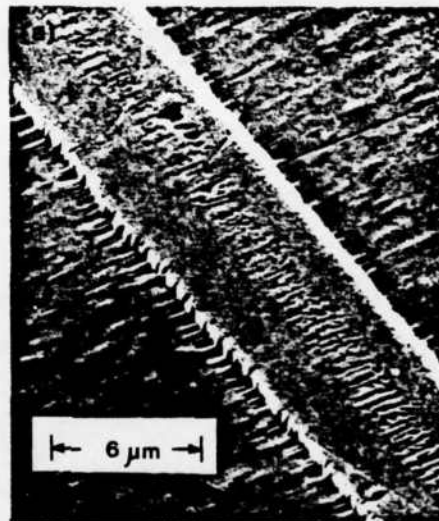


Figure 2(a). A scanning electron micrograph (SEM) of the laser etched GaAs (100) surface; note the smooth surface morphology. The SiO_2 direct mask writing procedure leaves the rough edge on the masked surface.

Figure 2· (b)

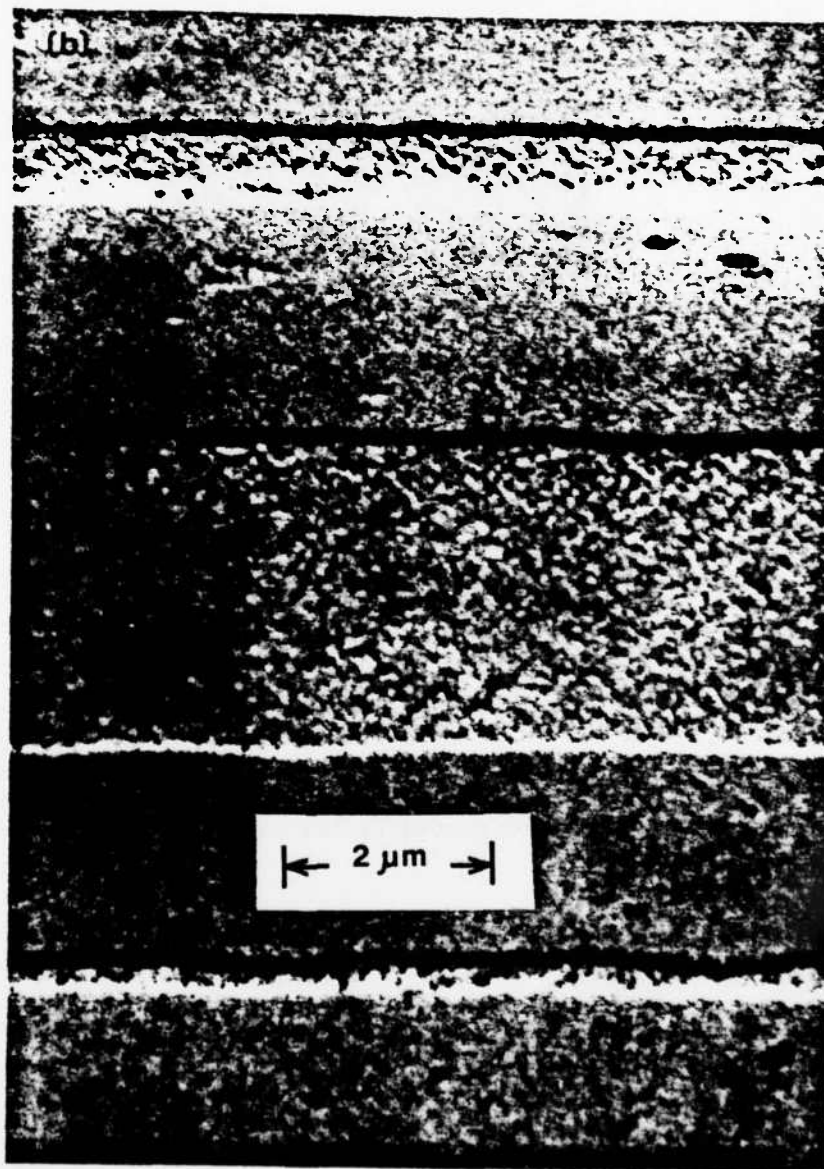


Figure 2(b). SEM of a UV-laser dry etched sample of GaAs (111)B, showing resolution of 200 nm.

orientations, (111)B, (100), and (111)A, the typical etching-rate ratios observed were 3:2:1, respectively.

It is important to determine whether simple laser heating of the surface, with subsequent thermally assisted reactions, could be responsible for the enhanced-etching phenomena observed in the direct-laser-substrate orientation. To determine whether the etching reaction results simply from thermochemistry on the laser-heated surface, we used a second excimer-laser wavelength. In particular, the 351-nm XeF-excimer laser was used, which has similar output characteristics to the ArF laser. However, it does not photodissociate the parent-gas-molecules but does produce the same surface heating. With this laser no etching reactions were observed, showing the etching reactions at 193 nm are photochemically initiated.

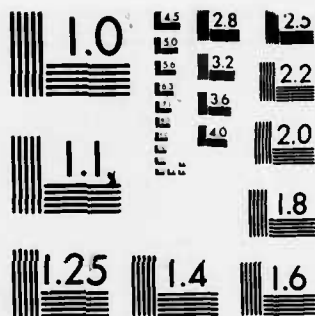
In order to gain further insight into the details of the etching reactions between the gas-phase photodissociation products and the GaAs substrates, the indirect laser-substrate orientation was employed to eliminate laser-surface interactions. Despite the rather simple reactants involved, there are many possible chemical pathways leading to as many as eight etching products. These are listed in Table I for both CF_3Br and CH_3Br , along with some associated physical data.⁽¹³⁾ At room temperature, the GaAs etching products observed after 193-nm laser irradiation of 1 Torr of either CH_3Br or CF_3Br appear in two forms: a clear, multicomponent liquid with B.P. $> 50^\circ\text{C}$ and a multicomponent gas. Based on the components with the highest volatility in Table I, the most likely gaseous products are those Ga and As compounds containing at least one methyl or trifluoromethyl group.

The incorporation of CH_3 or CF_3 radicals in the etching products is further supported by LIF spectral measurements. In these experiments, we measured the 417.2-nm Ga fluorescence first in a room-temperature cell

UNCLASSIFIED

RESEARCH INVESTIGATION DIRECTED TOWARD EXTENDING THE
USEFUL RANGE OF THE ELECTROMAGNETIC SPECTRUM(U)
COLUMBIA RADIATION LAB NEW YORK G W FLYNN 31 MAY 84
DAAG29-82-K-0080 F/G 20/3

NL



MICROCOPY RESOLUTION TEST CHART
NATIONAL BUREAU OF STANDARDS-1963-A

containing a saturated pressure of GaBr_3 vapor and then in a cell containing the reaction products from etching GaAs with CF_3Br . The LIF signal was observed to be 3x higher in the cell containing the etching products than in the cell containing the GaBr_3 vapor. In terms of the known reactivities of Ga(s) and As(s) with gas-phase radicals, both alkyl (CH_3 and CF_3) radical reactions have been reported.^{(7),(12)}

On the other hand, it has been previously reported that gas-phase Br radicals, from Br_2 , react with GaAs in a plasma discharge etcher.⁽¹³⁾ Since the products with the least volatility in our experiment are the fully brominated metal salts, we would expect to find them concentrated in the liquid product, which is present on the unheated sample. In fact, both GaBr_3 and AsBr_3 were observed when this liquid was studied with mass spectroscopy. In practical etching applications, the liquid-layer product will limit the etching rate and load the surface with impurities. However, in our experiments this problem was circumvented by mild substrate heating to $< 60^\circ\text{C}$.

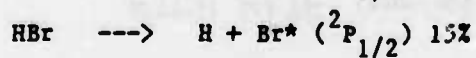
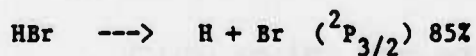
We have shown that the etch rate of GaAs increases exponentially with temperature. The predominate mechanism of this dependence could be a result of either thermal desorption of nonvolatile etching products,^{(4),(9)} leading to open reaction sites, or thermal-enhanced reactions of the photofragments with the GaAs surface. To distinguish between these two mechanisms, the temperature of the GaAs substrate was kept at a fixed temperature ($\sim 30^\circ\text{C}$) during the indirect laser-substrate etching process and then increased by 50°C while the excimer-laser beam was blocked (to avoid further photochemical production of reactants). After the temperature was reached the beam was unblocked and instantaneously the recorded Ga and As populations, as measured by the LIF probe, increased by an order of magnitude ($\times 10$). This indicates that the increase of the substrate temperature most dramatically effects those

products already formed on the GaAs. A similar experiment was performed without increasing the temperature of the GaAs substrate; in this case, no population change occurred. By using the above LIF detection scheme and slowly incrementing the temperature of the GaAs substrate, the overall temperature dependence of the Ga-etching products of CH_3Br and CF_3Br were found to be 13.0 and 10.5 kcal/mole, respectively. These results show that the predominate mechanism of the increase in etching rate with temperature is the thermal desorption of nonvolatile etching products which block reactive surface sites.

HBr Etching Gas Results

In order to further our investigation of photochemically-initiated dry etching of GaAs, we studied the HBr etching gas at the ArF laser wavelength. Several advantages exist for HBr as a candidate for dry-etching processes, namely: 1) a single GaAs-reactive radical is produced at 193 nm, viz. Br, 2) a high quantum yield and a high dissociation cross section at 193 nm and, 3) a high bond (~ 3.73 eV), thermodynamically favoring a low dark etch rate. An additional aspect of isolating Br atom etching reactions is that selective crystallographic etching is known to occur.⁽¹⁴⁾ Recently reported experiments using low-energy Br_2 plasmas⁽¹⁴⁾ have shown etching rates of greater than 30 $\mu\text{m}/\text{min}$ with selective anisotropic etching.

The primary photochemical processes of HBr at 193 nm are the production of ground-state Br and spin-orbit excited-state Br^* atoms. H atoms produced in the ground state are thought to be unreactive with the GaAs surface.⁽¹⁶⁾



The etch rate for GaAs (100) in the presence of 500 mTorr of HBr as a function of laser power density is shown in Fig. 3. Etch rates were

HBr ETCH RATE VS LASER POWER

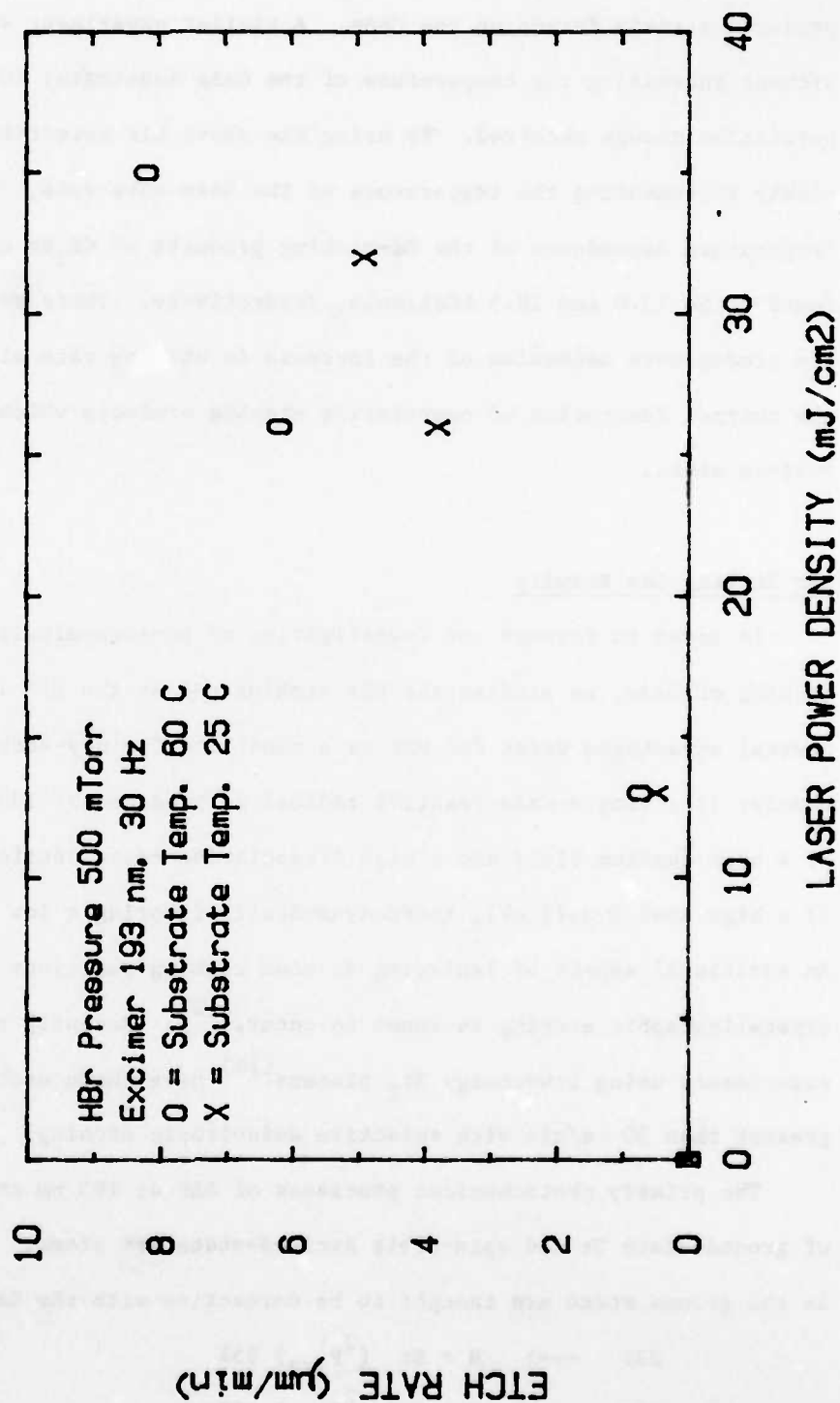


Figure 3. The etching rate of GaAs (100) by HBr as a function of laser power density (30 Hz) is plotted with substrate temperature.

determined after a 1-min exposure from masked samples under direct laser-substrate configurations. Etching rates appear to be linear with time. Since the dark etching rate at zero laser power is below $0.01 \mu\text{m/hr}$ the maximum light:dark ratio observed is $\sim 50,000:1$. The etch rate data is limited to laser energy densities below 35 mJ/cm^2 because above this value laser-ablative effects become important (see previous CF_3Br discussion).

The temperature dependence of the etch rate in Fig. 3 reflects the importance of surface reaction product removal. Using two temperatures (23°C and 60°C), it is observed that the etch rate increases with temperature. The cause of this increase is due to the volatilization of the surface products at the higher temperature. At the lower temperature, a film forms over the substrate blocking reactive surface sites.⁽¹⁴⁾ However, at both temperatures mirror-like surfaces are obtained.

Crystallographic Effects

Selective crystallographic etching is exhibited by the photodissociation products of HBr with GaAs . The cause of this highly anisotropic etching is the chemical reactivity of gas-phase Br atoms with specific crystal planes of the GaAs substrate. By using crystallographic masking techniques, the availability of certain crystal planes is limited. Studies were performed by masking GaAs (100) and (111)B samples normal and 45 degrees to the {110} cleavage planes. Samples were masked with straight-line photoresist patterns ($\sim 25 \mu\text{m}$ wide).⁽¹⁵⁾ Etching features were examined at one minute intervals to study the development of the crystal facets. All experimental conditions were as follows: sample temperature 60°C , HBr pressure 500 mTorr, and excimer laser power 30 mJ/cm^2 at 30 Hz. For GaAs (100) with masks oriented along the {110} planes, crystal facets develop at 45° to the $\langle 100 \rangle$ direction. Etching of

these planes, which are identified as the (111)A planes (see Fig. 4), self-terminate after ~7 mins to form v-grooves (see Fig. 5). On the other hand, by masking the GaAs (100) at 45° to the {110} cleavage planes (i.e. along the $\langle 100 \rangle$ direction), crystal facets also develop at 45° with substantial undercutting. These etched facets are identified as the (110) crystal planes. After 3-5 min of etching reverse-mesa structures are resolved. These mesas form because of two orthogonal (110) planes being present (Fig. 5). For GaAs (111)B samples, masks were oriented only 45° to the {110} cleavage planes. Crystal planes of the (100) family develop at 45° to the $\langle 111 \rangle$ direction.

The shapes in the preceeding discussion are explained as follows: the low order crystal planes etch with Br atoms in the order of (111)B > (100) ~ (110) > (111)A. Therefore when the (111)A planes are present in a particular masking orientation they are etched. For example, in masking orientations along the {110} cleavage planes of GaAs (100) substrates, the (111)A planes are present at 45° to the $\langle 100 \rangle$ direction and thus explain the observed crystal faceting (Fig. 5). On the other hand, on masking GaAs (100) at 45° to the {110} plane, only (110) and (100) planes are present. In this case, the (110) planes develop with extreme undercutting along the $\langle 100 \rangle$ direction, since both the (110) and the (100) planes etch at similar rates. The HBr crystallographic etching produces sharp edges and flat bottoms in all orientations studied.

Conclusion

In summary, we have demonstrated the utility of UV-laser photochemistry for large-area, dry-etching of GaAs using a variety of bromide derivatives. Etching rates were found to be typically 8.2 $\mu\text{m}/\text{min}$ for HBr and 0.5 $\mu\text{m}/\text{min}$ for

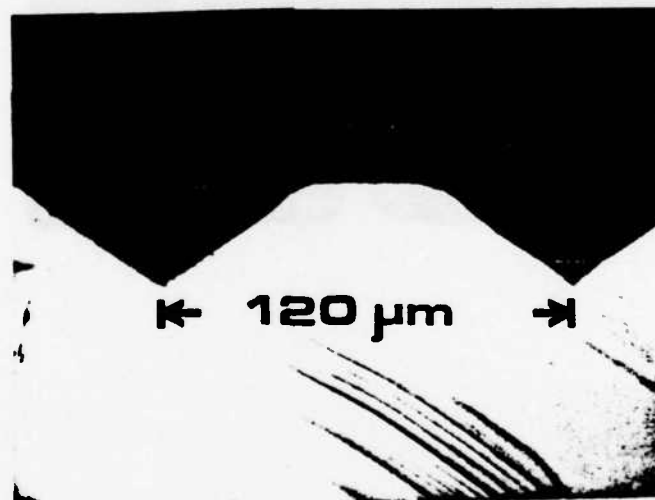
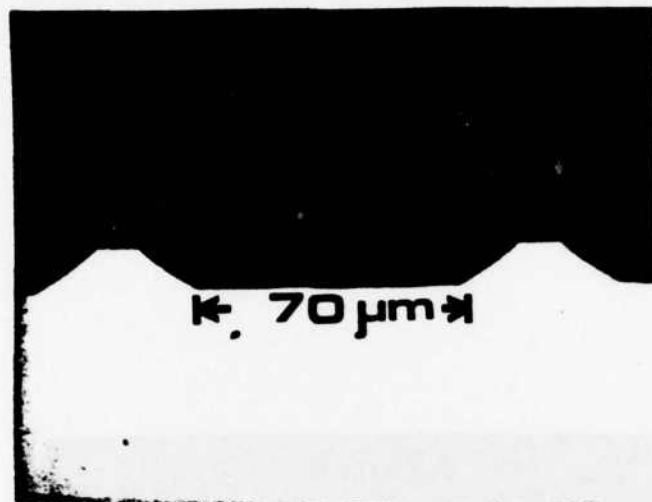


Figure 4. (Top) A SEM of selective crystallographic HBr laser-etching of GaAs (100). Exposed 45 planes are identified as (111)A. (Bottom) A SEM of v-groove structures formed by self-terminated etched (111)A planes.

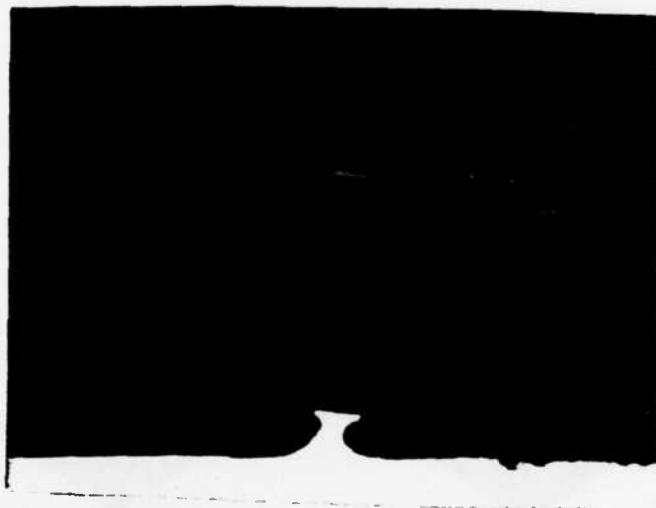


Figure 5. A reverse-mesa microstructure formed on GaAs (100) by intersecting (110) etched planes.

CH_3Br and CF_3Br . The etching process for HBr results in high anisotropy caused by Br reactions with specific planes of GaAs . Etch rates of the order $(111)\text{B} > (100) \sim (110) > (111)\text{A}$ explain the crystallographic etching. CH_3Br and CF_3Br also exhibit anisotropy but steeper side wall structures are observed. Smooth, minor like walls and surfaces are observed after etching. Chemically, the etching species are consistent with a combination of the CF_3 or CH_3 and Br radicals.

- (1) H. Winters, J. Coburn, and T. Chuang, *J. Vac. Sci. Technol.* B1(2), 469 (1983).
- (2) J. Steinfeld, T. Anderson, C. Reiser, D. Denison, L. Hartsough, and J. Hollahan, *J. Electrochem. Soc.* 127, 514 (1980). T. Chuang, *J. Chem. Phys.* 72, 6303 (1980).
- (3) T. Aridado, H. Okano, M. Sekine, and Y. Horike, paper presented at Material Research Society Conf., Boston (1983). A preliminary report of the present work was also presented: P. Brewer, S. Halle, and R. M. Osgood, Jr., Material Research Society Conf., Boston (1983).
- (4) D. Ehrlich, R. Osgood, and T. Deutsch, *Appl. Phys. Lett.* 36, 698 (1980).
- (5) S. Gandi, VLSI Fabrication Principles, (Wiley, New York, 1983).
- (6) S. Leone, *J. Phys. Chem.* 85, 3844 (1981).
- (7) J. Calvert and J. Pitts, Photochemistry, (Wiley, New York, 1966).
- (8) T. Chuang, in Laser Diagnostics and Photochemical Processing for Semiconductor Devices. R. M. Osgood, S. R. J. Brueck, and D. H. Schlossberg; Eds (North-Holland, New York, 1983) p 45.
- (9) T. Deutsch, in Laser Diagnostics and Photochemical Processing for Semiconductor Devices. R. M. Osgood, S. R. J. Brueck, and D. H. Schlossberg; Eds (North-Holland, New York, 1983) p 225.
- (10) R. Krchnavek, H. Gilgen, P. Brewer, S. Halle, and R. M. Osgood, paper presented at CLEO-83, Baltimore (1983).
- (11) See for example: H. Gatos and M. Levine, *J. Electrochem. Soc.* 107, 427 (1983) D. MacFadyen, *J. Electrochem. Soc.* 109, 1934 (1983).

- (12) See for example: J. Smith, The Chemistry of Arsenic, Antimony and Bismuth (Pergamon, New York, 1975). K. Wade and A. Banister, The Chemistry of Aluminum, Gallium, Indium and Thallium (Pergamon, New York, 1975).
- (13) Handbook of Organometallic Compounds, N. Hagihara, M. Kumada, and R. Okawara; Eds, (Benjamin, New York 1968).
- (14) D. Ibbotson, D. Flamm and V. Donnelly, J. Appl. Phys. 54, 5974 (1983).
- (15) Photoresist masking was performed using a JSEP-purchased mask aligner.

H. PHYSICS OF LASER SURFACE INTERACTIONS*

(H. Gilgen, J. Chen, D. Podlesnik, R. M. Osgood, Jr.)

(JSEP work unit 5, 1982-1985)

(Principal Investigator: R. M. Osgood, Jr. (212) 280-4462)

During the last year, we have actively pursued investigation of laser surface interactions for various new types of microfabrication for solid state electronics. As a result of this effort our laboratory has been the first to demonstrate the following microfabrication milestones:

- (1) Direct holographic etching of 100-nm-spacing diffraction gratings in GaAs
- (2) Direct writing of ultrahigh aspect ratio features on GaAs wafers, including a 1- μ m-diameter via through a 100- μ m thick wafer.
- (3) Laser-enhanced plasma etching of semiconducting materials.
- (4) Ultrarapid (1 μ m/min) anisotropic-dry etching of GaAs.

In doing the above work, we have been guided by a series of companion investigations into the basic-physics of laser surface interactions. Since much of the physical domain of these interactions is unexplored, i.e. the submicrometer reaction zones, heterogeneous photochemistry, metal alkyl molecular structure, we have uncovered several unexpected new phenomena. While the work has generally been motivated by needs in microelectronic processing, the understanding of these phenomena has implications in other fields such as metallorganic chemical vapor deposition, heterogeneous catalysis, and micromachining. In particular during this year, we have concentrated on three topics; a) ultraviolet photochemistry of relatively, simple organic molecules, b) surface enhancement of interface photochemical reactions using ordered surface microstructures, and c) ultraviolet radiation induced reactions in liquid solutions.

A. Ultraviolet Photochemistry of Simple Polyatomic Metallorganic Molecules

Photodissociation of dimethylzinc, dimethylcadmium and dimethylmercury is of interest for both fundamental and applied reasons. From the applied point of view, the first demonstration of the "direct writing technique" for microelectronics was based on the photodissociation of dimethylcadmium or dimethylzinc by a UV laser beam focused on the surface of the semiconductor substrate. Despite this interest there is only very limited knowledge of the excited electronic states of metal alkyls. The only measurements of the UV absorption spectra of dimethylzinc, dimethylcadmium and dimethylmercury were two photographic studies reported in the 1930's. Because of the paucity of experimental data, no theoretical analysis of the excited electronic states of these molecules has been made.

A new series of measurements of the UV absorption spectra of dimethylzinc, dimethylcadmium and dimethylmercury have been made. The spectra were measured from $30,000\text{ cm}^{-1}$ to $57,000\text{ cm}^{-1}$ for various gas temperatures and pressures. For each of the above organometallics, we have observed structured continua with clear and regular progressions of vibrational peaks. These spectra have enabled us to develop a model which clarifies the photodissociation process of these organometallics in their lower-two excited electronic states. In this model, the vibrational peaks result from direct but asymmetric photodissociation.

We have recently developed an analytic theory which allows us to make a quantitative comparison of the calculated envelope with the observed spectra. It is important to note that prior to the development of this analytic theory no accessible theory existed for explaining the structure which exists on the bound-free spectra of many simple important polyatomic molecules. Such structure plays an important role in modulating and determining the precise

value of photodissociation cross sections for ultraviolet photodissociation.

B. Surface-Enhanced Photochemical Reactions

In our previous year's report, we described the direct observation of surface-enhanced photochemistry. This work was done using isolated small metallic spheres covered with a metallorganic film and then irradiated with UV light. The results showed that enhanced photochemistry occurs near the particles due to a plasma resonance within the spheres. As a result of the microscopic anisotropy in the optical electric fields, the spherical particles slowly grow into ellipsoids during photodissociation of the adsorbed metallorganic film. Particles of this shape are of greater practical value for composite dielectric materials with selective-absorption in the infrared.

In our report this year, we discuss our observation of enhanced photochemistry in a coherent array of metal microstructures, viz. metal diffraction gratings. In principle such a phased array can form a greatly enhanced near optical field than in the case of individual particles.

The experiments to investigate photodeposition on metal gratings were accomplished with a 3-5 mW, frequency-doubled, argon-ion laser. This laser has sufficiently short wavelength to photodissociate the metal-alkyl carrier gas, (dimethylcadmium) used here, and, further, it has a useful temporal coherence length, ~20 cm. The laser beam was split and mixed on the rear surface of a quartz flat mounted on a sample-cell containing dimethylcadmium gas. The angle between the two laser beams could be adjusted so as to examine different grating spacings.

With our experimental setup, we readily obtained submicrometer diffraction gratings. In general, the best results were obtained when the sample cell, which contained 10 Torr of DMCd and 80 Torr of buffer gas, was

cooled to 15°C. At these temperatures physisorbed molecular layers are thick and the contribution from gas-phase photodissociation is minimized. Since the interfering UV beams enter the cell from glass with index $n = 1.43$, the minimum fringe spacing is

$$d_{\min} = \frac{\lambda}{2n \sin \theta_{\max}}$$

where θ_{\max} is the maximum angle which we could readily obtain, $\sim 80^\circ$. In fact, gratings with periods as small as 300 nm were readily made. Grating formation by photodeposition allows direct optical monitoring of the deposition by a noninvasive optical probe; in our case an He:Ne laser was used. The probe is used by observing the minus-first-order diffracted light from the metal grating. For small modulation depths, the intensity of the diffracted light is proportional to h , i.e., to the amplitude of the grating ripple. Thus, the grating growth rate can be monitored through the rate of increase in the diffracted intensity.

These measurements have shown clearly one of the most striking phenomena associated with optical growth of diffraction gratings. As the angle of interference is varied, sharp resonances are observed in the grating growth rates, see Fig. 1. These resonances are the result of enhanced coupling of light into surface confined waves within the metal film. The resonances occur when the grating spacing, d , is equal to an odd multiple of half wavelengths of the surface wave which exists at the frequency of the incident optical electric field, that is, when

$$d = (2m+1) \sqrt{\frac{|\epsilon_1| - 1}{\epsilon_1}} \frac{\lambda_s}{2}$$

where m is an integer, ϵ_1 is the real part of the metal dielectric constant, and λ_s is the wavelength of the ultraviolet light in the quartz window. At

the spacing of each resonance, the angle of one of the diffracted orders is such that the wavevector of the light is just parallel or along the surface of the metal. Thus, each resonance represents a spacing such that the amplitude of the surface-plasma-wave intensity is maximized. Since the local electric field, including incident and scattered waves, determines the rate of grating growth, the deposition is fastest at resonance spacings.

As seen in Fig. 1 the grating growth rate can be increased by as much as a factor of 8 at resonance compared to that for off resonance. For the laser powers and grating areas considered here, this means that relatively dense metallic gratings can easily be grown at resonance spacings whereas only very thin structures can be obtained at intermediate values.

C. UV Driven Liquid Phase Reactions

We have recently performed a series of experiments in which we have used, deep-ultraviolet laser light for fast, maskless wet etching of GaAs, including n, p, and semiinsulating (SI) substrates with (100) orientation. For all doping types, the etch rates, at low laser intensities, were higher in the deep-ultraviolet than in the visible. This rapid, room-temperature etching process has enabled us to etch, for example, micrometer-scale via-holes with perfectly vertical walls, through a standard GaAs wafer. We attribute the rapid etching rates to the new interfacial chemistry which occurs when deep-UV radiation illuminates a semiconductor surface in an aqueous solution.

The difference in UV and visible light etching is best shown by the etch-rate enhancement in the low-intensity region of Fig. 2. This difference cannot be explained simply by the fact that more minority carriers are created close to the surface under UV than under visible illumination. It is known that for n-type GaAs the photogenerated holes are driven to the surface by the

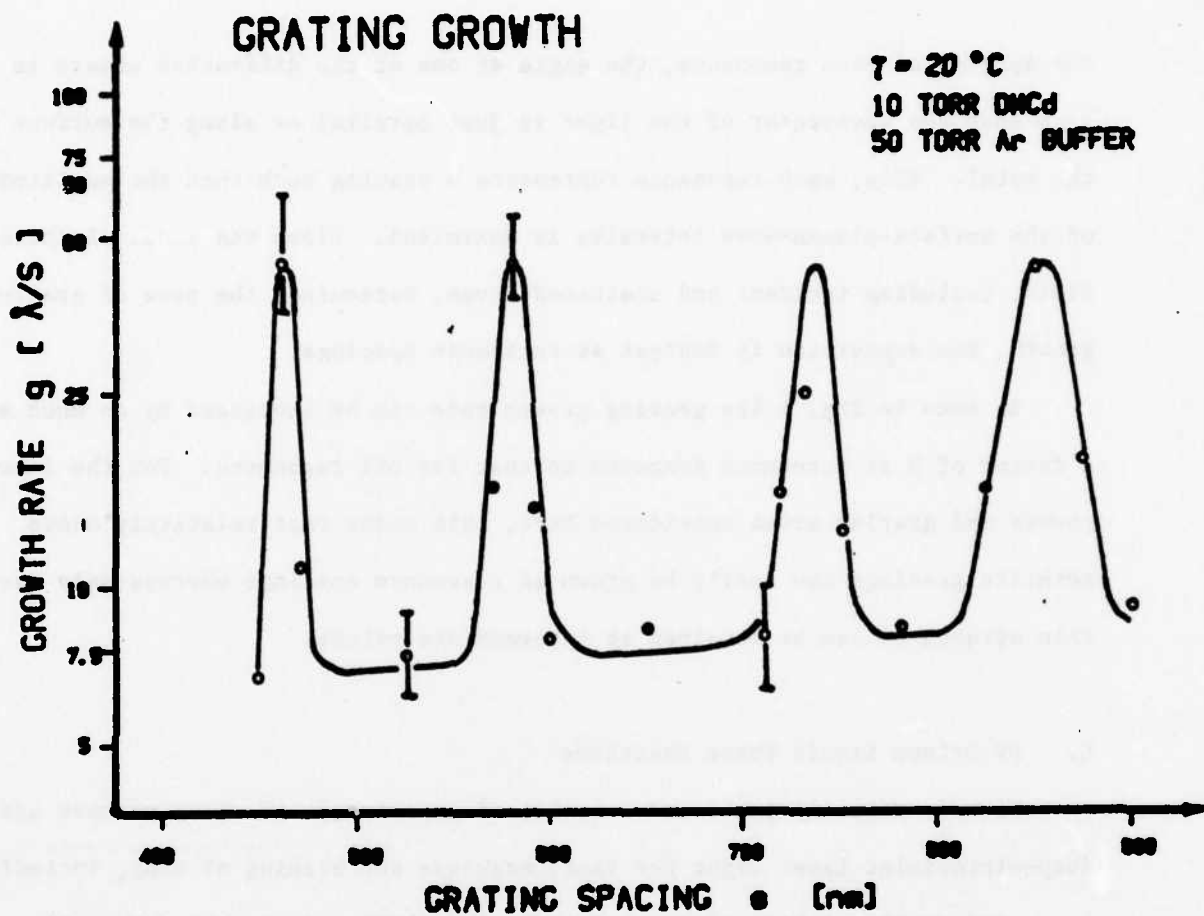


Figure 1. Growth rate versus grating spacing for metal gratings grown by photodeposition from adsorbed metal-alkyl molecules with 257-nm light.

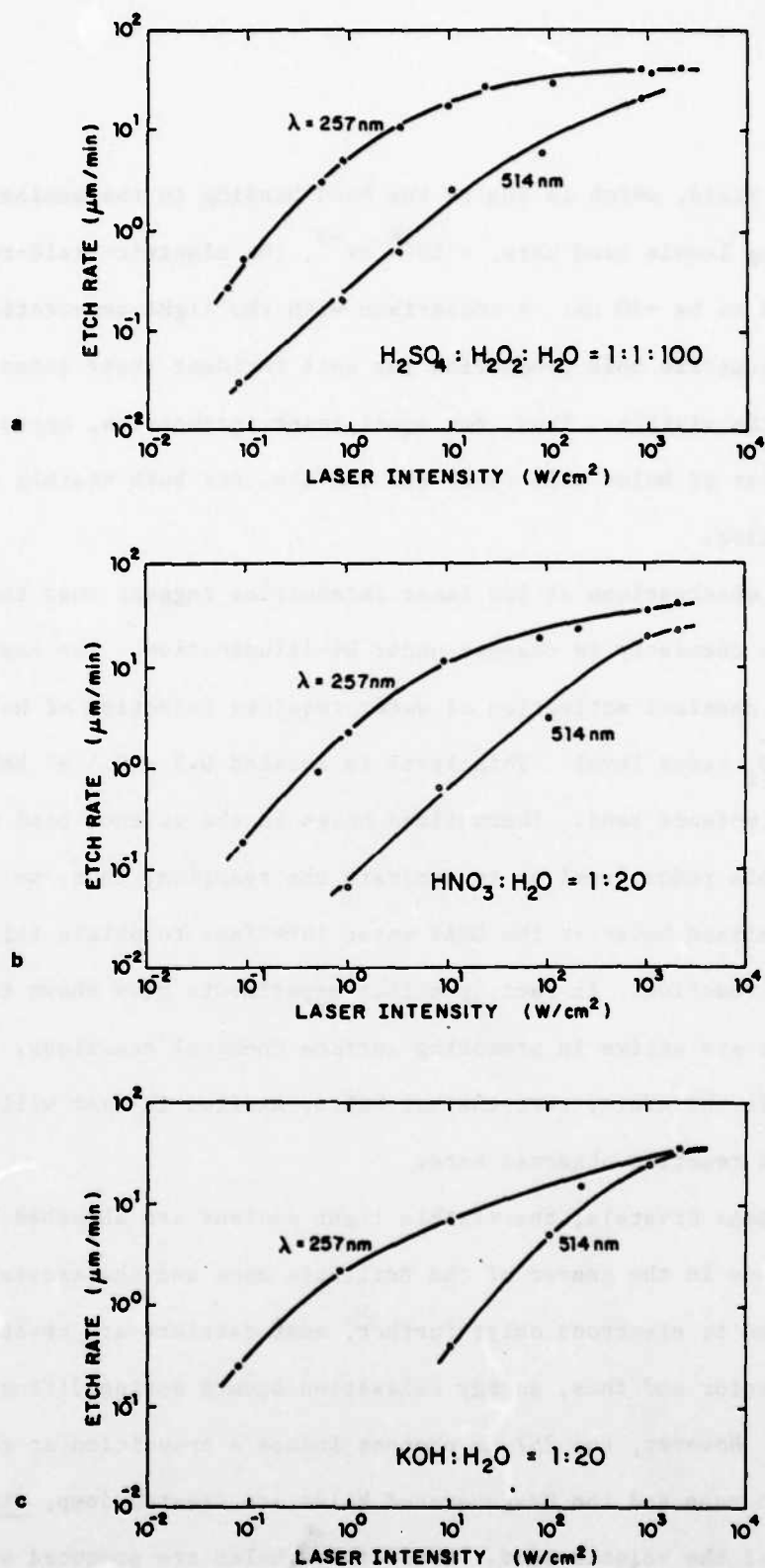


Figure 2. Etch rates for n-type GaAs as a function of laser intensity. Results are compared for green and UV light.

electric field, which is due to the band bending in the semiconductor. For the doping levels used here, $\sim 10^{18} \text{ cm}^{-3}$, the electric-field-region depth is estimated to be $\sim 30 \text{ nm}$. A comparison with the light-penetration in GaAs, the total volumetric hole production per unit incident laser intensity is smaller than in the visible. Thus, for equal laser intensities, approximately the same number of holes will reach the surface, for both visible and UV illumination.

The observations at low laser intensities suggest that the basic interface chemistry is changed under UV-illumination. For example, the observed chemical activation of water requires injection of holes from GaAs to the $\text{H}_2\text{O}/\text{O}_2$ redox level. This level is located $0.3 - 0.5 \text{ eV}$ below the top of the GaAs valence band. Thermalized holes in the valence band are not able to access this redox level or to activate the reaction; thus, we require hot, nonthermalized holes at the GaAs water interface to obtain this particular chemical reaction. In fact, previous experiments have shown that hot electrons are active in promoting surface chemical reactions. It is reasonable therefore, that the hot holes, excited in GaAs will cause the oxidation reaction observed here.

In GaAs crystals, the visible light photons are absorbed by the electron transitions in the center of the Brillouin zone and the excess photoenergy is transferred to electrons only; further, most carriers are created deep in the semiconductor and thus, energy relaxation occurs during diffusion to the surface. However, the 257-nm photons induce a transition at the X-edge of the Brillouin zone and the UV-generated holes are created deep, viz 2.5 eV , below the top of the valence band. Since these holes are produced within 5 nm from the liquid-solid interface, energy relaxation is incomplete for carriers reaching the surface. Using a physical model and rate data available for hot

electrons in GaAs, we conservatively estimate that the energy relaxation time for holes in our experiment is 10^{-12} s. This is considerably longer than the transit time, $\tau_t \sim 10^{-13}$ s, through the laser illuminated layer on the GaAs surface. This estimation predicts, that most of the photoexcited holes would reach the solid-liquid interface with enough excess-energy to access, for example, the H_2O/O_2 redox level. A more accurate calculation will need a detailed model for the recombination and transport of UV-generated carriers.

*This research was also supported by the Air Force Office of Scientific Research/DARPA under Grant F-49620-82-K-0080 and Army Research Office under Contract DAAG29-82-K-0089.

I. PHOTOCHEMICAL RECORDING OF PHASE DIFFRACTION GRATINGS ON SEMICONDUCTOR SURFACES*

(D. Podlesnik, H. Gilgen, R. M. Osgood, Jr.)
(JSEP work unit 5, 1982-1985)
(Principal Investigator: R. M. Osgood, Jr. (212) 280-4462)

Chemical etching of semiconductors is an important processing step in semiconductor technology. Among the different methods of the chemical etching, the light-sensitive etching is of significant importance. This method is based on the light-induced variation of the minority-carrier concentration on the semiconductor surface. Typically, the photogenerated minority carriers induce or accelerate the etching, thus enabling the recording of a given light pattern on the semiconductor surface. It has been previously shown that light-enhanced, wet etching is a simple and convenient method for fabrication of, for example, semiconductor gratings with spacings, from the hundred micrometer to the micrometer range. In general, versatility and simplicity of the maskless chemical etching favor its use over conventional lithographic techniques.

In many light-sensitive chemical processes, including the semiconductor etching, a coherent light source is preferred or even necessary. For example, the laser spatial coherence permits submicrometer focusing of the laser beam thus allowing a high-resolution, localized etching. Also, the temporal coherence of the laser source is important, for example, for recording optical information, viz for producing holograms.

In this report, we describe the ultra-high resolution profiling of GaAs crystals by using the light-sensitive, chemical etching. In this processing, two laser beams are interfered to produce the simplest hologram, namely phase diffraction gratings, across the semiconductor surface. These optical gratings had periods between 100 and 300 nm, and controllable and reproducible

optical properties. In addition, a variety of groove profiles, including blazed, sinusoidal, and "impulse" shape, can be made under different fabrication conditions. These gratings are potentially important for single-wavelength, distributed-feedback lasers and for couplers in integrated optics. A novel aspect of this direct fabrication technique is that the gratings can be optically monitored during fabrication which, in turn, allows for precise control over the grating depth and groove profiles. Further, because our gratings have very high resolution, the process of grating fabrication becomes a method for studying the micrometer-scale physical processes which influence the grating structure and growth, Fig. 1. These processes may involve, for example, the diffusion of excited species or the magnification of the optical fields at the grating surface.

The experimental arrangement used is simple, mechanically stable and is readily adjusted to obtain a wide range of grating spacings (see insert, Fig. 1). A laser beam from a moderate-power argon-ion laser passes through a spatial filter and a collimator before impinging on a right-angle corner. The corner, on which a mirror and a semiconductor sample are mounted, is inside an optical cell containing an $\text{H}_2\text{O}_2 : \text{H}_2\text{SO}_4 : \text{H}_2\text{O}$ etching solution. An interference pattern is produced by the superposition of the direct and the reflected beams inside the solution, which has an index of refraction greater than one, approximately 1.33, due to the high water content. The dissolution of GaAs in this solution is influenced by the number of carriers present at the semiconductor surface. For n-type GaAs, photogenerated holes accelerate the etching rate thus forming a photoengraved pattern in the solid surface. Detailed groove profiles were measured with a scanning electron microscope (SEM). The argon-ion laser was operated in one of two lines: 514.5, or 457.9 nm. The maximum laser intensity was 700 mW/cm^2 ; however, 300 mW/cm^2 was

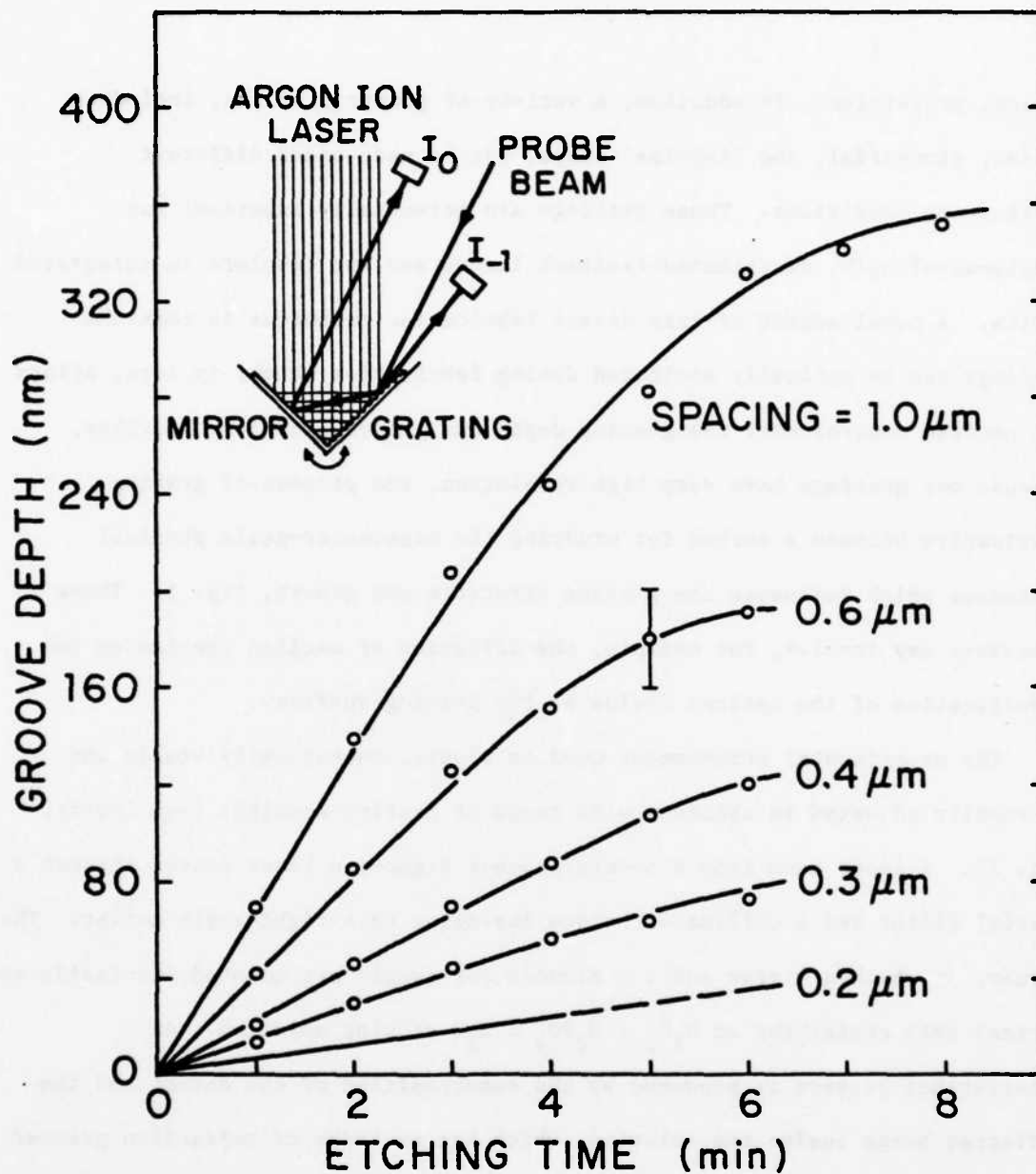


Figure 1. The measured grating-groove depth versus the etching time in an 1:1:100 solution for different grating spacings. The points are evaluated by SEM measurement. The curve for the 200-nm grating is obtained by *in situ* measurements. The insert shows a part of the experimental arrangement.

the typical intensity used in the experiments.

In general, the profile of the grating grooves depends on the details of the carrier movement within the semiconductor, the relative magnitude of the dark versus light-enhanced etching rate, and the anisotropy in the etching process. We investigated the profiles of gratings on n-type GaAs for several different crystal orientations using different spacings and etching solutions. For the dilute 1:1:100 solution used in the experiments, we found that crystal orientation did not influence the grating profiles and etch rates. Generally, gratings with spacings $>1 \mu\text{m}$ had a sinusoidal profile (see Fig. 3a), which is to be expected for a linear dependency between etching rate and light distribution on the surface. On the other hand, submicrometer gratings showed a deviation from simple sinusoidal profile; typically a cusped profile was observed. Figure 2 shows the development of characteristic groove-profile for a 300-nm grating. This deviation cannot be explained by a simple theory based on an isotropic diffusion of the holes at the semiconductor surface. Local variations in the hole drift due to photoinduced electric fields, both normal and transverse to the surface and the interference patterns, give rise to higher order components in the groove profile, as shown in Fig. 2.

Because of practical importance of blazed gratings, we have developed a simple technique for their fabrication. The approach was to tilt the semiconductor substrate so that the bisector of the angle of the interference was at an angle with respect to the surface normal. This tilting was accomplished by mounting the substrate on a non-right-angle corner; the deviation from 90° represents the blazed angle. The tilting of the substrate in conjunction with the continuous dark etching, which progresses normal to the surface, produces a clear, blazed profile, as shown in Fig. 3b. The profile can be triangular or cusped depending on the relative magnitude of the uniform and

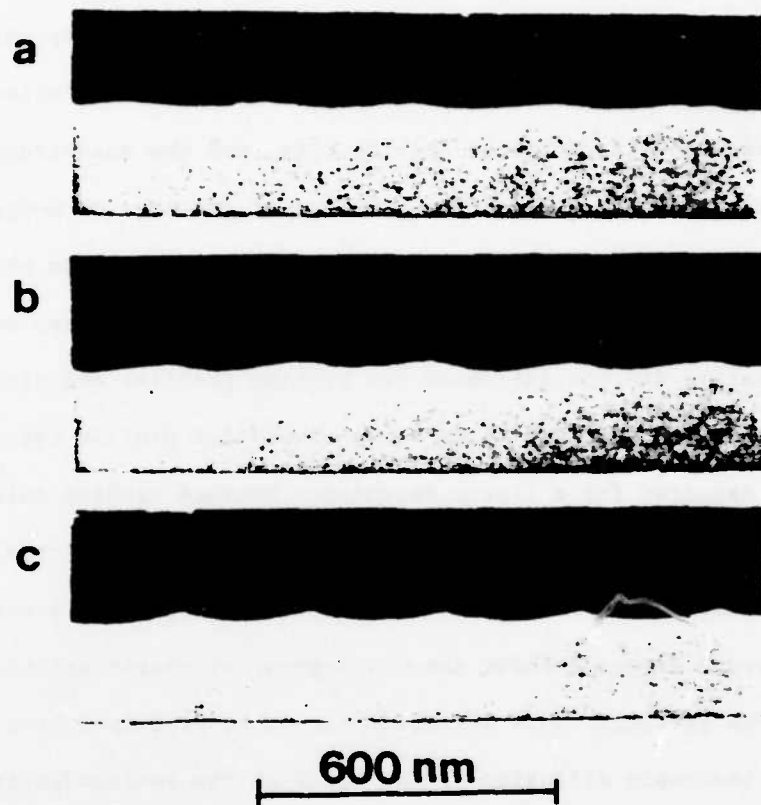


Figure 2. SEM micrographs of the groove-profile for 300-nm gratings on GaAs after different etching times in the 1:1:100 solution. The etching time was (a) 1 min, (b) 2 min, and (c) 3 min.

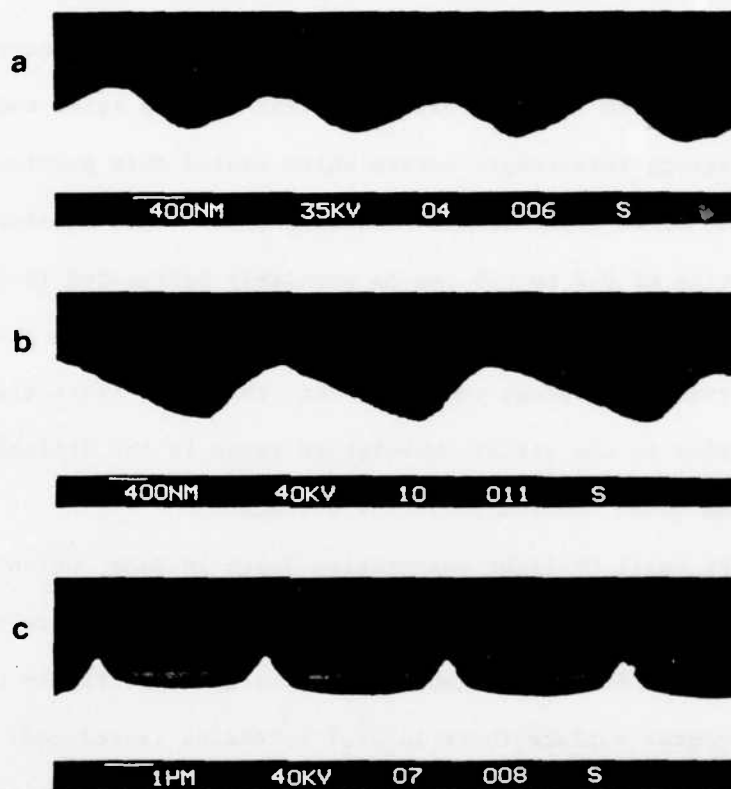


Figure 3. SEM micrographs of gratings with (a) sinusoidal, (b) blazed, and (c) "impulse" profile.

light-enhanced etching rate.

More unusual grating profiles could be produced under extreme conditions of etching. For example, using a solution with a 10 times higher H_2O_2 content than the value quoted above and a laser power-density of 1 kW/cm^2 , we produced a $3\text{-}\mu\text{m}$ impulse grating whose profile was a series of narrow peaks, see Fig. 3c. We believe that the extremely fast etching rates under these conditions had a strong anisotropic nature which caused this particular profile.

The above experimental results indicate that submicrometer gratings with s/d ratios of 0.2 to 0.8 can be precisely fabricated in GaAs using laser chemical etching with in situ monitoring. The groove profiles and growth rate for different spacings indicates that the chief limitation on process resolution in the visible wavelength range is the diffusion of carriers produced below the semiconductor surface.

The small UV-light penetration depth in GaAs, which is shorter than the depletion layer thickness, however, results in an ultra-high etching resolution. Since photogenerated holes are effectively created on the semiconductor surface their lateral spreading is reduced. Figure 4 shows a 100-nm grating which is the optical limit of the interferometry for UV-light (257 nm) used. Typically, the etching time was ~ 5 minutes at 10 mW/cm^2 . The best results were achieved with very dilute solutions, containing 1% H_2O_2 . The grating profiles were uniform and deep. In fact, due to the small lateral spreading of carriers, the depth of UV-light-produced grating is a factor of two greater than comparably spaced gratings produced with visible-light.

*This research was also supported by the Air Force Office of Scientific Research/DARPA under Grant F-49620-82-K-0080.

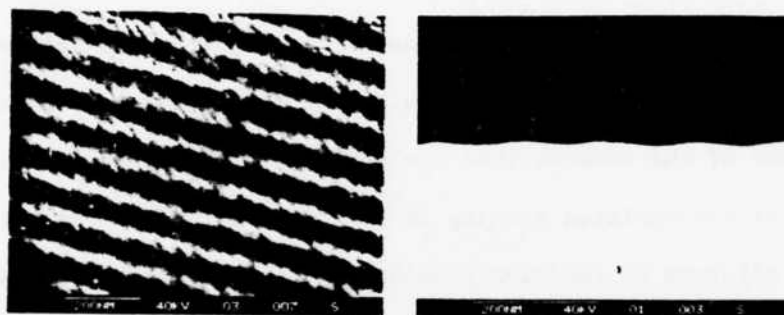


Figure 4. SEM micrographs of a 100-nm grating in n-type GaAs: (a) top view, and (b) cross section. The etching time for $1:1:100$ solution was 5 minutes at a laser intensity of $\sim 10 \text{ mW/cm}^2$.

J. LASER CONTROLLED PLASMA ETCHING*

(G. Reksten, W. Holber, R. M. Osgood, Jr.)

(JSEP work unit 5, 1982-1985)

(Principal Investigator: R. M. Osgood, Jr. (212) 280-4462)

Introduction

There are several reasons why it may be desirable to control or enhance the rate of a plasma-etching process with a laser beam. First, in many soft, semiconducting materials such as GaAs, it is important to achieve maximum etch rate with minimal ion bombardment, since surface damage often accompanies the latter. One of the reasons that ion bombardment seems an unavoidable aspect of plasma or ion assisted etching is that physical action is often necessary to remove adlayers of reaction products or other chamber contaminants. However, a number of recent laser-experiments in our laboratory have shown that low levels of laser light can remove these layers, although the exact mechanism for this removal is unclear at present. Thus, by subjecting the surface to illumination in a plasma etching reaction, it may be possible to operate the reactor in a region where physical bombardment and its concomitant surface damage is not necessary for satisfactorily high etch rates.

Second, for a variety of reasons, including surface cleanliness and the ability to generate highly reactive species, plasma etching is an important fabrication tool in modern microelectronics. One desirable capability, however, is absent from plasma processing - namely the ability to do local processing; in other words, if a particular fabrication step should require that the etching be confined or enhanced in one region of a semiconductor chip, this cannot be done at present in commercial reactors without separately masking the other portion of the chip. If the region of local etching is small compared to the remainder of the I.C. real estate, the additional masking step, of course, subjects a major portion of the wafer to the

additional processing steps involved in photolithographic patterning, thereby defeating at least a portion of the original reason for using dry etching. By using a maskless technique for enhancing plasma etching, which is based on patterned or focused laser light, local plasma processing can be done without requiring additional surface processing of the wafer.

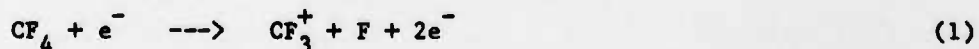
Third, in some plasma processing regimes selectivity of the etch process might be improved by illuminating large areas with unfocused laser light.

In the set of experiments described here, we have used visible, Ar^+ laser light to influence the etching of Si wafers in a commercial planar plasma etching system. A CF_4/O_2 plasma, at, typically, 100 torr gas pressure was used in conjunction with laser powers of up to 2 Watts. We have shown that the laser illumination of the Si surface in the plasma locally enhances the etch rate and may also reduce surface contamination.

Experimental

A commercial planar plasma etcher was used in conjunction with a CW argon ion laser. By modifying the r.f. (radio frequency) electrode through the installation of a laser port, the laser light could be focused onto the Si surface with an imaging system external to the plasma etcher. The presence of the port did not cause any change in the plasma etch rate. Fig. 1 illustrates the experimental arrangement. An 80% CF_4 /20% O_2 gas mixture was used, at 120 mTorr pressure. The r.f. power applied to the plasma etcher electrode was 0.1 W/cm^2 and the r.f. frequency 30 kHz.

Fluorine is liberated in the plasma environment typically through the reaction



Reaction products are adsorbed onto the Si surface and several possible

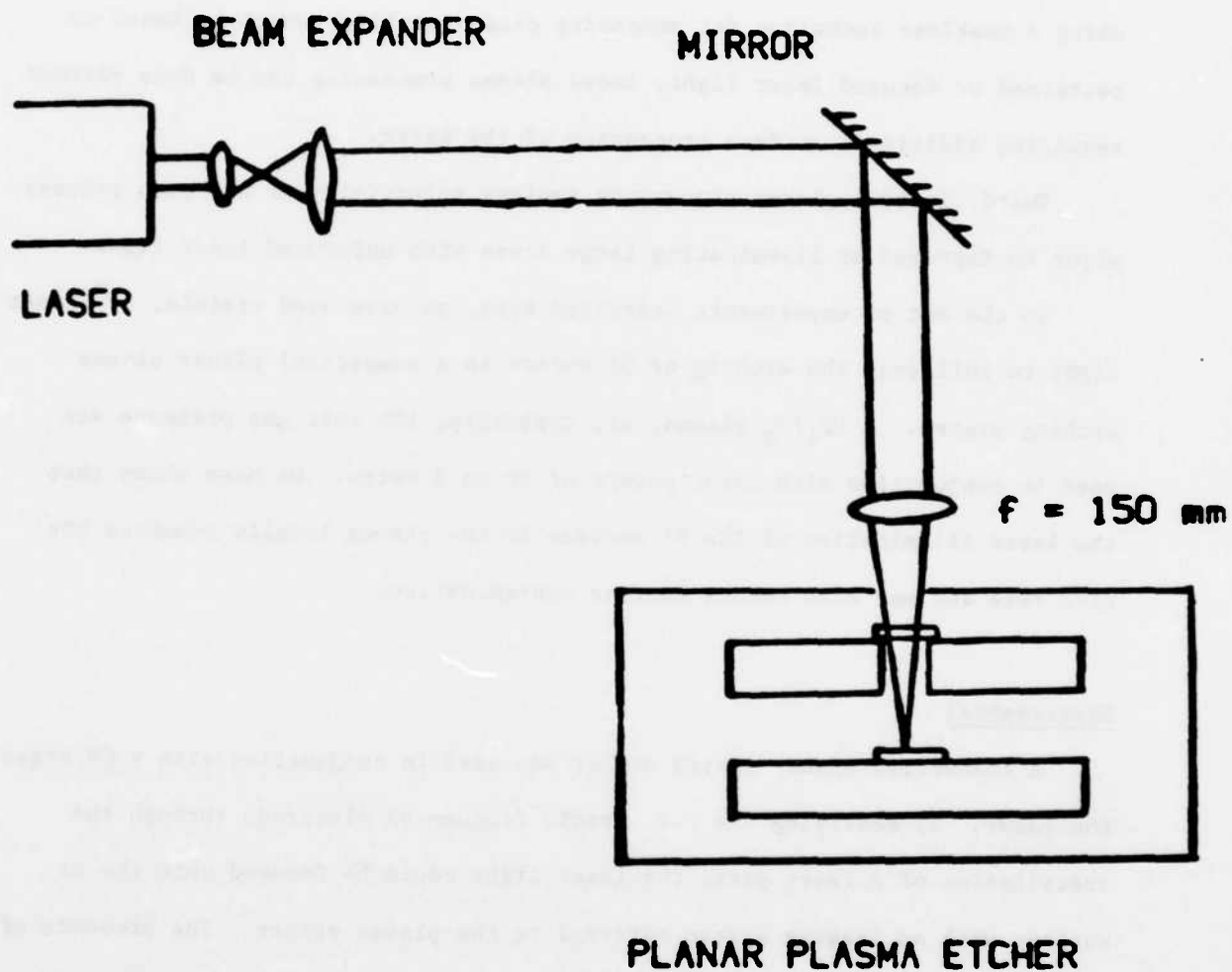


Figure 1. Experimental arrangement

surface reactions lead to the formation of SiF_4 , which is volatile. In our system "dark etch" rates of $\sim 0.2 \mu\text{m}/\text{min}$ were typical.

When the laser beam was introduced both thermal and nonthermal effects were observed. In the first experiment, an unfocused laser beam was used, essentially heating the bulk of the Si sample. A second Si sample was placed near the laser irradiated piece to enable a comparison between the dark etch rate and the photon enhanced etch rate to be made. Both Si samples were masked by an aluminum pattern and the etch depth measured with a mechanical stylus. The etch rate of the illuminated sample was significantly enhanced.

At a maximum laser power of 2W, thermal enhancements of 2.5 times the dark etch rate were possible. At this power the temperature rise of the Si surface was measured to be less than 100°C . When a heat sink compound was placed between the Si sample and the plasma etcher electrode, the enhancement did not occur, thus indicating that thermal effects were indeed responsible for the increased etch rates.

A cleaner surface was observed on the laser-irradiated Si wafer, indicating increased desorption of adlayers. This may lead to more vacant Si reaction sites and therefore to enhanced etch rates. Furthermore, increased desorption of SiF_4 may also enhance etch rates, depending on what the rate limiting step is.

The local effect of the laser beam on p- and n-type Si of different conductivities was investigated by focusing the laser to a 30-100 μm spot on the Si surface. The laser power density was varied from $100 \text{ W}/\text{cm}^2$ to $124 \text{ kW}/\text{cm}^2$. The laser irradiated piece was in good thermal contact with the grounded aluminum cathode. For each measurement made, the dark etch rate was measured by placing a second Si sample near the laser illuminated piece. The photon enhanced and the "dark etch" rates could thus be compared. The

enhancement was then normalized against the dark etch rate for each sample of Si investigated.

The results are plotted in Fig. 2. The curves show that at high laser powers ($> 6\text{ kW/cm}^2$) etching of p and n type Si of different conductivities is equally enhanced by the laser. At these power densities a substantial local temperature rise is expected. Since our earlier experiments showed that heating of the Si wafer caused significant etch enhancement, calculations were made to estimate the temperature rise at the center of the laser focal spot. Good thermal contact was assumed between the Si wafer and etcher electrode. For a constant laser focal spot of $50\text{ }\mu\text{m}$ diameter, the temperature is calculated to rise linearly with the laser power density. A plot of this is shown in Fig. 3. Below 1 kW/cm^2 laser power density, the temperature rise is less than 3°C . The temperature reaches 120°C at the maximum laser power densities investigated. (Not shown in Fig. 3, the focal spot diameter was in this case $30\text{ }\mu\text{m}$). Thus we conclude that the laser induced etch enhancement shown in Fig. 2 is to a great extent due to thermal effects.

From the enhancement observed at lower laser power densities, it is evident that substantial laser induced etch enhancement occurs also in the non-thermal regime. Fig. 4 illustrates this by showing the boxed area in Fig. 2 on an expanded scale. The laser power density range corresponds to that plotted against temperature in Fig. 3. In the nonthermal region the photon induced etch enhancement shows a strong doping dependence. Further experiments are planned to explain this.

Discussion

From the data obtained in our experiment it was not possible to determine which reactants are affected by the laser, and in this report we have

ETCH ENHANCEMENT VS LASER POWER

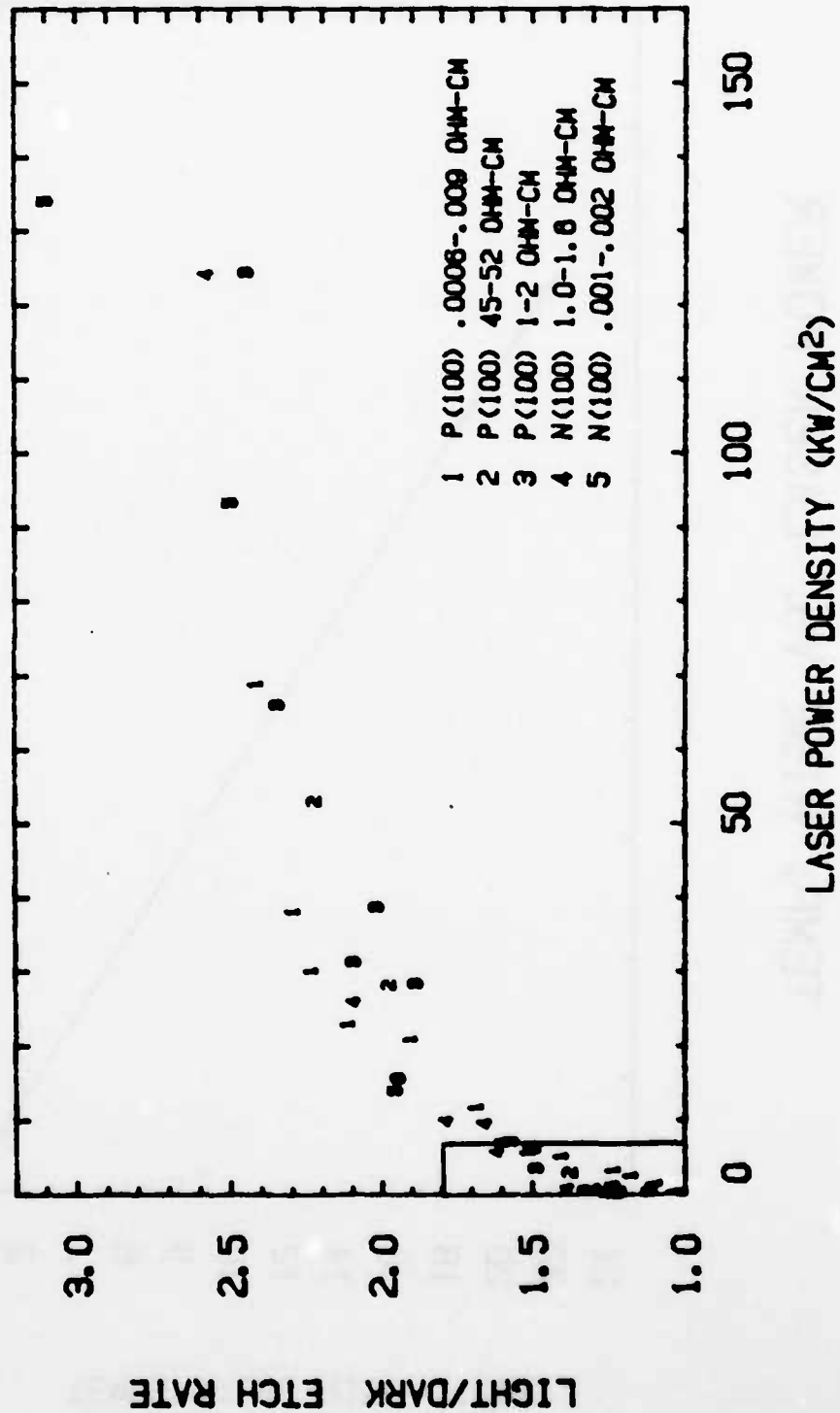


Figure 2

TEMP. RISE VS. LASER POWER

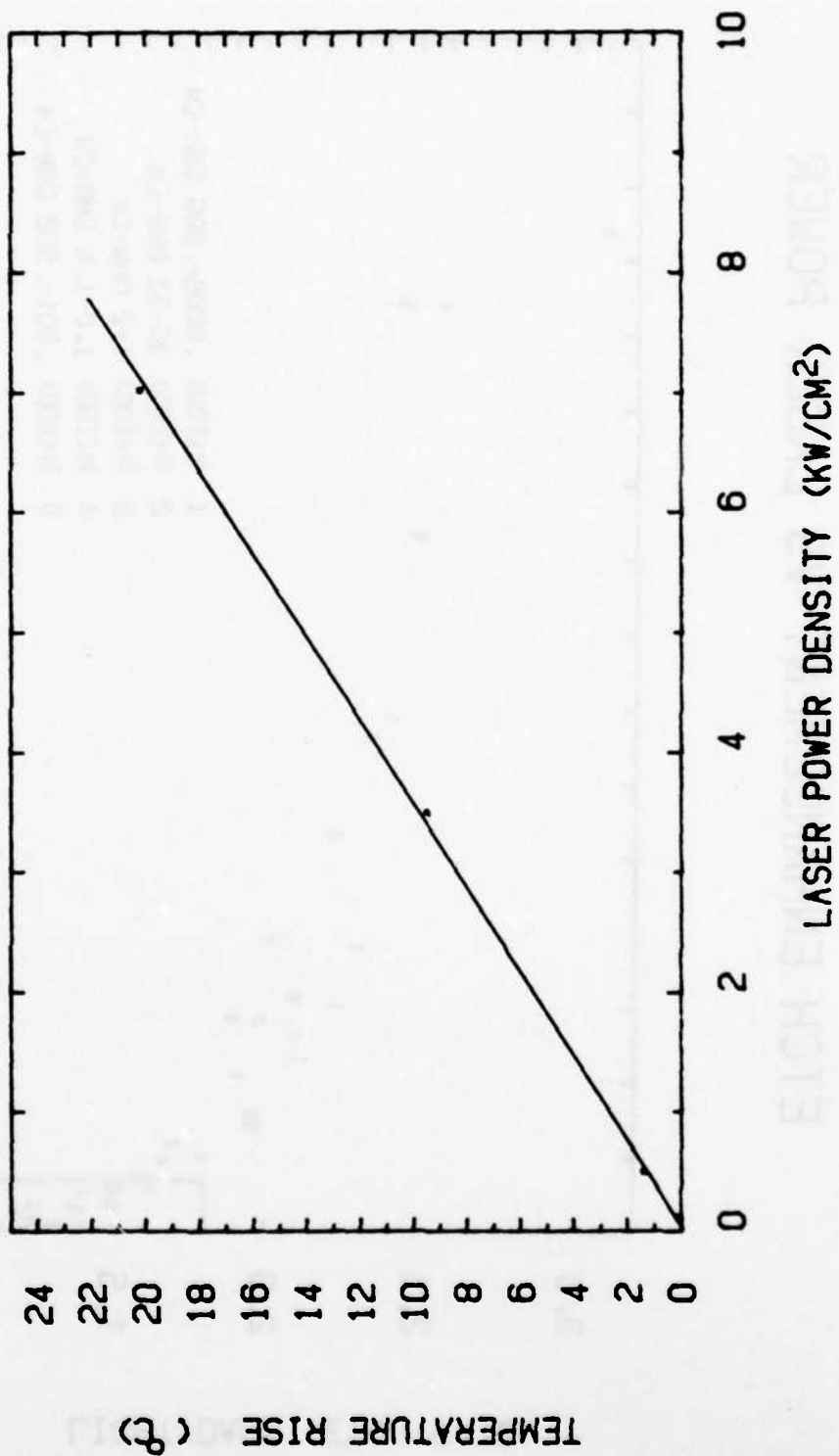


Figure 3

ETCH ENHANCEMENT VS LASER POWER

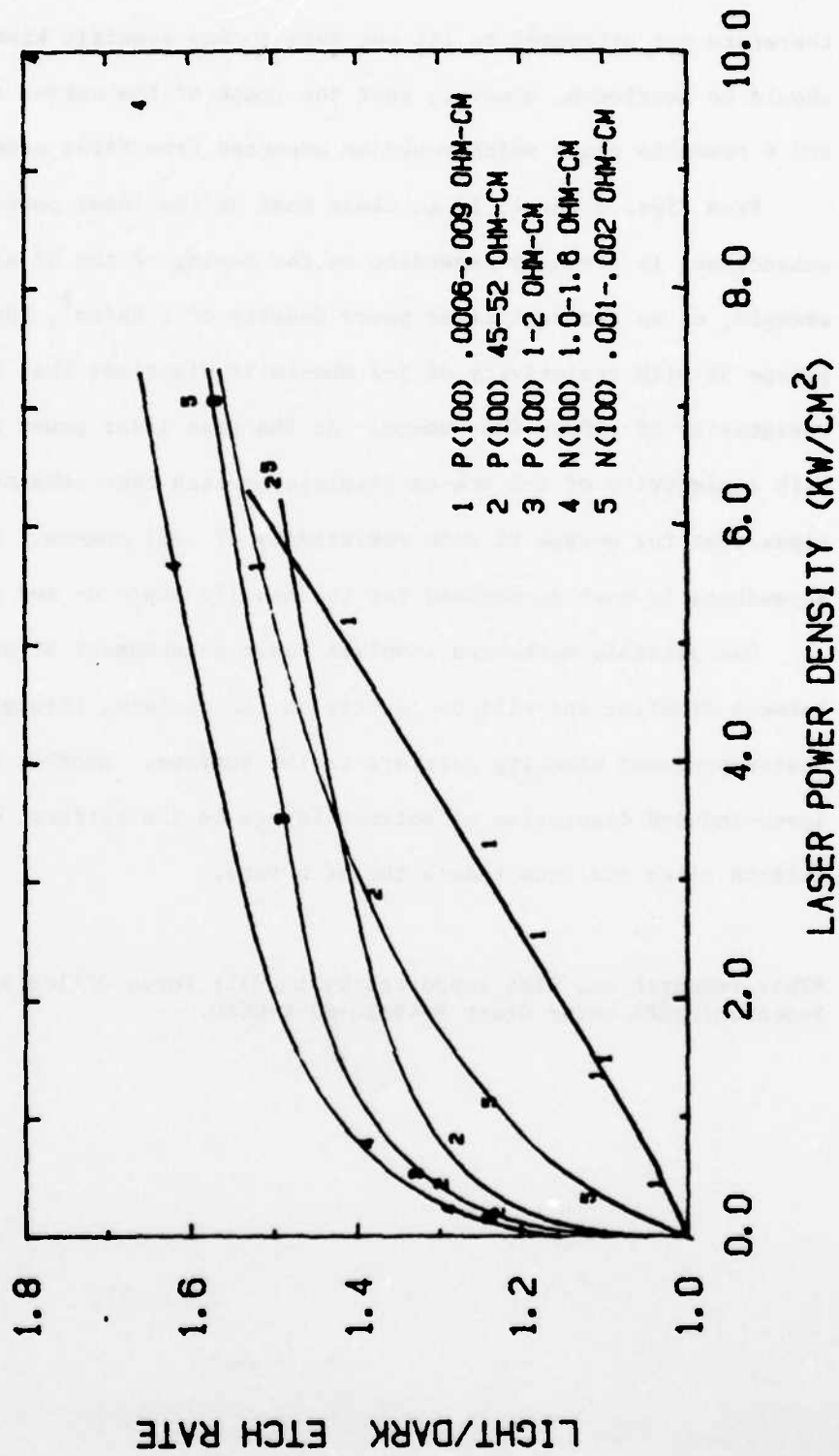


Figure 4

therefore not attempted to fit our data to any specific kinetic model. It should be mentioned, however, that the shape of the curves shown in Figs. 2 and 4 resemble those which would be expected from first order kinetic theory.

From Figs. 3 and 4, it is clear that at low laser powers, the etch enhancement is strongly dependent on the doping of the Si sample. For example, at an incident laser power density of 1 kW/cm^2 , the enhancement for p-type Si with resistivity of 1-2 ohm-cm is six times that for p-type Si with resistivity of .0006-.009 ohm-cm. At the same laser power density, n-type Si with resistivity of 1-2 ohm-cm displays an etch rate enhancement about four times that for n-type Si with resistivity of .001 ohm-cm. The doping dependence is most pronounced for the heavily doped n- and p- samples.

One possible mechanism involves laser enhancement of the reactions between fluorine and silicon centers on the surface, through the flow of photon-produced minority carriers to the surface. Another mechanism could be laser-induced desorption of polymer layers on the surface, which can block silicon sites and thus reduce the etch rate.

*This research was also supported by the Air Force Office of Scientific Research/DARPA under Grant F-49620-82-K-0080.

K. LASER PROCESSING FOR ELECTRO-OPTICAL COMPONENTS

(R. Krchnavek, R. M. Osgood, Jr.)

(JSEP work unit 5, 1982-1985)

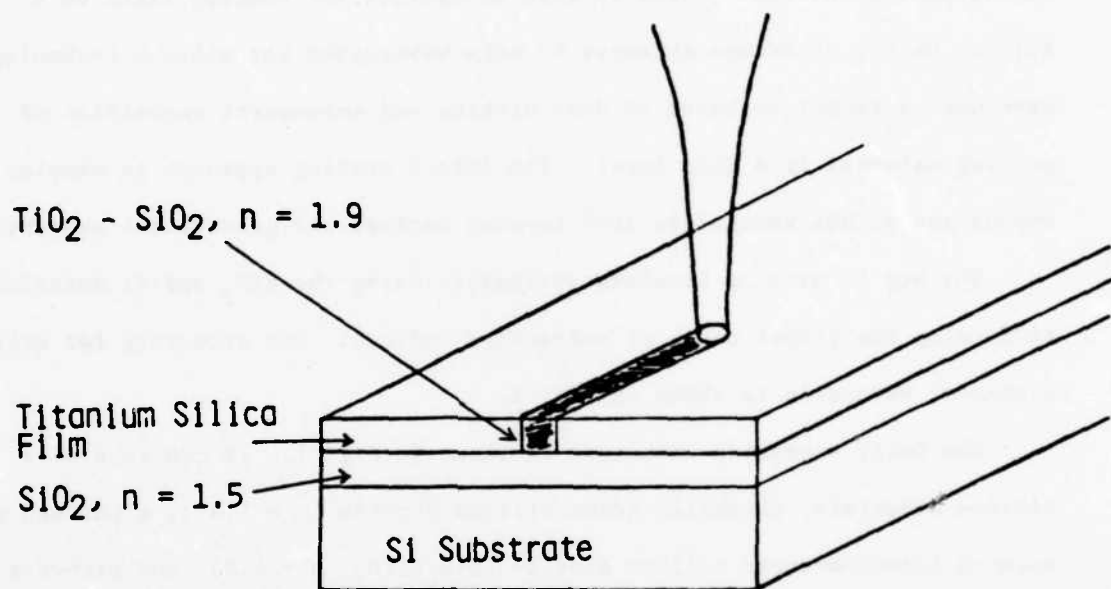
(Principal Investigator: R. M. Osgood, Jr. (212) 280-4462)

The SiO_2 line writing (to be published in the Journal of Vacuum Science and Technology B) can be used to form waveguides for routing light on a silicon wafer. Previous attempts to make waveguides for silicon technology have used a technique based on deep etching and subsequent deposition of guiding material in a SiO_2 layer. The direct writing approach is simpler to employ and allows waveguides with tapered optical and geometrical properties.

The key to writing lossless waveguides using the SiO_2 and Si materials is to develop the proper match of refractive indices. One structure for writing a channel waveguide is shown in Fig. 1.

The basic waveguide structure is shown in Fig. 1. It consists of a silicon substrate, thermally grown silicon dioxide ($n = 1.45$), a pattern of spin-on titanium-doped silicon dioxide ($\text{SiO}_2/\text{TiO}_2$, $n \sim 1.9$), and either a silicon dioxide top layer or atmospheric ambient. This three-layer structure is necessary because a rib waveguide is only stable if the rib consists of a higher index material on top of a lower index material, which in our case is undoped SiO_2 . The SiO_2 layer on the silicon substrate must be at least $1 \mu\text{m}$ thick to prevent coupling of the evanescent wave into the substrate, thereby creating a lossy rib waveguide structure. Because the SiO_2 must be at least $1 \mu\text{m}$ thick, we cannot use spin-on organosilicates to form the SiO_2 layer. Facilities necessary for producing $> 1 \mu\text{m}$ thick thermal oxides on silicon are just being completed.

Although the maximum index of refraction for titanium-doped silicon dioxide is 1.9, this is achieved only after a moderate thermal (400° , 15 min) cure. Tests of the index of refraction for low-temperature, cured samples



Laser direct writing of an optical waveguide on a silicon substrate

Figure 1

show the index to be between 1.45 and 1.9 - generally adequate for waveguiding. These low-temperature cures are more representative of the extent of curing achieved in the laser-writing scheme. If the laser curing were to prove inadequate, thermal (furnace) curing after patterning could easily be achieved.

The biggest problem to date has been detecting the waveguide and coupling the light into it. Early samples were made on glass cover slides to demonstrate the ability to directly write patterns of $\text{TiO}_2/\text{SiO}_2$ on SiO_2 . It was feared that possible strong bonding of the organosilicate to glass might make removal of unexposed sections difficult. This has not been the case, and we have found that we can readily write the guides on cover-glass slides and thin SiO_2 coated Si wafers. However, testing for waveguiding on these samples is extremely difficult because the glass substrate in air is itself a planar waveguide. The optical communications group headed by Prof. P. Prucnal is studying the problem by using a single mode optical fiber and end-coupling into the cleared rib waveguide structure.

L. MICROELECTRONICS FABRICATION INSTRUMENTATION*

(D. Rivera, R. M. Osgood, Jr.)

(JSEP work unit 5, 1982-1985)

(Principal Investigator: R. M. Osgood, Jr. (212) 280-4462)

During the past year the construction of the microelectronics clean room was completed. The clean room is rated as a class 10,000 room but was tested after its completion and could meet the class 1,000 specification.

The clean room contains two dry, laminar-flow class 100 benches and two wet, laminar-flow class 100 benches. Other equipment in the room includes one Kasper mask aligner, which was completely rebuilt, and two photoresist spinners. Inside the clean room, there is also access to a 3 tube Thermco diffusion furnace, supplied as a gift, from Bell Labs. The furnace is physically attached to the outside of the room and researchers can place wafers into the furnace from inside the clean room, with no contact with outside air. A pure water system, donated by IBM, for wafer processing, is being installed; the water will have 18 M Ω resistivity and low particulate levels. This water will be used for the final cleaning of wafers before and during processing.

The processes carried on in the clean room includes photolithographic device production on silicon and GaAs wafers. This is done by spinning a layer of photoresist on the wafers and then exposing a pattern of devices on the wafers using the mask aligner. The process is repeated several times to create devices. A similar process using spun on PMMA (a resist for lapur excimer laser lithography) has been routinely performed in the clean room. Oxide growth, which is an important part of semiconductor processing, is done using the diffusion furnace. A wafer or group of wafers, usually silicon, is placed in a quartz boat and then placed in a tube of the oven where it is baked for a specific amount of time, while a gas is leaked into the tube from

one end. The gas is determined by which kind of layer is desired, i.e. oxide, nitride etc. and the time of baking determines the thickness of the layer. The furnace can also be used to dope wafers by diffusing n or p dopants into the wafers, depending on what gas is being used in the system.

In conjunction with Prof. Prucnal's Optoelectronics Group, one specific type of device has been fabricated in the clean room. The optoelectronics group needs optical waveguides produced in a substrate. In order to create the waveguides, the humidity and temperature controlled atmosphere of the clean room must be used. The procedure entails spinning a layer of titanium-doped glass on a substrate. This procedure is very humidity dependent and, therefore, must be controlled. The thickness of the layer is controlled by the spinning and amount of material used. After depositing the layer of doped glass on the substrate the waveguides are created using a laser direct-writing technique.

*This research was also supported by IBM.

III. GENERATION AND DYNAMIC PROPERTIES OF METASTABLE SPECIES FOR QUANTUM ELECTRONICS

A. TRANSLATIONAL ENERGY CHARACTERISTICS OF RADICALS AND IONS IN A CAPILLARITRON SUPERSONIC NOZZLE DISCHARGE*

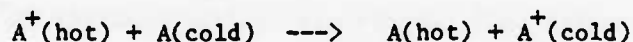
(T. Allik, B. Brady, G. Flynn, and G. Spector)
(JSEP work unit 7, 1982-1985)
(Principal Investigator: G. W. Flynn (212) 280-4162)

The formation and chemistry of ions and radicals are important in varied applications. For example, in the field of microelectronics, ions and radicals of many species play a role in the etching and implantation of semiconductor surfaces. Ions and radicals, which often have poorly characterized spectra are also important in many gas phase reactions. Since both ions and radicals are usually created with large amounts of excess energy, many different quantum states may be populated. This large variety of states gives rise to congested spectra and also allows for a myriad of competing processes in the reactions of these substances. If ions and radicals could be created in just a few of their lowest energy states, it would simplify the spectroscopy significantly, allow for the preparation of specific states and make possible the subsequent study of state-to-state reaction rates.

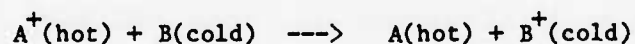
A supersonic beam or jet is one device which can be used to simplify the spectra of complex species such as ions and radicals. As an excitation source, many investigators⁽¹⁾⁻⁽⁴⁾ have used a laser to create radicals in or near the throat of a nozzle allowing them to cool in the expansion; others⁽⁵⁾ have used an electron gun further downstream to create ions from a cold neutral beam. In both cases the internal energies of these species are subsequently studied using laser-induced-fluorescence (LIF).^{(6),(7)} An alternative method of creating cold metastable species is by a discharge. Recently, electronic emission from rotationally cold OH radicals created in a corona discharge has been observed.⁽⁸⁾ Since the rotation-to-translation

energy transfer rates are fast in most species,⁽⁹⁾ hot fragments formed in discharges at the nozzle throat can cool to the temperature of the buffer gas.

One possible means of producing cold ions in a beam is via charge transfer collisions. Since charge transfer cross sections are relatively large ($10 - 100 \text{ \AA}^2$)⁽¹⁰⁾ and the pressure is appreciable along the beam axis (10^{-6} torr), efficient charge transfer reactions can occur. Parent and daughter ions born early in the supersonic expansion have the potential to be vibrationally and rotationally hot. As these ions flow from the nozzle throat, they can suffer charge transfer collisions. Symmetric resonant charge transfer of the type



will cool the ion distribution provided the concentration of $A(\text{cold}) \gg A^+(\text{hot})$. Asymmetric charge transfer of the type:



will produce a nascent distribution of B^+ . In the present work we have used a capillaritron-discharge-source⁽¹¹⁾⁻⁽¹⁴⁾ supersonic nozzle molecular beam apparatus to characterize the energy distributions of the ion and radical species in a beam. Radicals have been conveniently produced with this device and their velocity distribution is characterized by a very low temperature. We also find evidence for charge transfer processes which produce relatively low energy ion distributions.

Translational energy distributions of the neutral components of the beam were measured by a time of flight technique. Ion energies were measured electrostatically. For both ions and neutrals a quadrupole mass spectrometer was used to identify the species being studied.

Initial results showed that the major neutral portion of the beam is only slightly affected by the discharge. In beams of Ar and CF_4 the translational

temperature was found only to increase by 3K (from 2K to 5K for Ar) with a current of 3 milliamperes in the discharge.⁽¹⁵⁾ Further experiments on OH radicals generated in the discharge from CH₄ and CO₂ showed that even neutral fragments may be created "cold" in the capillaritron discharge. For OH the translational temperature is approximately 7K and the stream velocity is 1100 m/s. See Fig. 1.

Ions created in the capillaritron beam showed both a higher average value of the translational energy and a large velocity spread. Ar⁺ created under various conditions (.2 - .5 mA, 3 - 6 kV) exhibits a translational energy distribution centered at 10 eV and with a full-width at half maximum of 2 eV. This corresponds to a translational temperature of approximately 10⁴ K. Both the low energy (with respect to the field used to create the ions) and the extreme width of the distribution can be explained through charge transfer collisions of the ions with the slower neutrals. These collisions lower the energy because the charge transfer ion is created in a region of lower field strength than the original ion; the broadness of the distribution arises because not all the charge transfer collisions occur in regions of the same field strength.

This work is described in detail in a paper to be published in the Journal of Physical Chemistry.⁽¹⁶⁾

*This research was also supported by the National Science Foundation under Grant CHE-80-23747 and the Department of Energy under contract DE-AC-02-78ER04940.

- (1) T. A. Miller, B. R. Zegarski, T. J. Sears, and V. E. Bondybey, J. Phys. Chem. 84, 3154 (1980).
- (2) A. Carrington and R. Tuckett, Chem. Phys. Letts. 74, 19 (1980).
- (3) B. M. de Koven, D. H. Levy, H. H. Harris, B. R. Zegarski, and T. A. Miller, J. Chem. Phys. 74, 5659 (1981).

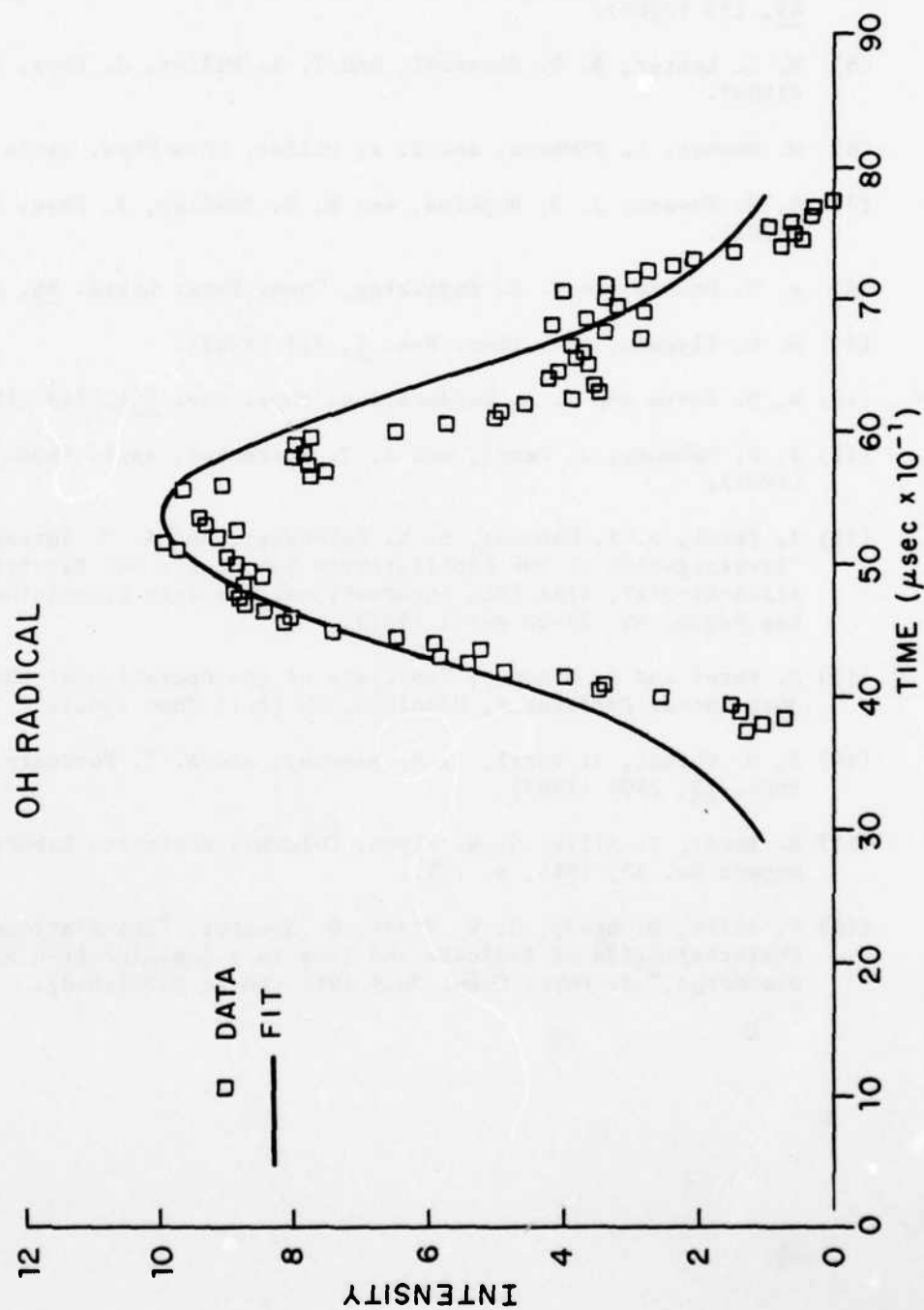


Figure 1

- (4) D. L. Monts, T. G. Dietz, M. A. Duncan, and R. E. Smalley, Chem. Phys. 45, 133 (1980).
- (5) M. I. Lester, B. R. Zegarski, and T. A. Miller, J. Phys. Chem. 87, 5228 (1983).
- (6) M. Heaven, L. DiMauro, and T. A. Miller, Chem Phys. Letts. 95, 347 (1983).
- (7) D. E. Powers, J. B. Hopkins, and R. E. Smalley, J. Phys. Chem. 85, 2711 (1981).
- (8) A. T. Droege and P. C. Engelking, Chem. Phys. Letts. 96, 316 (1983).
- (9) W. H. Flygare, Acc. Chem. Res. 1, 121 (1968).
- (10) W. D. Davis and T. A. Vanderslice, Phys. Rev. 131, 219 (1963)
- (11) J. F. Mahoney, J. Perel, and A. T. Forrester, Appl. Phys. Letts. 38, 320 (1981).
- (12) J. Perel, J. F. Mahoney, B. E. Kalensher, and A. T. Forrester, "Investigation of the Capillaritron Ion Source For Electric Propulsion," AIAA-81-0747, AIAA 15th International Electric Propulsion Conference, Las Vegas, NV (21-23 April 1981).
- (13) J. Perel and F. Mahoney, "Analysis of the Operation of the FACS," ASMS, 30th Annual Conference, Honolulu, HI (6-11 June 1982).
- (14) D. M. Goebel, J. Perel, J. F. Mahoney, and A. T. Forrester, J. Appl. Phys. 53, 2904 (1982).
- (15) B. Brady, T. Allik, G. W. Flynn, Columbia Radiation Laboratory Progress Report No. 33, 1983, p. 109.
- (16) T. Allik, B. Brady, G. W. Flynn, G. Spector, "Translational Energy Characteristics of Radicals and Ions in a Capillaritron Supersonic Nozzle Discharge," J. Phys. Chem. July 1984 (to be published).

B. INFRARED EMISSION STUDIES OF VIBRATIONAL EXCITATION IN CH_3 FRAGMENTS PRODUCED FROM ArF AND KrF LASER PHOTOLYSIS OF $\text{Cd}(\text{CH}_3)_2$ AND $\text{Zn}(\text{CH}_3)_2^*$

(J. O. Chu, G. W. Flynn, R. M. Osgood, Jr.)

(JESP work units 5 and 7, 1982-1985)

(Principal Investigators: G. W. Flynn (212) 280-4162

R. M. Osgood, Jr. (212) 280-4462)

Introduction

A study of the product energy distribution among the various degrees of freedom of molecular photo-fragments can reveal much information about the nature and dynamics of the dissociative states.⁽¹⁾ Furthermore, a knowledge of the detailed distribution of the excess energy can provide insights regarding the geometry of the dissociating species, and hence the symmetry and nature of the dissociative potential energy surfaces involved.⁽²⁾⁻⁽⁴⁾ From an applied point of view, laser photodissociation of organometallic (metal alkyls) has been employed for microdeposition of metal films.⁽⁵⁾ In particular, the demonstration of the laser "direct write technique" in microelectronics is based on the photodissociation of dimethylcadmium (or dimethylzinc) by a UV excimer laser beam focused on the surface of the semiconductor substrate.^{(6),(7)} However, there is still little understanding of the dissociation dynamics for these metal alkyls and only a limited knowledge of the nature of the excited electronic states due to a few experimental studies.⁽⁸⁾⁻⁽¹¹⁾ Recently, Chen and Osgood have made a spectroscopic study of measurements of the UV absorption spectra of these metal alkyls.⁽¹²⁾ Analysis of their spectroscopic data indicated that the first and second excited states are bent and linear, respectively, which would lead to excitation in three vibrational modes: the metal-carbon stretching mode, the methyl ν_2 "umbrella" mode, and the C-H asymmetric stretching mode. To further study these dissociation processes, the photo-decomposition of dimethylcadmium and dimethylzinc has been investigated here via infrared

fluorescence techniques to probe and examine the vibrational energy disposal in the CH_3 fragments. In this study, we present observations of time-resolved infrared fluorescence following 248 and 193 nm dissociation of $\text{Cd}(\text{CH}_3)_2$ and $\text{Zn}(\text{CH}_3)_2$, as well as evidence for high vibrational excitation in the CH_3 photofragments at both wavelengths. Moreover, the study focusses on a determination of the number of vibrational quanta of excitation in the "umbrella" or ν_2 out-of-plane bend relative to the number of ν_3 quanta in the anti-symmetric C-H stretch of the CH_3 fragments.

Experimental

The pulse ArF/KrF output of a Lambda Physik excimer laser was used to irradiate flowing sample of $\text{Cd}(\text{CH}_3)_2$ or $\text{Zn}(\text{CH}_3)_2$ in a cylindrical pyrex sample cell, which was fitted with quartz windows. Typically all experiments were performed at low or moderate laser fluences under unfocussed conditions in order to avoid multiphoton processes, which has been reported for the $\text{Zn}(\text{CH}_3)_2$ system.⁽¹³⁾ Infrared spontaneous fluorescence was observed at right angles to the laser beam through a KBr window. Broadband interference filters were employed to selectively view fluorescence at the desired wavelengths. Emission at wavelengths longer than 6 μm was monitored with a type "C" material HgCdTe detector (77K, <1 μs), while fluorescence in the 1-5 μm region was observed with an InSb detector (77K, < 1 μs). The output from the detector/preamplifier combination was further amplified using a Tektronix AM502 amplifier and then digitized with a Biomation 8100 transient recorder. Digitized signals were summed in a Nicolet 1170 signal averager, and then sent to a PDP 11-34 computer for storage and analysis by a nonlinear least squares fitting program. A conventional stainless steel vacuum system was used to flow gas samples through the fluorescence cell to prevent gas depletion and

build-up of reaction products. Sample flow rates were set to exchange gas in the cell every 0.5 seconds, and the laser repetition was kept less than 1 Hz. Pressures in the cell were monitored with an MKS Baratron capacitance manometer and typical pressures were about 50 mtorr. Dimethylcadmium and dimethylzinc, with a stated purity of 99% were obtained from Alfa Products, and further purified by repeated degassing at -78 C.

In order to determine the relative emission intensity of infrared fluorescence at different wavelengths, the sensitivity of each detector was determined as a function of wavelength using a blackbody source, an Eppley thermopile and a Bausch and Lomb monochromator with appropriate interference filters. The measured variation of sensitivity with wavelength agreed well with the manufacturer's published curves for each detector.

Results and Analysis

A typical strong IR emission (3.1 - 3.9 μm) signal observed in the ArF laser photolysis of $\text{Cd}(\text{CH}_3)_2$ at a low pressure of 60 mtorr is shown in Fig. 1a, for only a single excimer shot (with a pulse energy of ~ 15 mJ). The detected (wideband) emission corresponds to the total fluorescence from the vibrational transitions of the antisymmetric stretch (ν_3) of CH_3 centered at 3.16 μm . No prompt visible emission (from electronically excited Cd atoms) was observed by eye in either 193 or 248 nm dissociation under the present experimental conditions, which suggests a single photon dissociation process. The signal intensity was found to depend linearly on the laser power. Even at the low pressure indicated, the prompt initial rise of the fluorescence signal in the C-H stretch region is detector limited (~ 1 μsec) indicating the CH_3 fragments are directly produced with substantial excitation in the C-H antisymmetric stretch mode. Likewise, the emission observed through the

Photolysis of $\text{Cd}(\text{CH}_3)_2$ at 193nm

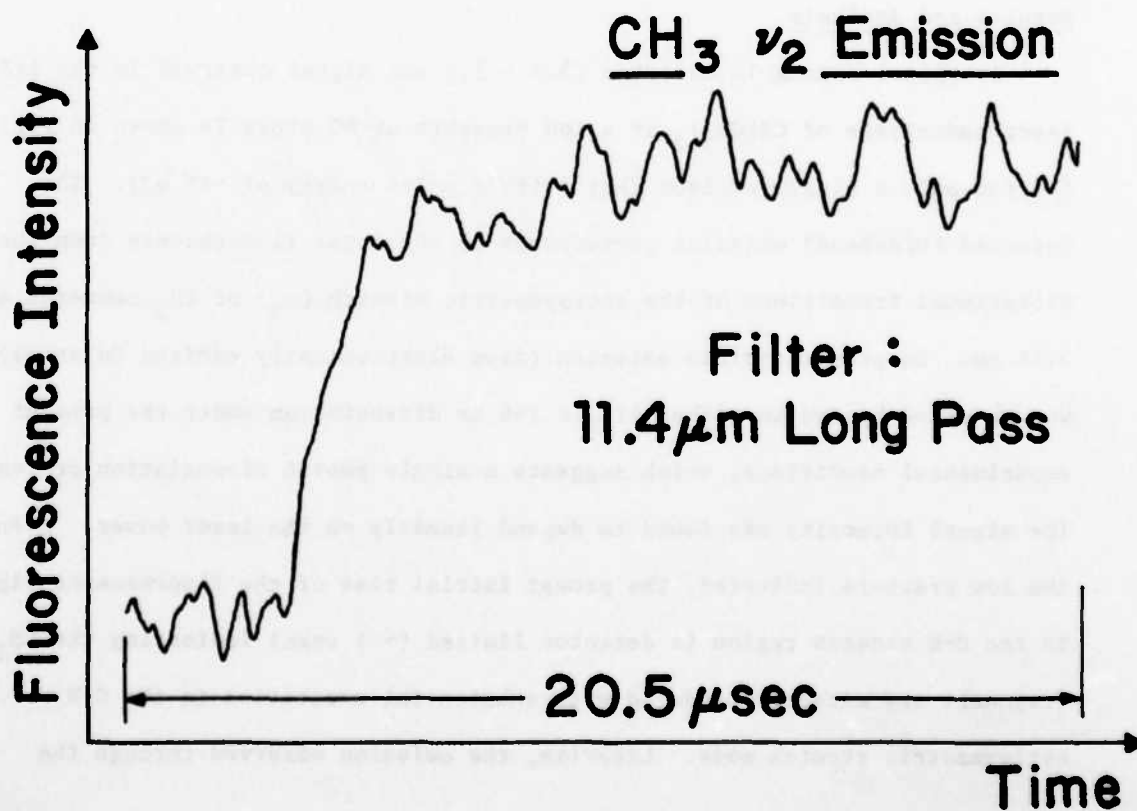
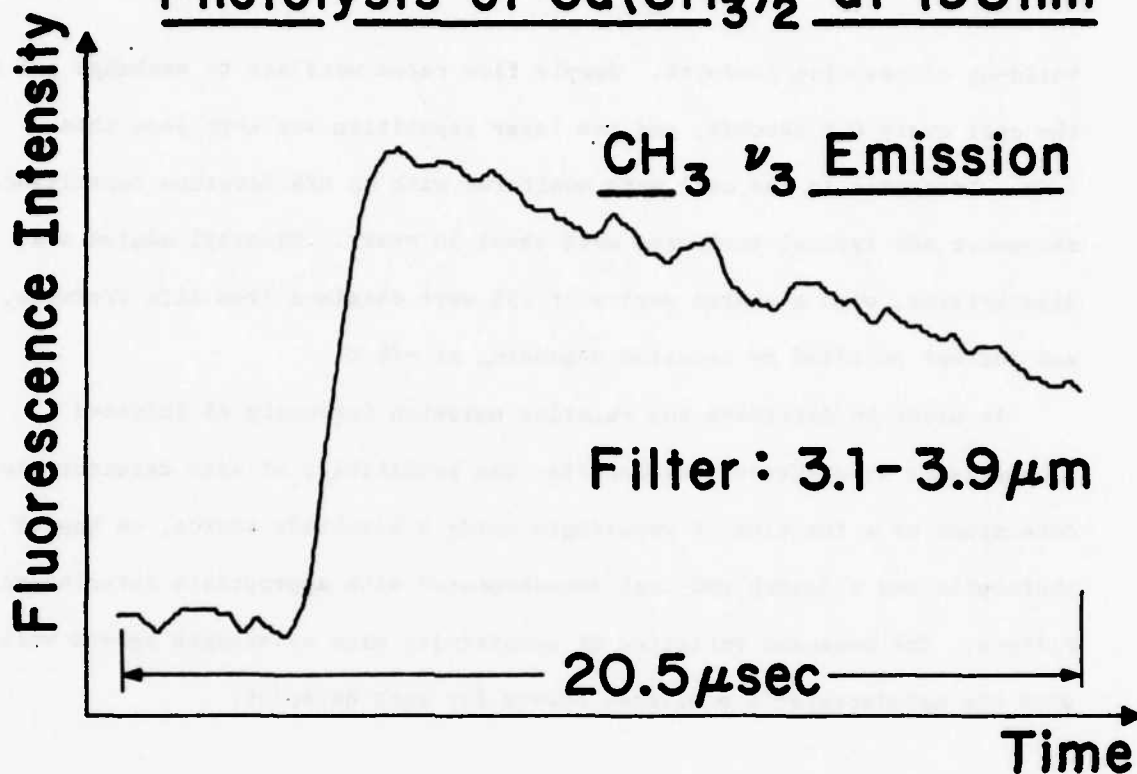


Figure 1

11.4 μm longpass filter (for 250 excimer laser shots, see Fig. 1b), which detects total ν_2 fluorescence, shows that the CH_3 ν_2 out-of-plane bend is also directly produced with much excitation from the dissociation process.

In the present experiment, the observed IR emission from the methyl fragments is sufficiently intense that it cannot be assumed to emanate only from the lowest ($v=1$) level of a particular mode. Thus emission from $v=2$ etc. or from combination bands must make a significant contribution to the fluorescence. Under these conditions the emission at each wavelength corresponding to a vibrational frequency (eg. 16.49 μm for ν_2 of CH_3 , 3.16 μm for ν_3 of CH_3) can be related to the number of quanta of a given kind produced in the photodissociation process. This will be true provided the molecule obeys the harmonic oscillator transition strength rule $|\mu_{\nu_1}(n \rightarrow n-1)|^2 = n|\mu_{\nu_1}(1 \rightarrow 0)|^2$ where μ_{ν_1} is the transition dipole moment for the transition at frequency ν_1 and n is the number of quanta of mode ν_1 in a given level. While CH_3 radicals in the present experiments do not behave like perfect harmonic oscillators, this approximation should be sufficiently accurate to determine at least roughly from the fluorescence data the relative number of CH_3 ν_2 and ν_3 quanta produced from the photodissociation process. Since the ν_2 and ν_3 emission signals were measured with different detectors and filters, the fluorescence intensity must be corrected for detector sensitivity and filter transmission (as well as for amplifier gain, laser energy, and number of laser shots) before it can be used to determine the relative number of ν_2 and ν_3 quanta. Furthermore, the experimentally corrected fluorescence data must also be adjusted for the difference in the CH_3 ν_2 (16 μm) and ν_3 (3 μm) emission strengths by reference to the band strengths S_1 , and degeneracies g_1 for these transitions. A detailed description of the fluorescence intensity normalization procedure is given elsewhere.⁽¹⁴⁾ The normalized intensity

ratio $I(\nu_3)/I(\nu_2)$ for $\text{Cd}(\text{CH}_3)_2$ at 193 nm is found to be 6.2 ± 0.9 , which is related to the ratio N_2/N_3 where N_1 is the number of ν_1 quanta, via the relationship

$$(N_2/N_3) = (I_2/I_3)(S_3/S_2)(g_2/g_3)(\nu_3/\nu_2)^3$$

Since, $|\mu_2/\mu_3|$ is estimated to be 2.8 by Amano et. al.⁽¹⁵⁾

$$S_3/S_2 = (\nu_3/\nu_2)|\mu_3/\mu_2|^2 = 0.665$$

and using $g_3 = 2$, $g_2 = 1$, $\nu_3 = 3160.8 \text{ cm}^{-1}$, $\nu_2 = 606.4 \text{ cm}^{-1}$ gives $N_2 = (8 \pm 1)N_3$. Thus there is a much larger number of ν_2 quanta produced relative to ν_3 quanta in the CH_3 fragments from photodissociation of $\text{Cd}(\text{CH}_3)_2$ at 193 nm.

At 248 nm, moderate laser fluences of about 20 mJ/cm^2 were employed in the experiment due to weaker absorption and again intense IR emission is observed in both the ν_3 C-H stretch region (for a single excimer shot), and in the ν_2 out-of-plane region (for 100 excimer shots) as shown in Figs. 2a and 2b respectively. The normalized emission intensity ratio $I(\nu_3)/I(\nu_2)$ is determined to be (23.0 ± 4.60) which then gives $N_2 = (2 \pm .4)N_3$. This result indicates only twice as many ν_2 quanta are produced as ν_3 quanta which suggests there is comparable excitation in the C-H stretch relative to the "umbrella" bend in the CH_3 fragments due to dissociation at 248 nm. Indeed, evidence of this relatively high excitation in the C-H stretch is demonstrated by the large amplitude rapid decay process out of the ν_3 vibrational manifold following the initial prompt rise in the ν_3 emission signal (see Fig. 2a). This rapid relaxation process is nearly detector limited, and is attributed to the fast equilibration of the ν_3 vibrational states of CH_3 with lower vibrational levels. Qualitatively, since the number of ν_2 quanta produced relative to ν_3 is much greater at 193 nm

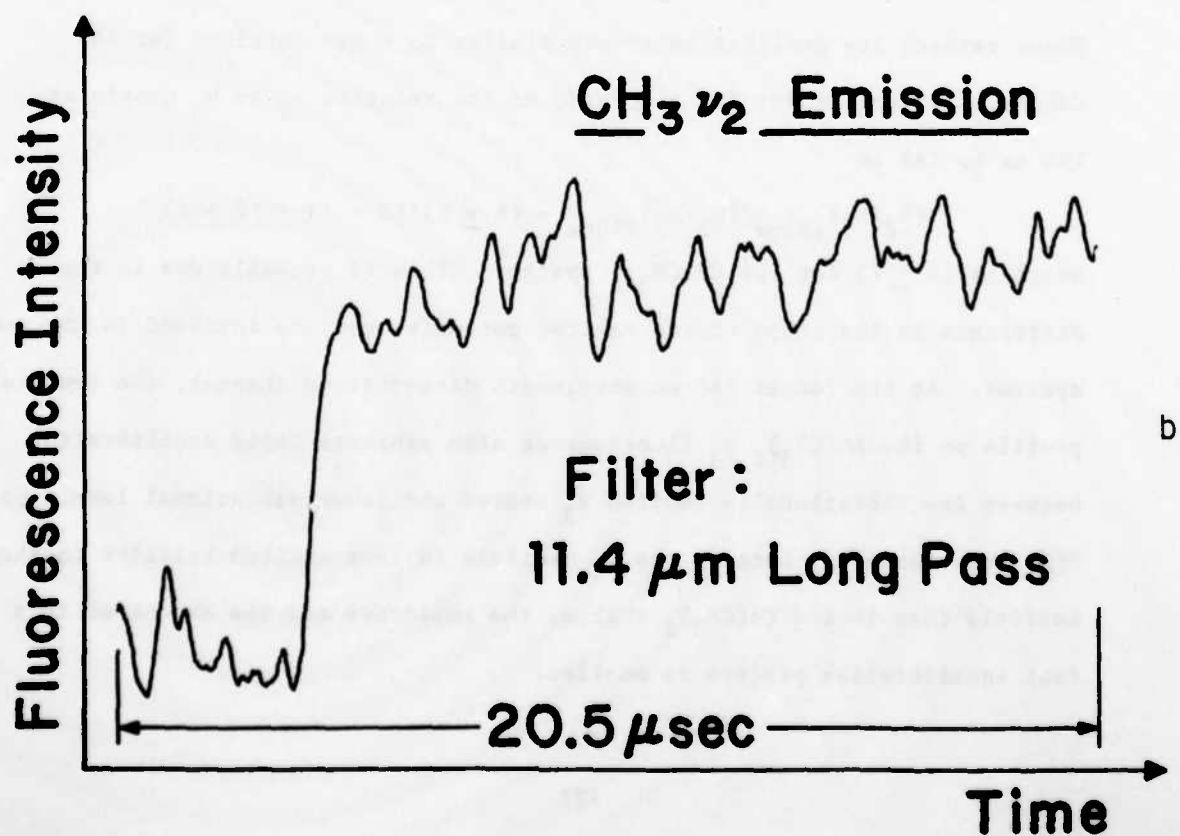
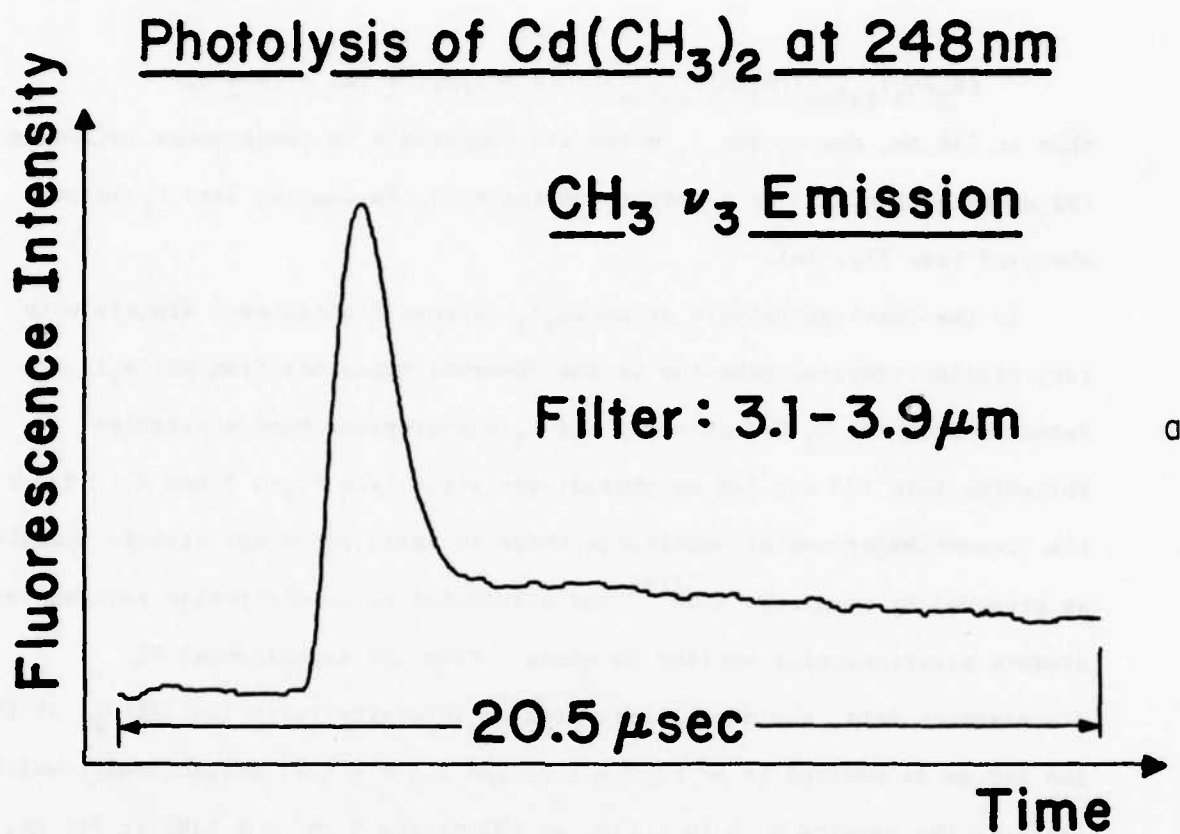


Figure 2

$$(N_2/N_3)_{193\text{nm}}/(N_2/N_3)_{248\text{nm}} = (8 \pm 1)/(2 \pm .4) = (4 \pm 1)$$

than at 248 nm, the ν_2 and ν_3 modes are comparable in temperature following 193 nm dissociation. As a result cooling of ν_3 by dumping into ν_2 is not observed (see Fig. 1a).

In the laser photolysis of $\text{Zn}(\text{CH}_3)_2$, strong fluorescence signals with very similar temporal behavior to the observed emissions from $\text{Cd}(\text{CH}_3)_2$ are detected from the ν_3 C-H stretch, and ν_2 out-of-plane bend excitation following both 193 and 248 nm photodissociation (see Figs. 3 and 4). Under the present experimental conditions there is again no prompt visible emission as observed by Karny et. al.⁽¹³⁾ and attributed to a multiphoton process to produce electronically excited Zn atoms. From the experimental IR fluorescence data, the normalized emission intensity ratio $I(\nu_3)/I(\nu_2)$ at 193 and 248 nm is derived to be (7.5 ± 1.2) and (13.6 ± 4.6) respectively, which leads to the results $N_2 = (6 \pm 1)N_3$ at 193 nm and $N_2 = (3 \pm 1)N_3$ at 248 nm. These results are qualitatively very similar to those obtained for the $\text{Cd}(\text{CH}_3)_2$ system, except for the ratio of the relative ν_2 to ν_3 quanta at 193 nm to 248 nm

$$(N_2/N_3)_{193\text{nm}}/(N_2/N_3)_{248\text{nm}} = (6 \pm 1)/(3 \pm 1) = (2 \pm 1)$$

which is (4 ± 1) for the $\text{Cd}(\text{CH}_3)_2$ system. This is probably due to the difference in the shape of the excited potential surface involved in the two systems. At the longer 248 nm wavelength dissociation channel, the temporal profile of the $\text{Zn}(\text{CH}_3)_2$ ν_3 fluorescence also exhibits rapid equilibration between the vibrationally excited ν_3 states and lower vibrational levels (see Fig. 3a). However, because the ν_3 manifold is less excited relative to the ν_2 manifold than in the $\text{Cd}(\text{CH}_3)_2$ system, the amplitude and the extent of this fast equilibration process is smaller.

Photolysis of $\text{Zn}(\text{CH}_3)_2$ at 193nm

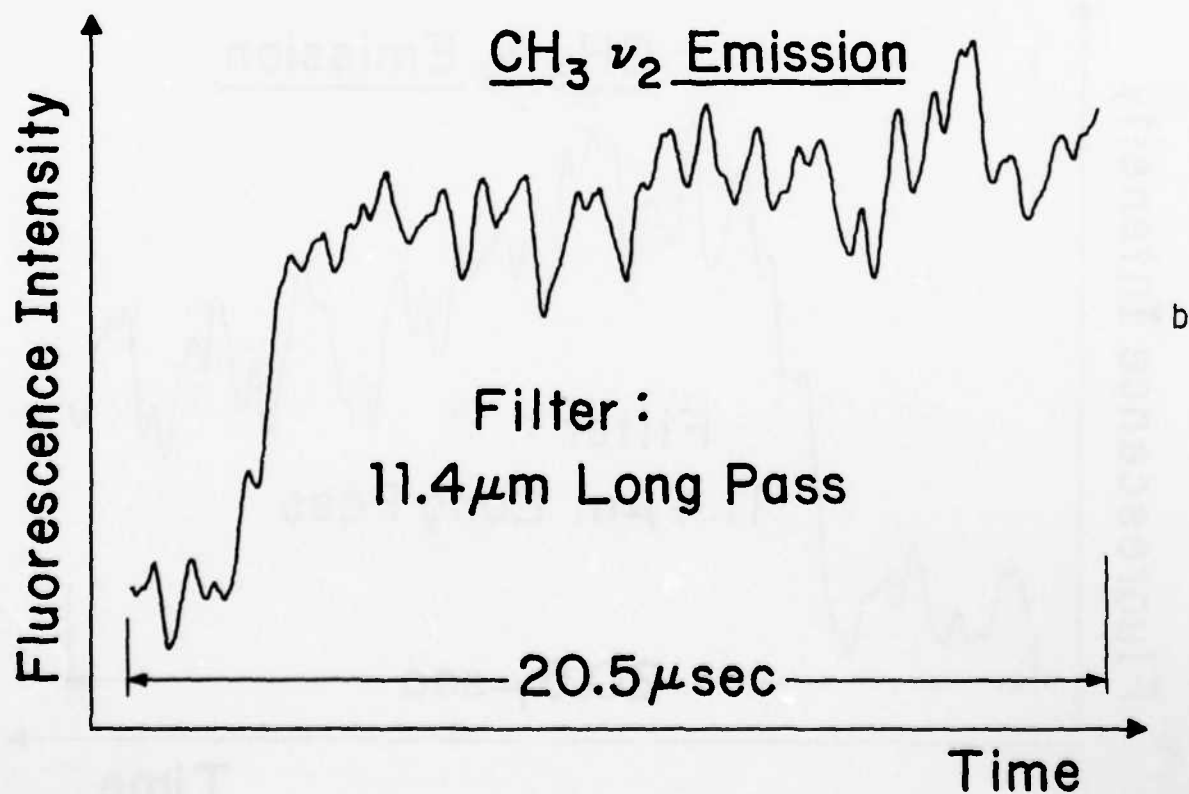
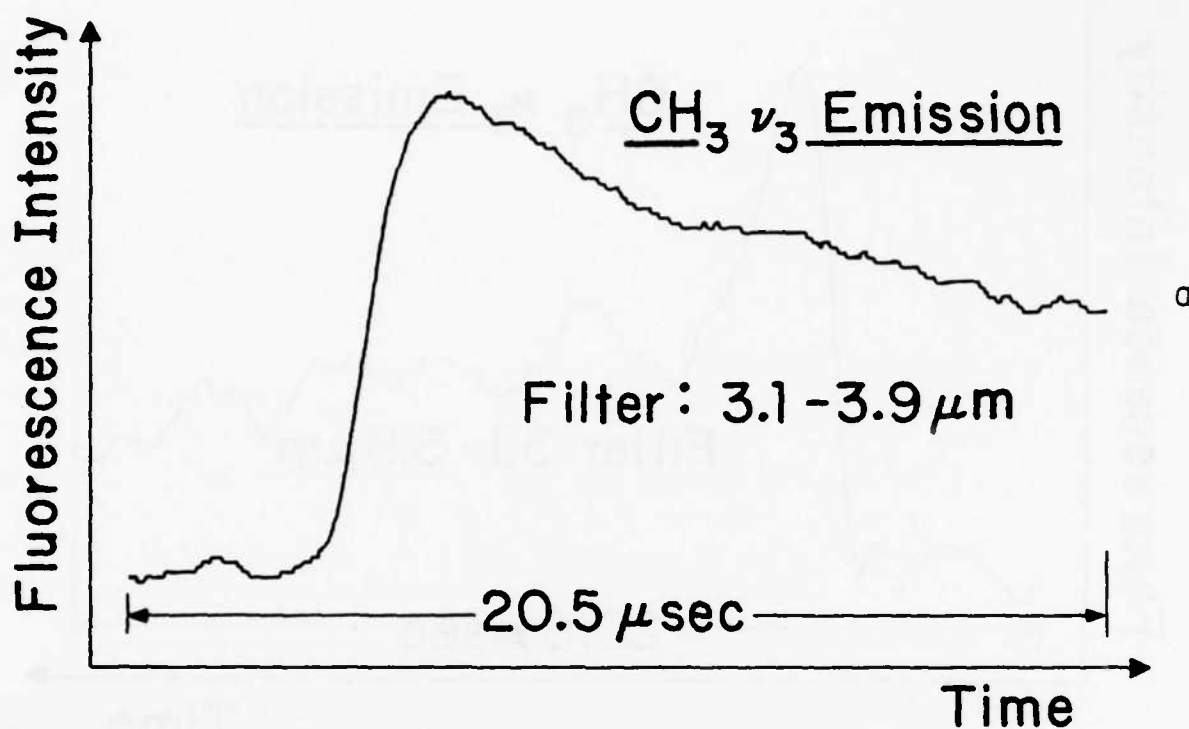


Figure 3

Photolysis of $\text{Zn}(\text{CH}_3)_2$ at 248 nm

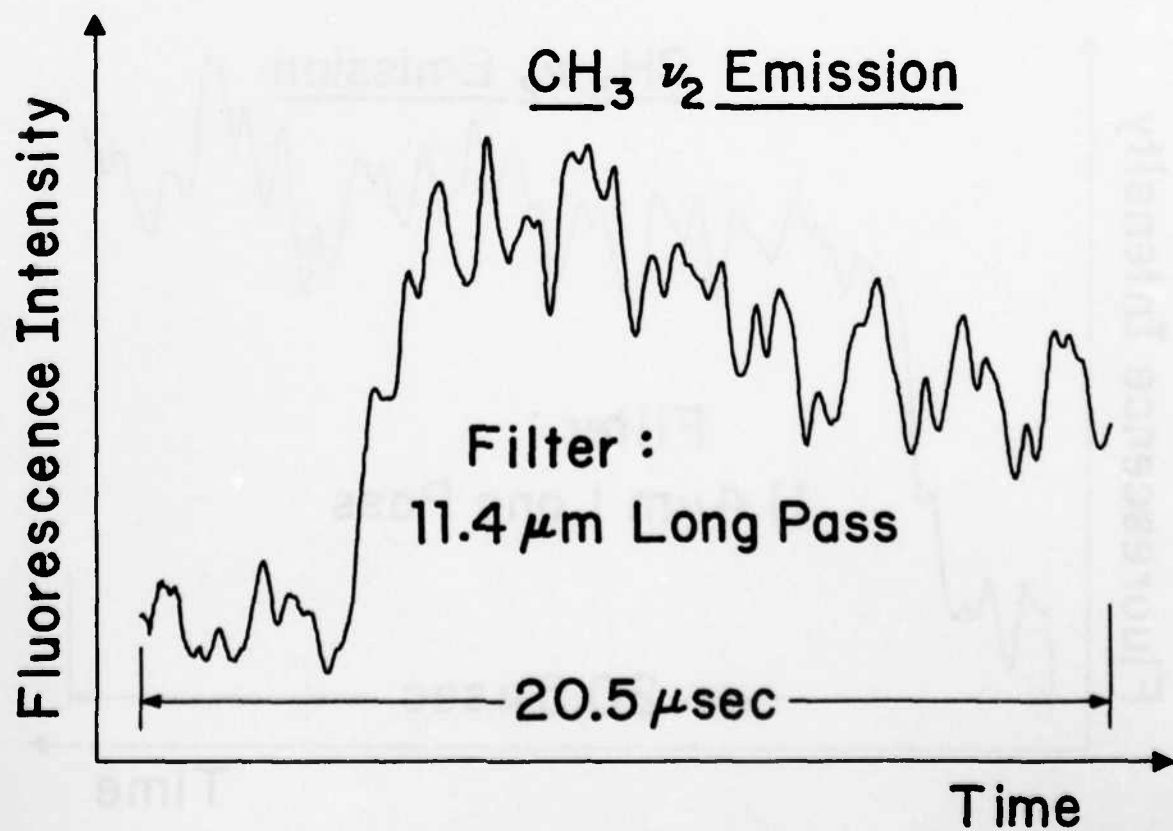
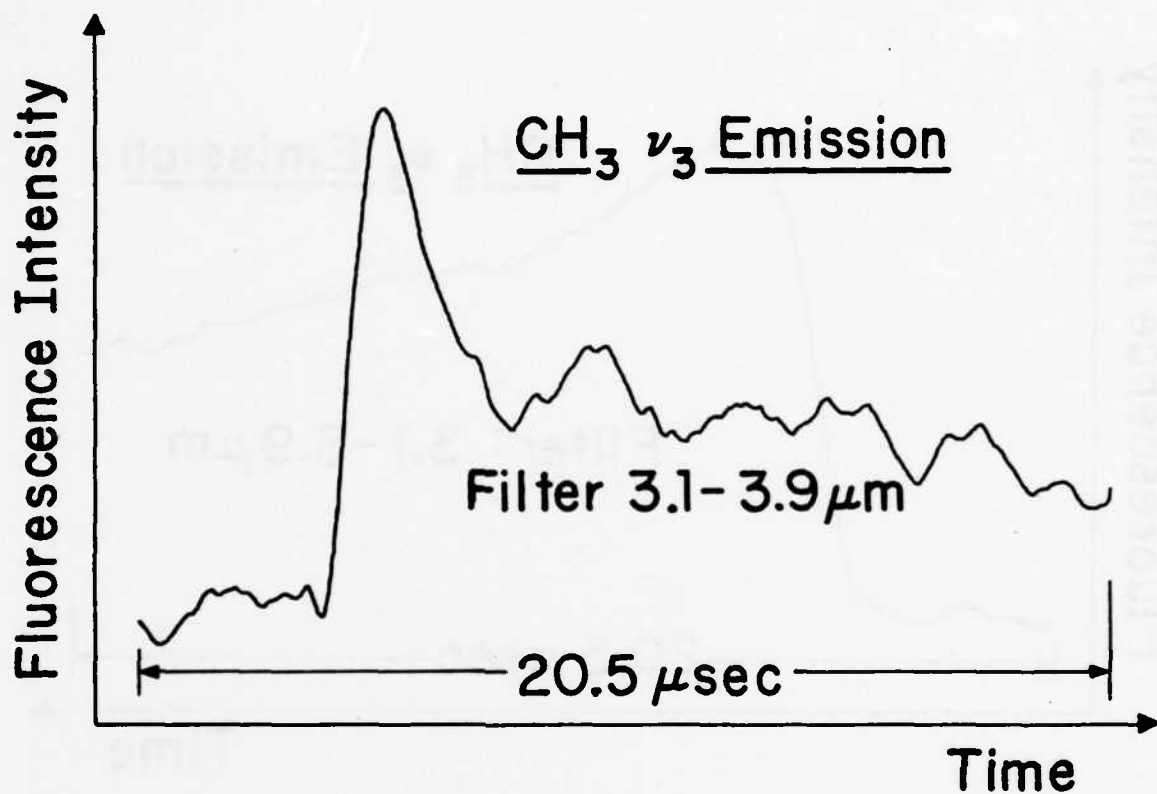


Figure 4

Discussion

It is most probable that single photon dissociation of $\text{Cd}(\text{CH}_3)_2$ and $\text{Zn}(\text{CH}_3)_2$ at 193 and 248 nm will result in complete decomposition into three fragments, two CH_3 radicals and a metal atom, perhaps in a stepwise manner as suggested for $\text{Cd}(\text{CH}_3)_2$ dissociation with a short-lived CdCH_3 intermediate.⁽¹⁰⁾ In the study of the CH_3 fragments, the present experimental results show that a substantial amount of the CH_3 radicals are directly produced with high vibrational excitation from both 193 and 248 nm photodissociation processes. At the shorter wavelength 193nm dissociative channel, most of the CH_3 radicals are produced with much more vibrational excitation in the ν_2 out-of-plane bend (relative to C-H stretch), whereas at the longer wavelength 248 nm dissociation channel there is comparable excitation in both the ν_2 bend and the ν_3 C-H stretch. This wavelength dependence does provide direct evidence that the dissociation dynamics are strongly governed by the excited state geometry and the shape of the excited potential surface, which is in agreement with the recent study by Chen and Osgood. However, because of the low resolution of infrared fluorescence technique, and the present slow detection system, bimodal distributions arising from radical production via different mechanisms, as in a sequential decomposition, cannot be detected or eliminated.

The photolysis of $\text{Cd}(\text{CH}_3)_2$ has been investigated by Kanfer and Bersohn⁽¹⁶⁾ via molecular beam techniques which revealed that only a small fraction of the excess energy from the 193 nm photolysis is deposited in the translational degrees of freedom, suggesting the possibility of high vibrational or rotational excitation in the CH_3 products. This is substantiated with the present observation of intense infrared emission in the photodissociation studies. Since the enthalpy for dissociation of $\text{Cd}(\text{CH}_3)_2$ into two CH_3 radicals and (ground state) $\text{Cd}(^1\text{S}_0)$ atoms is 65.6 Kcal/mole,⁽¹⁰⁾

the excess energy per mole of CH_3 produced from 193 nm is 41.3 Kcal/mole. In the beam experiment, Kanfer and Bersohn have determined that only about 13 Kcal/mole appear as translational energy for the methyl fragments. Equipartition of the remaining energy among the rotational and vibrational degrees of freedom would yield a vibrational/rotational temperature of ~2900 K. If the rotational energy content mimics the translational energy, the vibrational temperature would be ~2500 K. Qualitatively the present observation of relatively intense out-of-plane bending emission and high-frequency C-H stretch emission are in agreement with the prediction of a hot vibrational population.

*This research was also supported by the National Science Foundation under Grant CHE-80-23747 and the Department of Energy under contract DE-AC-02-78ER04940.

- (1) Stephen R. Leone, Adv. in Chem. Phys., Ed. by K. P. Lawley, vol. L. John Wiley and Sons, N.Y. (1982).
- (2) William M. Gelbart, Ann. Rev. Phys. Chem. 28, 323 (1982).
- (3) K. F. Freed and Y. B. Band, in "Excited States," Ed. by E. L. Lim, vol. 3, p. 110, Academic Press, N.Y. (1977).
- (4) M. Shapiro and R. Bersohn, Ann. Rev. Phys. Chem. 33, 409 (1982).
- (5) D. J. Ehrlich, R. M. Osgood, Jr., and T. F. Deutsch, IEEE J. Quan. E., QE-16, 1233 (1980).
- (6) D. J. Ehrlich, and R. M. Osgood, Jr., Chem. Phys. Lett. 79, 381 (1981).
- (7) Y. Rytz-Froidevaux, R. P. Salath, H. H. Gilgen, and H. P. Weber, Appl. Phys. A 27, 133 (1982).
- (8) H. W. Thompson, and J. W. Linnett, Proc. Roy. Soc. 156A, 108 (1936).
- (9) A. Terenin and N. Prileshajewa, Acta Physicochim. 1, 759 (1935).
- (10) C. John, P. Chandra, and R. Bersohn, J. Chem. Phys. 55, 1903 (1971).
- (11) S. L. Baughcum and S. R. Leone, Chem. Phys. Lett. 89, 183 (1982).
- (12) "A Spectroscopic Study of the Excited States of Dimethylzinc, Dimethylcadmium and Dimethylmercury," C. J. Chen and R. M. Osgood, Jr., accepted to J. Chem. Phys.

- (13) Z. Karney, R. Naaman, and R. N. Zare, Chem. Phys. Lett. 59, 33 (1978).
- (14) S. Datta, R. E. Weston, Jr., and G. W. Flynn, "Vibrational Excitation of CH_3F Excited by Collisions with Hot Hydrogen Atoms," J. Chem. Phys. 80, 0000 (1984).
- (15) T. Amano, P. F. Bernath, C. Yamada, Y. Endo, and E. Hirota, J. Chem. Phys. 77, 5284 (1982).
- (16) S. Kanfer, Ph.D. thesis, Columbia University 1981.

C. DIODE LASER PROBES OF BENDING AND STRETCHING EXCITATION IN CO₂ CAUSED BY COLLISIONS WITH HOT ATOMS FROM EXCIMER LASER PHOTOLYSIS*

(J. O. Chu, C. F. Wood, G. W. Flynn)

(JSEP work unit 7, 1982-1985)

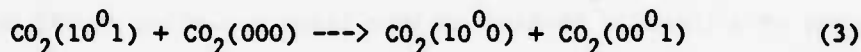
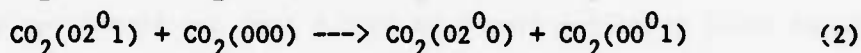
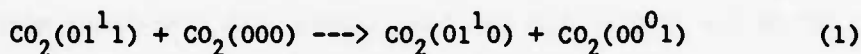
(Principal Investigator: G. W. Flynn (212) 280-4162)

Introduction

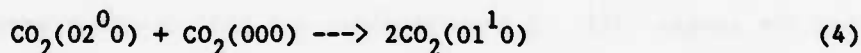
Vibrational and rotational excitation of small molecules caused by collisions with hot hydrogen atoms produced via laser photolysis has recently been studied using infrared fluorescence techniques.⁽¹⁾⁻⁽⁶⁾ This work provides considerable information about collisional (T-V/R) excitation processes in the energy range 1-3 eV. While infrared fluorescence detection is an extremely simple, useful probe method, it suffers from limited resolution ($\sim 30 \text{ cm}^{-1}$), and becomes difficult to apply to the study of vibrational states which have small or zero spontaneous emission coefficients. We describe here a technique for studying molecular dynamics and collisional excitation processes using a diode laser absorption probe which provides approximately 10000-fold improvement in spectral resolution over fluorescence methods. A high resolution (10^{-3} cm^{-1}) cw diode laser probe technique has been developed and used to determine the number of CO₂ vibrational quanta of each kind (ν_3 antisymmetric stretch, ν_2 bend, and ν_1 symmetric stretch) produced as a result of collisions between translationally hot hydrogen atoms and CO₂ molecules.⁽⁷⁾ The study focusses on the measurement of the number of vibrational quanta of CO₂ antisymmetric stretch and bend produced during collision with hot hydrogen atoms. The experimental method relies on probes of the CO₂ vibrational transition $mn^l_p \rightarrow mn^l_{(p+1)}$ all of which "ride" the large oscillator strength of the fundamental $00^0_0 \rightarrow 00^0_1$ antisymmetric stretching transition. Transitions with different values of m,n,l, and p are easily separated due to the narrow spectral characteristics of the diode laser, and signal intensities are

readily controllable through the absorption pathlength. The high resolution and sensitivity of the diode laser can provide state-to-state transition probabilities for T-V/R collision events or a variety of other dynamical processes.

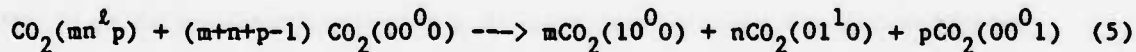
Fundamentally, this vibrational quantum counting technique utilizes rapid, ubiquitous (V-V) process of the type^{(8),(9)}



in addition to fast "ladder-climbing" processes such as



to couple any highly vibrationally excited state into "quasi-equilibrium" with the low-lying vibrational levels of CO_2 . The general state (mn^lp) will decompose to the fundamental vibrational levels by a succession of $m+n+p-1$ such rapid processes,



which produce a steady state vibrational energy distribution having m quanta of (10^00) , n quanta of (01^10) , and p quanta of (00^01) . The populations of these levels can be directly counted and measured by probing with the diode laser the transitions $01^10 \longrightarrow 01^11$, $10^00 \longrightarrow 10^01$, and $00^01 \longrightarrow 00^02$. In CO_2 , the intermode equilibration rate for coupling 00^01 to 10^00 and 01^10 is

very slow while coupling of $10^0 0$ and $01^1 0$ has recently been determined^{(10),(11)} and can be corrected for. The only criterion for the applicability of the method is that the concentration of $\text{CO}_2(000)$ be large compared to $\text{CO}_2(\text{mn}^2 \text{p})$, a condition which is easily achieved experimentally.

Experimental

A schematic diagram of the UV-IR double resonance apparatus is shown in Fig. 1. A 43 cm (or 18.5 or 6.0 cm) long sample cell containing mixtures of H_2S and CO_2 at total pressures from 0.02 to 0.6 torr was irradiated with the pulsed output of a Lumonics TE-860S excimer laser operating at 193 nm to produce hot H atoms (18600 cm^{-1} of translational energy) and HS. The cw probe beam from a standard Laser Analytics diode laser operating near $4.3 \text{ }\mu\text{m}$ was made collinear with the excimer beam and separated from it with a dichroic mirror after the sample cell. A monochromator and InSb detector/preamplifier (1 μs response time) were used to detect the diode laser radiation. Time-resolved absorption changes in the transmitted intensity of the $4.3 \text{ }\mu\text{m}$ probe beam were recorded and analyzed with a transient recorder/signal averager/computer combination which followed the detector and was triggered by a pulse from the excimer laser.

The CO_2 absorption lines were recorded and analyzed by phase-sensitive detection using a lock-in amplifier at a chopping frequency of about 400 Hz. The wavelengths of the absorption lines were determined in reference to either $^{13}\text{CO}_2$ lines (see Fig. 2) or to the excited-state absorption of $\text{CO}_2(001)$ (see Fig. 3) caused by direct CO_2 laser pumping. An etalon of 0.0475 cm^{-1} FSR was used to measure the distance between a CO_2 line and the reference line. In the present experimental technique, absolute vibrational populations are extracted directly from absorption intensity measurements of cold CO_2 gas

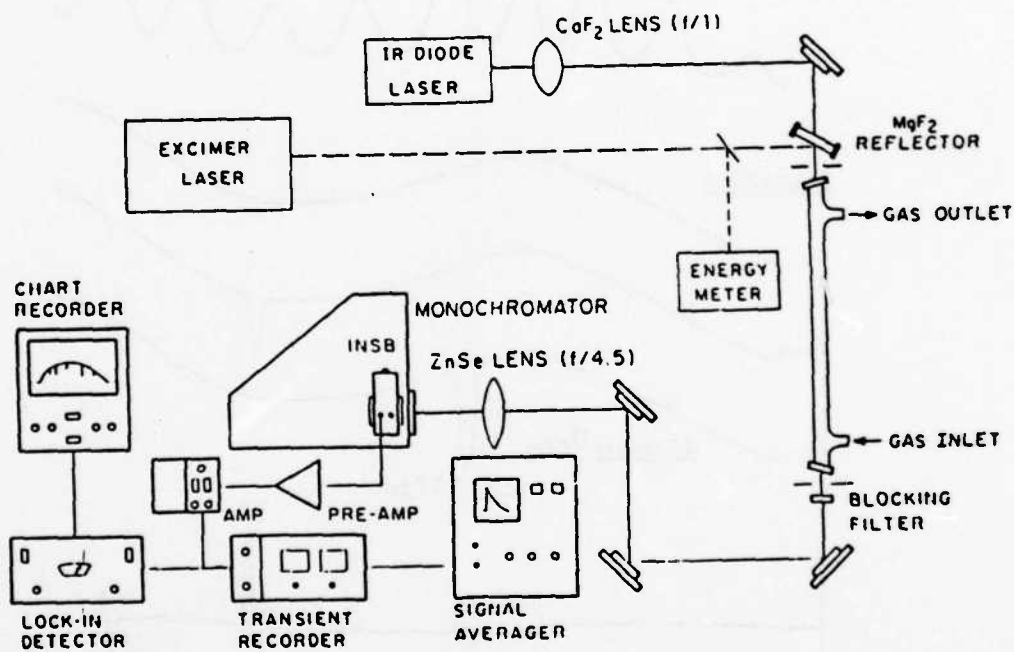


Figure 1

DIODE LASER SPECTRUM OF $^{13}\text{CO}_2$ AND $^{12}\text{CO}_2/\text{H}_2\text{S}$
(PATH LENGTH 18.5 cm)

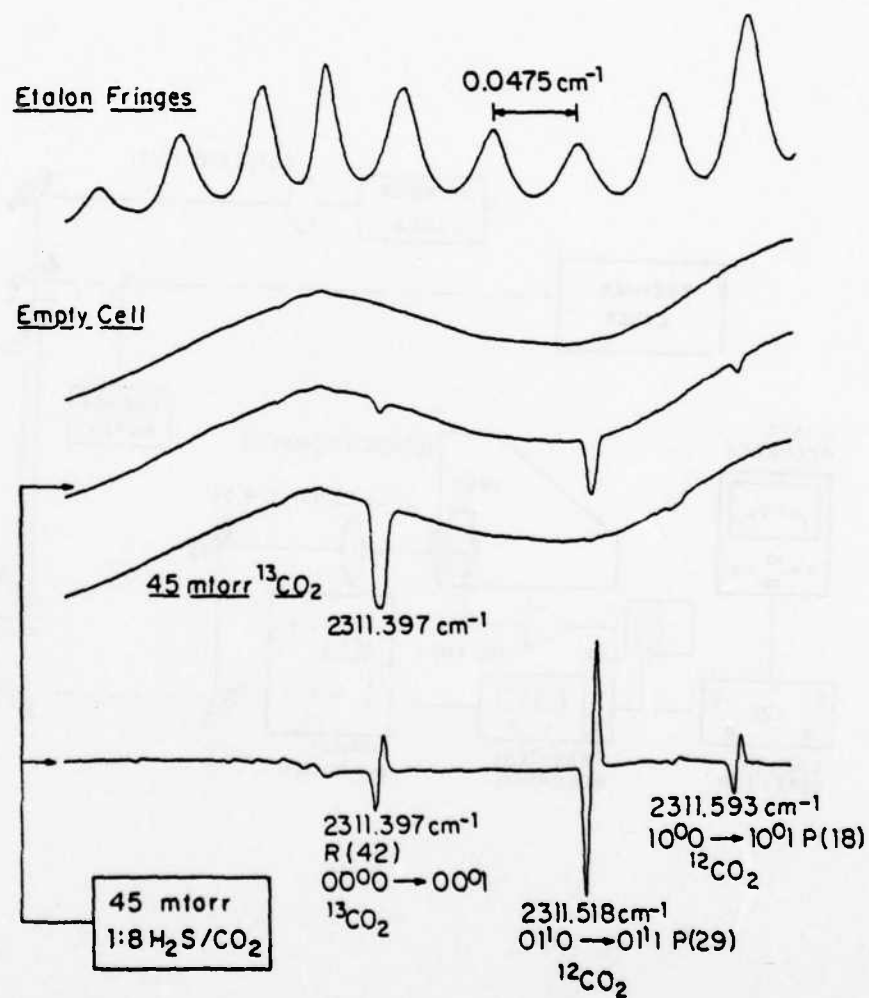


Figure 2

DIODE LASER SINGLE AND DOUBLE RESONANCE SPECTRUM OF CO₂
(PATH LENGTH 77.5cm, 0.75 torr, 1:4 H₂S/CO₂)

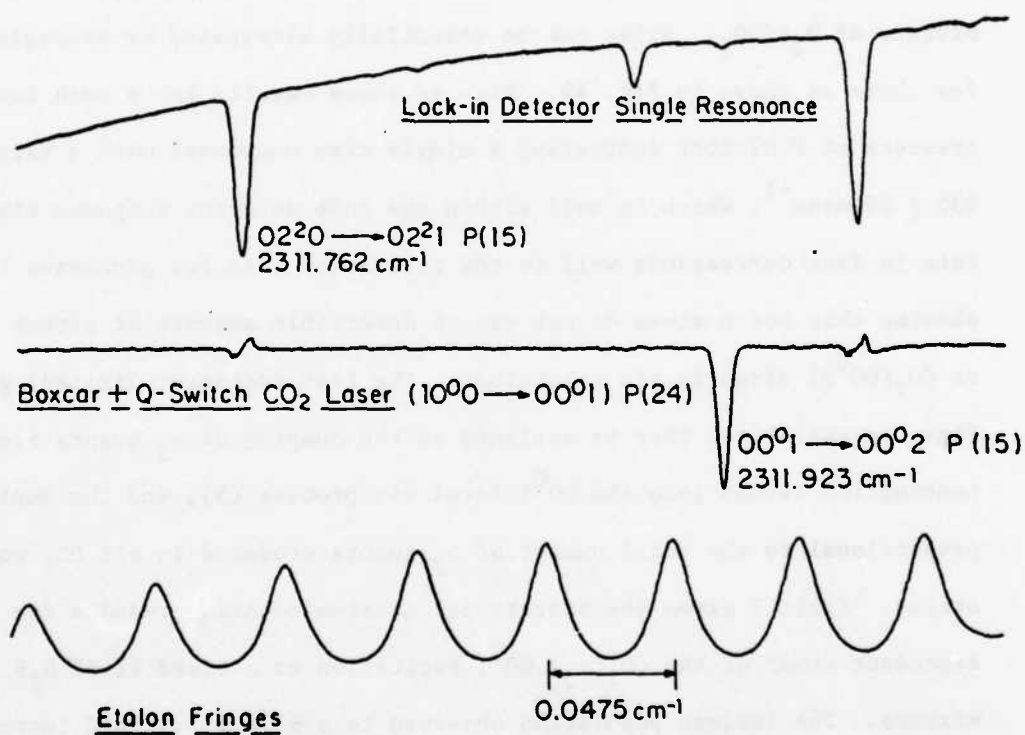


Figure 3

samples at room temperature (in the absence of excimer or CO₂ laser pumping).

Results

Figure 4a shows a typical trace of absorption changes recorded when the diode laser is tuned to the $00^0_1 \rightarrow 00^0_2$ P(15) CO₂ transition and only a single excimer laser shot is fired at a total pressure of 0.6 torr in a 1/8 mixture of H₂S/CO₂. Noise can be essentially eliminated by averaging for a few shots as shown in Fig. 4b. Fig. 4c shows results for a much lower total pressure of 0.02 torr indicating a single rise component with a rate of $135 \pm 20 \text{ msec}^{-1}$, which is well within the InSb detector response time. This rate in fact corresponds well to the relaxation rate for processes (1-3) showing that hot H atoms do not excite detectable amounts of either CO₂(00^0_1) or CO₂(00^0_2) directly via collisions. The fast (detector limited) growth in Figs. 4a and 4b can thus be assigned to the dumping of ν_3 quanta from combination levels into the 00^0_1 level via process (5), and the amplitudes are proportional to the total number of ν_3 quanta produced in all CO₂ combination states. Table I gives the vibrational quantum counting results for a pressure dependent study of the CO₂(ν_3) 00^0_1 excitation at a fixed 12.5% H₂S in CO₂ mixture. The largest population observed is a 67.8 ± 5.4 fold increase in the $\nu_3(00^0_1)$ state population over the ambient population at a pressure of 0.4 torr. Using the expression, (12)-(14)

$$N_1/N_0 = (g_1) \exp[-E_1/kT_1] \quad (6)$$

a vibrational temperature of 478 K is obtained for the ν_3 mode, which is equivalent to 68 quanta of ν_3 excitation.

In a separate experiment, the rate of direct (T-V) excitation of CO₂ ν_3 quanta produced by collisions with "hot" hydrogen atoms was measured via time-resolved fluorescence techniques. The total rate of growth for

T-V EXCITATION OF CO₂ BY H*

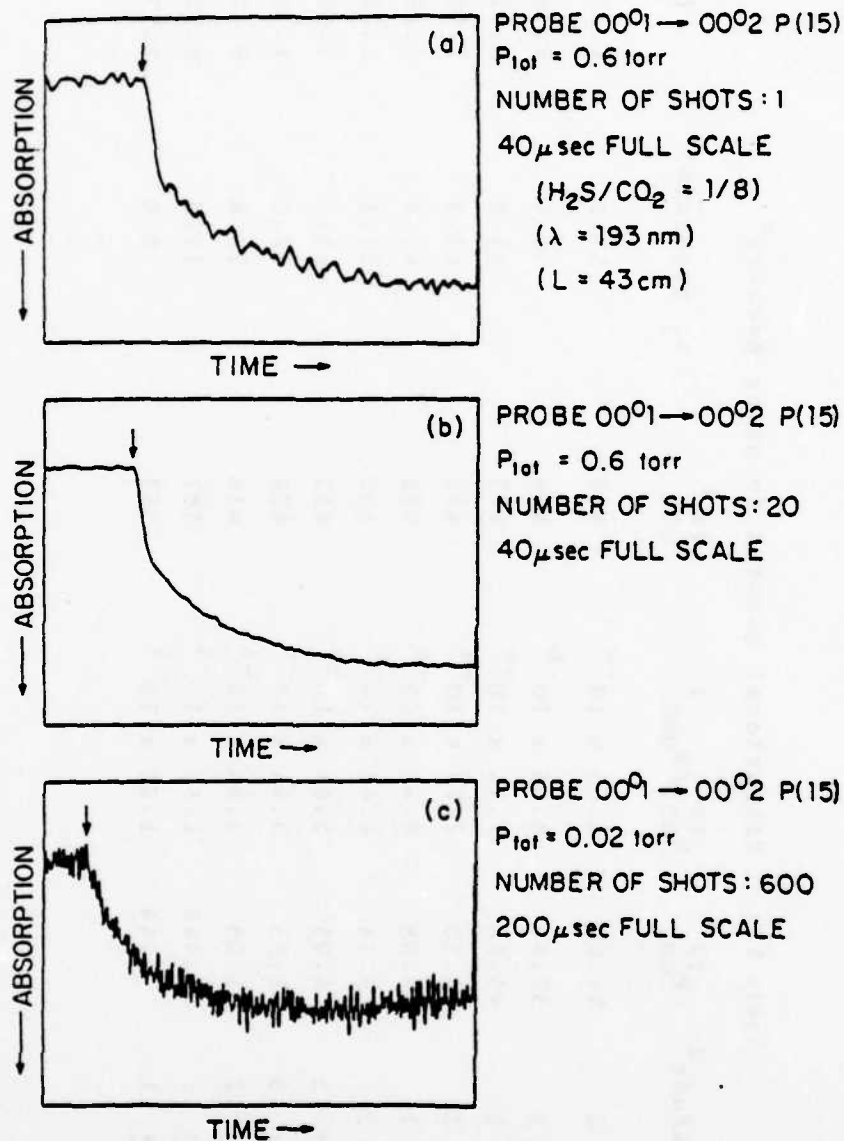


Figure 4

Table I. Vibrational Quantum Counting Results^a

P _{total} ^b	P _{CO2} ^c	Amplitude ^d	TV ^e P _{CO2}	TV ^f N ₀₀₁ /N ₀₀₀	TV ^g T ₀₀₁	ν_3 quanta(\bar{m}) ^h	[H [*]] ₀ ⁱ
2.00	1.778	99 + 2	94.69	6.65 x 10 ⁻⁴	462	53.2	1.33 x 10 ¹⁵
1.00	.899	80 + 2	57.99	8.06 x 10 ⁻⁴	474	64.5	9.76 x 10 ¹⁴
.80	.711	69 + 2	45.18	7.94 x 10 ⁻⁴	473	63.5	8.52 x 10 ¹⁴
.60	.533	56 + 2	33.20	7.79 x 10 ⁻⁴	472	62.3	7.01 x 10 ¹⁴
.40	.355	44 + 2	24.08	8.48 x 10 ⁻⁴	478	67.8	5.06 x 10 ¹⁴
.20	.178	19 + 2	9.14	6.41 x 10 ⁻⁴	460	51.3	2.78 x 10 ¹⁴
.10	.089	8.8 + .5	4.05	5.69 x 10 ⁻⁴	452	45.5	1.46 x 10 ¹⁴
.08	.071	4.3 + .3	1.95	3.44 x 10 ⁻⁴	424	27.5	1.21 x 10 ¹⁴
.06	.053	2.7 + .2	1.25	2.95 x 10 ⁻⁴	416	23.6	9.47 x 10 ¹³
.04	.035	.95 + .1	.449	1.60 x 10 ⁻⁴	387	12.8	6.82 x 10 ¹³
.02	.018	.29 + .1	.144	1.00 x 10 ⁻⁴	367	8.0	2.77 x 10 ¹³

Table I. Captions

- a) Changes in diode laser absorption ($\lambda \sim 4.3 \mu\text{m}$) for the $00^0_1 \rightarrow 00^0_2$ P(15) transition of CO_2 caused by collisions of CO_2 with hot hydrogen atoms followed by V-V equilibration of CO_2 via process (5) in the text. The hot hydrogen atoms are produced by 193 nm excimer laser photolysis of H_2S .
- b) Total pressure (Torr) of a 1/8 H_2S in CO_2 mixture.
- c) Partial pressure (Torr) of CO_2 in the mixture.
- d) Amplitude of the fast absorption changes (in 10^{-2} Volts/laser shot). See Fig. 4 for a typical signal. Amplitudes are normalized for amplifier gain settings and number of laser shots. For total pressures above 0.1 Torr, the amplitude changes recorded were for a single excimer laser shot.
- e) Calculated change in 300°K CO_2 pressure (Torr) required to produce the change in absorption recorded in column 3. The calibration data is given elsewhere (see Ref. 22). Corrections for the difference in length of the sample cells used for calibration and dynamics experiments were made. The actual change in absorption for the dynamics experiments was fit to the calibration data via a Beer-Lambert relation. Linear absorption was not assumed.
- f) Ratio of the population produced in the 00^0_1 level, by hot atom excitation and subsequent V-V relaxation via process (5) in the text, to the population of the ground state. At 300°K this ratio is 1.25×10^{-5} for an equilibrated sample of CO_2 .
- g) ν_3 vibrational temperature calculated using the data of column 5 and equation (6) of the text.
- h) Mean number of ν_3 vibrational quanta produced in all CO_2 states due to collisions with hot hydrogen atoms.
- i) Total number of H atoms produced by laser photolysis in the irradiated sample volume calculated from the known absorption coefficient of H_2S at 193 nm (see Ref. 23).

spontaneous emission at 4.3 μm was measured over the pressure range 0.02–0.2 torr for a (1/30) mixture of H_2S in CO_2 with an 0.1 μs response time Au:Ge detector/amplifier combination to provide a value for the relaxation rate of hot H atoms. A plot of the observed ν_3 initial risetimes versus CO_2 pressures is shown in Fig. 5, which from a least squares analysis yields a value of $(2.20 \pm 0.40) \times 10^4 \text{ msec}^{-1} \text{ torr}^{-1}$ for the total rate of cooling H atoms below the threshold for excitation of any CO_2 state containing a ν_3 quantum. A straightforward kinetic analysis^{(7),(22)} shows that the total rate of production of ν_3 quanta by hot H atom- CO_2 collision can be related to the amplitudes of the fast absorption changes in Figs. 4a and 4b via

$$k_3^{\text{TV}} [\text{CO}_2(000)] = \gamma_3 [\text{CO}_2^+] / [\text{H}^*]_0$$

where $[\text{CO}_2^+]$ is the total concentration of ν_3 quanta produced, $[\text{H}^*]_0$ is the initial concentration of hot atoms, $[\text{CO}_2(000)]$ is the ground state CO_2 concentration, and γ_3 is the total H atom cooling rate measured in the fluorescence experiments. From the present experiment, we obtain a value of $(1.66 \pm .43) \times 10^6 \text{ s}^{-1} \text{ torr}^{-1}$ for the microscopic rate constant, k_3^{TV} , for ν_3 excitation by H atoms.

The time-resolved transient absorption signal obtained with an 18 cm long cell for the CO_2 $01^10 \rightarrow 01^11$ P(29) transition is shown in Fig 6a. The initial fast rise component is detector limited, and the measured amplitude for this process represents a $(5.9 \pm 2.0)\%$ increase in the $\nu_2(01^10)$ state population over the ambient level. The large error limit arises from the relatively poor signal quality as seen in Fig 6a. A much better signal to noise ratio can be obtained for the $01^10 \rightarrow 01^11$ P(29) transition by shortening the cell length from 18 cm to 6 cm (as shown in Fig. 7). Here the transient absorption clearly exhibits two risetimes, a fast (detector limited)

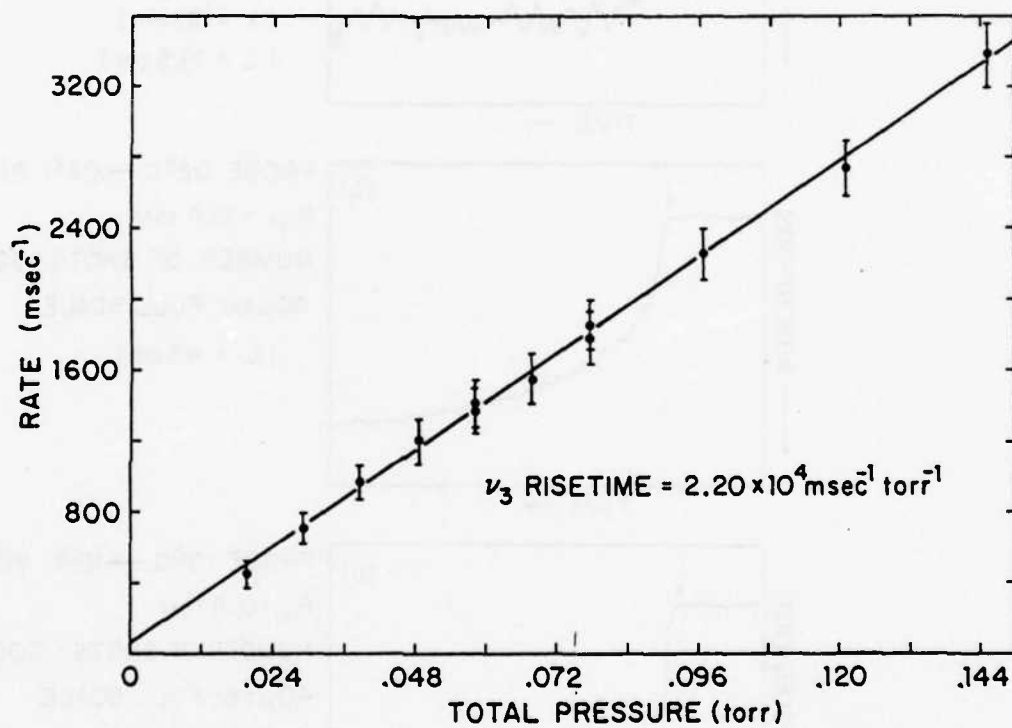


Figure 5

VIBRATIONAL QUANTUM COUNTING
(T-V EXCITATION OF CO₂ BY H*)

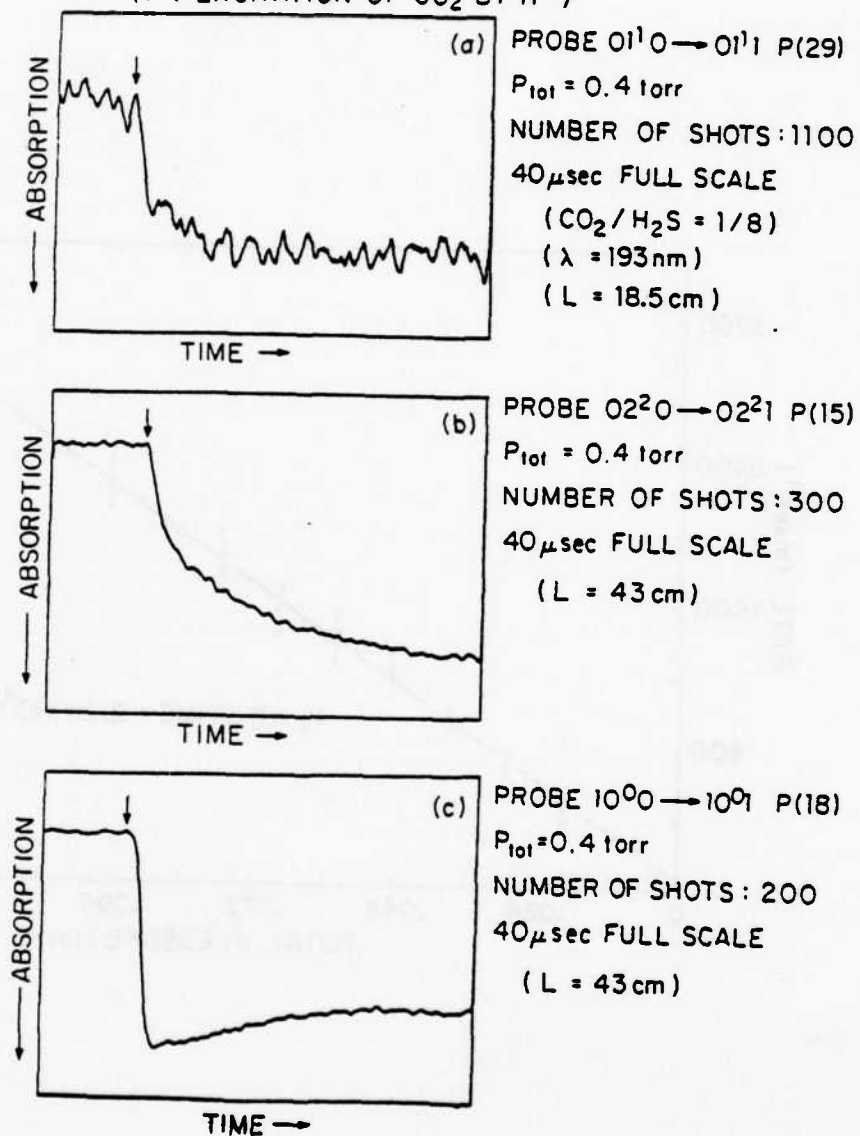


Figure 6

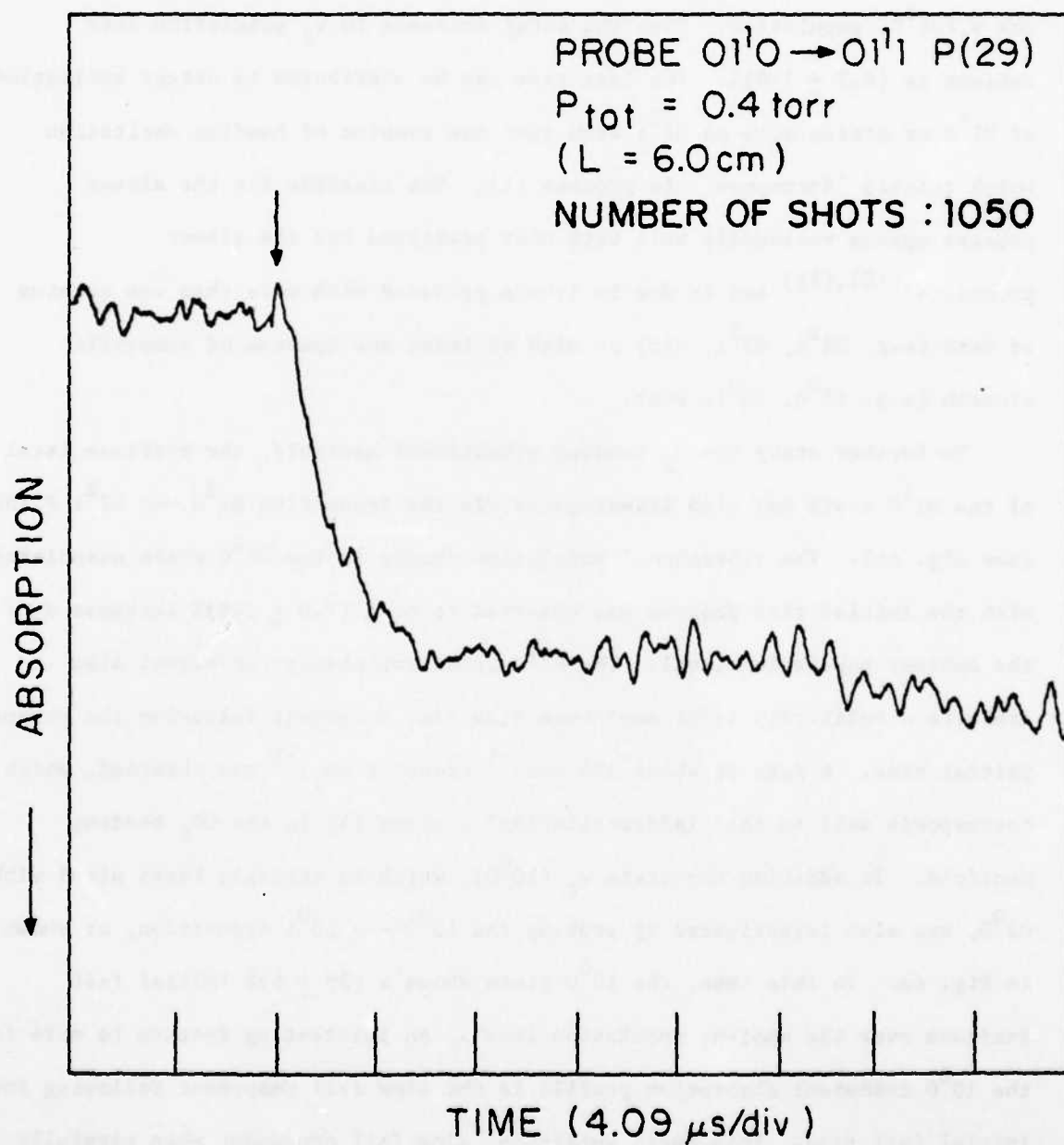


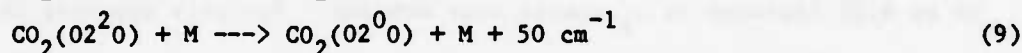
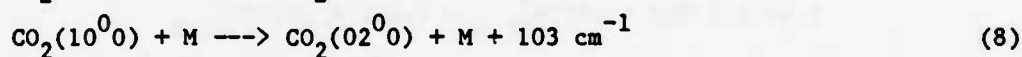
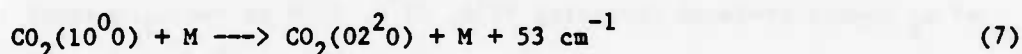
Figure 7

one which represents an increase of $(3.7 \pm 0.5)\%$ in the $\nu_2(01^10)$ population and a slower one which represents an additional increase of $(2.5 \pm 0.5)\%$ in the $\nu_2(01^10)$ population. Thus the total increase in ν_2 population over ambient is $(6.2 \pm 1.0)\%$. The fast rise can be attributed to direct excitation of 01^10 or states such as 01^11 with just one quantum of bending excitation which quickly "decompose" via process (1). The risetime for the slower process agrees reasonably well with that predicted for the slower process(4)^{(10),(11)} and is due to levels produced with more than one quantum of bend (e.g. 02^20 , 02^21 , etc) or with at least one quantum of symmetric stretch (e.g. 10^00 , 10^01 , etc).

To further study the ν_2 bending vibrational manifold, the overtone level of the 01^10 state was also investigated via the transition $02^20 \rightarrow 02^21$ P(15) (see Fig. 6b). The vibrational population change in the 02^20 state associated with the initial rise process was observed to be a $(7.0 \pm 1.4)\%$ increase over the ambient population level. The 02^20 transient absorption signal also exhibits a relatively large amplitude slow rise component following the prompt initial rise. A rate of about $390 \text{ msec}^{-1} (\text{torr of CO}_2)^{-1}$ was obtained, which corresponds well to the "ladder-climbing" process (4) in the CO_2 bending manifold. In addition the state $\nu_1(10^00)$, which is strongly Fermi mixed with 02^00 , was also investigated by probing the $10^00 \rightarrow 10^01$ transition, as shown in Fig. 6c. In this case, the 10^00 state shows a $(29 \pm 6)\%$ initial fast increase over the ambient population level. An interesting feature to note in the 10^00 transient absorption profile is the slow fall component following the initial fast rise. This small amplitude, slow fall component when carefully analyzed also exhibits a rate of about $340 \text{ msec}^{-1} (\text{torr of CO}_2)^{-1}$ comparable to the "ladder climbing" process (4).

The observed relatively slow ladder climbing process (4) in the signals

in Fig. 6 clearly show a certain amount of reequilibration among the 01^10 , 02^20 , 10^00 (and presumably 02^00) levels following H atom- CO_2 collisions. In fact, at pressures such as those shown in Figs. 6b and 6c, considerable redistribution of population between the levels 10^00 , 02^20 , and 02^00 is known to occur on the time scale of the fast rise due to processes such as



Experimentally we find that the relative change in the populations of levels 10^00 , 02^20 , and 01^10 does reach steady state after reactions (5, 7-9) and a quasi-equilibrium exist among these levels. Thus the present experiments do not provide an unambiguous differentiation between the number of bending quanta produced (ν_2 mode) and the number of symmetric stretch quanta produced (ν_1 mode) because of the rapid intermode energy transfer between ν_1 and ν_2 via reactions (7-9). Fortunately, the 01^10 level is relatively isolated from these intermode energy transfer processes because of somewhat slow equilibration between 01^10 and 02^20 via the ladder climbing process (4). Nevertheless, an accurate value for the number of symmetric stretch quanta cannot be obtained from the present experiments even though the number of ν_2 and ν_3 quanta are accurately counted. Actually, the molecules produced in both " 02^00 " and " 10^00 " have as much bending as symmetric stretching character due to the strong, Fermi coupling of these levels, and one can never accurately describe the production of a pure symmetric stretch level by hot atom collisions.

To obtain final values for the total number of ν_3 and ν_2 quanta produced

by hot atom excitation of CO_2 , the number of molecules "stored" in levels such as 01^1_1 (for ν_3) and 02^2_0 , 02^0_0 , 10^0_0 (for ν_2) at steady state must be determined. Including the population deviation for the 01^1_1 level, the total number of ν_3 quanta produced is

$$1.081 \times (67.8 \pm 5.4)N_{00\ 1}^0 = (73.3 \pm 5.8)N_{00\ 1}^0$$

or a 73 fold increase in ν_3 quanta over ambient. Similarly, the total number of ν_2 quanta produced (counting 02^2_0 , 02^0_0 , 10^0_0 as two ν_2 quanta) is

$$1.33 \times (.062 \pm .01)N_{01\ 0}^0 = (.082 \pm .013)N_{01\ 0}^0$$

or an 8.2% increase in ν_2 quanta over ambient. Strictly speaking this value is not purely a measure of ν_2 excitation since some feeding of ν_2 from ν_1 is clearly evident in Fig. 6. Taking into account this systematic error, a conservative value for the number of ν_2 quanta produced is $(.06 \pm .03)N_{0110}^0$. Using these values, the relative number of ν_2 versus ν_3 quanta produced is

$$\frac{(.06 \pm .03)N_{0110}^0}{(73.3 \pm 5.8)N_{0001}^0} = (8.2 \pm 5) \times 10^{-4} \left(\frac{N_{0110}^0}{N_{0001}^0} \right) = 5.3 \pm 3.2$$

Thus, about 5 times as many bending as asymmetric stretching quanta are produced by hot H atom excitation of CO_2 . Most of these ν_3 quanta are created in combination states with less than 10% being formed in the 00^0_1 level. If we take the 00^0_1 population directly produced by hot atom scattering to be $<0.1 \times 68N_{0011}^0$, we obtain a ratio of >57 for the total number of ν_2 quanta formed compared to the number of directly created 00^0_1 molecules. Again this ratio is only a lower limit set by the quality of the signals shown in Fig. 4c. The actual ratio is probably much larger than 57.

The collisional quenching of the translationally "hot" hydrogen atoms was investigated, and the thermalization rate with H_2S was determined relative to the T-V energy transfer rate. We find that the "hot" atom thermalization rate

due to H^*/H_2S is much greater (approximately 65 times) than the rate for collisional excitation of $CO_2 \nu_3$ quanta. In addition, the thermalization rate for cooling H^* atoms below the threshold for ν_3 excitation is about a factor of six smaller for H^*/CO_2 collisions than for H^*/H_2S . The enhanced efficiency of H_2S in slowing hot H atoms is probably due to the presence of hydrogen in the molecule. In taking the gas kinetic collision rate for H_2S and CO_2 to be the same ($z_{gk} = 27 \times 10^4 \text{ msec}^{-1} \text{ torr}^{-1}$) for the initially produced hot H^* atoms of velocity $2.11 \times 10^6 \text{ cm/sec}$, the following conclusions can be drawn:

- (1) Approximately two H_2S/H^* gas kinetic collisions are required to cool H^* below threshold for excitation of a $CO_2 \nu_3$ quantum.
- (2) Approximately 14 CO_2/H^* gas kinetic collisions are required to cool H^* below threshold for excitation of a $CO_2 \nu_3$ quantum.
- (3) Approximately 160 CO_2/H^* gas kinetic collisions are required to cool H^* below threshold for excitation of a $CO_2 \nu_3$ quantum.

The above results indicate clearly that the present experiments do not provide direct information regarding the probability that initially produced H^* will excite a ν_3 quantum. Rather the probability measured here represents an average over 5-10 H^*/CO_2 collisions.

Discussion

If the cross section for T-V excitation of a $CO_2 \nu_3$ quantum is strongly peaked to high energy so that only the first H atom/ CO_2 collision produces significant vibrational excitation, the present experimental results can be used to extract a cross section for ν_3 excitation, since the initial H atom velocity is known. Using $k_3^{TV} = 1.66 \times 10^3 \text{ msec}^{-1} \text{ torr}^{-1}$ (1/30, H_2S/CO_2 mixture) and $V_H = 2.11 \times 10^6 \text{ cm/sec}$ gives $\pi \sigma_3^2 = 0.25 \text{ \AA}^2$. This is the total cross section for producing a ν_3 quantum in any CO_2 vibrational state under these

assumptions. Since earlier fluorescence results⁽⁵⁾ show that about 15% of the ν_3 quanta are produced directly in the $01^1 1$ state the cross section for T-V excitation of $01^1 1$ would be $(0.15) \times (.25 \text{ \AA}^2) = 0.038 \text{ \AA}^2$ using the same assumptions. At the present time, there is some experimental evidence which suggest a strongly peaked cross section emphasizing only the first collisions for H atom excitation. Nevertheless, even if we assume that H atoms of one half the initial velocity (and hence one quarter the initial energy) are equally effective in producing ν_3 excitation, the cross section would only increase to a maximum of 0.5 \AA^2 . Thus the ν_3 CO_2 T-V excitation probability for H atoms in the 1.5-2.5 eV translational energy range appears to be about 10^{-2} gas kinetic (the CO_2 gas kinetic cross section is $\sim 50 \text{ \AA}^2$). The probability for excitation of the specific $01^1 1 \nu_3$ containing state, based on the earlier fluorescence data, is then about 1.5×10^{-3} gas kinetic. Lastly, assuming the thermalization rates for cooling H atoms below threshold for ν_3 excitation are the same for ν_2 excitation, the probability for T-V production of a ν_2 quantum is about 5×10^{-2} gas kinetic. Using the same assumptions, the probability of ν_1 excitation is $\sim 3 \times 10^{-3}$ gas kinetic, with the realization that the number of ν_1 quanta produced is only approximately known due to ν_1 - ν_2 thermalization.

Conclusions

1) A diode laser, absorption probe technique having a spectral resolution in excess of 10^{-3} cm^{-1} has been developed to study dynamic molecular processes. In the present work this method has been applied to the study of CO_2 vibrational excitation by hot hydrogen atoms produced from excimer laser photolysis of H_2S .

2) The number of ν_3 antisymmetric stretching quanta produced in all CO_2

vibrational states by H atom scattering has been quantitatively determined. The rate for excitation of ν_3 quanta was found to be $1.66 \times 10^3 \text{ msec}^{-1} \text{ torr}^{-1}$, and the probability for excitation of a ν_3 quantum is approximately 1% per gas kinetic collision.

3) Direct excitation of the fundamental antisymmetric stretch level 00^0_1 by hot hydrogen atoms has been found to be very small (<10% of the total ν_3 excitation) confirming an earlier observation using low resolution infrared fluorescence techniques.

4) Cooling of hot hydrogen atoms below threshold for excitation of a $\text{CO}_2 \nu_3$ quantum requires approximately 2 H_2S or 14 CO_2 gas kinetic collisions.

5) Production of ν_2 bending excitation in CO_2 by collisions with hot H atoms has been detected for the first time. Prompt (direct) excitation of the 01^1_0 bending fundamental is observed, and the total number of ν_2 quanta produced is found to be 5-6 times the total number of ν_3 quanta produced. Assuming equal rates for cooling H atoms below threshold for ν_3 and ν_2 excitation gives a probability for production of ν_2 quanta which is approximately 5% per gas kinetic collision.

6) Excitation of ν_1 symmetric stretch quanta by hot H atoms has also been observed for the first time, but rapid equilibration of the $\text{CO}_2 \nu_1$ and $2\nu_2$ levels prevents a precise determination of the number of ν_1 quanta produced. The probability for excitation of ν_1 quanta was found to be approximately 10^{-3} - 10^{-2} per gas kinetic collision.

7) Simple theoretical calculations employing either a spherically symmetric potential linearized in the CO_2 normal coordinate or a statistical argument do not fit the observed experimental data even qualitatively. However, more sophisticated calculations do reproduce the general trends in the data. (15)-(20)

8) The diode laser, absorption probe technique is a general one which can be applied to the study of other dynamic processes. By analogy with the present experiments, the nascent distribution of CO_2 vibrational states produced by excimer laser photodissociation of α -keto organic acids has already been probed⁽²¹⁾ and extension of the technique to the study of CO , CH_2 , CH_3 , and other molecular photofragments appears to be straightforward.

9) Although the present experiments have concentrated on a determination of the overall number of ν_3 , ν_2 , and ν_1 vibrational quanta produced by hot H atom/ CO_2 collisions, sufficient resolution, sensitivity, and speed exists with this method to determine excitation probabilities for specific CO_2 vibrational and rotational states. Indeed, since the laser probe linewidth is substantially less than the CO_2 4.3 μm transition Doppler width, probing of nascent CO_2 velocity distributions should even be possible.

10) Energy dependent scattering (and photodissociation) cross sections can be determined by varying the excimer laser photodissociation wavelength of the H atom precursor.

*This research was also supported by the National Science Foundation under Grant CHE-80-23747 and the Department of Energy under Contract DE-AC02-78ER-04940.

- (1) C. R. Quick, Jr., R. E. Weston, Jr., and G. W. Flynn, Chem. Phys. Lett. 83, 15 (1981).
- (2) F. Magnotta, D. J. Nesbitt, and S. R. Leone, Chem. Phys. Letts. 83, 21 (1981).
- (3) C. F. Wood, G. W. Flynn, and R. E. Weston, Jr., J. Chem. Phys. 77, 4776 (1982).
- (4) C. A. Wight and S. R. Leone, J. Chem. Phys. 78, 4875 (1983).
- (5) J. O. Chu, G. W. Flynn, and R. E. Weston, Jr., J. Chem. Phys. 78, 2990 (1983).
- (6) C. A. Wight and S. R. Leone, J. Chem. Phys. 79, 4823 (1983).

- (7) J. O. Chu, C. F. Wood, G. W. Flynn, and R. E. Weston, Jr., J. Chem. Phys. 80, 1703 (1984).
- (8) I. Burak, Y. Noter, and A. Szöke, IEEE QE-9, 541 (1973).
- (9) J. Finzi and C. B. Moore, J. Chem. Phys. 63, 2285 (1975).
- (10) R. K. Huddleston and E. Writz, Chem. Phys. Letts. 83, 174 (1981).
- (11) C. F. Wood, J. O. Chu, and G. W. Flynn, "Vibrational Energy Transfer Between the Symmetric Stretching and Bending Modes of CO₂: A Diode Laser Infrared Double Resonance Study," manuscript in preparation.
- (12) C. B. Moore, R. E. Wood, B. L. Hu, and J. T. Yardley, J. Chem. Phys. 46, 4222 (1967).
- (13) G. W. Flynn, Acc. Chem. Res. 14, 334 (1981); I. Shamah and G. W. Flynn, J. Chem. Phys. 69, 2474 (1978).
- (14) E. Weitz and G. W. Flynn in "Photoselective Chemistry," Part 2, J. Jortner, Ed., John Wiley and sons, Inc., 1981, p. 185.
- (15) N. M. Harvey, Chem. Phys. Letts. 88, 553 (1982).
- (16) G. C. Schatz and M. J. Redmon, Chem. Phys. 58, 195 (1981).
- (17) J. N. Bass, J. Chem. Phys. 60, 2913 (1974).
- (18) H. H. Suzukawa, M. Wolfsberg, and D. L. Thompson, J. Chem. Phys. 68, 455 (1978).
- (19) G. C. Schatz and T. Mulloney, J. Chem. Phys. 71, 5257 (1979).
- (20) D. C. Clary, J. Chem. Phys. 75, 209 (1981).
- (21) "Diode Laser Probes of CO₂ Produced by Photofragmentation of Pyruvic Acid," C. F. Wood, J. A. O'Neill, and G. W. Flynn, work in progress.
- (22) "Counting Vibrational Quanta with a Diode Laser Probe: Bending and Stretching Excitation in CO₂ Caused by Collisions with Hot Atoms from Excimer Laser Photolysis," J. O. Chu, C. F. Wood, G. W. Flynn, and R. E. Weston, Jr., accepted to J. Chem. Phys.
- (23) K. Watanabe and A. S. Jursa, J. Chem. Phys. 41, 1650 (1964).

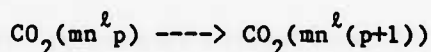
D. VIBRATIONAL ENERGY TRANSFER BETWEEN THE SYMMETRIC STRETCHING AND BENDING MODES OF CO₂: A DIODE LASER DOUBLE RESONANCE STUDY*

(C. F. Wood, J. O. Chu, G. W. Flynn)

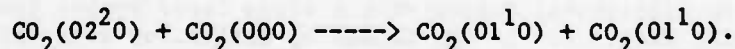
(JSEP work unit 7, 1982-1985)

(Principal Investigator: G. W. Flynn (212) 280-4162)

Recently we have investigated the vibrational energy equilibration among the four levels 01¹0, 02⁰0, 02²0, and 10⁰0 in CO₂⁽¹⁾ via diode laser infrared double resonance techniques⁽²⁾⁻⁽⁴⁾ where the diode laser resolution ($\sim 10^{-3}$ cm⁻¹) makes it possible to probe the populations of the individual rotational/vibrational states of CO₂. By selectively monitoring vibrational transitions of the type



all of which "ride" the strong oscillator strength of the ν_3 mode, we have observed the time evolution of the population changes in the 10⁰0, 02²0, 02⁰0, 01¹0 states following pulsed CO₂ laser depletion of either the 10⁰0 or the 02⁰0 level in a CO₂ sample. The vibrational energy transfer rates among these low-lying levels have been measured, and three distinct rates (eigenvalues) were observed (not including the slow V-T,R rate) indicating that these levels do kinetically form a four level system with one mass constraint. A relatively slow rate of $375 \pm 45 \text{ msec}^{-1} \text{ torr}^{-1}$ was obtained and attributed to the "ladder climbing" process



The second kinetic rate was measured to be $750 \pm 200 \text{ msec}^{-1} \text{ torr}^{-1}$, while the third rate was estimated to be $\geq 2400 \text{ msec}^{-1} \text{ torr}^{-1}$. The collisional coupling of the 02²0 level with the Q-switch CO₂ laser perturbed 10⁰0 or 02⁰0 levels has been observed for the first time, allowing the vibrational coupling mechanism among these four levels to be deduced. The main features and rates of this mechanism are (see Fig. 1):

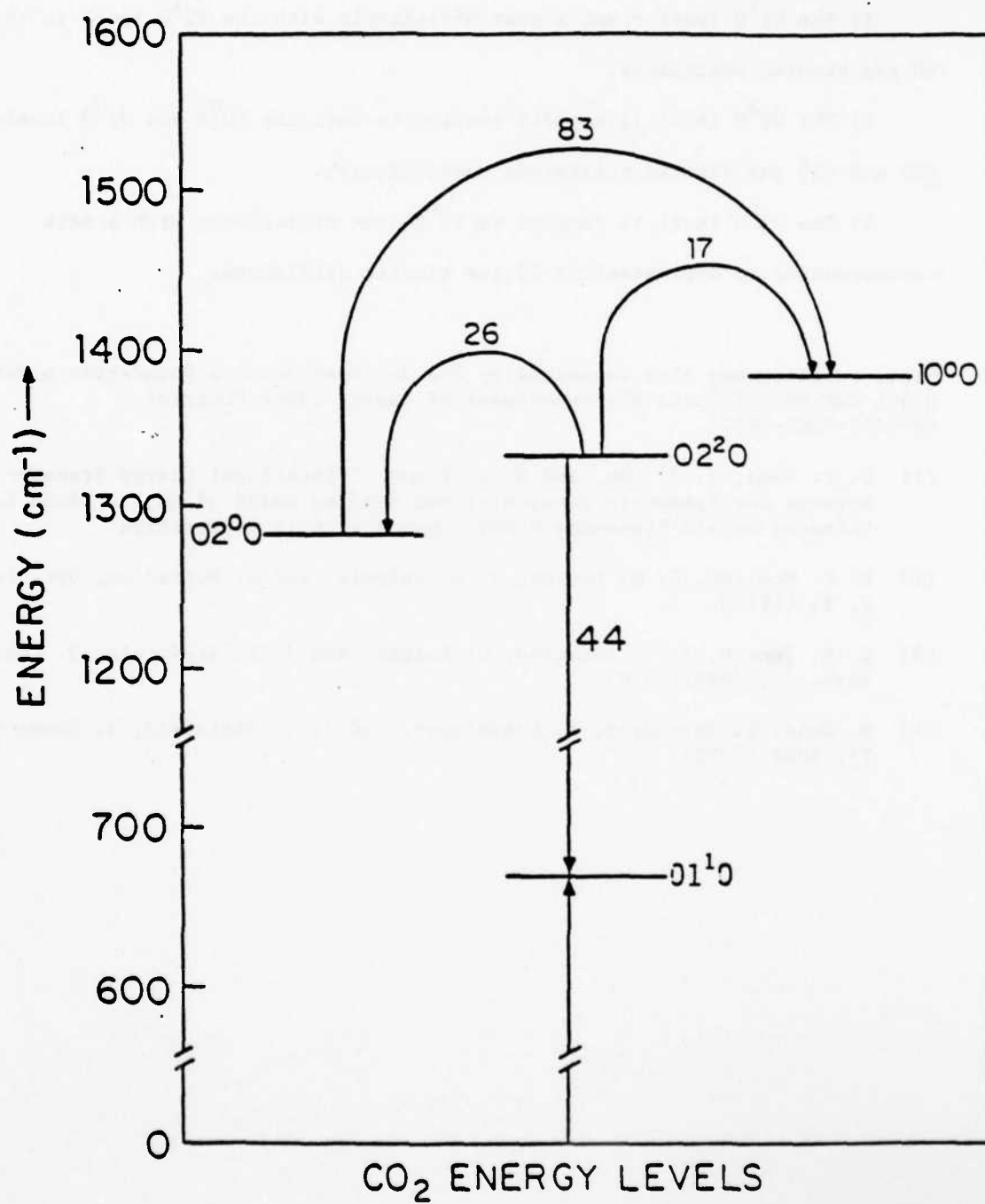


Figure 1

- 1) The $01^1 0$ level couples most efficiently with the $02^2 0$ level in about 40 gas kinetic collisions.
- 2) The $02^2 0$ level is rapidly coupled to both the $10^0 0$ and $02^0 0$ levels (in ≤ 20 and ≤ 30 gas kinetic collisions respectively).
- 3) The $02^0 0$ level is coupled to $10^0 0$ less efficiently with a rate corresponding to approximately 80 gas kinetic collisions.

*This research was also supported by the National Science Foundation under Grant CHE-80-23747 and the Department of Energy under Contract DE-AC02-78ER-04940.

- (1) C. F. Wood, J. O. Chu, and G. W. Flynn, "Vibrational Energy Transfer Between the Symmetric Stretching and Bending Modes of CO_2 : A Diode Laser Infrared Double Resonance Study," manuscript in preparation.
- (2) P. F. Moulton, D. M. Larsen, J. N. Walpole, and A. Mooradian, Opt. Lett. 1, 51 (1977).
- (3) C. C. Jensen, T. G. Anderson, C. Reiser, and J. I. Steinfeld, J. Chem. Phys. 71, 3648 (1979).
- (4) M. Dubs, D. Harradine, E. Schweitzer, and J. I. Steinfeld, J. Chem. Phys. 77, 3824 (1982).

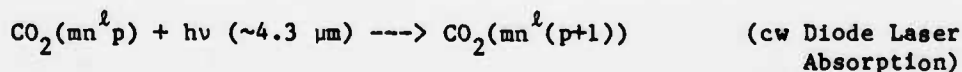
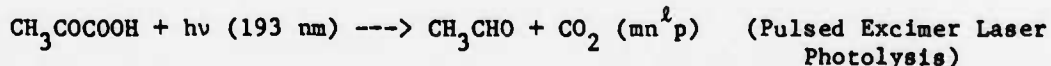
E. DIODE LASER PROBES OF PHOTOFRAGMENTATION PRODUCTS*

(C. F. Wood, J. A. O'Neill, G. W. Flynn)

(JSEP work unit 7, 1982-1985)

(Principal Investigator: G. W. Flynn (212) 280-4162)

Measurement of fragment energy distributions is one of the few methods available to obtain information about photodissociation processes.⁽¹⁾ A knowledge of this distribution can yield information on the geometry of the dissociating species and hence on the symmetry and nature of the dissociative potential energy surfaces involved.⁽²⁾⁻⁽⁴⁾ In the present work, we have used a tunable diode laser to probe the IR absorption of excimer laser photolysis products of pyruvic acid. The high resolution (0.001 cm^{-1}) as well as the tunability of this laser make state specific absorption studies possible in many molecules. Pyruvic acid is an α -keto acid which thermally and photochemically decomposes to yield acetaldehyde and CO_2 .⁽⁵⁾⁻⁽⁷⁾ We have used the IR diode laser to probe the CO_2 states produced by the photodissociation of pyruvic acid at 193 nm. Schematically this experiment can be described by the following steps:



Studies were undertaken to determine the absorption coefficient for pyruvic acid at 193 nm, the quantum yield for the production of CO_2 at 193 nm, and the fraction of CO_2 directly produced in various rovibrational energy states. The details of these studies are described in a forthcoming paper, and only the results will be summarized here.⁽⁸⁾

A diagram of the apparatus is shown in Fig. 1. Infrared radiation is produced by a tunable diode laser (Laser Analytics) operating at approximately

N-C-211002/10

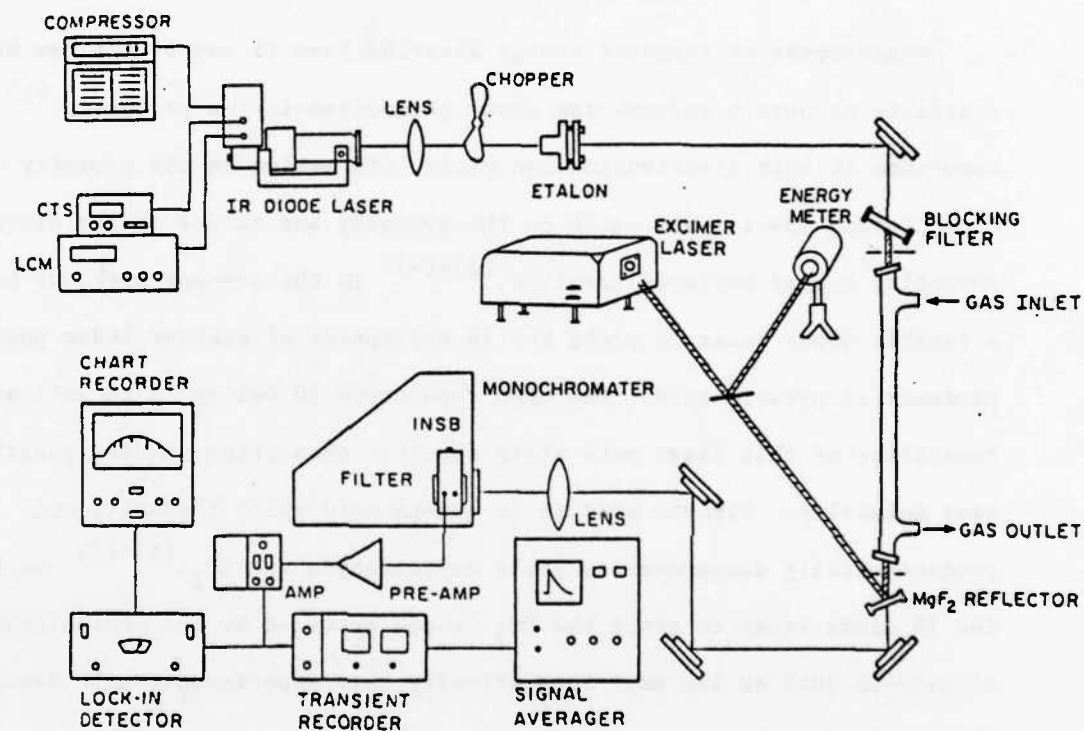


Figure 1

4.3 μm . The infrared and excimer (Lumonics model 860s) beams are made collinear by passing the IR beam through a MgF_2 flat which is coated for high reflectivity at 193 nm (ArF). The dissociation occurs in a cylindrical pyrex photolysis cell approximately 2.5 cm in diameter and either 43 cm or 180 cm long through which pyruvic acid is flowed. The infrared absorption was monitored with an InSb (1.5 μs response time) infrared detector, temporally resolved with a Biomation 8100 transient recorder, and signal averaged with a Nicolet 1174 averager. Analysis of time resolved absorption curves was performed on a PDP 11/34 or a VAX 11/780 computer. Transient absorption intensities were converted to "equivalent pressures" of ambient CO_2 (and thus, number of molecules) by comparison with changes in the diode laser intensity caused by known pressures of CO_2 in the same sample cell. The pyruvic acid was purchased from Aldrich chemical company and was repeatedly freeze-pump-thawed before use.

The absorption coefficient for pyruvic acid at 193 nm was found to be $0.05 \pm 0.015 \text{ cm}^{-1} \text{ torr}^{-1}$ for an excimer laser pulse energy of 2.9 mJ/pulse. Previous studies have demonstrated that the quantum yield for the formation of CO_2 in the photolysis wavelength range 370-300 nm is unity. At 193 nm an average of three typical quantum yield measurements gives a value of 1.03 ± 0.2 .

Irradiation of pyruvic acid at 193 nm while monitoring the IR absorption of CO_2 yielded transient absorption signals from the following CO_2 transitions:

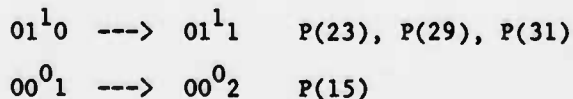
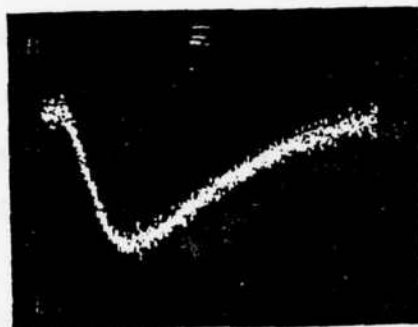


Figure 2 shows typical transient absorption curves for pure pyruvic acid for these transitions.

The $00^0 1 \longrightarrow 00^0 2$ transition was observed in pure pyruvic acid, in

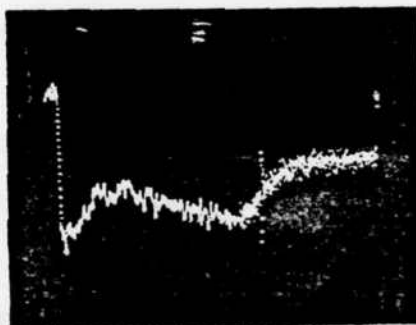
CO₂ Photofragment Absorption



0.05 Torr Pyruvic Acid
64 Excimer Loser Shots

Diode Loser Probes
 $00^0_1 \rightarrow 00^0_2$, P(15)

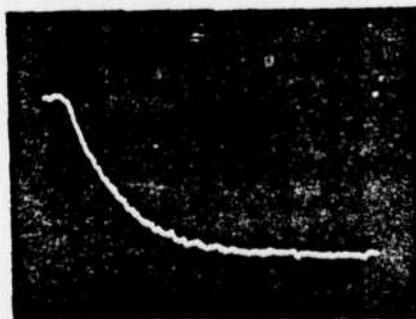
400 μ sec Full Scale



0.01 Torr Pyruvic Acid
512 Excimer Loser Shots

Diode Laser Probes
 $01^1_0 \rightarrow 01^1_1$, P(31)

Dual Time Base
60 μ sec, 800 μ sec



0.015 Torr Pyruvic Acid
0.50 Torr CO₂
50 Excimer Loser Shots

Diode Loser Probes
 $00^0_1 \rightarrow 00^0_2$, P(15)

100 μ sec Full Scale

Figure 2

pyruvic acid/ CO_2 mixtures, and in pyruvic acid/ CO_2 /Ar mixtures. The absorption changes in all of these cases rise at a rate which is dependent on the total gas pressure. None of these signals display a quickly rising component indicating that the ν_3 fundamental is not directly produced in the photodissociation process. The slow rise which is observed is most likely due to vibrational energy transfer in collisions with the acetaldehyde fragment which is expected to be vibrationally hot.⁽⁹⁾

For the $01^1 0 \rightarrow 01^1 1$ transition, the absorption increased at a rate that was greater than gas kinetic being limited by the response time of the detector even at pressures less than 50 mtorr of pure pyruvic acid. For typical experimental conditions with a pyruvic acid pressure of 0.5 torr, the photofragmentation process produces an absorption in the $01^1 0 \rightarrow 01^1 1$ transition equivalent to $1-2 \times 10^{-4}$ torr of cold CO_2 . From this we can conclude that $3.1 \pm 1.0\%$ of the CO_2 molecules produced by photodissociation appear directly in the $01^1 0$ vibrational level. In order to establish the absolute population changes beyond doubt, the corresponding higher order transitions such as $01^1 1 \rightarrow 01^1 2$ must also be studied. Further experiments are planned to monitor the amount of ground state ($00^0 0$), symmetric stretch ($10^0 0$), bending overtone ($02^2 0$), and combination states ($01^1 1$) as well as the dependence of product state distributions on photolysis wavelength.

*This research was also supported by the National Science Foundation under Grant CHE-80-23747 and the Department of Energy under Contract DE-AC02-78ER-04940.

- (1) Stephen R. Leone, Adv. in Chem. Phys. Ed. by K. P. Lawley, (John Wiley and Sons, New York 1982).
- (2) William M. Gelbart, Ann. Rev. Phys. Chem. 28, 323 (1982).
- (3) K. F. Freed and Y. B. Band, in "Excited States," Ed. by E. L. Lim, (Academic Press, New York 1977).

- (4) M. Shapiro and R. Bersohn, *Ann. Rev. Phys. Chem.* 33, 409 (1982).
- (5) M. Urion, *Ann. Chem.* 1, 5 (1934).
- (6) J. F. Arnett, D. B. Larson, and S. P. McGlynn, *J. Am. Chem. Soc.* 95, 7599 (1982).
- (7) P. A. Leermakers and G. F. Versley, *J. Am. Chem. Soc.* 85, 3776 (1963).
- (8) C. F. Wood, J. A. O'Neill, and G. W. Flynn, "Infrared Diode Laser Probes of Photofragmentation Products: Bending Excitation in CO₂ Produced by Excimer Laser Photolysis of Pyruvic Acid", (submitted for publication).
- (9) R. N. Rosenfeld and B. Weiner, *J. Am. Chem. Soc.* 105, 3485 (1983).

F. LASER-INDUCED FLUORESCENCE OF OH RADICALS PRODUCED IN REACTIONS OF LASER-GENERATED HOT HYDROGEN ATOMS*

(W. Hollingsworth, J. Subbiah, G. W. Flynn)
(JSEP work unit 7, 1982-1985)
(Principal Investigator: G. W. Flynn (212) 280-4162)

Introduction

There have been many experiments studying the translational-to-vibrational (T-V) energy transfer that occurs due to collisions of hot hydrogen atoms with various small molecules.^{(1),(2)} These hot atoms are created from the UV photolysis of hydrogen sulfide and the hydrogen halides using a pulsed excimer laser. With this method, effective translational temperatures of up to 25,000 K for the hydrogen atoms can be achieved.

Along with the T-V channel, complementary reactive channels can occur. Because of the high amount of energy contained in the hydrogen atoms, even very endothermic channels, or reactions with high activation barriers can be probed. In this way, valuable kinetic and dynamic information can be obtained on reactions of atmospheric and combustion interest.

Once the product molecules have been created through the reaction of these hot hydrogen atoms with other molecules, they are monitored through laser-induced fluorescence. This technique⁽³⁾ serves as a sensitive, time-resolved probe for the vibrational and rotational state distributions of the products. The probe laser can be delayed in time with respect to the initial photolysis laser in order to obtain a "delay curve", expressing the time behavior of the concentration of the product molecule. This curve contains kinetic information on the important reactions. Once the important reactions have been surmised, the system can be effectively modeled. This modeling assists in determining if the experimental results are in fact describing the assumed mechanism.

The production of OH radicals has already been observed from the molecules CO_2 , H_2O , and O_2 .^{(4),(5)} Ideally, these reacting molecules should be completely transparent to the wavelength of the photolyzing UV-laser pulse. If this is not true, then complicating effects of other reactive channels leading to production of the molecules of interest are possible. In the two molecules that we have studied, N_2O and NO , we have found that the small, but finite, absorptions of these molecules do affect the interpretations of the experimental results. The remainder of this report will discuss the results that we have obtained, and methods that we have used to circumvent the complicating effects. In addition, future plans will be briefly outlined.

Experimental

The experimental apparatus that we have used is shown in Figure 1. The appropriate gas mixture is flowed through the cell. The timing of the two lasers is controlled by a digital delay generator, capable of producing time delays down to the nanosecond range. A frequency doubler is used to double the frequency of the output of an excimer-pumped dye laser for resonance excitation of the products. The two beams are slightly focused and then counterpropagated through the reaction cell. Placed perpendicularly to the cell is a photomultiplier tube (PMT) fronted with filters cutting off laser scatter and accepting only the wavelength range of the molecular emission of interest. Inside the reaction cell are a series of baffles which further reduce the amount of laser scatter impinging on the PMT. The output of the PMT is sent to a boxcar averager whose gate is set to collect most of the molecular fluorescence. Excitation scans, resulting from the coincidences of the laser frequency with molecular

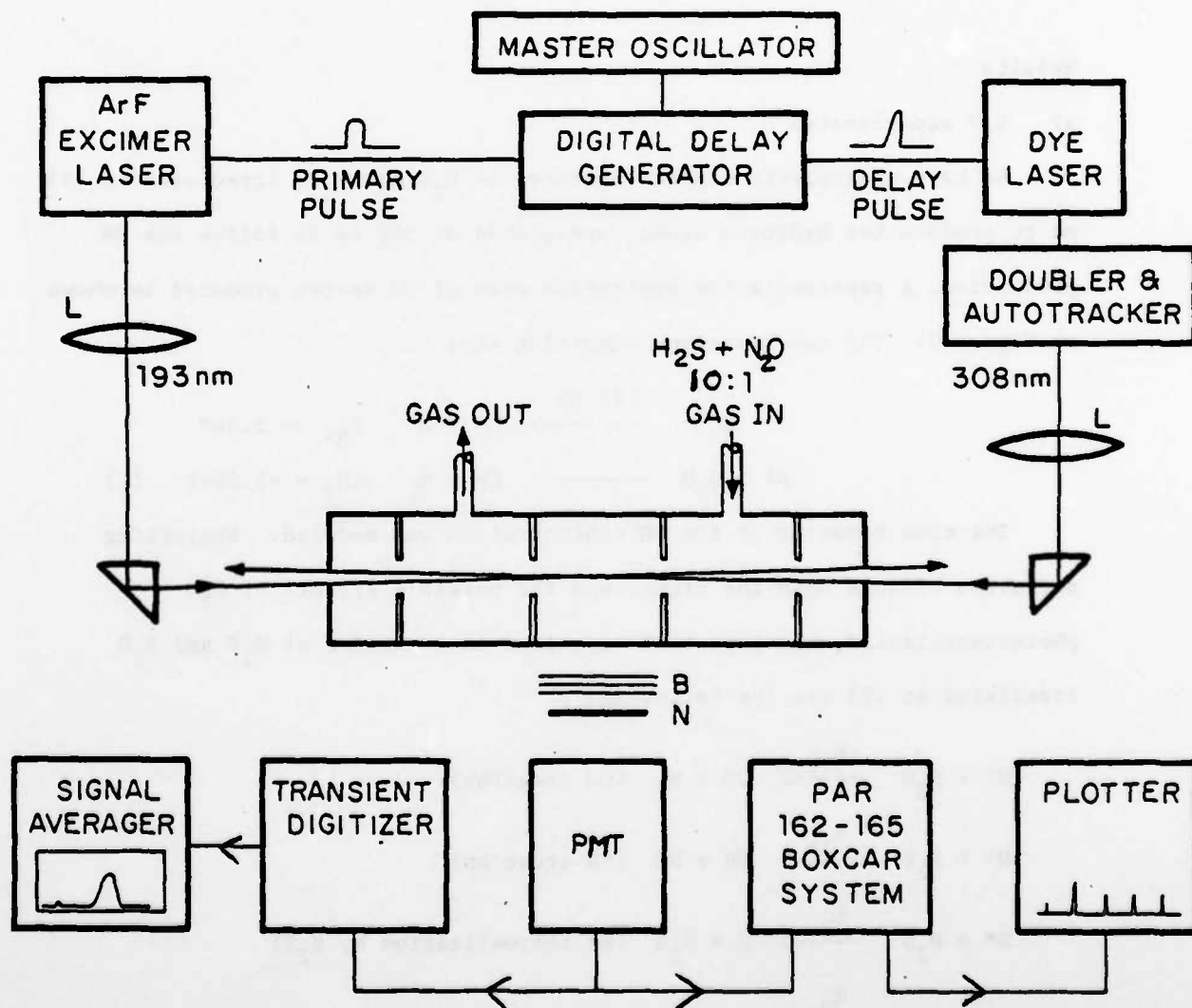


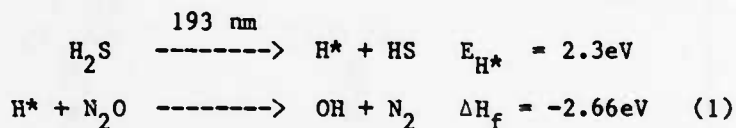
Figure 1

absorptions, are plotted out on a strip-chart recorder as the dye laser is scanned. Once the data are corrected for dye-laser power and absorption probabilities, relative populations can be determined for various nascent rotational states of the product.

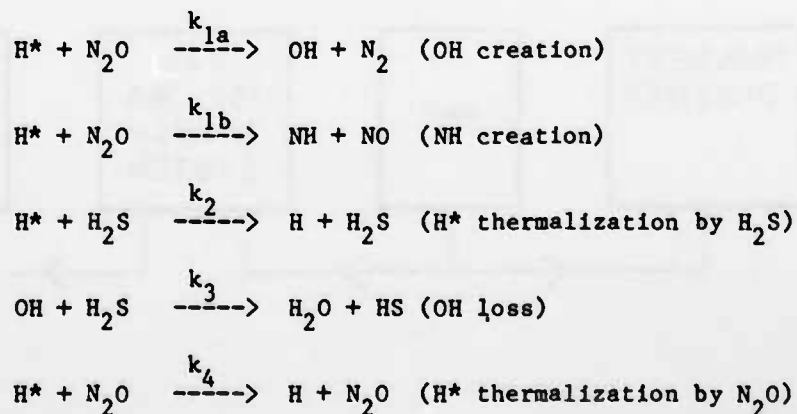
Results

a) N_2O experiments.

We have extensively studied mixtures of H_2S and N_2O , irradiated at 193 nm to produce hot hydrogen atoms, and probed at 308 nm to follow the OH production. A representative excitation scan of OH states produced is shown in Figure 2. The two reactions occurring are:



The time behavior of the OH concentration was modeled. Neglecting diffusion effects upon the signal and the possible effects of N_2O photodissociation, the important reactions in a mixture of H_2S and N_2O irradiated at 193 are the following:



The solution to this set of equations yields the following equation for the time dependence of OH concentration:

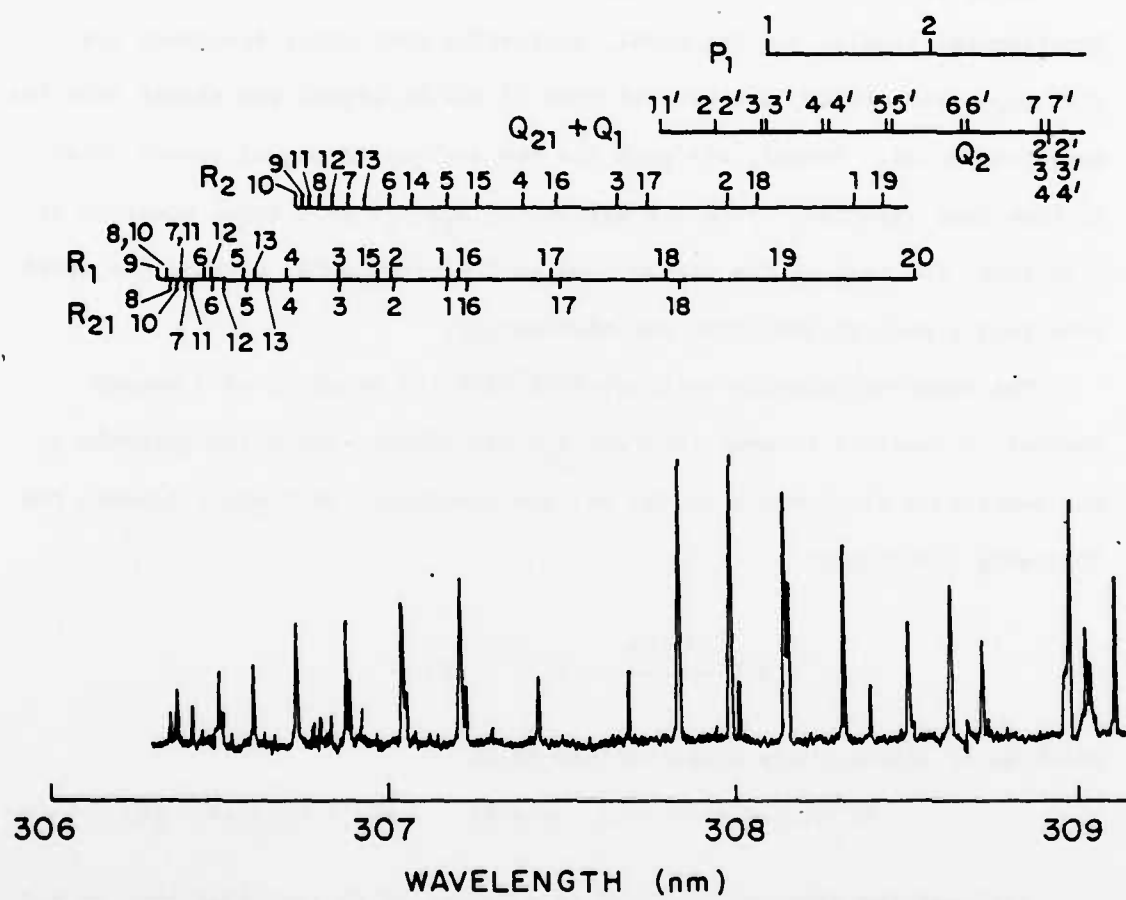
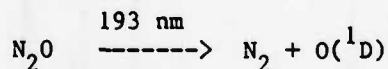


Figure 2

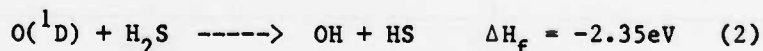
$$[\text{OH}]_t = \frac{k_{1a}[\text{H}^*]_0[\text{N}_2\text{O}]}{(k_{1a}+k_{1b}+k_4)[\text{N}_2\text{O}]+(k_2-k_3)[\text{H}_2\text{S}]} \left(e^{-k_3[\text{H}_2\text{S}]t} - e^{-((k_{1a}+k_{1b}+k_4)[\text{N}_2\text{O}]+k_2[\text{H}_2\text{S}])t} \right)$$

Using this model, several major differences were observed between the experimental results and the model, indicating that other reactions are also important. First, the rate of rise of the OH signal was slower than the model predicted. Second, the peak for the maximum OH signal occurs later in time than expected. In a 1:1 mixture of $\text{H}_2\text{S}:\text{N}_2\text{O}$ at a total pressure of 0.50 torr, the peak of the signal came at 3 microseconds, whereas the model predicted a peak at less than one microsecond.

The observed behavior is consistent with the presence of a second channel. A feasible channel involves N_2O absorption, since the molecule is not completely transparent at 193 nm, and undergoes, to a small extent, the following photolysis:



which would subsequently react to form OH by



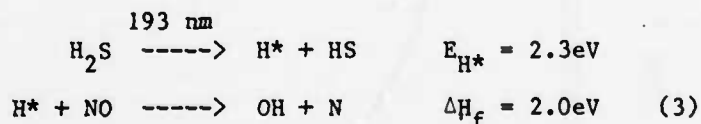
Although the absorption of N_2O is a factor of 80 less than that of H_2S at 193 nm, it appears to compete with the hot atom channel 1. The presence of this $\text{O}(^1\text{D})$ channel was confirmed through the observation of OH from a $\text{N}_2\text{O}/\text{CH}_4$ mixture, again photolyzed at 193 nm and probed for OH at 308 nm. Since CH_4 has no absorption at 193 nm, it cannot contribute any hydrogen atoms, and the signal is clearly from N_2O photodissociation.

Attempts were made to mitigate the effects of this second channel. First, the ratio of H_2S to N_2O was increased to emphasize the hot atom

channel. However, the undesired $O(^1D)$ channel could not be completely eliminated. Another way to minimize the competing reaction of channel 2 is to take advantage of the different quenching rates of H^* and $O(^1D)$ with the various rare gases. It has been demonstrated, for example, that the hot hydrogen atoms are easily quenched by the addition of helium.⁽⁴⁾ However, due to the size mismatch between xenon and hydrogen, xenon is much less efficient at thermalizing the hydrogen, whereas it is efficient (taking approximately one collision) at quenching $O(^1D)$ to $O(^3P)$. Since $O(^3P)$ has insufficient energy to react with H_2S to form OH, this should effectively remove channel 2 for OH production. However, the relative concentrations of xenon to the other gases must be high enough to completely quench the $O(^1D)$, but low enough to avoid cooling down the hot hydrogen atoms. Initial experiments suggest that this technique will indeed clear up the two-channel competition.

b) NO experiments

Mixtures of H_2S/NO also produce observable concentrations of OH. In this case, the presumed OH, hot-atom channel is



Results indicate that this is not the only reaction. In fact, the above reactive system is only slightly exothermic, so that if some energy is lost in other modes, the reaction will not occur. Also arguing against this channel are results which show a slow rise time of the OH signal and a late time for peak levels of OH intensity, as shown in the delay curve in Figure 3. When this system was modeled, a peak of under one microsecond was

AD-A142 209

RESEARCH INVESTIGATION DIRECTED TOWARD EXTENDING THE
USEFUL RANGE OF THE ELECTROMAGNETIC SPECTRUM(U)

3/3

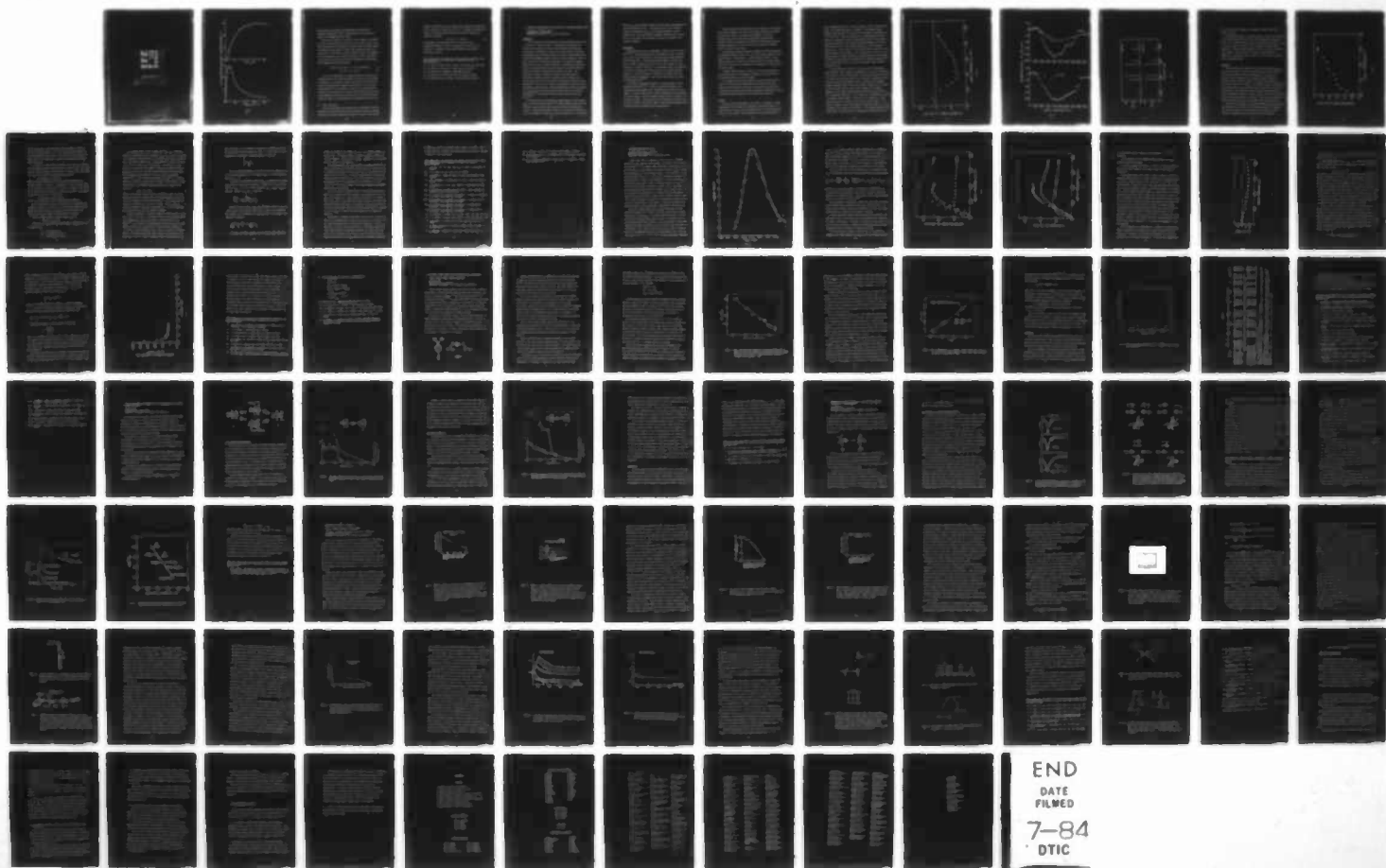
UNCLASSIFIED

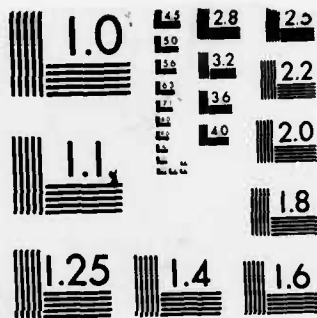
COLUMBIA RADIATION LAB NEW YORK G W FLYNN 31 MAY 84

DAAG29-82-K-0080

F/G 20/3

NL





MICROCOPY RESOLUTION TEST CHART
NATIONAL BUREAU OF STANDARDS-1963-A

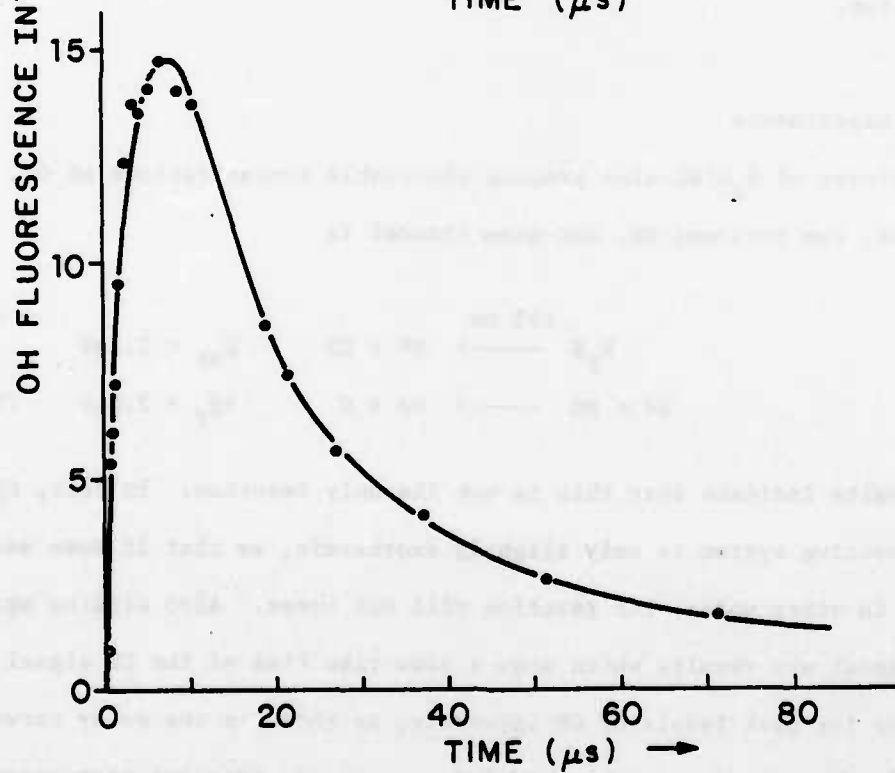
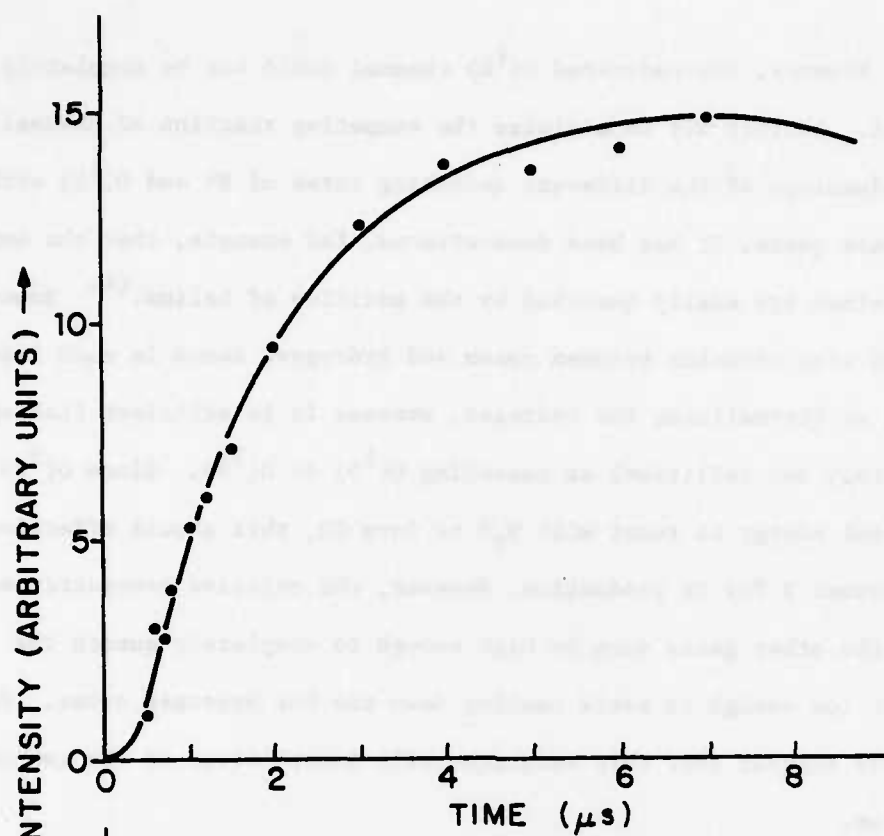
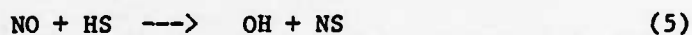
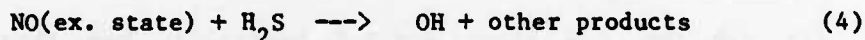


Figure 3

again predicted. In addition, high overpressures of helium do not completely extinguish the signal, indicating that at least some of the signal is not dependent upon hot H atoms.

The source of the OH is not yet clear. NO does absorb to some extent at 193 nm, but the absorption is down by a factor of 200 from that of H₂S. With the absorption of 193 radiation, NO has just under the energy required to dissociate, thus placing it in either high vibrational levels of the ground state, or more likely, in excited electronic states. The dependence of the OH concentration upon excimer laser power is linear, showing that only one species in the reaction mixture has absorbed the excimer energy. The following reactions are conceivable:

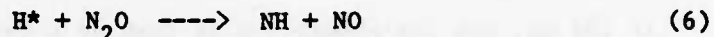


A new line of experiments is in progress which should elucidate the involvement of NO. Since the NO absorption is discrete at 193 nm instead of continuous, it is possible to remove the parts of the laser line which the NO can absorb before it reaches the reaction cell. If a cell with a high concentration of NO is placed in the path of the excimer before the reaction cell, then this will selectively remove any portions of the laser line absorbed by NO, and only the portions of the laser line which cannot absorb will remain. This should remove any NO absorption in the reaction.

c) Future experiments

There are many molecules which should react with hydrogen to form OH. Indeed OH is an attractive species for monitoring by LIF due to its strong absorption and extensive spectroscopic data base. However, other suitable

radicals and molecules can also be probed, since information on them exists as well, though not as extensively as for OH. For example, studying the NH channel in the $\text{H}_2\text{S}/\text{N}_2\text{O}$ system mentioned in the modeled scheme above is energetically possible:



One advantage of this NH channel is that it should be free of complicating channels since there is rigorously only one route to NH production. In addition, NH can be easily probed by laser-induced fluorescence at 336 nm.

*This research was also supported by the National Science Foundation under Grant CHE-80-23747 and the Department of Energy under Contract DE-AC02-78ER-04940.

- (1) J.O. Chu, G.W. Flynn, and R.E. Weston, J. Chem. Phys. 78, 2990 (1983).
- (2) C.A. Wight and S.R. Leone, J. Chem. Phys. 79, 4823 (1983).
- (3) R.N. Zare and P.J. Dagdigan, Science 185, 739 (1974).
- (4) C.R. Quick and J.J. Tise, Chem. Phys. Lett. 100, 223 (1983).
- (5) K. Kleinternann and J. Wolfrum, J. Chem. Phys. 80, 1446 (1984).

G. VIBRATIONAL PREDISSOCIATION OF SF_6 CLUSTERS IN A SUPERSONIC MOLECULAR BEAM*

(G. Spector, B. Brady, G. Flynn)

(JSEP work unit 7, 1982-1985)

(Principal Investigator: G. W. Flynn (212) 280-4162)

Introduction

Cluster formation in molecular beams of various species has been a source of interest for a number of years.⁽¹⁾ Spectroscopists, dynamicists and theorists have studied Van der Waal's molecules using varied techniques. Unfortunately, the detection of clusters in molecular beams is not always a straightforward task. Many weakly bound Van der Waal's species dissociate in the electron-bombardment ionization region of a mass spectrometer. Thus, the major fraction of the clusters may be detected at the monomer or fragment masses, with no clue as to their original size. Although some signal may be detected at the parent cluster mass, such peaks do not provide an absolute measure of the amount of that particular cluster in the beam. Mass spectrometry, therefore, provides only limited information about the distribution of various clusters in a molecular beam. Similarly, flux detection has been found to be inaccurate in calculating the absolute cluster percentage.⁽²⁾ Thus, the use of lasers to predissociate clusters has become an alternative method of study. Vibrational predissociation has been observed with visible lasers in the electronically excited states of Van der Waal's molecules⁽³⁾⁻⁽⁵⁾ and IR lasers can induce predissociation in the ground state.^{(6),(7)}

Our previous work was concerned with the measurement of internal energy (E_{int}) in a molecular beam of SF_6 .⁽⁸⁾⁻⁽¹⁰⁾ Using a bolometer, mass filter and flux meter, E_{int} at various laser and thermal excitation conditions was obtained. An isenthalpic expansion equation for conservation of enthalpy in a free jet was employed to predict E_{int} from time-of-flight data. The predicted

values of E_{int} were considerably larger than those measured experimentally at high nozzle temperatures (T_{nz}). One concern was that cluster formation affected the measurement of E_{int} in the thermal experiments. The data presented here, taken under similar experimental conditions, give a clearer idea as to the interaction and possible interference of clusters in the previous experiments.

Experimental

The technique used in these experiments is similar to that of Scoles et. al. (11)-(14). A molecular beam of SF_6 is intersected at 90° by a low power, cw CO_2 laser in the collisionless or near-collisionless regime downstream from the nozzle exit. A liquid helium cooled bolometer on the beam axis detects changes in energy flux with and without laser irradiation (lock-in detection). If clusters dissociate in a collisionless regime, the probability is high that the fragments will leave the beam axis, reducing the number density, n , of the beam molecules. Therefore, the bolometer signal will decrease with laser irradiation. Such an effect has been seen in SF_6 with mass spectrometry. (15)-(17)

The molecular beam apparatus employed in these experiments has been described previously. (8), (10) In brief, the apparatus consists of four differentially pumped chambers with a supersonic nozzle source in the first chamber. The third chamber houses an electron-bombardment ionizer-quadrupole mass filter assembly. The fourth chamber contains either the bolometer or an ion gauge flux meter. The CO_2 laser is used to irradiate the molecular beam at various locations in the source chamber. Several slight modifications have been made for these experiments and are described below.

1) Thermal experiments previously made use of heating tape to resistively heat the nozzle assembly. The nozzle is now heated conductively by heating the Monel oven to which it is attached using HOTWATTS. The present configuration allows for simultaneous laser/thermal experiments with excitation inside the capillary nozzle through the IR-transparent ZnSe plate. The heating experiments are thus restricted to low temperature increases ($<100^{\circ}\text{C}$) to protect the ZnSe plate.

2) The molecular beam was mechanically chopped as in earlier experiments. The modulated signal with laser on vs. laser off provided a measure of laser induced signal vs. beam intensity. In some experiments, however, a laser chopper, operating at ~ 100 Hz, was used (beam chopper off), giving a greater sensitivity and S/N ratio by eliminating the DC component of the signal due to the molecular beam.

3) Higher backing pressures (> 1000 torr), and thus better expansions have been achieved due to improvements in conductance of the gas line and improved pumping speed in the source chamber.

4) The range of irradiation positions of the laser has been extended to allow for irradiation farther downstream (2-3 mm) from the nozzle exit. Absolute positions along the nozzle axis, from the back of the capillary to the skimmer, were determined by aligning a HeNe laser collinearly with the CO_2 laser and observing the location of the focused visible laser spot.

Results

When a molecular beam impinges on the surface of a bolometer, a signal proportional to total energy flux is observed. The bolometer signal, W , is proportional to $n\langle v \rangle E_{\text{tot}}$, where n is number density, $\langle v \rangle$ is average velocity and E_{tot} is total energy. Laser irradiation of the SF_6 beam outside the

nozzle (downstream) was found to reduce this signal. Thus, the laser-induced change in the bolometer signal, W_L , is negative. The maximum "negative" bolometer signal was found to occur with laser irradiation 1-2 mm downstream of the nozzle exit. This can be compared to the maximum absorption of SF_6 monomer ~ 1 mm upstream of the exit, as determined earlier⁽⁹⁾ and confirmed in the present experiments. Fig. 1 shows the pressure dependence of the laser induced [P(16) 10.6 μm , 7.5 W] bolometer signal (W_L). With no backing pressure ($P_{\text{nz}} = 0$ torr), there is no laser-induced signal, indicating that the bolometer detects no laser scatter. At low pressures (< 150 torr), the laser enhanced signal is positive, indicating a probable absorption by SF_6 monomer, as observed in early studies of SF_6 under similar experimental conditions.⁽⁸⁾ As P_{nz} increases above 150 torr, the laser "enhancement" becomes negative, peaking at 400 torr.

As P_{nz} increases above 400 torr, the absolute value of the negative signal decreases. Fig. 2 depicts the parameters, W_L vs P_{nz} , for the different laser lines P(12), P(16), P(20) and P(24). All the laser lines had a power of 7.5W except P(12) which had a power of 6W. The graph is normalized for power. As the laser probes IR wavelengths further to the red of the fundamental monomer IR absorption band, the peak in the negative signal occurs at higher P_{nz} and the positive signal at low pressure disappears. The pressure dependence of the negative bolometer signal becomes broad and diffuse with P(24) irradiation, while P(12), a laser line blue of the fundamental, produces a much smaller negative signal. The CO_2 laser line dependence of the SF_6 bolometer signal at a) 400 torr and b) 700 torr is shown in Fig. 3. Also shown for comparison is the room temperature absorption spectrum (---) of the fundamental of SF_6 , adapted from reference 10. The negative bolometer signal clearly shows a red shift from the room temperature absorption spectrum of

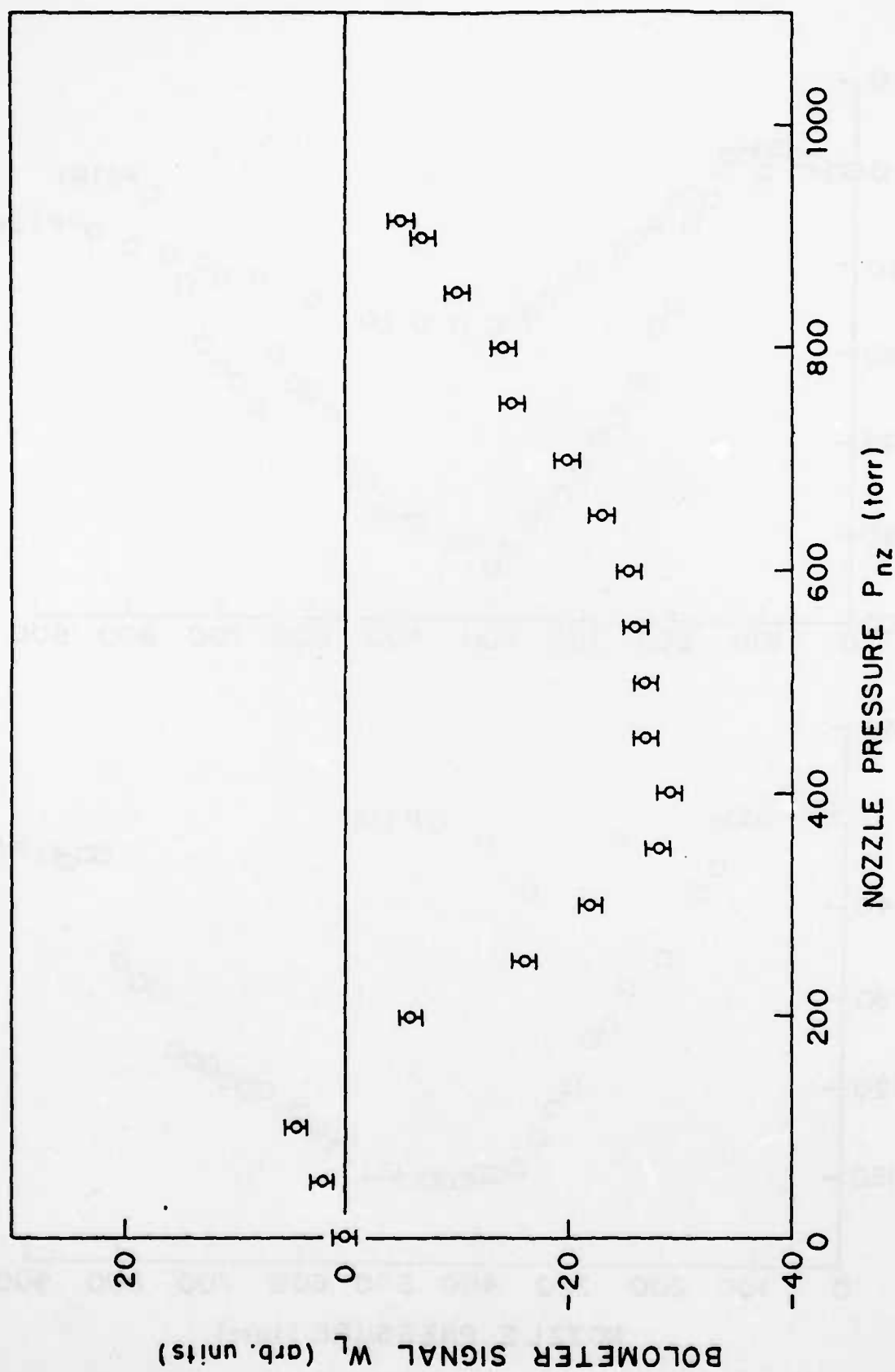


Figure 1

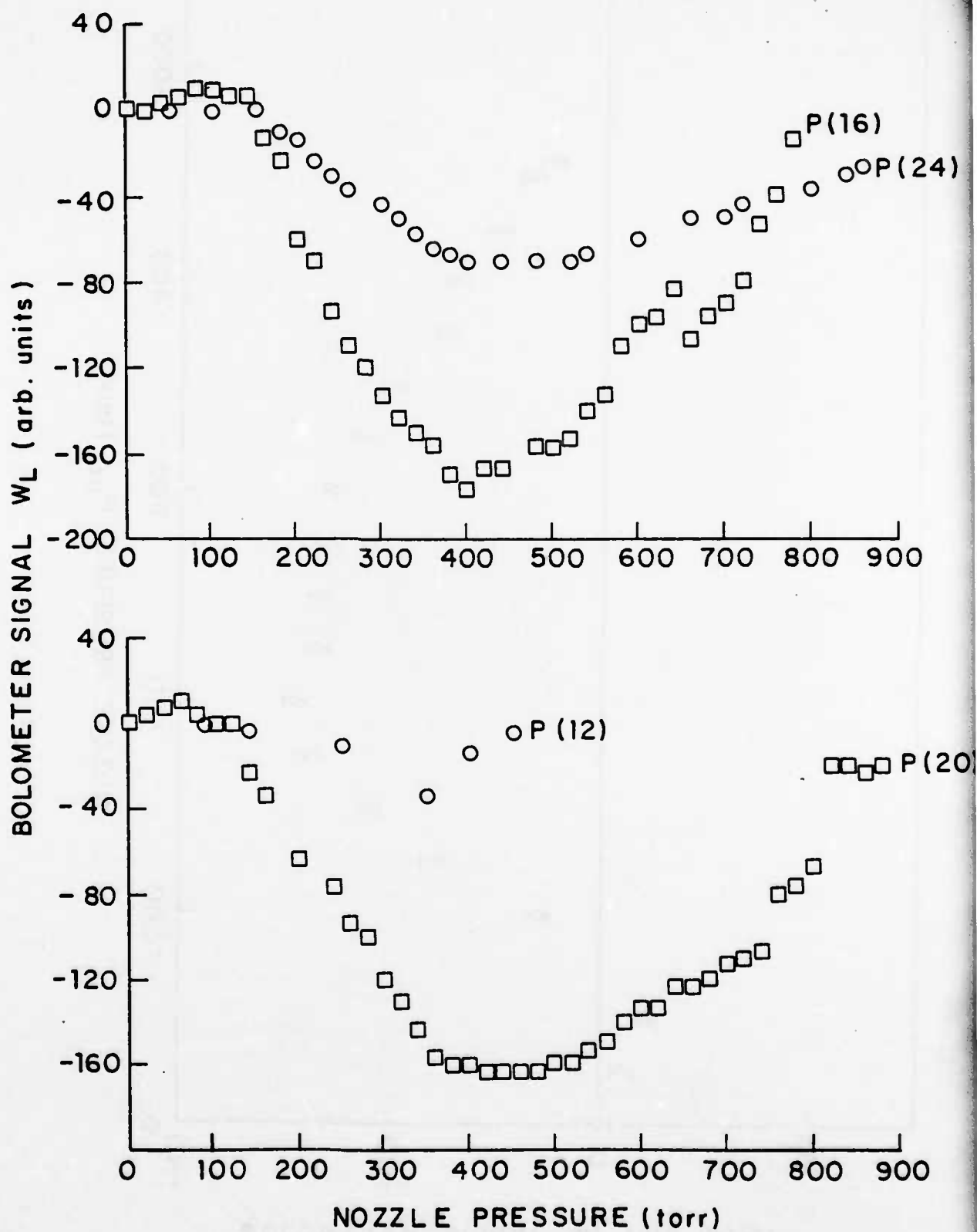


Figure 2

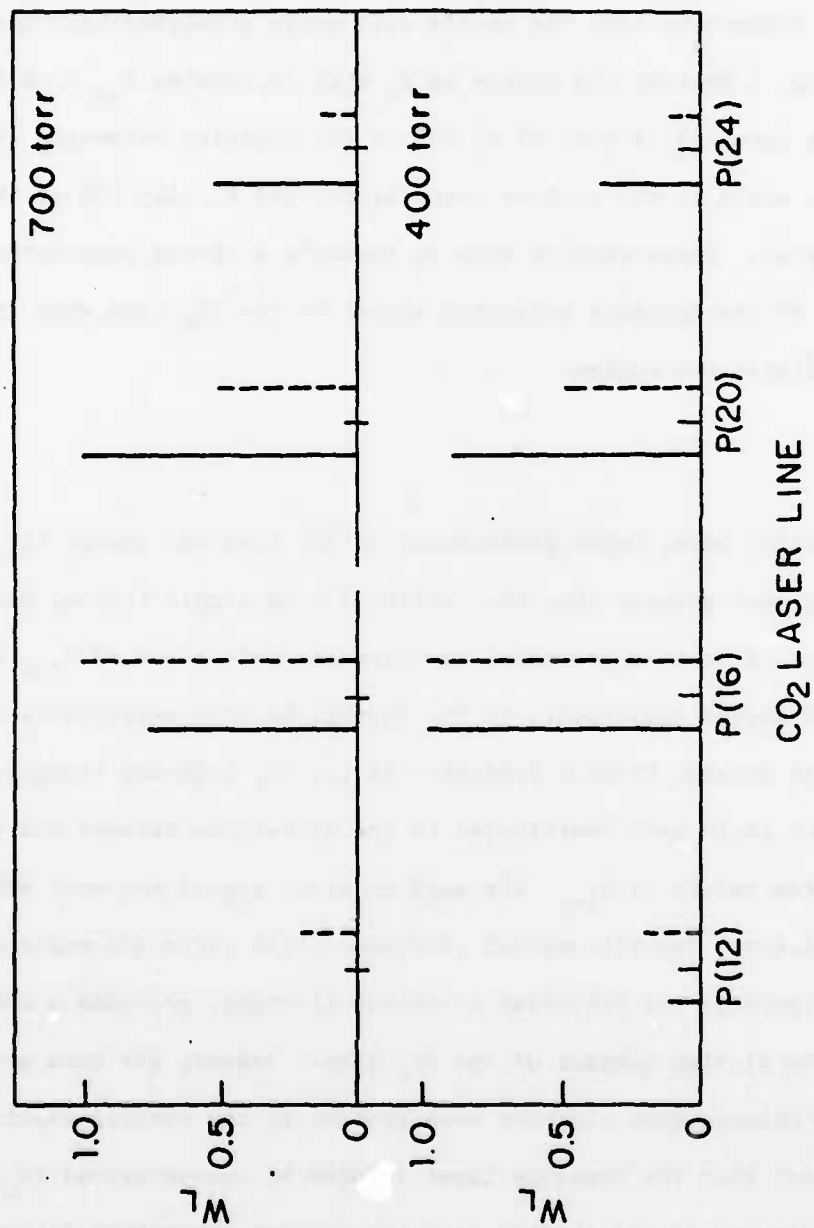


Figure 3

SF_6 . In addition, with higher P_{nz} , the negative bolometer signal shifts further to the red.

In a separate experiment, the SF_6 beam with $P_{\text{nz}} = 400$ torr was irradiated with P(16) downstream from the nozzle exit while simultaneously heating the nozzle. Fig. 4 depicts the change in W_L with increasing T_{nz} from 292 K to 353 K. With an increase of only 25 K, 50% of the negative bolometer signal disappears, while at the maximum temperature, 353 K, only 10% of the negative signal remains. These results seem to indicate a strong temperature dependence of the negative bolometer signal in the SF_6 beam when irradiating in the collisionless regime.

Discussion

In earlier work, laser enhancement of SF_6 internal energy (E_{int}) was found to be much greater than that obtained from simple thermal heating.⁽¹⁰⁾ The discrepancy between predicted and experimental values of E_{int} as a function of nozzle temperature in the thermal heating experiments was discussed in detail. Cluster formation in the SF_6 beam was recognized as a factor which could have contributed to the difference between the experimental and predicted values of E_{int} , although no dimer signal was ever detected by the mass filter. The vibrational predissociation technique employed here, which incorporates the bolometer to detect clusters, provides a more sensitive probe of the cluster content of the SF_6 beam. Indeed, the data presented in this work indicate that clusters were present in the earlier experiments.

The fact that the negative laser induced bolometer signal (W_L) increases with pressure and is red shifted from the monomer absorption is consistent with a signal arising from the predissociation of clusters in the beam. Similarly, increasing the nozzle temperature reduces the negative

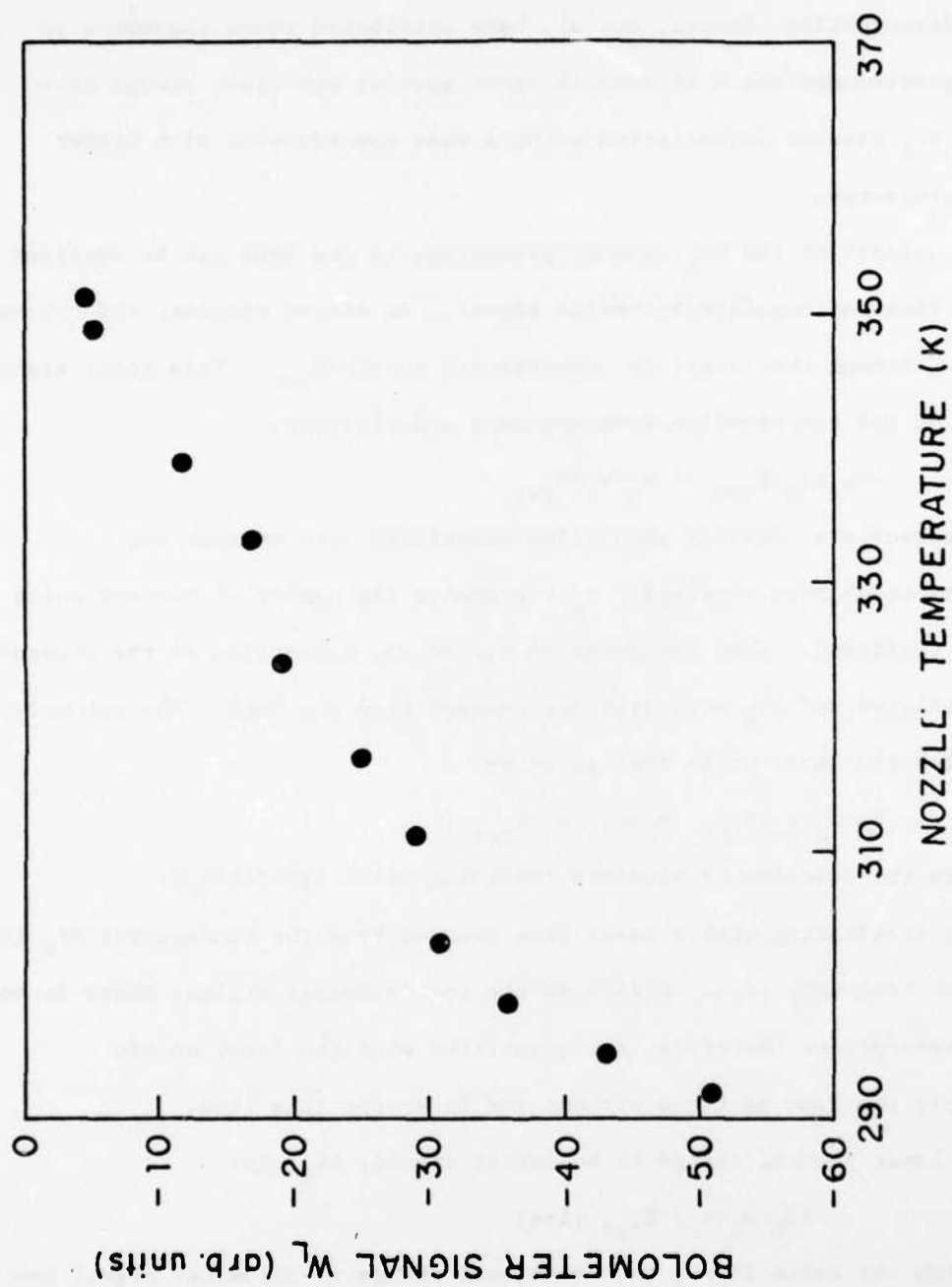


Figure 4

laser-induced signal, another indication that this signal is related to cluster dissociation. Scoles, et. al. have attributed these phenomena to cluster predissociation with several other species and other groups have detected SF_6 cluster dissociation using a mass spectrometer with higher backing pressures.

An estimate of the SF_6 cluster percentage in the beam can be obtained from the observed negative bolometer signal. As stated earlier, the bolometer signal W (without the laser) is proportional to $n\langle v \rangle E_{\text{tot}}$. This total signal is a sum of the contribution from monomers and clusters.

$$W \propto n_m \langle v_m \rangle E_{\text{tot}_m} + n_c \langle v_c \rangle E_{\text{tot}_c} \quad (1)$$

where m subscripts identify quantities associated with monomer and c subscripts those with clusters. n_c represents the number of monomer units that are clustered. When the laser is turned on, a fraction of the clusters are dissociated and SF_6 molecules are removed from the beam. The bolometer signal with the laser on is then given by

$$W_L \propto n_m \langle v_m \rangle E_{\text{tot}_m} + a[n_c \langle v_c \rangle E_{\text{tot}_c}] \quad (2)$$

where a is the fraction of clusters remaining after irradiation.

When irradiating with a laser line removed from the fundamental SF_6 IR transition frequency (i.e., $P(24)$) in the collisionless regime, there is no monomer absorption; therefore, the quantities with the laser on are effectively the same as those without the laser for this line.

The laser induced change in bolometer signal, ΔW_L , is:

$$\Delta W_L \propto n_c \langle v_c \rangle E_{\text{tot}_c} [1-a] \quad (3)$$

Taking the ratio $\Delta W_L/W$, the fractional change in bolometer signal due to the laser, gives:

$$\frac{\Delta W_L}{W} = \frac{n_c \langle v_c \rangle E_{\text{tot}_c} [1-a]}{n_m \langle v_m \rangle E_{\text{tot}_m} + n_c \langle v_c \rangle E_{\text{tot}_c}} \quad (4)$$

In a molecular beam, it can be assumed that $\langle v_m \rangle = \langle v_c \rangle$. The total energy can be separated into its components, $E_{\text{tot}} = E_{\text{kin}} + E_{\text{int}} + E_a$, where E_a is the adsorption energy imparted to the bolometer surface upon SF_6 condensation. The kinetic energies, E_{kin} , per SF_6 monomer are the same, since $\langle v_m \rangle = \langle v_c \rangle$ (i.e., for a dimer, $E_{\text{kin}_d} = 2n_c \langle v_c \rangle E_{\text{kin}_m}$). The sum $E_{\text{int}} + E_a$ for a cluster is less than that for a monomer. Clusters are unlikely to have as much E_{int} per molecule as a monomer, because the weak Van der Waal's bond would be expected to predissociate at the E_{int} found in the average monomer.⁽¹⁰⁾ E_a , which has been approximated by $-H_{\text{vap}}$ ^{(8),(10)} in previous work must be less for a cluster than for a monomer. Since energy is a state function, $E_a(c)$, the adsorption energy per molecule in a cluster can be written as

$$E_a(c) = E_a - D_0/i \quad (5)$$

where i is the number of monomer units in a particular cluster, E_a is the adsorption energy for a monomer and D_0 is the energy required to dissociate the cluster completely to its monomer components. It can be seen that the average E_a per monomer unit is less for a cluster. Thus, $E_{\text{tot}_c}/E_{\text{tot}_m} < 1$. If all of the clusters in the beam are predissociated, $a = 0$ and an expression can be derived for the ratio of clusters to monomers.

The Rabi frequency for a transition pumped by a coherent source is given by $\omega = \mu E/\hbar$. In our case ω , the transition dipole for the cluster absorption can be approximated by that of the monomer ν_3 absorption which is 0.4 debye.⁽¹⁸⁾ E is the electric field strength calculated from the laser power density, 10^4 W/cm^2 , as 1.8 statvolts/cm. This gives a Rabi frequency of $7.2 \times 10^8 \text{ Hz}$. The beam diameter is about 1 mm and the speed of the beam is 362 m/s. This means the absorbing cluster spends 2.7 microseconds in the laser field. As this is orders of magnitude greater than the time for one

Rabi oscillation it can be assumed the transition is saturated and all the clusters present have been dissociated. Thus, $a = 0$ and a lower limit can be established for the number of clustered monomers in the beam:

$$\frac{n_c}{n_m} > \frac{1}{\frac{W}{\Delta W_L} - 1} \quad (6)$$

The ratio $\Delta W_L/W$ was measured to be 0.18 at 400 torr by comparing the size of the laser-induced effect on the bolometer signal to the total beam signal.

Thus, $n_c/n_m > .22$.

It has been stated previously that the E_{kin_c} per molecule is the same as E_{kin_m} since the velocities are equivalent. A lower limit on E_{tot_c} would occur when $E_{a_c} + E_{int_c} = 0$. Thus, at these conditions, $E_{tot_c} = E_{kin_c} = E_{kin_m}$ per molecule. The ratio E_{tot_c}/E_{tot_m} is given by

$$\frac{E_{tot_c}}{E_{tot_m}} \geq \frac{E_{kin_m}}{E_{kin_m} + E_{int_m} + E_{a_m}} \quad (7)$$

Using the values for E_{kin_m} , E_{int_m} , E_{a_m} determined in Ref. 10, $E_{tot_c}/E_{tot_m} > .303$. From the above ratio, an upper limit on n_c/n_m can be established.

When combined with the expression for the lower limit, the following boundary conditions are defined:

$$\left(\frac{1}{\frac{W}{\Delta W_L} - 1} \right) < \frac{n_c}{n_m} \leq 3.3 \left(\frac{1}{\frac{W}{\Delta W_L} - 1} \right) \quad (8)$$

If we make the further assumption that no clusters higher than dimer are

present in the beam, we can convert the fraction of clustered monomers into a percent dimer. The number of dimers, n_d , would be one-half the number of clustered monomers. Therefore, $10\% < \frac{n_d}{n_d + n_m} = \frac{n_c/2}{n_c/2 + n_m} < 26\%$ and the beam contains between 10% and 26% dimer.

The backing pressure, P_{nz} , in the previous SF_6 experiments was 200 torr. Cluster formation in a molecular beam increases with P_{nz} ; thus fewer clusters are expected in the beam at 200 torr than at 400 torr, in agreement with the trends in the data of Fig. 1. In the earlier experiments, the isenthalpic expansion equation predicted $E_{int} = 1.15 \times 10^{-20}$ J molec⁻¹ at 290 K, within experimental error of the E_{int} measured by the bolometer, 0.97×10^{-21} J molec⁻¹.⁽¹⁰⁾ As the T_{nz} increased, the discrepancy between experimental and predicted E_{int} also increased.

Since the isenthalpic expansion equation was experimentally verified at 290 K, it is apparent that cluster formation in the beam did not affect the E_{int} at that temperature. Cluster formation could account for a measured value of E_{int} that is lower than the true value, because, as discussed above, clusters may deliver less energy to the bolometer as E_{int} and E_a are smaller for clusters than monomers. Energy conservation, however makes it impossible for the true E_{int} to be greater than that predicted by the isenthalpic expansion.

Since there is a maximum of 26% dimers at 400 torr, Fig. 1 shows that at 200 torr, the maximum percent of dimers is only about 4%. At 400 torr, 90% of the clusters disappear with an 80 K increase in temperature. At 520 K, the highest T_{nz} achieved in previous experiments, it is extremely doubtful that the SF_6 beam contained any significant percentage of clusters. As noted above, the 4% of clusters at $P_{nz} = 200$ torr, $T_{nz} = 290$ K did not cause a significant deviation from the E_{int} predicted by the isenthalpic expansion.

At higher T_{nz} , there are considerably fewer clusters in the beam. Thus, the internal energy is not likely to have been affected in any way by the presence of clusters at high temperatures.

*This research was also supported by the National Science Foundation under Grant CHE-80-23747 and the Department of Energy under contract DE-AC-02-78ER04940.

- (1) D. H. Levy, Ann. Rev. Phys. Chem. 31, 197 (1980) and references cited therein.
- (2) W. R. Gentry, Rev. Sci. Instr. 53, 1492 (1982).
- (3) C. Parmenter, J. Phys. Chem. 86, 1735 (1982) and references cited therein.
- (4) D. V. Brumbaugh, J. E. Kenny, and D. H. Levy, J. Chem. Phys. 78, 3415 (1983).
- (5) R. E. Smalley, D. H. Levy, and L. Wharton, J. Chem. Phys. 64, 3266 (1976).
- (6) M. Hoffbauer, C. F. Giese, and W. R. Gentry, J. Phys. Chem. 88, 181 (1984) and references cited therein.
- (7) M. F. Vernon, D. J. Krajnovich, H. S. Kwok, J. M. Lisy, Y. R. Shen, and Y. T. Lee, J. Chem. Phys. 77, 47 (1982).
- (8) D. R. Coulter, F. R. Grabiner, L. M. Casson, G. W. Flynn, and R. B. Bernstein, J. Chem. Phys. 73, 281 (1980).
- (9) M. I. Lester, D. R. Coulter, L. M. Casson, G. W. Flynn, and R. B. Bernstein, J. Phys. Chem. 85, 751 (1981).
- (10) M. I. Lester, L. M. Casson, G. B. Spector, G. W. Flynn, and R. B. Bernstein, J. Chem. Phys. 80, 1490 (1984).
- (11) T. E. Gough, R. E. Miller, and G. Scoles, J. Chem. Phys. 69, 1588 (1978).
- (12) T. E. Gough, R. E. Miller, and G. Scoles, J. Phys. Chem. 85, 4041 (1981).
- (13) T. E. Gough, R. E. Miller, and G. Scoles, Chem. Phys. Lett. 97, 155 (1983).
- (14) D. Bassi, A. Boschetti, G. Scoles, M. Scotoni, and M. Zen, Chem. Phys. 71, 239 (1982).
- (15) J. Geraedts, S. Setiadi, S. Stolte, and J. Reuss, Chem. Phys. Lett. 78, 277 (1981).

- (16) J. Geraedts, S. Stolte, and J. Reuss, Z. Phys. 304A, 170 (1982).
- (17) P. Melinon, R. Monot, J. M. Zellweger, and H. Van der Bergh, Chem. Phys. 84, 345 (1984).
- (18) C. C. Jensen, T. G. Anderson, C. Reiser, and J. I. Steinfeld, J. Chem. Phys. 71, 3648 (1979).

H. A MOLECULAR BEAM STUDY OF C_4F_8 *

(G. Spector, B. Brady, G. W. Flynn)

(JSEP work unit 7, 1982-1985)

(Principal Investigator: G. W. Flynn (212) 280-4162)

In early 1983, work was completed on a study of laser vs. thermal excitation of SF_6 supersonic molecular beams, the results of which have since been published.⁽¹⁾ The bolometric/mass spectrometric technique used to study internal energy was then extended to octafluorocyclobutane (C_4F_8), a molecule with considerably more internal energy than SF_6 . The IR absorption of C_4F_8 overlaps several transitions of the CO_2 laser, providing an opportunity to study the effect of internal energy enhancement at various wavelengths. Other investigators have studied a variety of physical properties of C_4F_8 ,⁽²⁾⁻⁽⁶⁾ but none of this research incorporated a molecular beam. Energy characterization experiments have been performed on beams of C_4F_8 , and the internal energy per C_4F_8 molecule was determined to be considerably lower than expected. We believe that cluster formation in beams of C_4F_8 prevents an accurate measure of the internal energy of this molecule, but simple models presented here can be used to estimate limits on that energy. In addition, experiments with molecular beams of CO_2 were performed to experimentally test the models.

The molecular beam apparatus used for these experiments has been described previously.⁽⁷⁾ In brief, a liquid He cooled bolometer measures energy flux, W ($W \propto n\langle v \rangle E_{tot}$), a flux meter measures beam flux, F ($F \propto n\langle v \rangle$), and a mass spectrometer measures number density, n , and average velocity, $\langle v \rangle$, using time-of-flight (TOF) techniques. From the TOF studies, translational energy distributions are obtained; thus, the internal energy can be determined by difference. Fig. 1 shows a typical TOF spectrum of C_4F_8 for a molecular beam at room temperature (290 K) and a backing pressure (P_{nz}) of 250 torr. The stream velocity is $v_g = 370$ m/s while the beam translational temperature

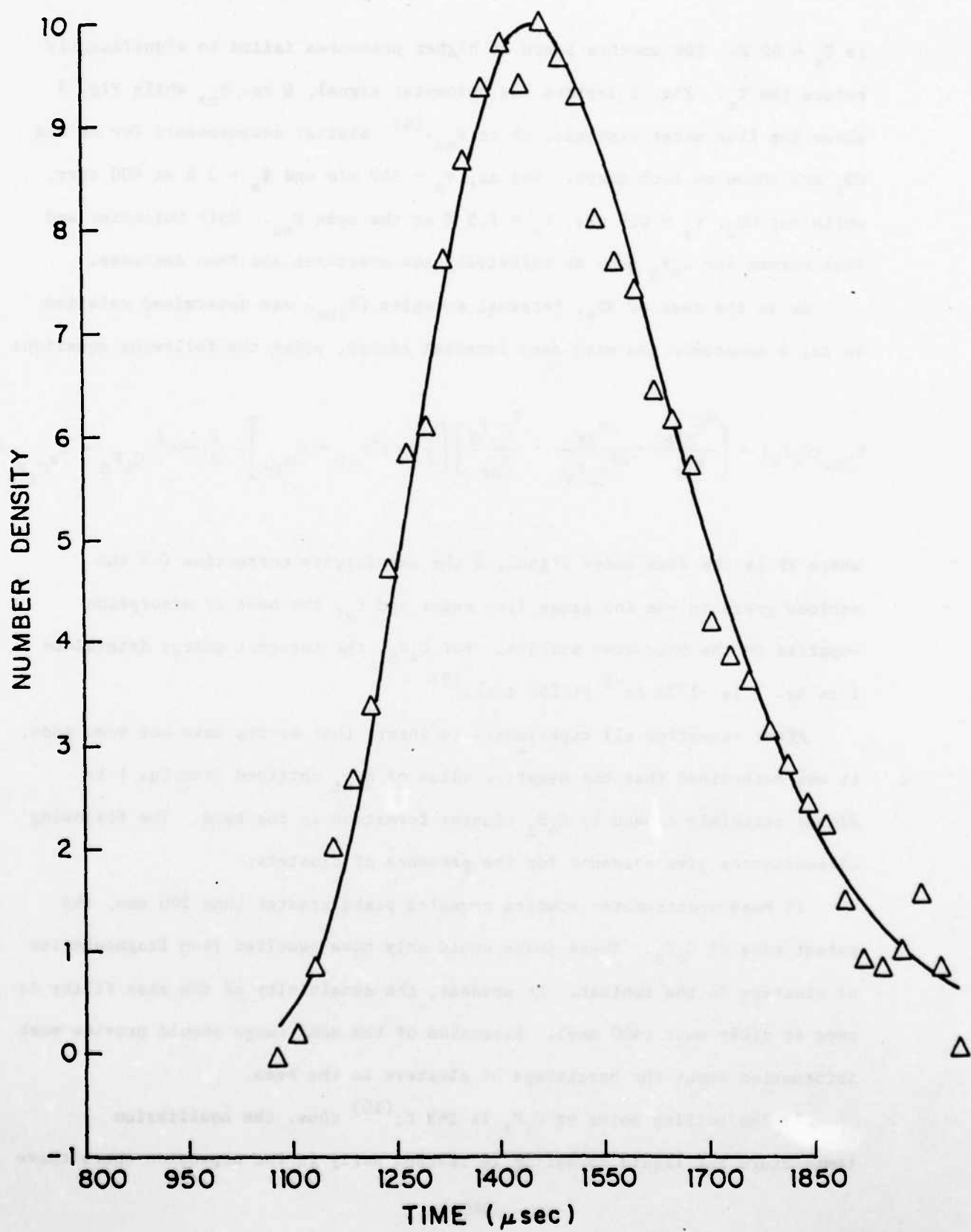


Figure 1
185

is $T_g = 60$ K. TOF spectra taken at higher pressures failed to significantly reduce the T_g . Fig. 2 depicts the bolometer signal, W vs. P_{nz} while Fig. 3 shows the flux meter response, ΔP to P_{nz} .⁽⁸⁾ Similar measurements for Ar and CO_2 are shown on each graph. For Ar, $v_g = 540$ m/s and $T_g = 3$ K at 400 torr, while for CO_2 , $v_g = 619$ m/s, $T_g = 7.5$ K at the same P_{nz} . Both bolometer and flux curves for C_4F_8 peak at relatively low pressures and then decrease.

As in the case of SF_6 , internal energies (E_{int}) are determined relative to Ar, a monatomic gas with zero internal energy, using the following equation:

$$E_{int}(C_4F_8) = \left[\frac{W_{C_4F_8}}{W_{Ar}} \cdot \frac{\Delta P_{Ar}}{\Delta P_{C_4F_8}} \cdot \frac{S_{C_4F_8}}{S_{Ar}} \right] \left[\frac{1}{2} m \langle v^2 \rangle_{Ar} + E_{a,Ar} \right] - \frac{1}{2} m \langle v^2 \rangle_{C_4F_8} - E_{a,C_4F_8} \quad (1)$$

where ΔP is the flux meter signal, S the sensitivity correction for the various gases in the ion gauge flux meter and E_a , the heat of adsorption imparted to the bolometer surface. For C_4F_8 , the internal energy determined from Eq. 1 is -1730 cm^{-1} at 250 torr.⁽⁹⁾

After repeating all experiments to insure that errors have not been made, it was determined that the negative value of E_{int} obtained from Eq. 1 is almost certainly caused by C_4F_8 cluster formation in the beam. The following circumstances give evidence for the presence of clusters:

1) Mass spectrometer studies revealed peaks greater than 200 amu, the parent mass of C_4F_8 . These peaks could only have resulted from fragmentation of clusters in the ionizer. At present, the sensitivity of the mass filter is poor at dimer mass (400 amu). Extension of the mass range should provide more information about the percentage of clusters in the beam.

2) The boiling point of C_4F_8 is 269 K;⁽¹⁰⁾ thus, the equilibrium temperature for liquid formation is reached early in the expansion where there

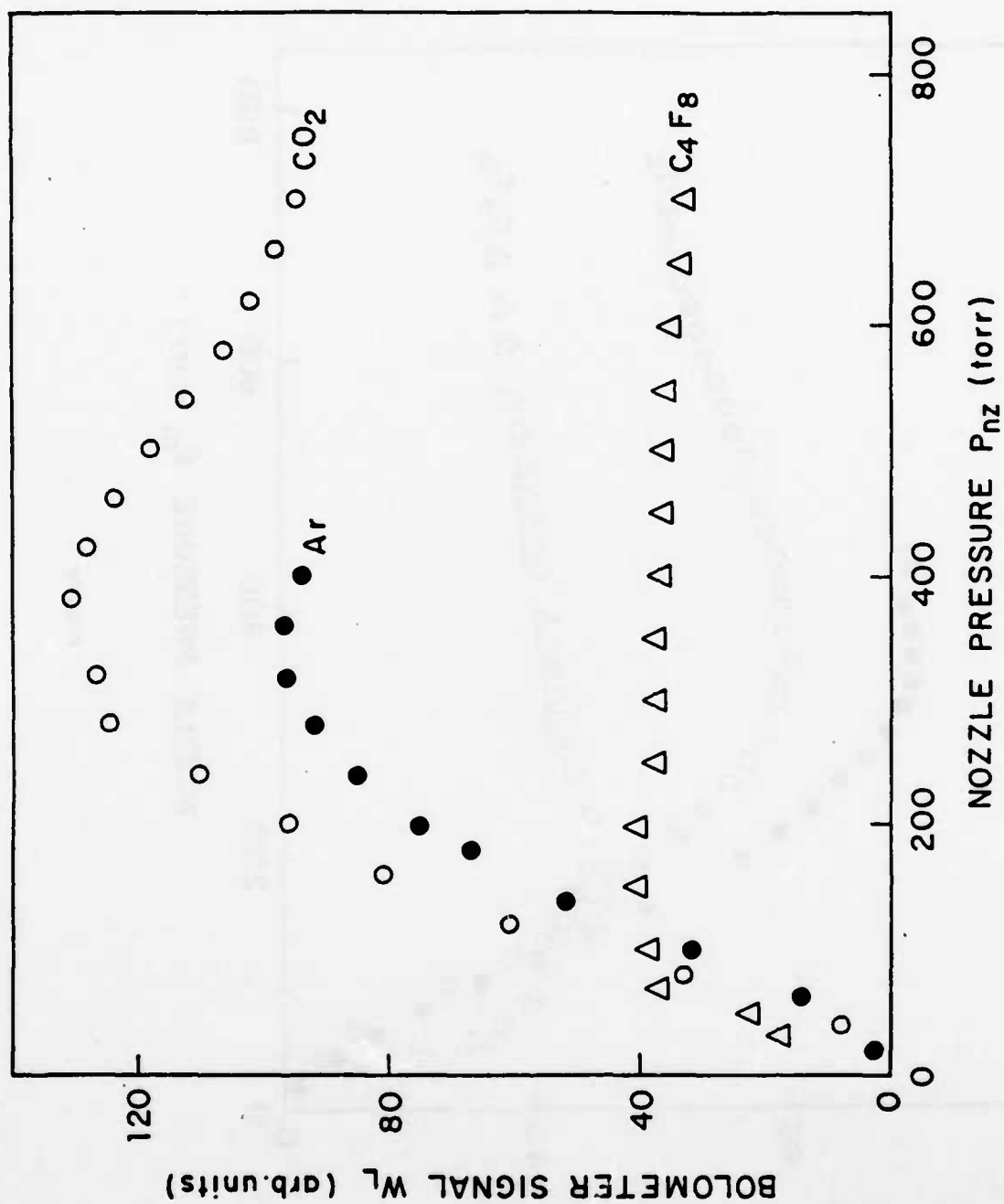


Figure 2

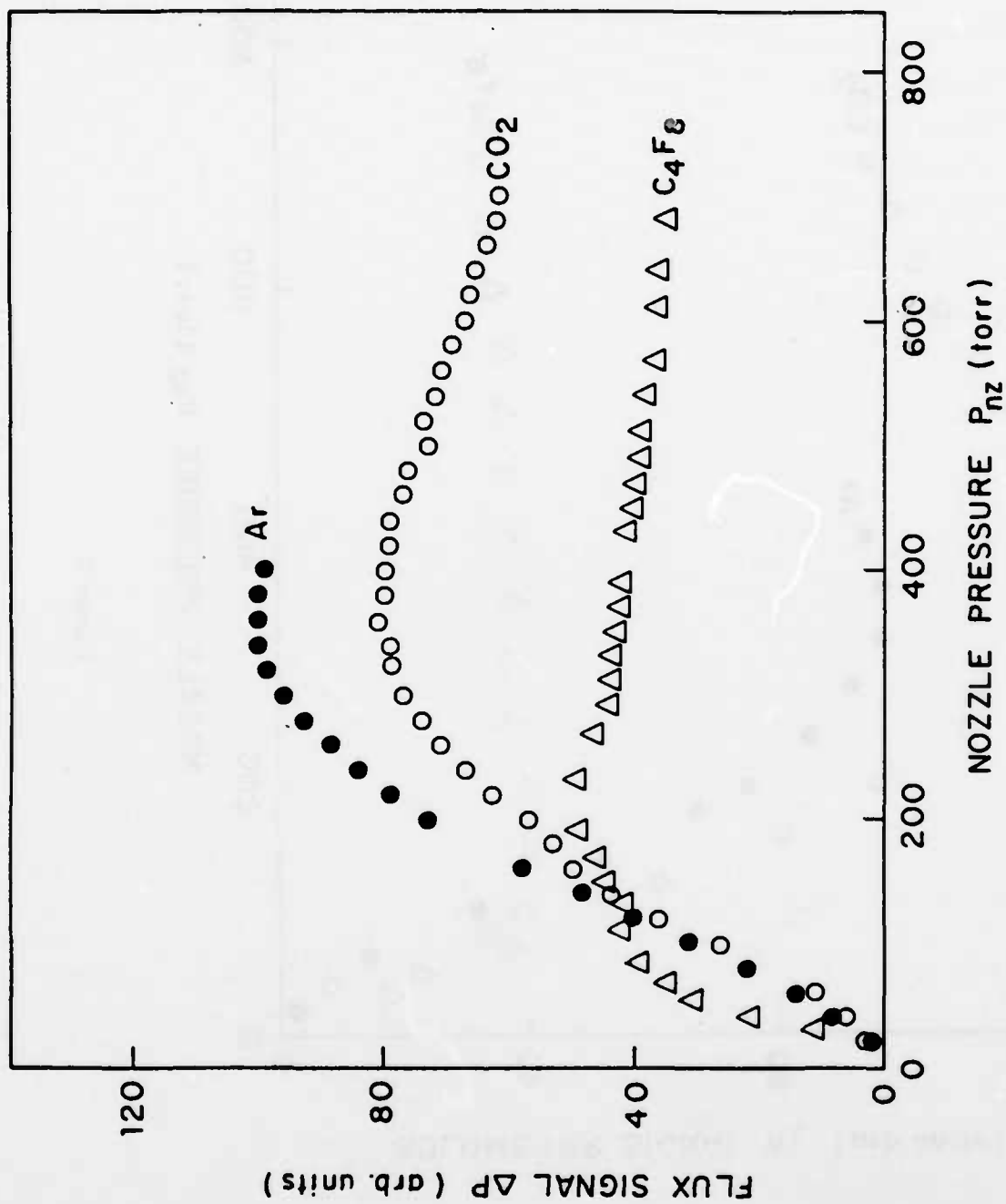


Figure 3

are still many collisions, leading to high condensability and cluster formation.

3) The beam will not cool translationally much below 60 K despite "extreme" expansion conditions.

4) The C_4F_8 potential well depth, ϵ , is 400 cm^{-1} ,⁽¹¹⁾ much the same as that for CO_2 , which is known to form clusters under similar expansion conditions.

5) In separate experiments, negative bolometer signal was observed by vibrational predissociation in the near-collisionless or collisionless region of the beam in a manner similar to that of Scoles, et. al.⁽¹²⁾⁻⁽¹⁴⁾ The molecular beam is crossed at 90° with a CO_2 laser downstream from the nozzle exit. Identical experiments using SF_6 are described elsewhere in this report. Fig. 4 shows the negative bolometer signal, W_L , resulting from loss of number density when dissociated cluster fragments leave the beam axis, graphed vs. P_{nz} . These results were obtained irradiating the beam with the R(10) line of the $10.6 \mu\text{m}$ branch, the laser line used for C_4F_8 absorption experiments.⁽¹⁵⁾ As the laser is "red" shifted toward the P branch, the negative signal increases significantly despite decreasing laser power. Unfortunately, the "red" shift of the spectrum due to cluster formation appears to be to wavelengths at which our CO_2 laser cannot be tuned, i.e. between the P and R branches. Therefore, we can conclude that there is cluster formation in the beam but cannot make a prediction as to the relative concentration of units above monomer.

Cluster formation in the beam makes Eq. 1 inaccurate for predicting E_{int} since it assumes that the bolometer and flux meter read number density identically. Certainly, the flux meter counts monomers, as all clusters hitting a hot wire filament will fragment. In contrast, what happens when a

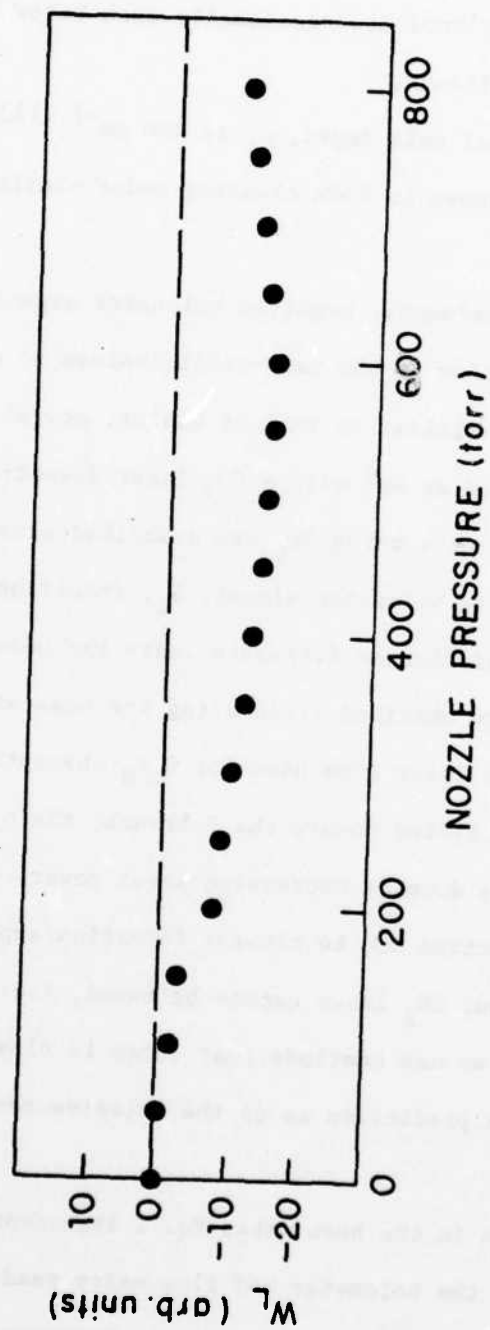


Figure 4

cluster hits a cold surface like a bolometer chip? Does it fragment? If so, how is the E_a affected?

To make some estimation of E_{int} , Eq. 1 was rewritten, since E_a for monomer C_4F_8 is not accurate for a clustered beam. Therefore, inserting W , S , P and $\langle v \rangle$ from the data,

$$E_{int} + E_a = 218 \text{ cm}^{-1} \quad (2)$$

where both E_{int} and E_a are unknown. The isenthalpic expansion equation for an ensemble of molecules exiting from a nozzle and forming a free jet used in our earlier studies⁽¹⁾ predicts $E_{int}(C_4F_8) = 1100 \text{ cm}^{-1}$ at 290 K. From Eq. 2, it is apparent that E_{int} must be considerably less. For C_4F_8 , $\epsilon = 400 \text{ cm}^{-1}$; if ϵ is taken to be the dimer bond energy (D_0), it indicates that the internal energy per C_4F_8 molecule in the dimer must be less than 200 cm^{-1} , or the dimer would dissociate. With higher order clusters, the problem compounds itself, predicting lower internal energies per C_4F_8 molecule. Thus, low E_{int} values are compatible with cluster formation in a beam. The missing internal energy has apparently relaxed into translational degrees of freedom.

For E_a , the heat of adsorption, the model is a bit more complicated. Because energy is a state function, it is path independent. Thus, the assumption can be made that when the cluster hits the bolometer surface it dissociates completely to monomers. If so, one can assume that n calculated from the bolometer is the same as n measured by the flux meter in Eq. 1, and all of the effect on bolometer signal due to clustering can be found in the E_a value. The bolometer equation can be rewritten as a sum of energies over various cluster sizes:

$$W \propto n \langle v \rangle E_{tot} = \sum_i (E_{kin} + E_{int} + E_a) n_i \langle v_i \rangle \quad (3)$$

where i represents the size of a cluster and E_{kin_i} , E_{int_i} and E_{a_i} represent, respectively, the translational, internal and adsorption energies per molecule in cluster size i . In a molecular beam, $E_{kin_c} = iE_{kin_m}$, since all molecules are effectively moving at the same speed ($\langle v_i \rangle = \langle v \rangle$). From earlier discussion, E_{int} is a small number in a large cluster. If E_{a_i} is the adsorption energy per molecule for cluster size i ,

$$E_{a_i} = E_{a_1} - D_0(i)/i \quad (4)$$

where D_0 is the energy required to dissociate the cluster to monomers.

If ϵ is taken to be the dimer dissociation energy, and if the number of bonds per cluster is determined from close-packed geometries, then

$$E_{a_i} = E_{a_1} - \epsilon/2 \quad (i=2); \quad E_{a_i} = E_{a_1} - \left(\frac{3i-6}{i}\right) \epsilon \quad (i > 2) \quad (5)$$

The bolometer measures an average adsorption energy, \bar{E}_a :

$$\bar{E}_a = \frac{\sum_{i=1}^{\infty} E_{a_i} n_i}{\sum_{i=1}^{\infty} n_i} \quad (6)$$

where n_i is the number of clusters of size i . Fig. 5 depicts \bar{E}_a as function of i , assuming n has a Gaussian distribution. It is apparent that if $\langle i \rangle > 6$, \bar{E}_a is less than $200 \text{ cm}^{-1}/\text{molecule}$ and that larger clusters would reduce \bar{E}_a to a very small value. Therefore, both E_a and E_{int} can be very small with cluster formation.

Experiments using CO_2 were run to determine if the models described here are valid. Mass spectra of CO_2 beams at 700 torr indicated that $(\text{CO}_2)_n$, $n = 1-9$ were present (the limit of our mass sweep is 400 amu at present). Thus,

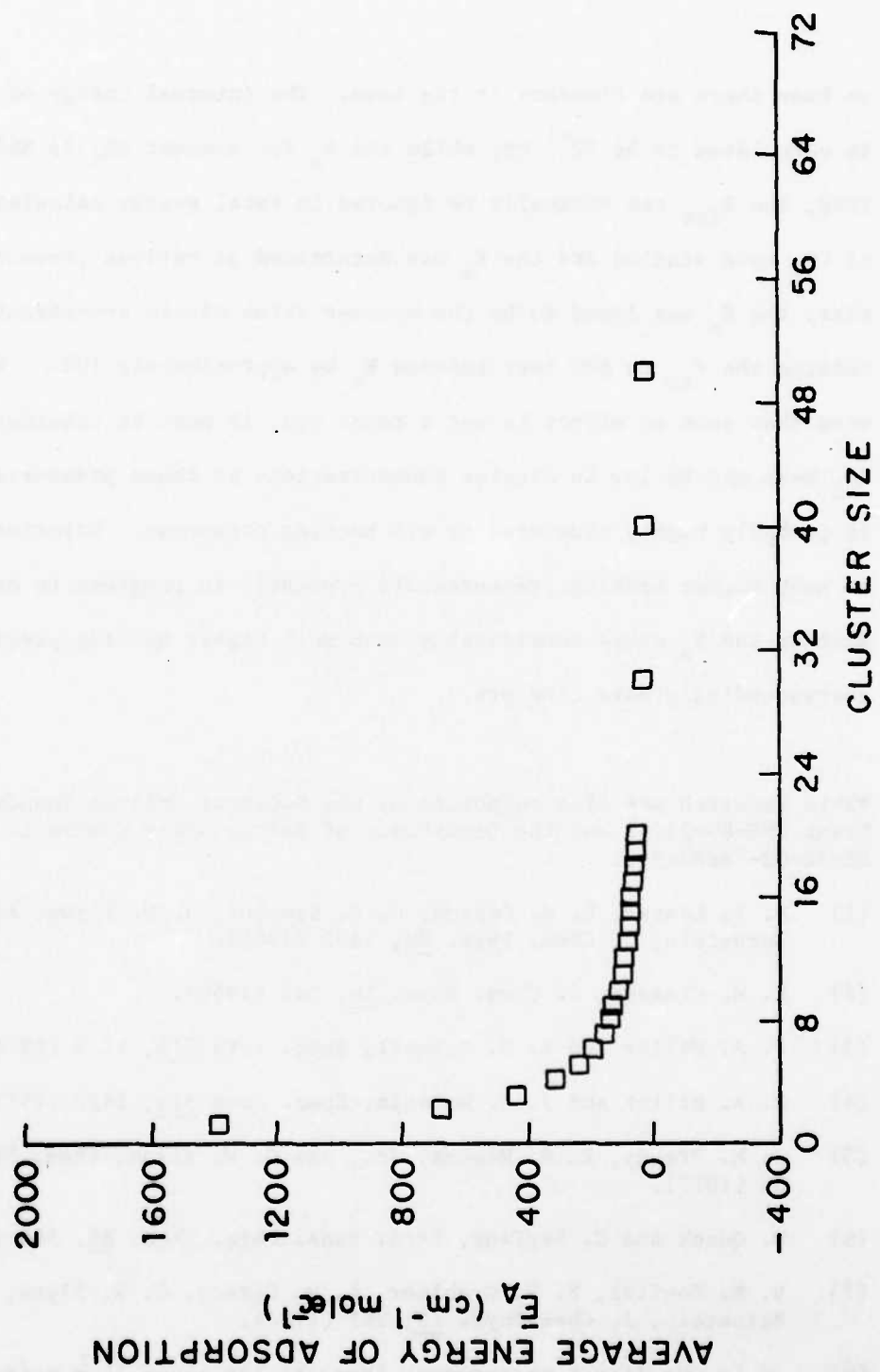


Figure 5

we know there are clusters in the beam. The internal energy of CO_2 at 290 K is calculated to be 52^{-1} cm, while the E_a for monomer CO_2 is 860^{-1} cm.⁽¹⁰⁾ Thus, the E_{int} can virtually be ignored in total energy calculations. Beams of CO_2 were studied and the E_a was determined at various pressures. At 400 torr, the E_a was found to be the monomer value within experimental error; raising the P_{nz} to 600 torr reduces E_a by approximately 10%. While it may seem that such an effect is not a major one, it must be considered that the CO_2 beam may be low in cluster concentrations at these pressures, while C_4F_8 is probably highly clustered at all backing pressures. Experiments with CO_2 at much higher backing pressures are presently in progress to determine whether the E_a drops considerably with much higher backing pressures and correspondingly more clusters.

*This research was also supported by the National Science Foundation under Grant CHE-80-23747 and the Department of Energy under contract DE-AC-02-78ER04940.

- (1) M. I. Lester, L. M. Casson, G. B. Spector, G. W. Flynn, and R. B. Bernstein, *J. Chem. Phys.* 80, 1490 (1984).
- (2) H. H. Claasen, *J. Chem. Phys.* 18, 543 (1950).
- (3) F. A. Miller and R. J. Capwell, *Spec. Acta* 27A, 1113 (1971).
- (4) F. A. Miller and J. A. Wolanin, *Spec. Acta* 31A, 1427 (1975).
- (5) J. M. Preses, R. E. Weston, Jr., and G. W. Flynn, *Chem. Phys. Lett.* 46, 64 (1977).
- (6) M. Quack and G. Seyfang, *Bern. Buns. Phys. Chem.* 86, 504 (1982).
- (7) D. R. Coulter, F. R. Grabner, L. M. Casson, G. W. Flynn, and R. B. Bernstein, *J. Chem. Phys.* 73, 281 (1980).
- (8) ΔP is the direct measurement from the ion gauge flux meter. The flux, $F = \Delta P/S$, where S is the sensitivity correction for the individual gases.

- (9) The following are the values used in evaluating Eq. 1.

$$S_{C_4F_8} = 2.80$$

$$S_{Ar} = 1.36$$

$$E_{a, Ar} = 523 \text{ cm}^{-1} (-\Delta H_{vap})$$

$$E_{a, C_4F_8} = 1938 \text{ cm}^{-1} (-\Delta H_{vap})$$

$$1/2 m\langle v^2 \rangle_{Ar} = 493 \text{ cm}^{-1}$$

$$1/2 m\langle v^2 \rangle_{C_4F_8} = 1273 \text{ cm}^{-1}$$

- (10) Matheson Co. Inc., Matheson Gas Data Book, 4th ed., 1966.

- (11) A. G. DeRocco and W. G. Hoover, *J. Chem. Phys.* **36**, 916 (1962).

- (12) T. E. Gough, R. E. Miller, and G. Scoles, *J. Chem. Phys.* **69**, 1588 (1978).

- (13) T. E. Gough, R. E. Miller, and G. Scoles, *J. Phys. Chem.* **85**, 4041 (1981).

- (14) T. E. Gough, R. E. Miller, and G. Scoles, *Chem. Phys. Lett.* **97**, 155 (1983).

- (15) E. Pochnon, R. E. Weston, Jr., and G. W. Flynn, "Infrared Multiphoton Dissociation of Octafluorocyclobutane with a Two Frequency Q-Switched CO_2 Laser," in press.

IV. PICOSECOND ENERGY TRANSFER AND PHOTOFRAGMENTATION SPECTROSCOPY

A. TWISTED INTERNAL CHARGE TRANSFER PHENOMENA*

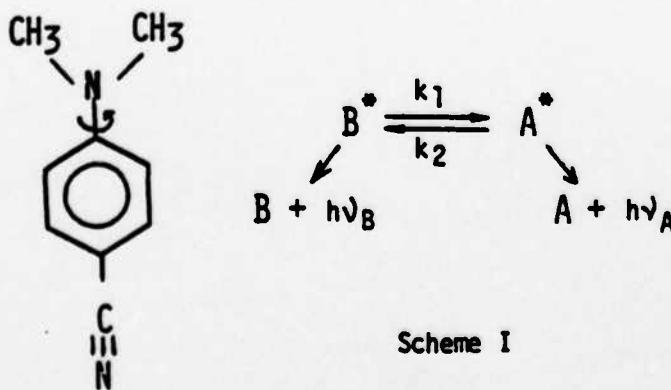
(K. Eisenthal)

(JSEP work unit 8, 1982-1985)

(Principal Investigator: K. B. Eisenthal (212) 280-3175)

Twisted internal charge transfer (TICT) states have been of interest to photochemists and photophysicists as excited states which strongly interact with polar solvent environments.⁽¹⁾ Many spectroscopic studies, both steady-state in nature⁽¹⁾⁻⁽¹²⁾ and time-resolved,⁽¹³⁾⁻⁽¹⁹⁾ have been performed on p-dimethylaminobenzonitrile (DMABN) and its derivatives in an attempt to understand the role of the solvent in the twisting and charge separation process. Despite these numerous studies, it is not yet understood exactly how the solvent affects the energetics and dynamics of TICT.

According to the TICT model, DMABN in its excited state undergoes a bond twisting between the dimethylamino and phenyl moieties.⁽²⁾ The initially excited state B^* , which is planar, undergoes a radiationless transition to the nonplanar state A^* , the TICT state. The twisting of the dimethylamino group with respect to the plane of the phenyl ring effects a charge separation (the A^* state) which is stabilized in polar media.



Scheme I

CNDO/S-CI calculations done for DMABN based on the TICT model show that the charge on the amino nitrogen peaks sharply at the bond twist angle 90° .⁽²⁰⁾ The molecule must therefore very nearly reach the perpendicular conformation before charge separation can occur. The sudden change in the solute dipole moment and the stabilization of the TICT state is directly connected with the interaction with the solvent.

In our recent studies of the effects of the solvent on the twisted internal charge transfer phenomena we established for alcohol solvents that the key factor in the dynamics and stabilization were short range interactions. These local forces are manifested by the formation of complexes between alcohol and DMABN molecules. In our current studies we have chosen aprotic solvents, i.e. non-hydrogen bonding solvents, to complement our studies in the strongly hydrogen bonding alcohols. The solvents we selected were normal nitriles and nitrile/alkane mixtures.

For all of the liquids studied, scheme I has been verified. The fluorescence lifetimes for the A^* and B^* states were measured, and were found to be within experimental error of each other ($3.0 \pm .2$ ns), which confirms that equilibrium is attained between the excited state species in these solvents.

Table I gives the results of experiments conducted in neat normal nitriles. In all cases, single exponential behavior for the formation of the A^* state and fast decay of the B^* state was observed. The observed formation and decay rates (k_{obs}) are equal within experimental error, which confirms that the A^* population originates from the B^* population.

In addition to k_{obs} , the fraction of fluorescence at the short wavelength due to the slowly decaying component (R) is also measured. From these two observables, it is possible to calculate k_1 , k_2 , and the excited state

equilibrium constant, K_{eq} , by equations obtained from the solutions of the full kinetic differential equations. If it is assumed that the excited state rates, k_1 and k_2 , are fast compared to the lifetimes of the two states, k_A and k_B , then equations 1-3 are obtained.

$$k_{obs} = k_1 + k_2 \quad (1)$$

$$k_2 = R \times k_{obs} \quad (2)$$

$$K_{eq} = k_1/k_2 = (1-R)/R \quad (3)$$

The determination of K_{eq} gives important information about the relative energies of the B^* and A^* forms. The effect of polarity on the fluorescence spectrum of DMABN has been well studied,^{(1),(9),(10)} and it has long been known that by increasing the polarity of the medium, the position of the A^* band can be red-shifted. This solvochromatic shift is the basis for estimating the dipole moment of the A^* state.⁽⁹⁾

By measuring the equilibrium constants for $B^* \rightleftharpoons A^*$ in different solvents, we have found evidence that the more polar solvents stabilize the A^* state relative to the B^* state. Figure 1 shows that ΔG , the free energy difference between the planar and twisted forms of DMABN, decreases linearly with increasing $E_T(30)$, an empirical parameter which is a measure of the solvent polarity. This has implications for the prediction of TICT rates; as the polarity increases, the barrier between the two states will be lowered, and thus, the $B^* \rightleftharpoons A^*$ conversion rate should increase.

Several authors have suggested that, for many TICT compounds, the rate-determining step of the formation of the A^* species is viscosity controlled.^{(2)-(4),(6),(16),(17),(19),(20)} The twisting of the substituent group with respect to the benzene ring on excitation of these compounds is thought to displace solvent molecules, and therefore to experience "friction"

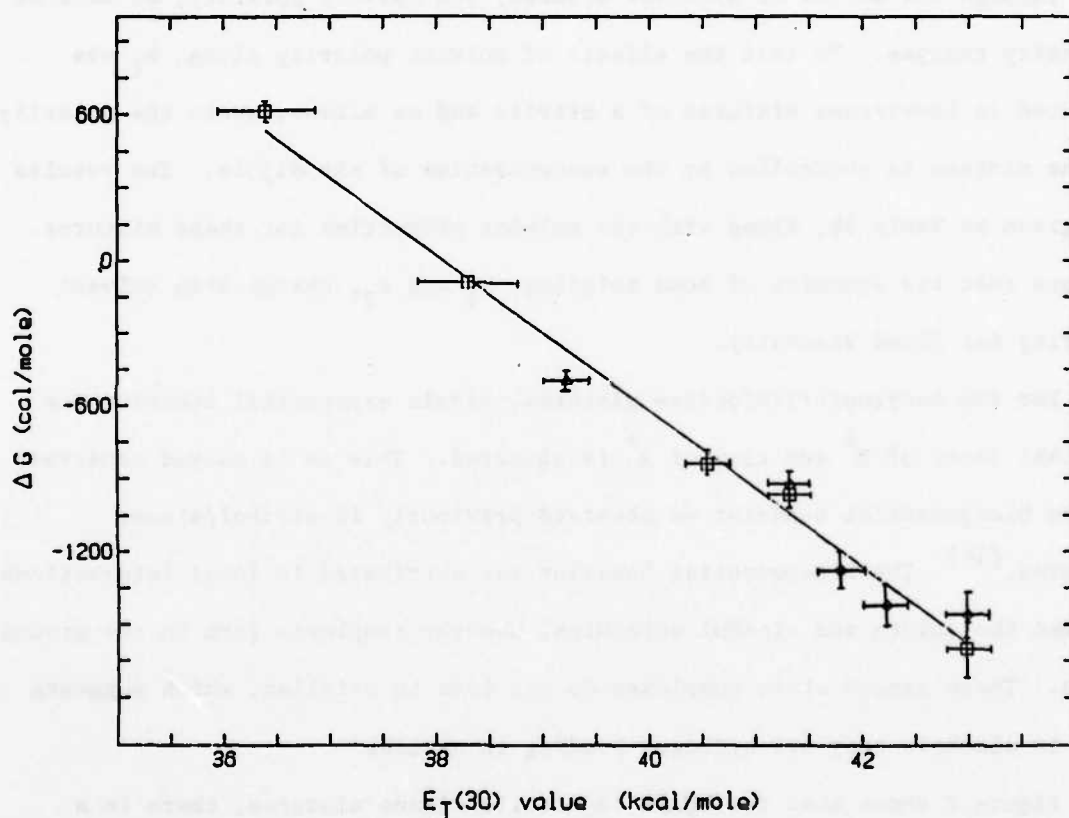


Figure 1. Free energy difference between the planar and twisted forms of DMABN in neat nitriles (diamonds), in butyronitrile/octane mixtures (squares), and in 1.8 M octyl cyanide/tetradecane (delta) vs. the polarity of those solvents. Slope = -321 ± 15 , intercept = $12,200 \pm 600$, correlation = .984.

imposed by the solvent environment. Examination of molecular models suggests that, for DMABN, the twisting of the dimethylamino group about the benzene ring sweeps out a very small volume with respect to the size of the molecule and the solvent molecule. The geometric change of DMABN may, in fact, be virtually unimpeded by solvent molecules.

Through the series of nitriles studied, the solvent polarity, as well as viscosity changes. To test the effects of solvent polarity along, k_1 was measured in isoviscous mixtures of a nitrile and an alkane, where the polarity of the mixture is controlled by the concentration of the dipole. The results are given in Table Ib, along with the solvent properties for these mixtures. We note that the dynamics of bond twisting, k_1 and k_2 , change with solvent polarity for fixed viscosity.

For the butyronitrile/octane mixtures, single exponential behavior for the fast decay of B^* and rise of A^* is observed. This is in marked contrast to the biexponential behavior we observed previously in alcohol/alkane mixtures.⁽¹⁶⁾ The biexponential behavior was attributed to local interactions between the solute and alcohol molecules, whereby complexes form in the ground state. These ground state complexes do not form in nitriles, which suggests that in alcohols they are hydrogen-bonding in nature.

Figure 2 shows that for DMABN in nitrile/alkane mixtures, there is a linear relationship between the logarithm of k_1 and the solvent polarity parameter, $E_T(30)$. Although it is not clear whether $E_T(30)$ is measuring long or short range interactions, or a combination of both, we can tentatively interpret our studies as follows: The charge transfer state, having the larger dipole moment, is better stabilized than the planar state in more polar fluids, and this causes a lowering of the barrier between the two states.

There are some examples in the literature of a linear activation energy

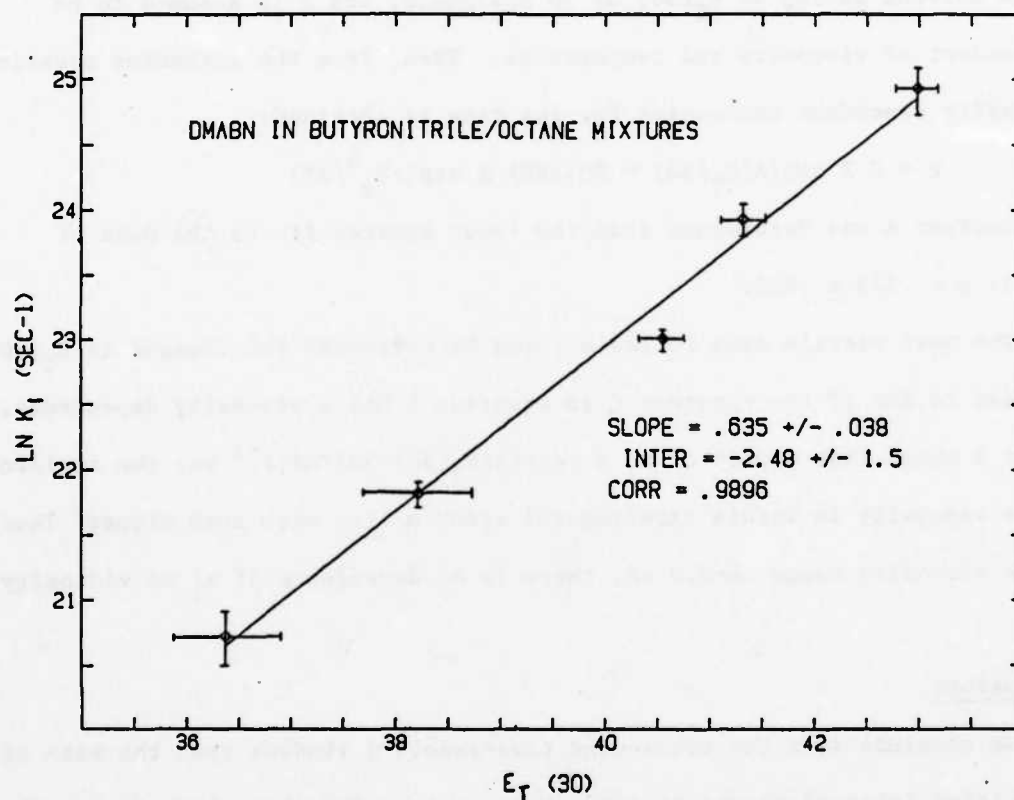


Figure 2. Plot of logarithm of k_1 for DMABN in butyronitrile/octane mixtures vs. the polarity of those mixtures. Slope = $.641 \pm .038$, intercept = 16.53 ± 1.5 , correlation = .9897.

relationship with solvent $E_T(30)$ values.^{(22),(23)} If we assume that the activation energy of the TICT process decreases linearly with increasing solvent $E_T(30)$:

$$E_a = E_a^0 - A[E_T(30) - 30] \quad (4)$$

where $E_T(30)$ is the polarity parameter, E_a^0 is the activation energy in an alkane solvent having an $E_T(30)$ of 30 kcal/mole, and A is assumed to be independent of viscosity and temperature. Then, from the Arrhenius equation, a polarity dependent expression for the rate is obtained:

$$k = C \times \exp\{A[E_T(30) - 30]/RT\} \times \exp(-E_a^0/RT) \quad (5)$$

The constant A was determined from the least squares fit to the data of Fig. 2: $A = .373 \pm .022$.

The neat nitrile data in Table I can be corrected for changes in $E_T(30)$ in order to see if the constant C in equation 5 has a viscosity dependence. Figure 3 shows that a plot of $k_1 \times \{\exp[A(E_T(30)-30)/RT]\}^{-1}$ vs. the reciprocal of the viscosity is within experimental error a line with zero slope. Thus, in the viscosity range .6-2.0 cP, there is no dependence of k_1 on viscosity.

Conclusions

We conclude from our picosecond time-resolved studies that the rate of the twisted internal charge transfer process in p-dimethylaminobenzonitrile is extremely rapid in the aprotic nitrile solvents, achieving equilibrium between the planar and nonplanar (twisted) forms of the excited molecule.

The rate of formation of the charge transfer state is found to depend exponentially on the solvent polarity as measured by the empirical solvent polarity parameter $E_T(30)$. Indeed the equilibrium constant is found to scale with $E_T(30)$ as well. There is no evidence for or against complex formation in

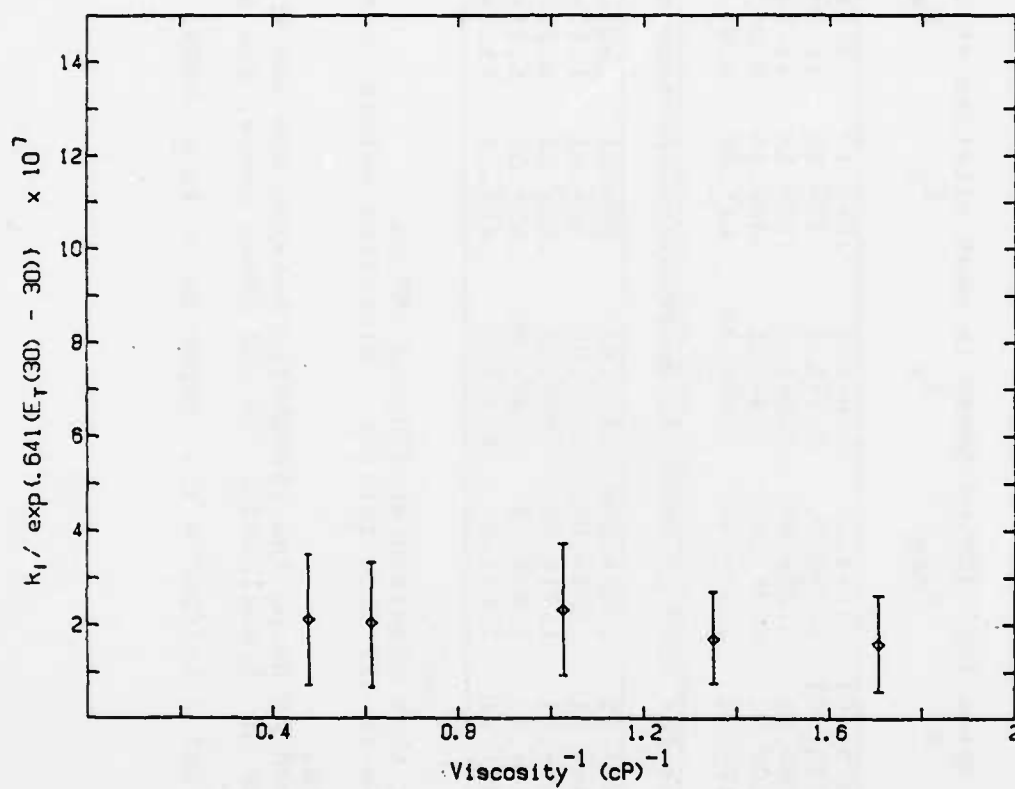


Figure 3. Plot of $k_1 \times \{\exp[A(E_T(30)-30)/RT]\}^{-1}$ for DMABN in neat nitriles vs. $(\text{viscosity})^{-1}$.

Table I

Table Ia: Rates for TICT of DMABN in neat nitriles at 20 °C

Solvent	R	k _{obs}	k ₁	k ₂	k _{eq}	η	E _T (30) Δf ^b
Butyronitrile (n-C ₄ H ₇ N)	.075±.01	7.1±1.2	6.6±1.4	.54±.17	12.3±1.8	.586	43.0
Valeronitrile (n-C ₅ H ₉ N)	.078±.01	6.7±1.0	6.1±1.2	.52±.16	11.8±1.6	.741	42.8
Capronitrile (n-C ₆ H ₁₁ N)	.08±.01	6.25±.89	5.8±1.0	.50±.14	11.5±1.6	.975	42.2
Heptyl cyanide (n-C ₇ H ₁₅ N)	.10±.01	4.35±.91	3.9±1.1	.44±.14	9.0±1.0	1.632	41.8
Octyl cyanide (n-C ₈ H ₁₇ N)	.17±.01	3.57±.28	2.96±.37	.61±.09	4.9±.4	2.092	41.3

Table Ib: Rates for TICT of DMABN in Butyronitrile/Octane mixtures at 20 °C

0.4 M Butyronitrile	.74±.01	.386±.009	.10±.02	.29±.01	.35±.02	.54	36.4 ^a	.0602
0.8 M Butyronitrile	.46±.01	.555±.016	.00±.03	.26±.01	1.17±.05	.54	38.3 ^a	.0993
1.8 M Butyronitrile	.19±.01	1.21±.06	.98±.08	.23±.02	4.26±.28	.54	40.6	.1568
3.6 M Butyronitrile	.16±.01	2.94±.22	2.47±.29	.47±.07	5.25±.39	.55	41.3	--
11.5 M Butyronitrile	.06±.01	7.1±1.0	6.7±1.2	.43±.14	15.7±2.8	.62	43.0	.2801

All rates given in units of 10¹⁰ sec⁻¹.

k_{obs} is the average value for that observed at 350 and 450 nm.

Viscosity values (cp) in Table Ia are from ref. 21. Viscosity values in Table Ib were measured (error) is .04 cp).

E_T(30) values are in kcal/mole.

a) These values were determined by using the lipophilic betaine dye and the relation E_T^o = .9143 E_T(30) + 3.434, and have error of .5 kcal/mole. In all other cases, the error in E_T(30) is .2 kcal/mole.

b) Δf = [(ε - 1)/(2ε + 1)] - [(n² - 1)/(2n² + 1)]. Error in Δf is ± .0005.

the TICT stabilization, as was the case with alcohols, nor was there any viscosity dependence in the range investigated.

Further studies are underway to measure the barrier height and to determine if it is the short range or long range interactions with the solvent or both which are chiefly responsible for the observed TICT phenomenon.

*This work is also supported by the Air Force Office of Scientific Research under Grant AFOSR-84-0013 and the National Science Foundation under Grant NSF-CHE82-11593.

- (1) E. Lippert, W. Luder, and H. Boos, in *Advances in Molecular Spectroscopy*, ed. A. Mangini (Pergamon Press, Oxford, 1962) p. 443.
- (2) Z. Grabowski, K. Rotkiewica, W. Rubaszewska, and E. Kirkor-Kaminska, *Acta Physica Polonica A* 54, 767 (1978).
- (3) W. Rettig, *J. Luminescence* 26, 21 (1980).
- (4) W. Rettig and E. Lippert, *J. Molec. Struct.* 61, 17 (1980).
- (5) K. Rotkiewicz and W. Rubaszewska, *Chem. Phys. Lett.* 70, 444 (1980).
- (6) G. Wermuth, W. Rettig, and E. Lippert, *Ber. Bunsenges. Phys. Chem.* 85, 553 (1981).
- (7) A. Ayuk, W. Rettig, and E. Lippert, *Ber. Bunsenges. Phys. Chem.* 85, 553 (1981).
- (8) W. Rettig, *J. Phys. Chem.* 86, 1970 (1982).
- (9) W. Rettig, *J. Molec. Struct.* 84, 303 (1982).
- (10) Z. Grabowski and J. Dobkowski, *Pure and Appl. Chem.* 55, 245 (1983).
- (11) R. Visser and C. Varma, *J. C. S. Faraday II* 76, 453 (1980).
- (12) R. Visser, C. Varma, J. Konijnenberg, and P. Bergwerf, *J. C. S. Faraday II* 79, 347 (1983).
- (13) N. Nakashima, H. Inoue, N. Mataga, and C. Yanamaka, *Bull. Chem. Soc. Jap.* 46, 2288 (1973).
- (14) W. Struve and P. Rentzepis, *J. Chem. Phys.* 60, 1533 (1974).
- (15) Y. Wang, M. McAuliffe, F. Novak, and K. Eisenthal, *J. Phys. Chem.* 85, 3736 (1981).
- (16) Y. Wang and K. Eisenthal, *J. Chem. Phys.* 77, 6076 (1982).

- (17) D. Huppert, S. Rand, P. Rentzepis, P. Barbara, W. Struve, and Z. Grabowski, J. Chem. Phys. 75, 5714 (1981).
- (18) Y. Takagi, M. Sumitani, and K. Yoshihara, Rev. Sci. Instrum. 52, 1003 (1981).
- (19) F. Heisel and J. Mieke, Chem. Phys. Lett. 100, 183 (1983).
- (20) E. Lippert, A. Ayuk, W. Rettig, and G. Wermuth, J. Photochem. 17, 237 (1981).
- (21) Landolt-Bornstein, Zahlenwerte und Funktionen, Band II, Teil 5a.
- (22) C. Lussan and J. Jungers, Bull. Soc. Chim. 2678 (1968).
- (23) S. Smith, A. Fainberg, and S. Winstein, J. Am. Chem. Soc. 83, 618 (1961).

B. KINETICS AND WAVELENGTH DEPENDENCE OF THE PHOTOFRAGMENTATION OF SINGLET OXYGEN PRECURSORS*

(K. Eisenthal)

(JSEP work unit 8, 1982-1985)

(Principal Investigator: K. Eisenthal (212) 280-3175)

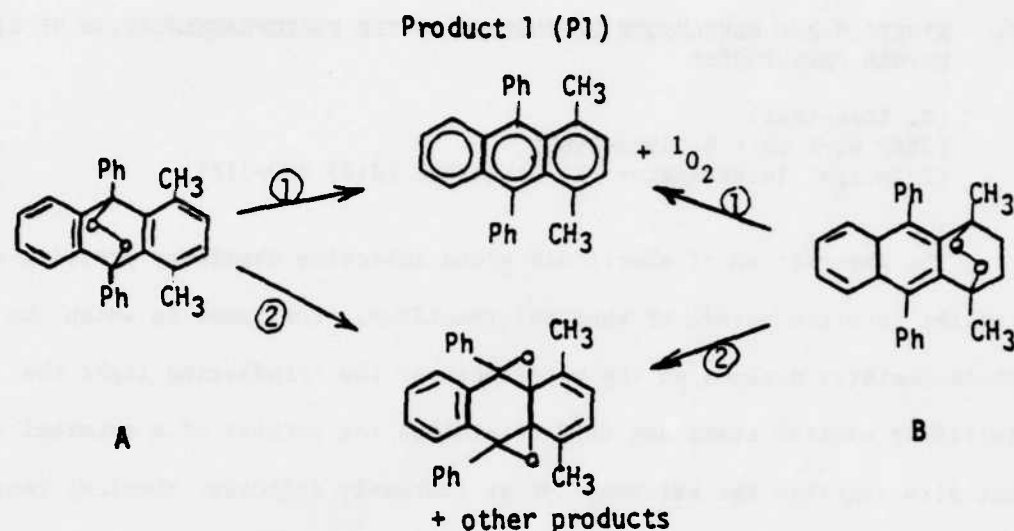
The observation of electronic state selective chemistry provides valuable insight into the nature of chemical reactions. For cases in which the photochemistry depends on the wavelength of the irradiating light the initially excited state not only determines the pathway of a chemical reaction but also requires the existence of an extremely efficient chemical reaction to compete with rapid energy relaxation processes.

Endoperoxides are compounds known to undergo wavelength dependent photochemistry. We have extended our studies of these molecules, characterized by an O-O peroxide bridge, to better understand the nature of the photofragmentation process and its dependence on the wavelength of the exciting light.

We were also motivated by the importance of these compounds as a useful source of singlet molecular oxygen, $^1\text{O}_2$, an active species in the degradation of chemical and biological substances and as an energy pump for the high powered iodine laser.

The issues we have addressed are: (1) the effect of the endoperoxide structure on the photofragmentation process; (2) the dependence of the products in the excitation wavelength.

We have studied the two isomeric endoperoxides of 1, 4 dimethyl-9, 10-diphenylanthracene.



Picosecond Kinetic Measurements

Direct observation of the kinetics of anthracene formation following UV laser photodecomposition of endoperoxides A and B was accomplished using the laser induced fluorescence (LIF) method. The experiment consisted of irradiation of an acetonitrile solution for the endoperoxide ($2\text{--}5 \times 10^{-4}$ M) with a picosecond laser pulse at 266 nm from a passively mode-locked Nd:YAG laser (25–30 psec FWHM < 0.01 mJ). The formation rate of 1,4-dimethyl-9,10-diphenylanthracene was monitored by laser induced fluorescence using a weak probe pulse at 355 nm at variable time delays. The results of the picosecond dynamic measurements are shown in Figure 1.

Using the measured system response a best fit to the LIF data was obtained for an exponential risetime of 45 ± 15 psec for B and 75 ± 20 for A. These experiments demonstrate that the formation of the parent hydrocarbon proceeds at a noninstantaneous rate following photoexcitation.

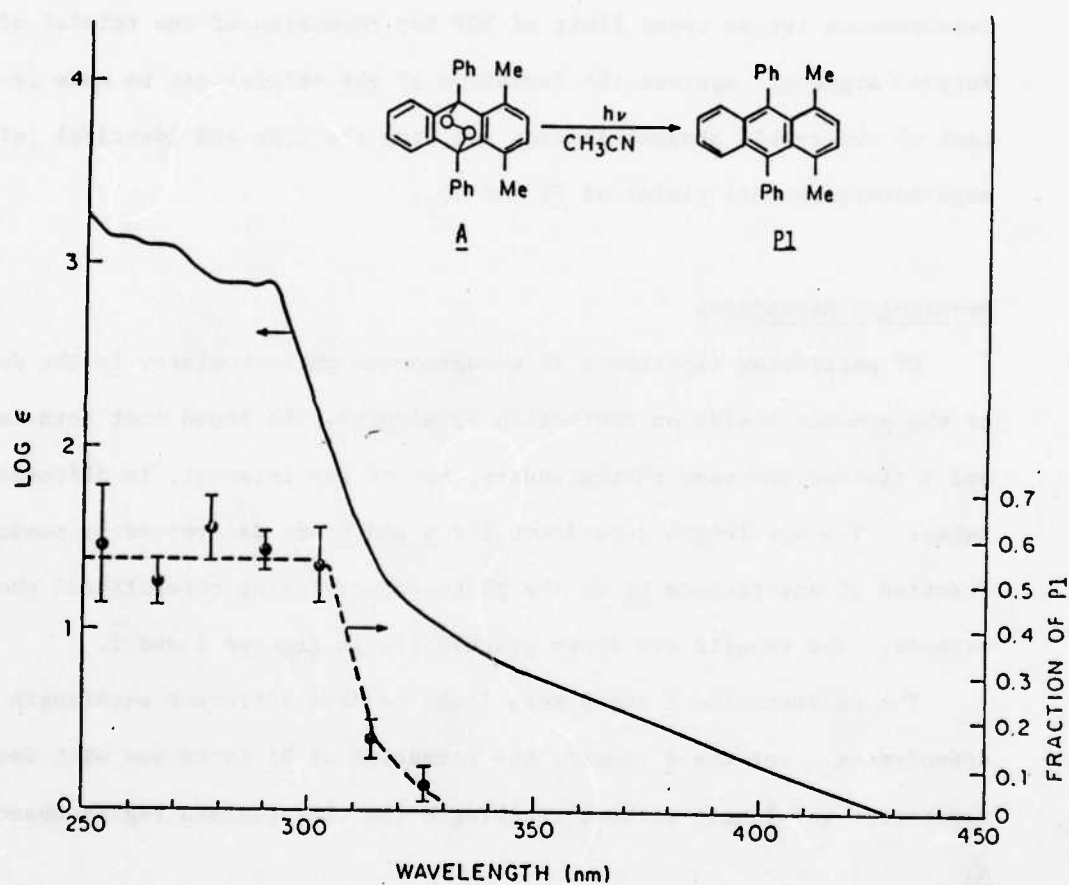


Figure 1. Electronic absorption spectrum of the 9,10-isomer (**A**) in CH_3CN and wavelength dependence of the fraction of **P1** in the product of **A** in CH_3CN .

Although a triplet pathway for formation of the observed products is possible no triplet-triplet absorption from anthracene P1 was observed immediately after photoexcitation of A or B. Using a conservative value for the triplet absorption of P1, based on values of similar anthracenes⁽¹⁾⁻⁽³⁾ and taking the triplet of 9-fluorene^{(4),(5)} as a standard, the picosecond measurements set an upper limit of 10% for formation of the triplet of P1. Further arguments against the formation of the triplet can be made from the lack of observable phosphorescence and from the high and identical (within experimental error) yields of P1 and 1O_2 .

Wavelength Dependence

Of particular importance in endoperoxide photochemistry is the dependence of the product yields on excitation wavelength. We found that both isomer A and B yielded the same photoproducts, but of key interest, in different ratios. The wavelength dependence for A and B was determined by measuring the fraction of anthracene P1 in the photoproducts using conventional photolysis methods. The results are shown graphically in Figures 1 and 2.

The endoperoxide A and B were found to have different wavelength dependences. For the B isomer, the formation of P1 increases with decreasing excitation wavelength without reaching a limiting plateau region observed for A.

Excitation into the $S_0 \rightarrow S_1$ band of A results in predominant formation of the products derived from cleavage of the O-O bond (i.e. diepoxides, rearrangement, etc.). The absorption at wavelengths less than 310 nm ($\epsilon \approx 10^2 - 10^3 \text{ M}^{-1} \text{ cm}^{-1}$) corresponds to the $S_0 \rightarrow S_2$ ($\pi \pi^*$) transition. Irradiation into this band results in predominant formation of P1 and 1O_2 . The yield of these two products is constant down to 254 nm. These results,

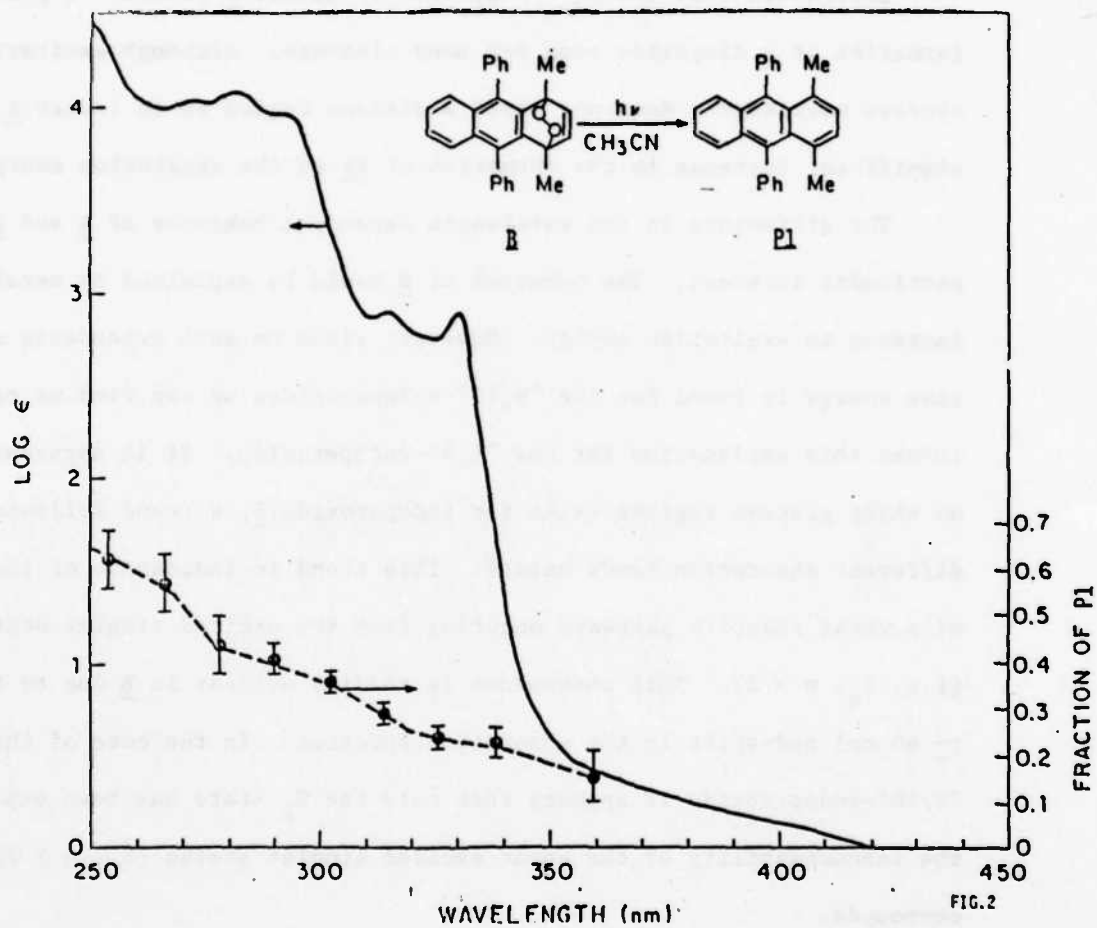


Figure 2. Electronic absorption spectrum of the 1,4-isomer (**B**) in CH_3CN and wavelength dependence of the fraction of **P1** in the product mixture upon photolysis of the 1,4-isomer in CH_3CN .

along with the lack of triplet sensitized formation of Pl, indicate that photofragmentation of A and Pl and 1O_2 is a state selective process occurring from an upper excited singlet state of A (S_n , $n \geq 2$).

Excitation into the $S_0 \rightarrow S_1$ band of isomer B results in predominant formation of a diepoxide from O-O bond cleavage. Although excitation at shorter wavelengths does not yield a plateau region as in isomer A, there is a significant increase in the formation of Pl as the excitation energy increases.

The difference in the wavelength dependent behavior of A and B is of particular interest. The behavior of B could be explained by merely an increase in excitation energy. However, since no such dependence on excitation energy is found for the "9,10"-endoperoxides we can find no reason to invoke this explanation for the "1,4"-endoperoxide. It is apparent that while no sharp plateau regions exist for endoperoxide B, a trend following the different absorption bands exists. This trend is indicative of the presence of several reactive pathways occurring from the excited singlet state manifold (i.e. S_n , $n > 2$). This phenomenon is readily evident in B due to the large (~ 40 nm) red-shift in the absorption spectrum. In the case of the "9,10"-endoperoxide it appears that only the S_2 state has been explored due to the inaccessability of the upper excited singlet states (S_n , $n > 2$) of these compounds.

Conclusion

The laser induced fluorescence measurements here are the first direct, time resolved studies of the production of the parent aromatic hydrocarbon obtained from the photolysis of aromatic endoperoxides. From these studies we have confirmed and extended our knowledge of the wavelength dependence of the photochemistry of these endoperoxides and provide evidence, in the case of B,

for reactivity from higher excited singlet states (S_n , $n > 2$). This higher energy pathway produces 1O_2 with an efficiency three times greater than the "9,10"-endoperoxides studied. The observation of the delayed appearance of the anthracene P1 following photoexcitation of the endoperoxide can be explained by two mechanisms. One is the simultaneous rupture of the two C-O bonds with prompt formation of singlet oxygen followed by a slower rearrangement and relaxation of the monitored anthracene fragment P1. The second mechanism is a sequential bond rupturing scheme in which a single C-O bond breaks giving a peroxy radical followed by breaking of the second C-O bond to give 1O_2 and the anthracene moiety. We are currently trying to resolve these concerted and non-concerted mechanisms for 1O_2 production.

*This work is also supported by the Air Force Office of Scientific Research under Grant AFOSR-84-0013 and the National Science Foundation under Grant NSF-CHE82-11593.

- (1) D. H. Ting, Chem. Phys. Lett. 1, 335 (1967).
- (2) H. Labhart and W. Heizelmann, "Organic Molecular Photophysics", J. Birks, Ed., John Wiley and Sons: New York, 1975, Vol. 1, Chapter 6.
- (3) Y. H. Meyer, R. Astier, and J. M. Leclercq, J. Chem. Phys. 56, 801 (1972).
- (4) Nakajima, Mol. Photochem. 7, 251 (1976).
- (5) T. Kobayashi and S. Nagakura, Chem. Phys. Lett. 43, 49 (1976).

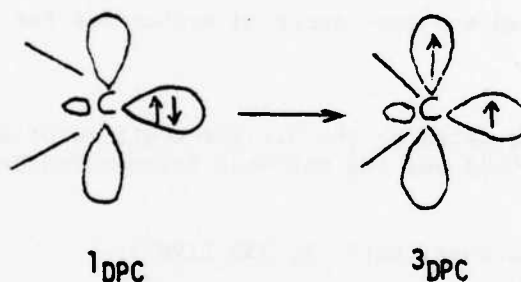
C. PHOTOPHYSICS AND PHOTOCHEMISTRY OF A DIVALENT CARBON CHEMICAL INTERMEDIATE - DIPHENYLCARBENE*

(K. Eisenthal)

(JSEP work unit 8, 1982-1985)

(Principal Investigator: K. B. Eisenthal (212) 280-3175)

We have expanded our studies of divalent carbon species (carbenes), an important class of chemical intermediates, based on our initial success in investigating energy relaxation in diphenylcarbene, a prototypical aromatic carbene. In our earlier study (reported last year) we succeeded in measuring the rate of intersystem crossing from an excited singlet state to the ground triplet state.



This result was important since the chemistry of ^1DPC and ^3DPC is different and thus the rate of crossing k_{ST} and the equilibration, if it occurs, between these states determines the reactions which occur. In addition by measuring k_{ST} and the reverse process k_{TS} we obtained information on the energy gap separating these states.

In this last year we have made significant advances in:

(1) characterizing the effects of the solvent environment on the intramolecular dynamics of intersystem crossing; (2) exploring for the first time the photochemistry of a carbene, i.e. its excited state properties. We find that the reactivity patterns of the photoexcited triplet, $^3\text{DPC}^*$, are significantly different from those of the ground state ^3DPC . Furthermore, we

have observed a new chemical reaction for a carbene, namely a charge transfer reaction with simple electron donors.

Solvent Effects on Singlet-Triplet Relaxation

To address the issue of intermolecular interactions on singlet to triplet intersystem crossing we measured k_{ST} in a series of solvents, mostly at room temperature. The results obtained showed that intersystem crossing depends strongly on the choice of solvent (Fig. 1). In isooctane, a hydrocarbon solvent, the time of intersystem crossing, k_{ST}^{-1} , was found to be 95×10^{-12} s, a factor of three faster than in acetonitrile (310×10^{-12} s). For the wide range of solvents used, it turned out that there was a clear ordering between the rate of singlet to triplet conversion and the polarity of the solvent, the rate being larger in the less polar solvents. No correlation was obtained with other solvent parameters which would be related to possible carbene-solvent complexes or parameters such as viscosity which could influence the dynamics of the structural change associated with different singlet and triplet geometries.

To understand how solvent polarity could affect spin conversion, it is useful to consider the electronic nature of the singlet and triplet states. The singlet state, with both unshared electrons in the same orbital, localized on the central carbon will be significantly more polar than the triplet state (Fig. 2). It is, therefore, to be expected that the polar singlet will be strongly stabilized in the polar solvents, whereas the less polar triplet will experience less stabilization. This differential stabilization would, therefore, result in the singlet-triplet energy gap decreasing as the solvent polarity increases. This prediction was confirmed experimentally. We found from measurements of k_{ST} and k_{TS} in polar acetonitrile and nonpolar isooctane

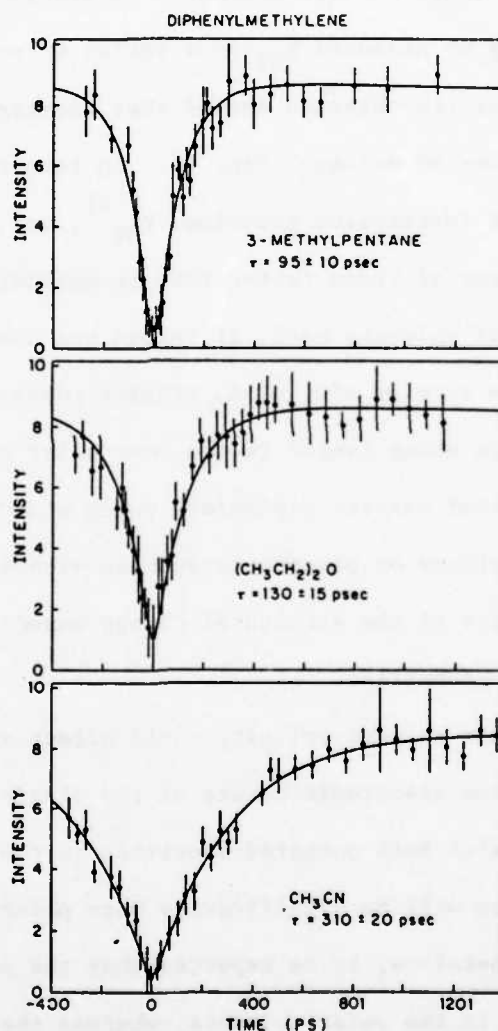


Figure 1. Laser induced fluorescence as a function of time delay between excitation and probe pulses yielding $\text{DPC} \rightarrow \text{DPC}^+$ for diphenylcarbene in (a) 3-methylpentane, (b) diethyl ether, and (c) acetonitrile. The units of time are picoseconds (ps).

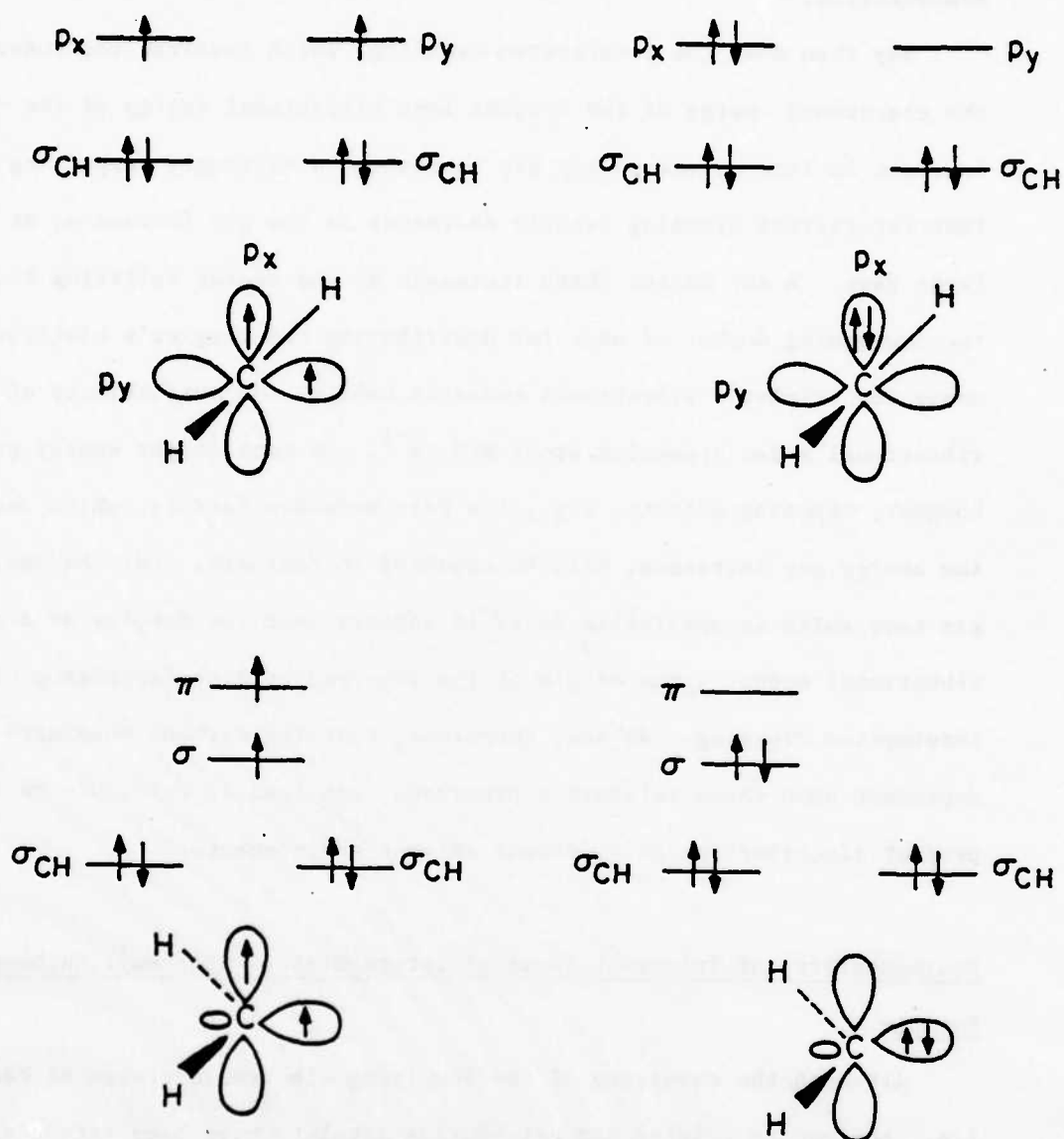


Figure 2. Energy level and orbital representations of bent and linear geometries of methylene. Top (a): Description of the two lowest energy configurations of the linear methylene structure. To the left is a description of the low energy configuration. To the right is a description of the high energy configuration. Bottom (b): To the left is a description of a "slightly" bent methylene. To the right is a description of a "strongly" bent methylene.

that the energy gap in isooctane is 1400 cm^{-1} compared with 870 cm^{-1} for acetonitrile.

Why then does the intersystem crossing, which involves the conversion of the electronic energy of the singlet into vibrational energy of the triplet, increase in rate as the energy gap increases; a seemingly surprising result in that intersystem crossing usually decreases as the gap increases, at least for large gaps. A key factor which increases as the energy splitting increases is the increasing number of ways for distributing the singlet's electronic energy among the triplet's vibrational modes as well as the availability of new vibrational modes appearing above 870 cm^{-1} . At some larger energy gap, however, opposing effects, e.g., the Franck-Condon factors, which decrease as the energy gap increases, will be expected to dominate. For the small energy gap case which is applicable here, it appears that the density of accepting vibrational modes is the origin of the observed solvent dependence of intersystem crossing. We see, therefore, that the carbene chemistry, dependent upon these relaxation processes, can lead in principle to different product distributions in different solvent environments.

Photochemistry of Transient Chemical Intermediates - Diphenyl Carbene as an Example

Although the chemistry of the low lying electronic states of carbenes, i.e., the ground triplet and neighboring singlet, have been extensively studied, the chemistry and general properties of the higher electronic states of carbenes remain unknown. Due to the transitory nature of reactive ground state intermediates, it is usually difficult to generate their excited states in sufficient concentration to probe their chemical properties. Thus, reactions of the lower thermally accessible states can destroy the chemical

intermediate before it is pumped up with light to excited electronic states. What is necessary is to generate the excited intermediate in a time which is short compared to the reaction time of the lower states.

Using picosecond laser methods we have succeeded in generating the carbene and then exciting the carbene to higher electronic states.⁽¹⁾ For the case of diphenylcarbene a picosecond ultraviolet laser pulse was used to photodissociate the diphenyldiazomethane precursor. A second picosecond laser pulse, arriving at the sample at some later time after the photodissociation pulse is then used to excite the triplet ground state carbene to an excited triplet state carbene. Using this experimental approach we were able to explore the interactions of reactant molecules with the excited triplet diphenylcarbene ^3DPC .

The first notable observation of our studies is ^3DPC reacts vigorously with various molecules which the ground triplet ^3DPC reacts only sluggishly with. Fig. 3 shows the marked effect of methanol and isoprene on the lifetime of the excited triplet state ^3DPC . With isoprene the reactions are faster with ^3DPC by at least four orders of magnitude relative to the ground state ^3DPC . We furthermore find the ^3DPC does not react with methanol in the same way that ^3DPC does, namely by attack on the C-H bond, but rather by attack of the O-H bond. We have proposed a scheme of carbene reactivity based on molecular orbital occupancy which explains the different reactions of ^1DPC , ^3DPC and ^3DPC with alcohols.

For the quenching of ^3DPC by amines we find that the quenching constant 3k varies exponentially with the ionization potential of the amine, Fig. 4. On the basis of these results which indicates a single electron transfer process we propose that ^3DPC undergoes photoreduction by amines, Am, forming a triplet charge transfer intermediate as the primary step in quenching,

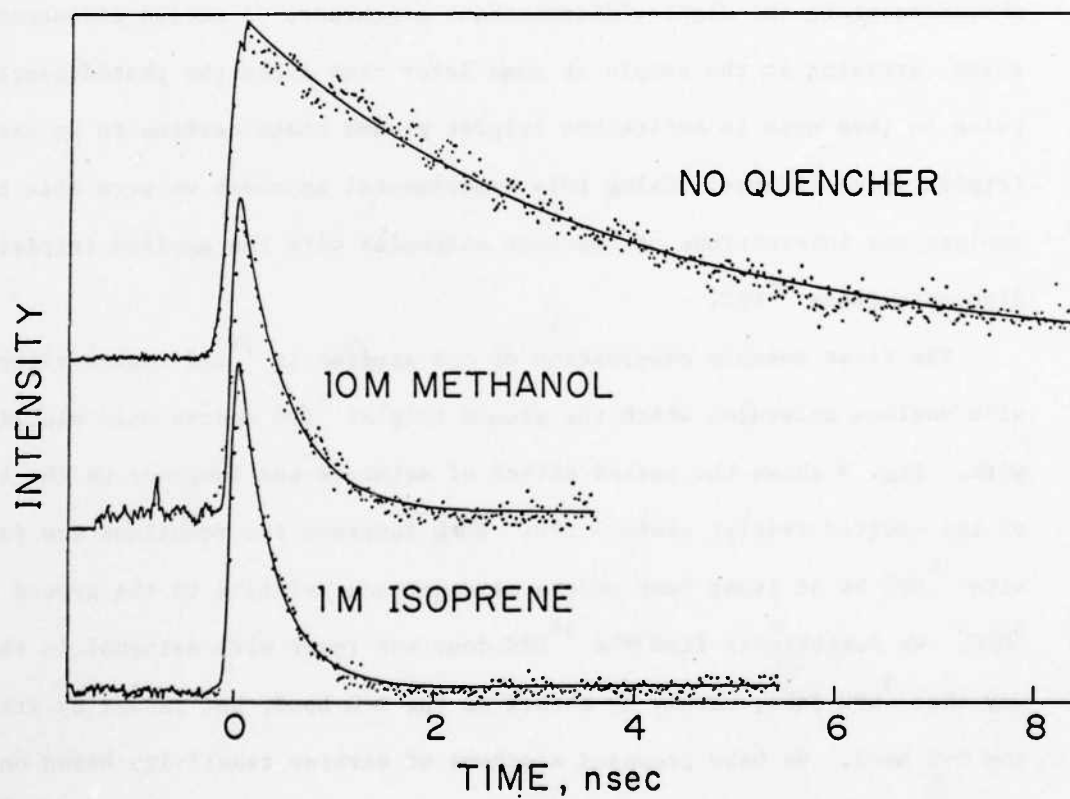


Figure 3. Variation in the lifetime of ^3DPC under various conditions. The units of time are nanoseconds (ns).

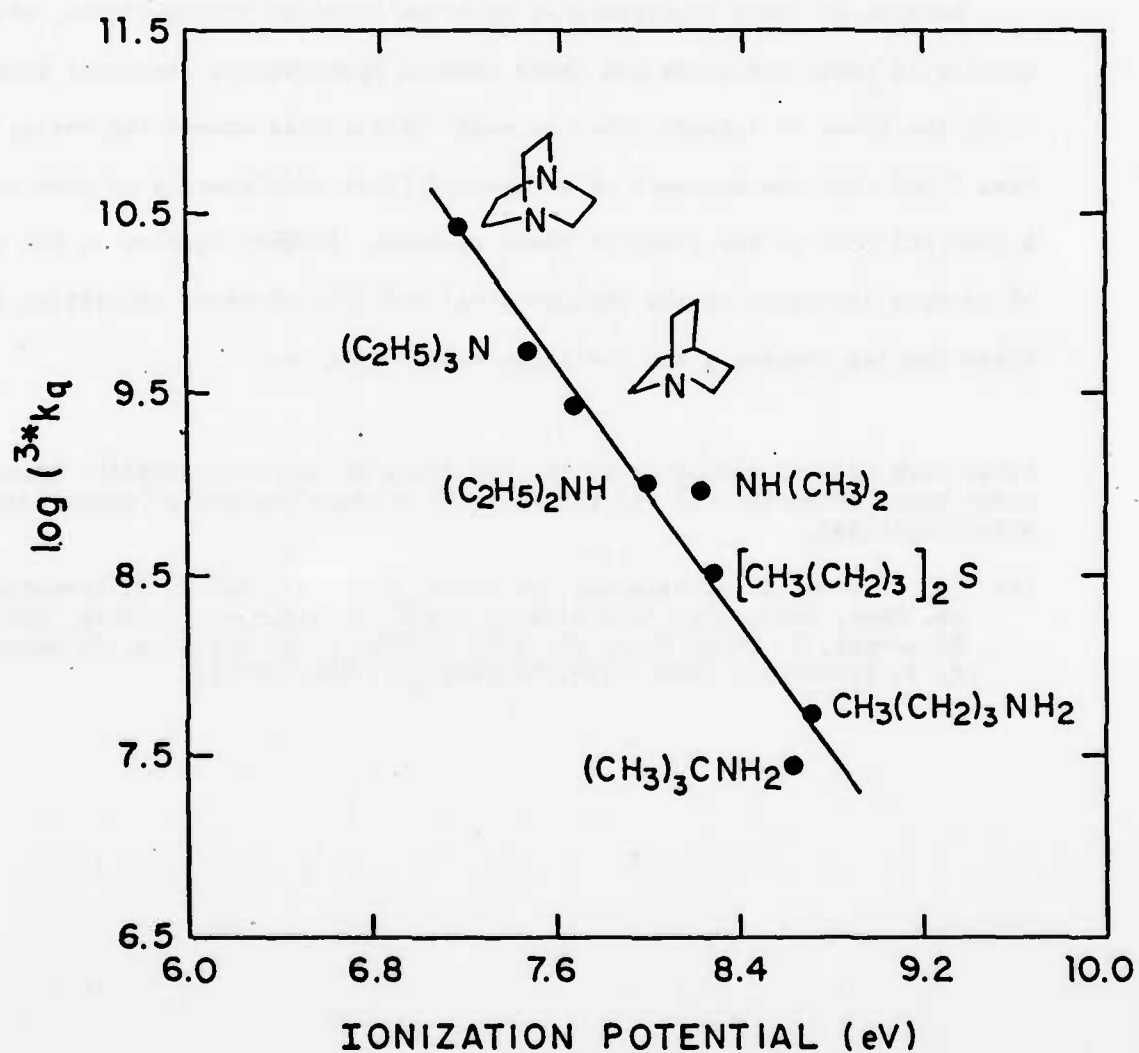
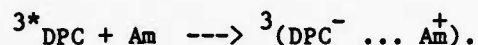


Figure 4. Quenching of excited triplet diphenylcarbene as a function of donor ionization potential in acetonitrile, at 20°C.



The charge transfer intermediate can then decay back to the original reactants or to singlet and triplet state products.

Because of their importance as reactive chemical intermediates, the novelty of their reactions and their unusual spectroscopy, carbenes continue to be the focus of intense study in many laboratories around the world. We have found that the approach of picosecond laser spectroscopy we have used is a powerful tool in the study of these systems. Further studies on the effects of carbene structure on the photophysical and photochemical properties of these species remains a key challenge confronting us.

*This work is also supported by the Air Force Office of Scientific Research under Grant AFOSR-84-0013 and the National Science Foundation under Grant NSF-CHE82-11593.

- (1) (a) Y. Wang, E. V. Sitzmann, F. Novak, C. DuPuy, and K. B. Eisenthal, *J. Am. Chem. Soc.*, **104**, 3238 (1982); (b) E. V. Sitzmann, Y. Wang, and K. B. Eisenthal, *J. Phys. Chem.* **87**, 2283 (1983); E. V. Sitzmann, J. Langan, and K. B. Eisenthal, *Chem. Phys. Letters* **102**, 446 (1983).

V. GENERATION AND CONTROL OF RADIATION

A. OPTICAL COHERENT TRANSIENT SPECTROSCOPY*

(R. Beach, D. DeBeer, R. Kichinski, E. Xu, S. R. Hartmann)
(JSEP work unit 9, 1982-1985)
(Principal Investigator: S. R. Hartmann (212) 280-3272)

With all four experimental stations in our laboratory now using the same design dye laser (Littman cavity with a 4-prism beam expander) we have achieved a greater flexibility in the setting up, and modifying of experiments. Currently ten of these dye lasers are being used, all pumped by the second or third harmonic of our two centrally located YAG lasers. Our centralized computer system, which we use for data acquisition and experiment control as well as data analysis, has been upgraded, doubling the amount of RAM available to users and making 80 M bytes of on-line disc as well as 20 M bytes of magnetic tape storage available for use by each of the experimental stations.

Angled beam photon echo experiments in atomic lithium vapor have been extended to the $2^2S_{1/2} - 2^2P_{1/2}$ transition, complementing the work previously done on the $2^2S_{1/2} - 2^2P_{3/2}$ transition. The results of these two sets of experiments are in good agreement with the predictions of the Elliptical Billiard Ball Echo model for the effects of excitation beam angling on the photon echo intensity.⁽¹⁾ Figure 1 presents our experimental results for the decay of the photon echo intensity with increasing pulse separation for experiments performed at two different beam anglings.

Fig. 2 shows the sequence of events leading to an echo signal in an angled beam experiment as they would be viewed in the Elliptical Billiard Ball Model. The imperfect overlap of ground and excited states results from the use of angled beams and leads to a smaller echo intensity than would be

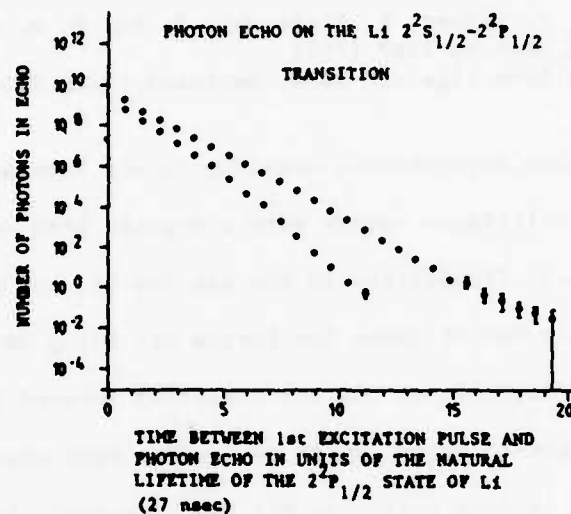


Figure 1. Number of photons in the echo vs. time between pulse 1 and the echo in units of the natural lifetime of the $2^2P_{1/2}$ state of lithium (27 nsec). The angles between the excitation pulses are 0.70 ± 0.06 and 1.35 ± 0.06 for the solid and open dots, respectively. These experiments were performed at a temperature of 609 K, as measured by thermocouples strapped to the outside of the sample cell.

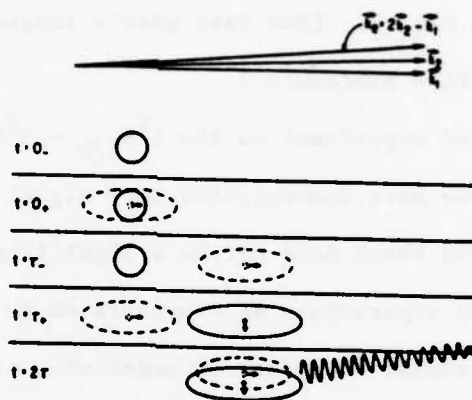


Figure 2. Sequence of events leading to an echo with sub-Doppler, angled beams, as viewed in the Elliptical Billiard Ball Echo Model. Sub-Doppler linewidth excitation pulses at times $t=0$ and τ generate the wavepacket amplitudes that lead to the photon echo at time 2τ . The imperfect overlap of ground (solid line contour) and excited (dashed line contour) states at time 2τ results from the non-parallel excitation beams.

observed had parallel excitations been used. As with the earlier $2^2S_{1/2} - 2^3P_{3/2}$ experiment⁽²⁾ we compare our results with the predictions of the Elliptical Billiard Ball Model by plotting the ratio of the two signals at the two different excitation beam anglings along with the corresponding prediction of the model in Fig. 3. (See last year's progress report for a more detailed description of this procedure.)

In a related experiment on the $3^2S_{1/2} - 3^2P_{3/2}$ transition of atomic sodium,^{(3),(4)} we have demonstrated that signal degradation due to the use of angled excitation beams need not be a significant factor even when working at very large pulse separations as demonstrated by the data presented in Fig. 4. The data spans almost 12 orders of magnitude, allowing us to see signals from atoms that had been in their excited state more than 23 natural lifetimes. The smallest signal corresponds to a lifetime decay term in of $e^{-23.3} = 7.6 \times 10^{-11}$, while the degradation due to beam angling, a factor of $e^{-2(q_0 v_{\text{recoil}})^2 \tau^2}$ in the expression for echo intensity as a function of excitation beam angling and time separation, is only 0.4. One of the important results of this experiment, in addition to demonstrating the large dynamic range over which echoes can be observed, is that it establishes the angled beam technique as a useful method for separating the excitation pulses from the echo signal even in situations where the intention is to measure something other than the effect of beam angling on echo intensity.

A new line of investigation concerns the use of chaotic (thermal) excitation pulses to generate photon echoes. We have just completed such an experiment on the $3^2S_{1/2} - 3^2P_{3/2}$ transition of atomic sodium, generating optical coherent transient signals by means of incoherent excitations. Optical coherent transient experiments have traditionally been performed with coherent (laser) light.⁽⁵⁾⁻⁽¹³⁾ While this may be essential for experiments

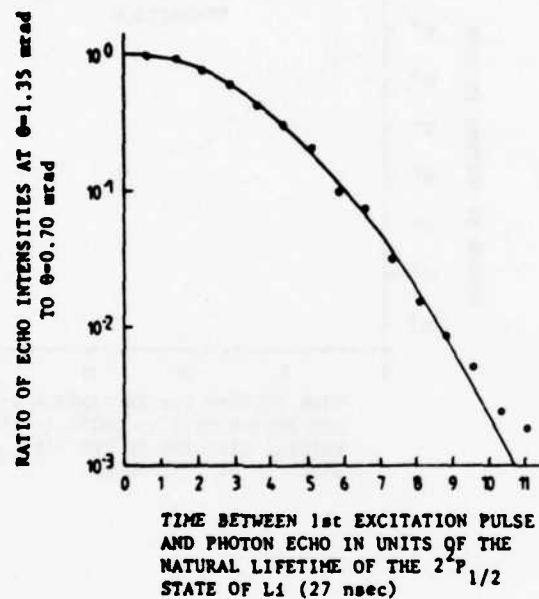


Figure 3. The ratio of the echo signals for the two angles plotted separately in Fig. 1 (circles). The solid line is the prediction of the Billiard Ball model for this ratio.

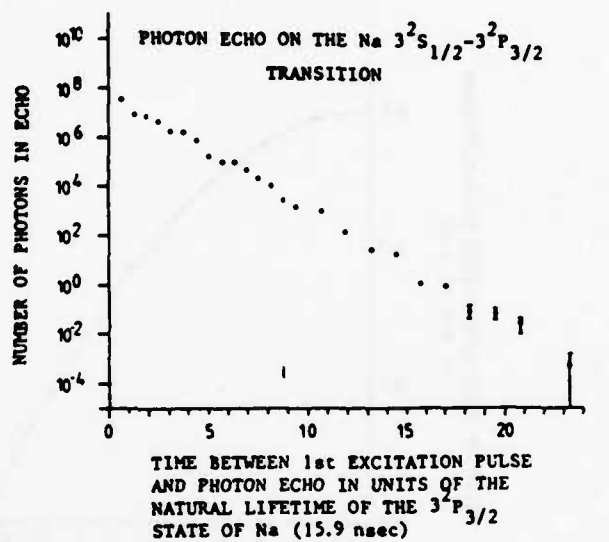


Figure 4. Echo intensity vs. time between the first excitation pulse and the echo in a two-pulse photon echo experiment performed on the Na $3^2S_{1/2} - 3^2P_{3/2}$ transition with an angle of 0.64 ± 0.07 mrad between the excitation beams. Time is indicated in units of the 15.9 nsec natural lifetime of the $3^2P_{3/2}$ state.

involving self-induced transparency and perhaps others, it appears to not be a universal requirement. Indeed not only can optical coherent transients be generated with an incoherent lamp replacing a coherent laser, but there are decided advantages in doing so. Optical transitions can be induced only within the bandwidth of the excitation source: for a laser oscillating in at most a few well-defined modes, this means that only a small fraction of the atoms or molecules within the resonance line participate in an experiment. Even worse, if a given experiment requires successive excitation of a single resonance by more than one laser, tuning requirements are determined by the width of the lasing modes rather than the much broader width of the optical inhomogeneous or Doppler broadened resonance line. These problems are circumvented with the use of (broadband) thermal sources.

The key to dealing with what one might call noise-induced coherent transients is to focus attention on the bandwidth $\Delta\omega = \pi/\tau$, determined by the length τ of the pulse, around any specific frequency. Within this bandwidth, the fields must be coherent no matter what their source by virtue of the uncertainty principle. In the small pulse area limit a coherent pulse of length τ only excites optical transitions lying within this bandwidth.⁽¹⁾ Successive applications of noise pulses can therefore be analyzed separately in each frequency interval $\Delta\omega = \pi/\tau$ by standard methods and the results from the sum of distinct frequency intervals covering the thermal line, incoherently combined. Even though the radiation source for each interval $\Delta\omega = \pi/\tau$ is chaotic and not coherent the resulting induced radiative moment is still very large.

The practical realization of an intense tunable narrow band thermal source is obtained by removing the output mirror from a Hänsch-type dye laser. This output can be spatially filtered and further amplified to produce thermal

pulses of arbitrary intensity. With a pair of such sources we have generated echoes from the 3S-3P transition in Na vapor, as shown in Fig. 5. These echoes were generally the same size as the echoes we observed using laser-produced coherent excitation pulses.

In a pulse of thermal light, the relative probability of finding n photons in a single mode is given by the Bose-Einstein formula

$$\rho_n = [1 - \exp(-h\nu/kT)] \exp(-nh\nu/kT) \quad (4)$$

which we use in the high temperature limit

$$\rho_n = \bar{n}^{-1} \exp(-n/\bar{n}) \quad (5)$$

where $\bar{n} = kT/h\nu$ is the average number of photons per mode, h is Plank's constant, $\nu = \omega/2\pi$ is the optical center frequency, k is Boltzmann's constant and T is the temperature.⁽¹⁴⁾ For a collimated beam of light of cross-sectional area A , with electric field amplitude E and duration τ , the number of photons associated with the mode whose bandwidth is $\Delta\omega = \pi/\tau$ is then obtained by equating the field energy $(1/8\pi)E^2 A c \tau$, where c is the velocity of light, to the total photon energy $nh\nu$. The corresponding pulse area θ is $\gamma E \tau = \gamma \sqrt{(8\pi h \tau / A \lambda)} \bar{n}$ where γ is the gyroelectric ratio.

We start by restricting ourselves to a single mode. For an excitation sequence of two pulses of area θ' and θ'' the regenerated dipole moment which gives rise to the photon echo is given by

$$p_{\text{echo}} = p_0 \sin \theta' (1 - \cos \theta'')/2 \quad (6)$$

where p_0 is the maximum possible value of p_{echo} . The radiated echo intensity is proportional to the average value of p_{echo} which for incoherent excitations - incoherent also with respect to each other - we obtain by taking the product of the average value of $\sin^2 \theta'$,

$$\sin^2 \theta' = \int_0^\infty \bar{n}_1^{-1} \exp(-n/\bar{n}_1) \sin^2(\theta_1 \sqrt{n/\bar{n}_1}) dn, \quad (7)$$

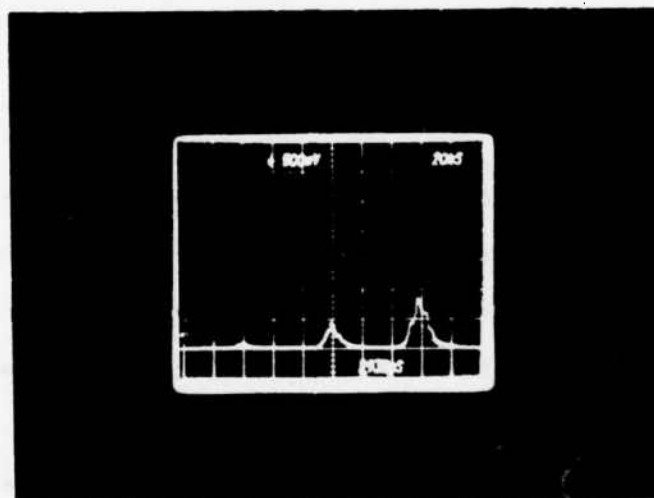


Figure 5. Oscilloscope trace of excitation pulse 1, 2, and the photon echo on the $3^2S_{1/2} - 3^2P_{3/2}$ transition in Na vapor as seen at the output of a photomultiplier. Excitation pulse separation is 60 nsec so the echo appears more than 7 lifetimes after the first pulse. Echo signals at shorter pulse separations are as much as 1,900 times larger.

with the average value of $[(1-\cos\theta'')/2]^2$,

$$\overline{[(1-\cos\theta'')/2]^2} = \int_0^\infty \bar{n}_2^{-1} \exp(-n/\bar{n}_2) [(1-\cos\theta_2 \sqrt{n/\bar{n}_2})/2]^2 dn. \quad (8)$$

Denoting by θ_j the rms pulse area associated with $n = \bar{n}_j$ we find

$$\overline{\sin^2\theta'} = f(\theta_1) \quad (9)$$

and

$$[(1-\cos\theta'')/2]^2 = f(\theta_2/2) - (1/4)f(\theta_2), \quad (10)$$

where $f(\theta) = \theta \exp(-\theta^2) \int_0^\theta \exp(t^2) dt$. The product $\overline{\sin^2\theta' [1-\cos\theta'']/2^2}$ reaches its maximum value of $(.64)(.51) = .33 \sim 1/3$ at $\theta_1 = 1.5 = (.96)(\pi/2)$ and $\theta_2 = 3.1 = (.97)(\pi)$. The average echo intensity is thus expected to be down by a factor of three from the intensity of a laser induced echo. In any event, these results only obtain outside the small angle limit where the approximate treatment we present does not apply. In the small angle limit the regenerated moment, Eq. (6), is linear in θ' and θ''^2 , suggesting that our results can be corrected in an approximate manner by introducing multiplicative factors η and η^2 into the terms $\sin \theta'$ and $(1-\cos\theta'')/2$, respectively. The expected regenerated moment squared then becomes

$$P_{\text{echo max}}^2 = (1/3)\eta^6 P_0^2 \quad (11)$$

where $\eta < 1$. As we shall see, our experimental work suggests that $\eta = .8$.

Assuming that the excitation pulses cover the resonance linewidths the total radiated photon echo signal is greater than the intensity calculated for a single mode by the ratio of the resonance linewidth to the mode bandwidth $\Delta\Omega/\Delta\omega$. The adjacent modes of the noise field, separated by more than $\Delta\omega = \pi/\tau$, cannot interfere and must be incoherently combined. For a pulse width of $\tau = 7$ nsec and a sample such as sodium, $\Delta\Omega/2\pi = 2\text{GHz}$, whereas $\Delta\omega/2\pi = 70$ MHz:

there is echo enhancement over that which would be attained by a single mode laser by a factor of $(29)(1/3)n^6 = 10n^6$.

The apparatus used in the experiment is shown in Figs. 6 and 7. Except for the replacement of two dye laser oscillators by two thermal radiation sources (TS) (i.e., zero point photon amplifiers) this is the apparatus that would be used in an ordinary two-pulse angled-beam echo experiment.⁽²⁾ The pump beams are the frequency-doubled outputs of two Quanta-Ray DCR-1A YAG lasers. The output pulses from the thermal radiation sources are 7 nsec long (FWHM) and have a bandwidth of approximately 10 GHz as viewed on a 14.5 GHz free spectral range Fabry-Perot etalon. No stable mode structure was observed on this 10 GHz line as would be observed with coherent laser radiation. The central frequency of these thermal radiation pulses can be varied within the gain curve of the dye being used (R610 in methanol) by rotation of the 2400 g/mm Littrow grating, as indicated in Fig. 7. Tuning the two radiation sources to the resonance line is easier than if lasers had been used, as now the relevant bandwidth of the radiation is 10 GHz rather than the transform-limited 70 MHz bandwidth associated with the active modes in our laser. The output pulses from the thermal radiation sources are amplified once in a longitudinally-pumped flowing-dye (R610 in methanol again) cell, and finally combined at a small angle of about 0.6 mrad. The excitation pulses are then sent through a telescopic beam expander and into a sample cell approximately 10 cm long and 1.5 cm in diameter containing sodium vapor. The echo, observed to emerge from the sample in the direction of $2\vec{n}_2 - \vec{n}_1$ where \vec{n}_1 and \vec{n}_2 are the directions of pulses 1 and 2 respectively, is separated from the excitation pulses by means of a combination of spatial filtering and time gating of a Pockels cell shutter.

Fig. 5 is a photograph of an echo generated with excitation pulses

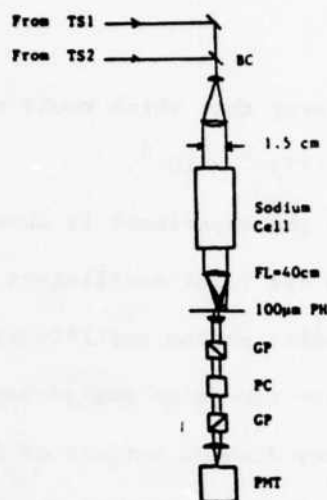


Figure 6. Schematic diagram of our experimental setup. Here TS stands for thermal radiation source, BC for beam combiner, PH for pinhole, GP for Glan prism, FL for focal length, and PC for Pockels cell shutter.

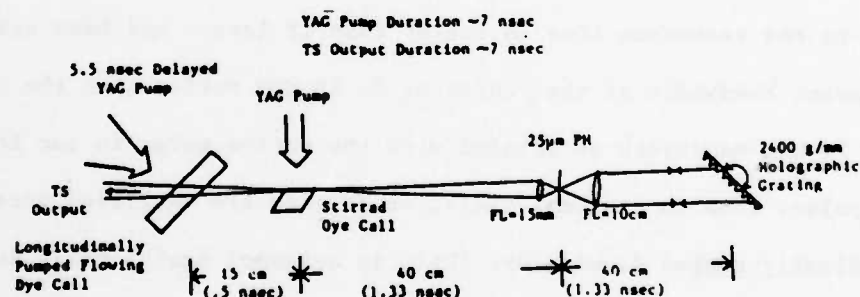


Figure 7. Schematic diagram of the thermal radiation sources used to generate the excitation pulses in our experiment. The dimensions were chosen to minimize the possibility of forming an optical cavity by spurious reflections or scatterings. The formation of such a cavity would lead to a stable mode structure in the output and destroy the chaotic (thermal) nature of the desired excitation pulses.

separated by 60 nsec. The central frequencies of the thermal radiation sources had been tuned to the sodium $3^2S_{1/2} - 3^2P_{3/2}$ transition. Pulses 1 and 2 contained roughly 1.3×10^{12} photons and 8.1×10^{12} photons, respectively. These pulses are greater in intensity than the corresponding excitation pulses used with a laser source by the order of the ratio of the 10 GHz thermal bandwidth to the transform-limited 70 MHz bandwidth. After optimizing the excitation pulse amplitudes and the sodium cell temperature the echoes at $(2)(60) = 120$ nsec after the first excitation pulse contained roughly 3.5×10^4 photons. The optimum temperature was found to be the same as that which optimized echo experiments performed with coherent laser sources replacing the thermal sources.

In order to make a connection with our theoretical estimates of incoherently generated echo intensity, we compare the number of photons in the incoherently generated echo at an excitation pulse separation of 60 nsec with the number of photons in a coherently (laser) generated echo under the same experimental conditions. The incoherent echo intensity corresponded to 3.5×10^4 photons at a pulse separation of 60 nsec, while the number of photons in a coherently generated echo was found to be 2.5×10^4 at this pulse separation. For the coherently generated echo, lasers were used that generally ran in two modes so that the number of photons per mode in this case was approximately 1.2×10^4 . This gives for the echo enhancement calculated previously $10n^6 = \frac{3.5 \times 10^4}{1.2 \times 10^4} \sim 3$, yielding $n = .8$ for our experiment. This result supports our analysis. Clearly there are more complicated processes taking place than our calculation considers and very likely an analysis that takes pulse propagation effects^{(15),(16)} and interference between neighboring modes into account is necessary. In this regard it is noteworthy that we saw no evidence of pulse breakup at increased temperatures. When previously working with laser

excitations we have always observed pulse breakup effects and in fact we have exploited them in the initial frequency tuning of the apparatus prior to performing an echo experiment. The absence of pulse breakup when using incoherent sources is to be expected as it is inherently due to large pulse area effects which we expect cannot build up with incoherent sources because of interferences from neighboring modes.

As a check on the thermal character of our excitation pulses, we generated a four-wave-mixed signal from a thermal source by taking an output pulse, splitting it, optically delaying part of it, and then recombining the two parts with a small angle ($\sim .6$ mrad) between them. The signal was then detected in the phase matching direction $2\vec{n}_2 - \vec{n}_1$, where \vec{n}_1 and \vec{n}_2 are the directions of pulses 1 and 2, respectively. This signal, measured as a function of the delay between the pulses, is displayed in Fig. 8. The corresponding four-wave-mixed signal when we used an oscillator cavity in place of the thermal source always displayed a strong beating with period $2L/c$, where L is the cavity length of the oscillator. No such structure was observed with our thermal source.

The effective rise time of the four-wave-mixed signal in Fig. 4 near zero delay was on the order of 100 psec. This suggests that echo experiments using incoherent excitations may be performed with a time resolution in that order.

Echo experiments in sodium vapor using coherent excitations have shown a weak modulation of echo intensity with pulse separation^{(3),(4)} and we observe the same with incoherent excitation. This is to be expected as each regenerated moment associated with each interval $\Delta\omega$ is similarly modulated. The implication of the above work is that echo generation is possible on resonance lines of arbitrary width. But even though the linewidths are wide echo modulation effects due to coherent beating of the hyperfine levels are

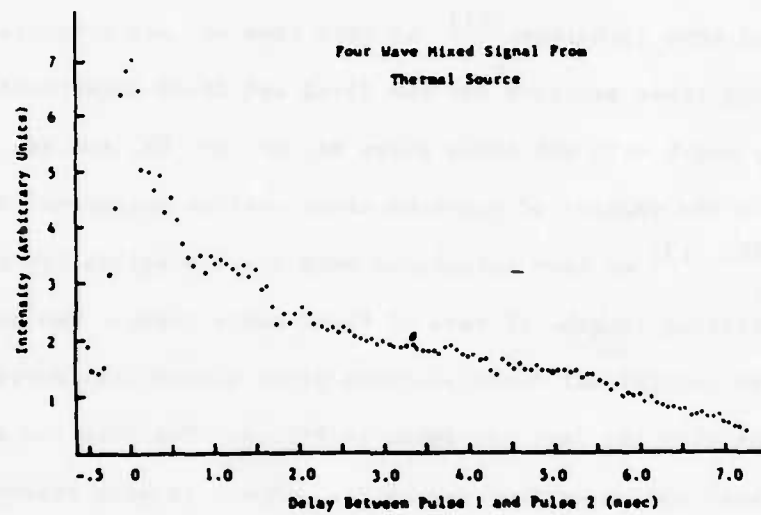


Figure 8. Four-wave-mixed signal, generated using one thermal source, as a function of pulse separation. The absence of any large scale beating demonstrates that there is no stable mode structure in the thermal excitation pulses.

still present so that high resolution spectroscopy is still feasible. Broadband information storage and retrieval possibilities are thereby expanded.

In another ongoing series of experiments we are measuring the noble gas induced relaxation of similar parity states in atomic lithium using a tri-level echo technique.⁽¹⁷⁾ At this time we have completed measurements of broadening cross sections for the 2S-nS and 2S-nD superposition states for $n = 4, 5$, and 6 with the noble gases He, Ne, Ar, Kr, and Xe.

From the results of previous cross section measurements in atomic sodium^{(18),(19)} we have calculated more precise values for the polarizability and scattering lengths of each of these noble gases. Two parameters fit to the 3S-nS collisional cross-sections gives theoretical curves in good agreement with the data, as shown in Fig. 9. The data for lithium thus far, using these sodium-derived parameters, appear to give reasonable agreement between theory and experiment for all the noble gases but neon, as shown in Fig. 10. We do not yet know the reason for this.

To facilitate measuring 2S-nS and 2S-nD cross sections for higher n states we are now incorporating a non-linear doubling crystal into our dye laser system. This will allow us to double a dye laser frequency at the red end of the spectrum. We have otherwise been unable to generate sufficiently intense excitation pulses for our measurements at a wavelength of ~ 380 nm by using a blue dye in our laser and pumping with the 3rd harmonic of the YAG.

At the present time we are setting up an experiment to see if we can observe a collisionally generated coherence in atomic Na vapor. The photon echo, because of its large dynamic range is an ideally suited method for trying to observe such an electronic state coherence produced in a combined laser field-collisional reaction. The experiment now under development will be carried out on the $3^2S_{1/2} - 3^2P_{3/2}$ transition of sodium. Three lasers will

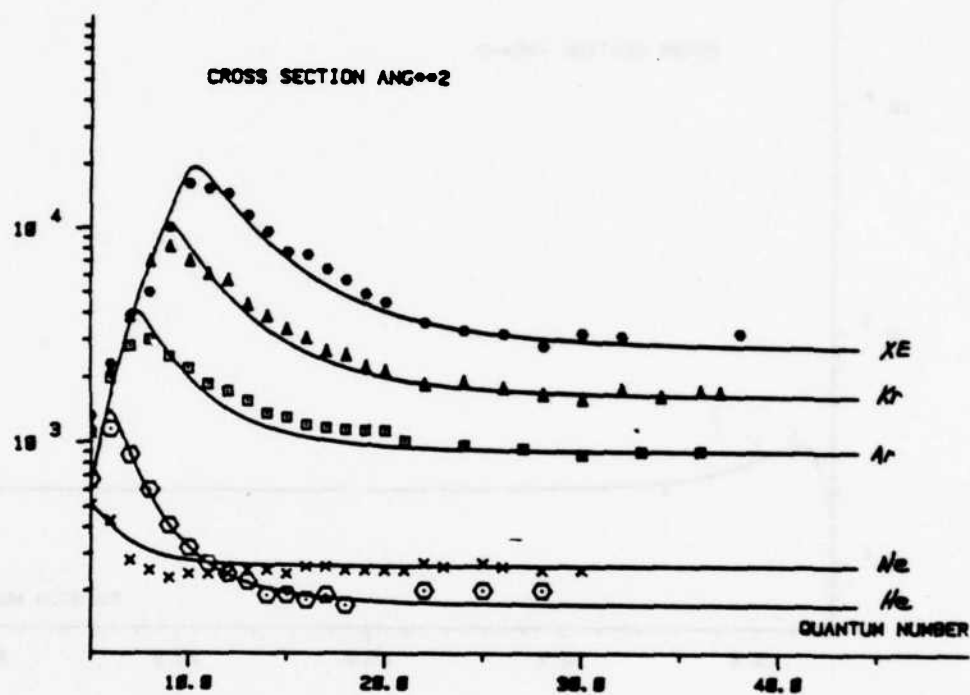


Figure 9. Collisional broadening cross sections for sodium perturbed the noble gases. The solid line is a theoretical fit to the 3S-nS superposition state cross sections.

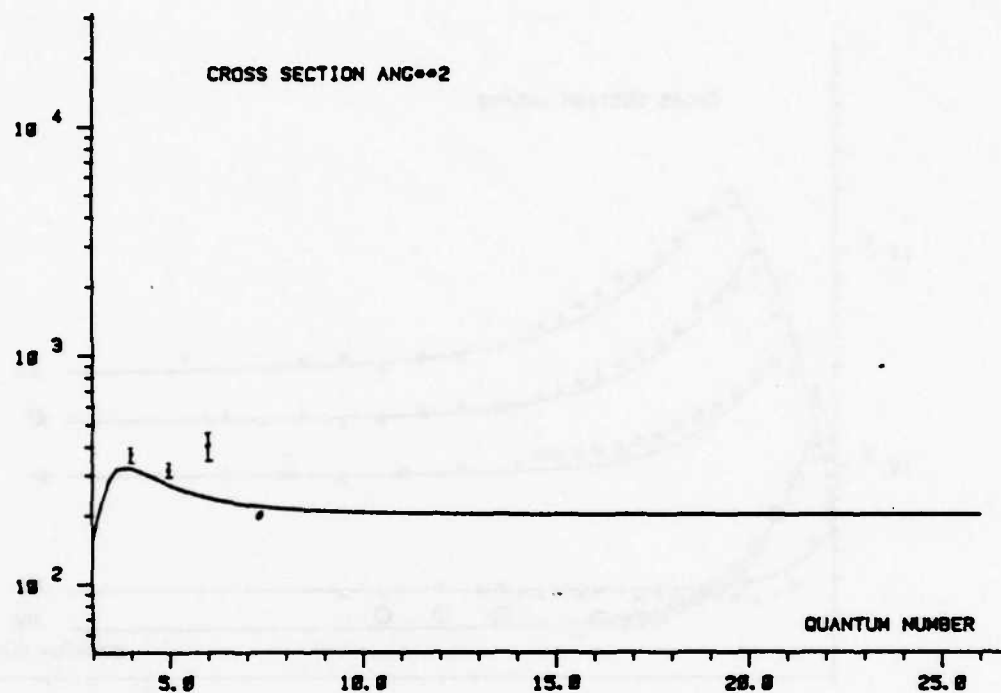


Figure 10. Broadening cross sections for lithium 2S-nS and 2S-nD superposition states perturbed by Ne, measured using a tri-level echo. The solid line is the theoretical prediction.

be used. One will be tuned to the center of the Doppler broadened line of this transition and the other two will be tuned off the line, one above, and the other by the same amount below. The detuning of the second and third lasers will be by an amount on the order of $k_B T$ so that in the absence of collisions between sodium atoms and perturber gas atoms there will be no signal. Figure 11 displays the recoil and energy level diagram for the process under consideration. By measuring the coherence producing cross section as a function of the strength and frequency of the applied excitations information about the sodium-perturber gas interatomic potentials can be gained. (20), (21)

In another series of experiments, we used two beams from a single dye laser to probe the $^3P_0 - ^3H_4$ transition in $\text{LaF}_3:\text{Pr}^{3+}$. We have observed unexpected "satellite" echoes as far as 12 \AA away from the center of the line ($\lambda = 4777 \text{ \AA}$), averaging only 100 smaller than the echo signal on the main transition which itself is only 10 - 100 smaller than the excitation pulses. The excitation beam configuration was that of the "backward wave" photon echo, (22) which results in perfect phase matching and a high signal-to-noise ratio. The signal spectrum is roughly as shown in Fig. 12.

These satellite echoes have yet to be explained. Echo signals at the center of this transition ($\lambda = 4777 \text{ \AA}$) were a factor of 10 - 100X smaller than the excitation pulses, which in this case were approximately 20-30 kW apiece in peak power. With the expected installation of two independent dye lasers at this frequency echo signals on the order of 1 kW (peak power for a 10 nsec. pulse) will be readily attainable. Echo modulation studies will then be possible to shed light on the origin of these signals.

Finally we have observed excited state photon echoes on the $^3P_0 - ^3H_6$ transition of $\text{LaF}_3:\text{Pr}^{3+}$ whose level scheme is shown in Fig. 13. The

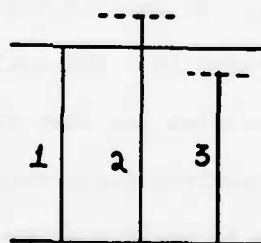
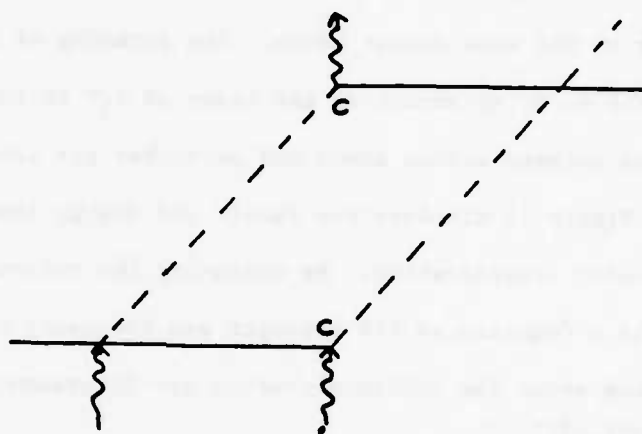


Figure 11. (a) Recoil diagram for electronic state coherence produced in combined laser-field-collisional reaction. The solid and dashed lines denote ground and excited state trajectories respectively. A c denotes vertices that represent collisionally aided transitions. (b) Energy level diagram showing the three excitation energies used. Pulse 2 is detuned above the resonance by the same amount as pulse 3 is tuned below it.

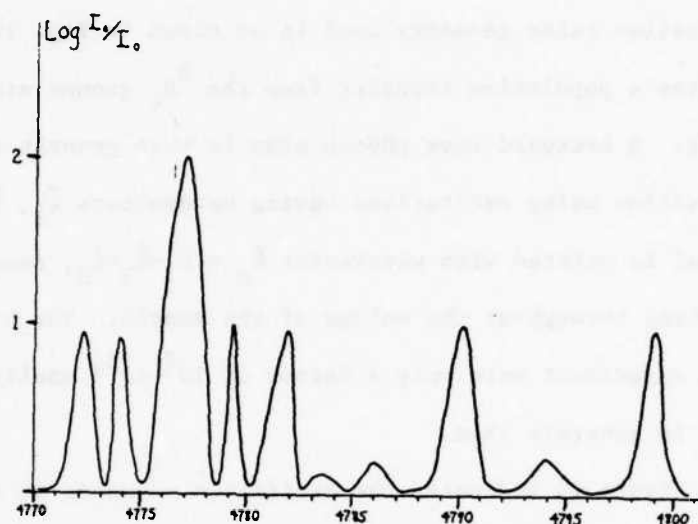


Figure 12. Spectrum of "satellite" echoes in the vicinity of the ${}^3P_0 - {}^3H_4$ transition of $\text{LaF}_3:\text{Pr}^{3+}$.

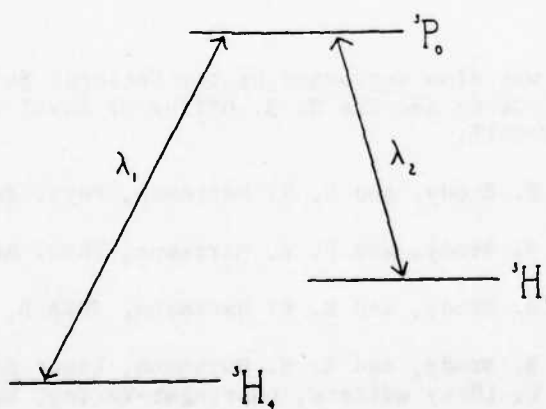


Figure 13. Level scheme for relevant states. 3H_4 is the ground state in $\text{LaF}_3:\text{Pr}^{3+}$. $\lambda_1 = 4777 \text{ \AA}$, $\lambda_2 = 5985 \text{ \AA}$.

excitation pulse geometry used is as shown in Fig. 14. In this figure, \vec{k}_4 excites a population transfer from the 3H_4 ground state to the 3P_0 excited state. A backward wave photon echo is then generated on the $^3P_0 - ^3H_6$ transition using excitations having wavevectors \vec{k}_1 , \vec{k}_2 and \vec{k}_3 . The echo signal is emitted with wavevector $\vec{k}_e = \vec{k}_1 - \vec{k}_2 + \vec{k}_3$, resulting in perfect phase matching throughout the volume of the sample. The biggest signals observed in this experiment were only a factor of 10^2 - 10^3 smaller than the excitations used to generate them.

Figure 15 indicates the excitation sequence we will use to generate a tri-level echo on these same transitions. The tri-level echo experiment is important as it will tell us how the energy levels of Pr^{3+} are correlated in the LaF_3 crystal due to the inhomogeneous crystal strain field.⁽²³⁾ We plan to investigate the topology of the 3H_4 , 3P_0 , 3H_6 , etc., energy surfaces by performing generalized tri-level echo experiments in non-equivalent configurations.

*This research was also supported by the National Science Foundation under Grant NSF-DMR80-06966 and the U. S. Office of Naval Research under Contract No. N00014-78-C-0517.

- (1) R. Beach, B. Brody, and S. R. Hartmann, Phys. Rev. A, 27, 2537 (1983).
- (2) R. Beach, B. Brody, and S. R. Hartmann, Phys. Rev. A, 27, 2925 (1983).
- (3) R. Beach, B. Brody, and S. R. Hartmann, JOSA B, 1, 189 (1984).
- (4) R. Beach, B. Brody, and S. R. Hartmann, Laser Spectroscopy VI, H. P. Weber and W. Lüthy editors, (Springer-Verlag, New York, 1983).
- (5) N. A. Kurnit, I. D. Abella, and S. R. Hartmann, Phys. Rev. Lett. 13, 567 (1964); Phys. Rev. 141, 391 (1966).
- (6) S. L. McCall and E. L. Hahn, Phys. Rev. Lett. 18, 908 (1967); Phys. Rev. 183, 457 (1969).
- (7) C. K. N. Patel and R. E. Slusher, Phys. Rev. Lett. 20, 1087 (1968).

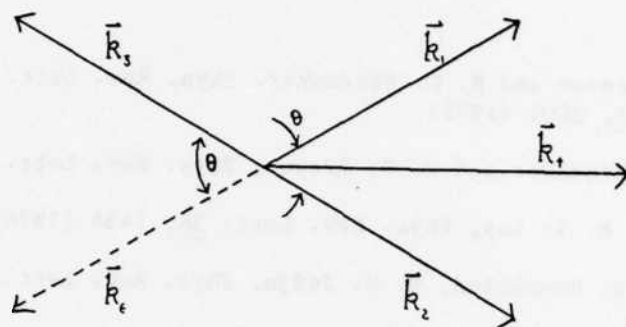


Figure 14. Pulse scheme for excited state photon echo in $\text{LaF}_3:\text{Pr}^{+3}$. Wave vectors are shown for relevant laser pulses, $|\vec{k}_1| = |\vec{k}_2| = |\vec{k}_3| = 2\pi/\lambda_2$, $|\vec{k}_4| = 2\pi/\lambda_1$.

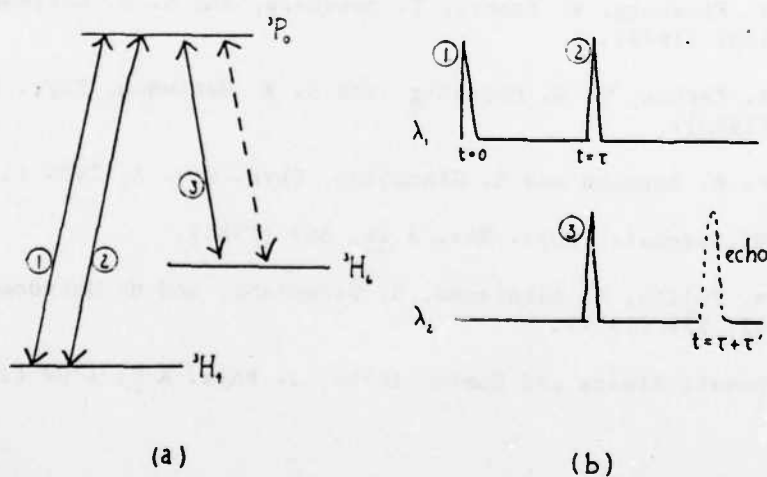


Figure 15. (a) Same level scheme as before, but different pulse sequence. Numbers refer to \vec{k}_1 , \vec{k}_2 , \vec{k}_3 , dotted line indicates echo. $|\vec{k}_1| = |\vec{k}_2| = 2\pi/\lambda_1$. $|\vec{k}_3| = 2\pi/\lambda_2$. (b) Pulse timing sequence. τ is separation between pulses 1 and 2. τ' is separation between pulse 3 and echo.

- (8) R. G. Brewer and R. L. Shoemaker, Phys. Rev. Lett. 27, 631 (1971); Phys. Rev. A 6, 2001 (1972).
- (9) R. L. Shoemaker and R. G. Brewer, Phys. Rev. Lett. 28, 1430 (1972).
- (10) Michael M. T. Loy, Phys. Rev. Lett. 36, 1454 (1976).
- (11) P. Hu, S. Geschwind, T. M. Jedju, Phys. Rev. Lett. 37, 1357, 1733(E) (1976).
- (12) T. Mossberg, A. Flusberg, R. Kachru, and S. R. Hartmann, Phys. Rev. Lett. 39, 1523 (1977).
- (13) M. Fujita, H. Nakatsuka, H. Nakanishi, and M. Matsuoka, Phys. Rev. Lett. 42, 974 (1979).
- (14) Marian O. Scully and Willis E. Lamb, Jr., Phys. Rev. 159, 108 (1967).
- (15) E. L. Hahn, N. S. Shiren, and S. L. McCall, Phys. Lett. 37A, 285 (1971).
- (16) R. Friedberg and S. R. Hartmann, Phys. Lett. 37A, 285 (1971).
- (17) T. Mossberg, A. Flusberg, R. Kachru, and S. R. Hartmann, Phys. Rev. Lett. 39, 1523 (1977).
- (18) A. Flusberg, R. Kachru, T. Mossberg, and S. R. Hartmann, Phys. Rev. A 19, 1607 (1979).
- (19) R. Kachru, T. W. Mossberg, and S. R. Hartmann, Phys. Rev. A 21, 1124 (1980).
- (20) P. R. Bermann and E. Giacobino, Phys. Rev. A, 2900 (1983).
- (21) M. Dagenais, Phys. Rev. A 26, 869 (1982).
- (22) M. Fujita, H. Nakatsuka, H. Nakanishi, and M. Matsuoko, Phys. Rev. Lett. 42, 974 (1979).
- (23) Masaki Aihara and Humino Inaba, J. Phys. A 6, 1709 (1973).

SIGNIFICANT ACCOMPLISHMENTS AND TECHNOLOGY TRANSITION REPORTS

Significant Accomplishments

I. Quantum Detection and Sensing of Radiation

We have shown from a theoretical point of view that the particle-like properties of electrons can be transferred to photons on a one-to-one basis, leading to a method for generating a new kind of "quiet" light.

Using orthogonal modulation (frequency-shift keying and pulse-position modulation) in a fiber optic system, we have demonstrated experimentally a 4dB improvement in performance compared to nonorthogonal (amplitude) modulation.

We have investigated and understood the effects of crosstalk and suboptimal threshold on the performance of a fiber optic system.

II. Physical and Photochemical Properties of Electronic Materials

We have developed a new theoretical model to understand the performance and collection efficiency of thin-film metal-insulator-semiconductor (MIS) photovoltaic devices.

The laser-induced photoconductance transient response of polycrystalline silicon has been studied theoretically and experimentally.

MOSFETs with one quarter micrometer and sub-quarter micrometer channel lengths, which operate with controlled punchthrough current, were analyzed by two-dimensional numerical modeling. A new novel technique for fabricating ultra-short gates on MOSFETs has been discovered and a patent application filed.

Ultraviolet photolysis, using an ArF excimer laser, has been used to

dry-etch a large area of single-crystal GaAs. When HBr molecules are used as the etching parent molecules, the process is extremely rapid, i.e. $\sim 6 \mu\text{m}/\text{min}$, and anisotropic. In this process, the charge particle damage which is seen in plasma processing is absent.

We have investigated systematically the variation of the conductivity of laser-written metal lines with changes in several of the major deposition parameters. Lines with a resistivity of ~ 4 times that of the bulk metal were obtained.

We have found that controlled holographic photochemical etching of GaAs can be used to produce submicrometer gratings with unusual and reproducible profiles on GaAs. In addition, we have recently made 100-nm period gratings using this technique and discovered that deep-UV radiation can be used to etch, nonthermally and rapidly, unique $1\text{-}\mu\text{m}$ -wide vias through $150 \mu\text{m}$ -thick GaAs wafers. This work has elicited a good deal of interest for making electrooptical devices of compound semiconducting material.

III. Generation and Dynamic Properties of Metastable Species for Quantum Electronics

We have produced ion and radical molecular beams using a simple supersonic expansion coupled with an electrical discharge. All neutrals in the beam were found to have a low translational temperature (17 K for CF_4) while the ions were found to be energetic (25 eV) with a considerable spread in translational energy (2.5 eV).

We have determined the vibrational energy distribution of CH_3 radicals produced when $\text{Cd}(\text{CH}_3)_2$ and $\text{Zn}(\text{CH}_3)_2$ are photodissociated using ultraviolet laser light. These fundamental photophysical and photochemical phenomena are important in developing laser direct writing for microelectronics.

We have determined experimentally the collisional energy transfer rates for the lower levels of the CO_2 laser in pure CO_2 gas. These transfer rates, which have remained unknown despite advances in techniques for the study of vibrational energy transfer, are of fundamental importance for the engineering of a CO_2 laser.

Using a new, extraordinarily powerful, very high resolution diode laser probe technique, we have determined the energy transfer dynamics of collisions between hyperthermal H atoms and CO_2 . In addition we have used this same experimental method to map the states produced during the photodissociation of medium sized molecules.

IV. Picosecond Energy Transfer and Photofragmentation Spectroscopy

The first studies of the excited state chemistry of a carbene, an important class of reactive, short-lived, chemical intermediates have been made. New, very rapid reactivities, vastly different from the ground state, were observed for the excited triplet state of diphenylcarbene.

A very large solvent effect was observed for the first time in the intramolecular relaxation of diphenylcarbene. This result has important implications in the chemistry and photophysics of this class of molecules.

We have shown that rapid equilibration between the highly polar twisted form (12 Debye) and the less polar planar form of dimethyl-amino benzonitrile (DMABN) occurs not only in hydrogen bonding solvents but also in non-hydrogen-bonding solvents, e.g. nitriles. We have found that the key role of the solvent in the dynamics of the excited state structural change can be analytically expressed as an exponential dependence of the rate constant on the solvent polarity.

V. Generation and Control of Radiation

Photon echoes have been generated in atoms excited more than 23 lifetimes earlier. These experiments were performed in atomic sodium vapor where signals were observed over an unprecedented dynamic range exceeding 10^{11} .

Photon echoes have been generated using incoherent (thermal) excitation pulses. This suggests that echo signals can be generated on arbitrarily wide transitions expanding the possibilities for broadband information storage and retrieval.

Technology Transition Reports

1. The first direct-detection frequency-shift keyed fiber optic system has been built at Columbia, at 100 Mbits/sec, with a frequency shift of 2.5 nm, and an error rate of 10^{-9} at 51 dB optical loss between source and detector.
2. The fabrication of submicrometer gratings by laser photochemical holography has been pioneered in the Columbia Radiation Laboratory. One of the obvious applications of this technology is in the fabrication of gratings for distributed feedback (DFB) diode lasers. A group at Bell Laboratories is, in fact, using the techniques developed at Columbia to produce DFB lasers.
3. The research in laser-direct writing of conductors at Columbia continues to draw outside interest. Applications of this technology to industries include repair of electronic packaging and IC testing. IBM and ITT have expressed interest in using this work for packaging and testing, respectively.

4. The development of a Microelectronics Sciences Laboratory at Columbia has been recognized by nearby industries as an important focal point for basic research and education in microelectronics in the New York tristate area. During this year, this recognition has been exemplified by a multiplicity of visits between Columbia and companies such as ITT, Grumman, and Singer-Kearflot. In addition, IBM has helped to enhance the research capabilities of the microelectronics laboratories in a more concrete way by donating \$300,000 to help equip the microfabrication laboratory and a laboratory for undergraduate research. They also have donated an ion implanter and several smaller surplus items to the laboratory.

5. A patent is pending which describes "A Simple Method for Fabricating Ultra-Short-Gates on MOSFETs" developed by Professor Hwang with graduate students Fang and Grossman.

PERSONNEL

Faculty

K. Eisenthal, Professor of Chemistry
G. Flynn, Professor of Chemistry, Director
S. Hartmann, Professor of Physics
W. Hwang, Associate Professor of Electrical Engineering
R. Osgood, Professor of Electrical Engineering
P. Prucnal, Associate Professor of Electrical Engineering
I. Rabi, University Professor Emeritus
M. Teich, Professor of Engineering Science
E. Yang, Professor of Electrical Engineering

Visiting Scientists

Dr. Z. Baborigic
Dr. B. Brody
Mr. J. Cai
Dr. J. Perina
Dr. B. Saleh
Dr. D. Stoler

Research Associates

Dr. R. Beach	Dr. W. Lotshaw
Dr. P. Brewer	Dr. D. Miller
Dr. J. Chu	Dr. G. Reksten
Dr. H. Gilgen	Dr. E. Sitzmann
Dr. Z. Ho	Dr. M. Spencer
Dr. W. Hollingsworth	Dr. M. Vandersall

Graduate Research Assistants

T. Allik	G. Pinto
P. Beeken	D. Podlesnik
R. Bowman	E. Poon
B. Brady	E. Sanchez
C. Chen	M. Santoro
D. DeBeer	P. Shaw
H. Evans	F. Shoucair
M. Glick	T. Shu
B. Grossman	P. Siegel
J. Hicks	S. So
W. Holber	J. Song
K. Kasturi	G. Spector
R. Kichinski	J. Subbiah
R. Krchnavek	F. Tong
S. Kuo	A. Wilner
J. Langan	C. Wood
K. Matsuo	X. Wu
D. McClure	E. Xu
J. O'Neill	

Administration

Ms. K. Edwards
Ms. G. Gibson
Ms. I. Moon
Ms. W. Spiccia
Ms. V. Zell

Technician

D. Rivera

Undergraduate Technicians

G. Alli	A. Laudico
S. Anandakrishnan	W. Morrow
B. Burchfield	J. Ngai
T. Cacouris	Y. Pang
G. Escher	S. Ross
P. Fontenla	S. Stern
C. Foudas	B. Swain
W. Kang	S. Tudorov
T. Kobylarz	R. Turcott
T. Larchuk	A. Vaseekaran

JSEP REPORTS DISTRIBUTION LIST

DEPARTMENT OF DEFENSE

Director
National Security Agency
ATTN: Dr. G. Burdage, R-57
Fort George G. Meade, MD 20755

Defense Technical Information Center
ATTN: DDC-DDA
Cameron Station
Alexandria, VA 22314

Defense Advanced Research Proj. Agency
ATTN: Dr. R. Reynolds
1400 Wilson Boulevard
Arlington, VA 22209

Dr. Leo Young
Office of the Deputy Under Secretary
of Defense for Research and
Engineering (R&AT)
Room 3D1D67
The Pentagon
Washington, DC 20301

DEPARTMENT OF THE ARMY

Commander
U. S. Army Armament R&D Command
ATTN: DRDAR-TSS # 59
Dover, NJ D78D1

Director
U. S. Army Ballistics Research Lab.
ATTN: DRDAR-BL
Aberdeen Proving Ground
Aberdeen, MD 21005

Commander
U. S. Army Communications Command
ATTN: CC-OPS-PM
Fort Huachuca, AZ 85613

Commander
U. S. Army Missile Command
Redstone Scientific Inf. Center
ATTN: DRSMI-RPRD (Documents)
Redstone Arsenal, AL 35809

Commander
U. S. Army Satellite Comm. Agency
Fort Monmouth, NJ D7703

Commander
U. S. Army Atmospheric Sciences Lab.
ATTN: OELAS-AD-DM (Tech Wrtg)
White Sands Missile Range, NM 88002

Director
THI-FAC
ATTN: TT-AD (K. Lape')
Fort Monmouth, NJ D7703

Executive Secretary, TCC/JSEP
U. S. Army Research Office
P. O. Box 12211
Research Triangle Park, NC 27709

Commander
Harry Diamond Laboratories
ATTN: Technical Inf. Branch
2800 Powder Mill Road
Adelphi, MD 20783

HQDA
Washington, DC 20310

Director
U. S. Army Electronics Technology
and Devices Laboratory
ATTN: DELET-E (Dr. Jack A. Kuhn)
Fort Monmouth, NJ D7703

Commander
U. S. Army Comm. R&D Command
ATTN: DRSEL-TES-CR (Mr. David Haratz)
Fort Monmouth, NJ D7703

Director
U. S. Army Electronics Technology
and Devices Laboratory
ATTN: DELET-M (Mr. V. Gelnovatch)
Fort Monmouth, NJ D7703

Commander
U. S. Army Electronics R&D Command
ATTN: DRDEL-SA (Dr. W. S. McAfee)
Fort Monmouth, NJ D7703

U. S. Army Research, Development
and Standardization Group - CA
National Defense Headquarters
Ottawa, Ontario
CANADA KIA DK2

Commander
U. S. Army Comm. Electronics Command
ATTN: DRSEL-CDM-RM-4 (Dr. F. Schwing)
Fort Monmouth, NJ D7703

Director
U. S. Army Electronics Technology
and Devices Laboratory
ATTN: DELET-I (Mr. Harold Borkan)
Fort Monmouth, NJ D7703

Director
U. S. Army Electronics R&D Command
Night Vision and Electro-Optics Labs
ATTN: Dr. Randy Longshore, OELNV-IT
Fort Belvoir, VA 22060

Commander
U. S. Army Research Office
ATTN: ORKRO-EL (Dr. Jemee Mink)
P. O. Box 12211
Research Triangle Park, NC 27709

Commander
Harry Diamond Laboratories
ATTN: DELHD-RT-A (Mr. J. Selerno)
2800 Powder Mill Road
Adelphi, MD 20783

Director
U. S. Army Electronics R&D Command
Night Vision and Electro-Optics Labs
ATTN: DELNV-IRTD (Dr. John Pollard)
Fort Belvoir, VA 22060

Commander
U. S. Army Research Office
ATTN: DRXRD-EL (Dr. William A. Sender)
P. O. Box 12211
Research Triangle Park, NC 27709

Director
U. S. Army Electronics Technology
and Devices Laboratory
ATTN: DELET-ES (Dr. A. Tauber)
Fort Monmouth, NJ D7703

Director
Division of Neuropsychiatry
Walter Reed Army Inst. of Research
Washington, DC 20012

Commander
USA ARRADCDM
ATTN: DRDAR-SCF-ID (Dr. J. Zavada)
Dover, NJ D7801

Director
U. S. Army Signals Warfare Lab
ATTN: DELSW-D-OS
Vint Hill Farms Station
Werreneton, VA 22186

Director
U. S. Army Electronics Technology
and Devices Laboratory
ATTN: DELET-ED (Dr. E. H. Poindexter)
Fort Monmouth, NJ D7703

Commander
U. S. Army Research & Standardization
Group (Europe)
ATTN: (Dr. F. Rothwerf)
Box 65
FPD NY D9510

U. S. Army Research Office
ATTN: Library
P. O. Box 12211
Research Triangle Park, NC 27709

Commander
U. S. Army Communications Command
ATTN: DRSEL-COM-RF (Dr. T. Klein)
Fort Monmouth, NJ D7703

Mr. Jerry Brookshire
Guidance and Control Directorate
U. S. Army Missile Command
ATTN: DRSMI-RGG, Bldg. 4381
Redstone Arsenal, AL 35898

Dr. Michael Fahey
Advanced Sensors Directorate
U. S. Army Missile Command
ATTN: DRDMI-RER
Redstone Arsenal, AL 35898

Dr. Charles Bowden
U. S. Army Missile Command
Research Directorate
ATTN: DRSMI-RSD
Redstone Arsenal, AL 35898

Dr. Arthur R. Sindoris
Harry Diamond Laboratories
ATTN: DELHD-PO-P
2800 Powder Mill Road
Adelphi, MD 20783

Dr. Horst R. Wittmann
U. S. Army Research Office
P. O. Box 12211
Research Triangle Park, NC 27709

Dr. Jimmie R. Suttle
U. S. Army Research Office
P. D. Box 12211
Research Triangle Park, NC 27709

Mr. Charles Greff
U. S. Army Comm. - Electronics
Command
ATTN: DRSEL-CDM-RF-Z
Fort Monmouth, NJ 07703

Mr. Edward Herr
U. S. Army Comm. - Electronics
Command
ATTN: DRSEL-CDM-RX-4
Fort Monmouth, NJ 07703

Mr. Roland Wright
Night Vision & Electro-Optics
Labs
Fort Belvoir, VA 22060

Dr. Robert Rohde
Night Vision & Electro-Optics
Labs
Fort Belvoir, VA 22060

Dr. Donn V. Campbell
U. S. Army Comm. - Electronics
Command
ATTN: DRSEL-CDM-RN-4
Fort Monmouth, NJ 07703

Dr. Nick Karayienis
Harry Diamond Laboratories
ATTN: DELHD-RT-CA
2800 Powder Mill Road
Adelphi, MD 20783

Dr. T. N. Chin
U. S. Army ARRA/CDM
ATTN: DRDAR-SCF-10
Dover, NJ 07801

Dr. John Malemus
Night Vision & Electro-Optics
Labs
Fort Belvoir, VA 22060

Dr. Rudolf G. Buser
Night Vision & Electro-Optics
Labs
ATTN: DELNL-L
Fort Belvoir, NJ 22060

Dr. W. Ealy
Night Vision & Electro-Optics
Labs
ATTN: DELNV-AC
Fort Monmouth, NJ 22060

Dr. J. Hell
Night Vision & Electro-Optics
Labs
ATTN: DELNV-AC
Fort Belvoir, NJ 22060

Dr. J. Burgess
Night Vision & Electro-Optics
Labs
ATTN: DELNV-RM-RA
Fort Belvoir, NJ 22060

DEPARTMENT OF THE AIR FORCE

Dr. E. Champagne
AFWAL/AADD-1
Wright-Patterson AFB, OH 45433

Mr. W. Edwards, Chief
AFWAL/AAD
Wright-Patterson AFB, OH 45433

Professor R. E. Fontana
Head, Department of Electrical
Engineering
AFIT/ENG
Wright-Patterson AFB, OH 45433

Dr. Alvin Gerscadden
AFWAL/POOC-3
Air Force Aeronautical Labs
Wright-Patterson AFB, OH 45433

Mr. Alvin R. Bernum (CD)
Rome Air Development Center
Griffiss AFB, NY 13441

Chief, Electronic Research Branch
AFWAL/AADR
Wright-Patterson AFB, OH 45433

Mr. John Mott-Smith (ESD/ECE)
HQ ESD (AFSC), Stop 36
Hanscom AFB, MA 01731

Dr. J. Ryles
Chief Scientist
AFWAL/AS
Wright-Patterson AFB, OH 45433

Dr. Allan Schall
RADC/EE
Hanscom AFB, MA 01731

Dr. J. Brem
AFOSR/NM
Bolling AFB, DC 20332

Dr. David W. Fox
AFOSR/NM
Bolling AFB, DC 20332

Dr. J. Neff
AFOSR/NE
Bolling AFB, DC 20332

Dr. N. H. DeAngelis
RADC/ESR
Hanscom AFB, MA 01731

Dr. Gerald L. Witt
Program Manager
Electronic & Material
Sciences Directorate
Department of the Air Force
AFOSR
Bolling AFB, DC 20332

Mr. Allan Barnum
RADC/IS
Griffiss AFB, N.Y. 13411

Dr. Tom Walsh
AFOSR/NE
Bolling AFB, DC 20332

Dr. Edward Altschuler
RADC/EEP
Hanscom AFB, MA 01731

DEPARTMENT OF THE NAVY

Naval Surface Weapons Center
ATTN: Technical Library
Code DX-21
Dehlgren, VA 22448

Dr. Gernot M. R. Winkler
Director, Time Service
U. S. Naval Observatory
Massachusetts Avenue at
34th Street, NW
Washington, DC 20390

G. C. Dilworth, Jr.
Technical Director
Naval Coastal Systems Center
Panama City, FL 32407

Naval Air Development Center
ATTN: Code - 301 A. Witt
Technical Library
Worminster, PA 18974

R. S. Allgaier, R-45
Naval Surface Weapons Center
Silver Spring, MD 20910

Office of Naval Research
800 North Quincy Street
ATTN: Code 250
Arlington, VA 22217

Office of Naval Research
800 North Quincy Street
ATTN: Code 414
Arlington, VA 22217

Office of Naval Research
800 North Quincy Street
ATTN: Code 411MA
(Dr. Stuart L. Brodsky)
Arlington, VA 22217

Commanding Officer
Naval Research Laboratory
ATTN: Dr. S. Taitler, Code 6801
Washington, DC 20375

Commanding Officer
Naval Research Laboratory
ATTN: Mrs. D. Folen, Code 2627
Washington, DC 20375

Commanding Officer
Naval Research Laboratory
ATTN: Mr. J. E. Davey, Code 6810
Washington, DC 20375

Commanding Officer
Naval Research Laboratory
ATTN: Mr. S. D. McCombe, Code 6800
Washington, DC 20375

Commanding Officer
Naval Research Laboratory
ATTN: Mr. W. L. Faust, Code 6504
Washington, DC 20375

Technical Director
Naval Underwater Systems Center
New London, CT 06320

Naval Research Laboratory
Underwater Sound Reference Detachment
Technical Library
P. O. Box 8337
Orlando, FL 32856

Naval Ocean Systems Center
ATTN: Dr. P. C. Fletcher, Code 92
San Diego, CA 92152

Naval Ocean Systems Center
ATTN: Mr. W. J. DeJka, Code 8302
San Diego, CA 92152

Naval Ocean Systems Center
ATTN: Dr. Alfred K. Nedoluha,
Code 922
San Diego, CA 92152

Naval Weapons Center
ATTN: Dr. G. H. Winkler, Code 381
China Lake, CA 93555

Dr. Donald E. Kirk (62)
Professor and Chairman, Electrical
Engineering
SP-304
Naval Postgraduate School
Monterey, CA 93940

Dr. D. F. Dence
Naval Underwater Systems Center
New London Laboratory
ATTN: Code 34
New London, CT 06320

Director, Technology Assessment
Division (OP-987)
Office of the Chief of Naval Oper.
Navy Department
Washington, DC 20350

Mr. J. W. Willis
Naval Air Systems Command
AIR-310
Washington, DC 20361

Naval Electronics Systems Command
NC #1
ATTN: Code 61R
2511 Jefferson Davis Highway
Arlington, VA 20360

Department of the Navy
Naval Sea Systems Command
ATTN: W. W. Bleine (SEA-62R)
Washington, DC 20362

David Taylor Naval Ship Research
and Development Center
ATTN: Mr. G. H. Gleisner, Code 18
Bethesda, MD 20084

Mr. Martin Mandelberg
Coast Guard R&D Center
Avery Point
Groton, CT 06340

Naval Underwater Systems Center
New London Laboratory
ATTN: 101E (Dr. Edward S. Eby)
New London, CT 06320

Mr. Thomas J. Manuccia, Head
Chemistry and Application Section
Code 6543
Naval Research Laboratory
Washington, DC 20375

Dr. Stephen G. Siehop, Head
Semiconductor Branch
Code 6870
Naval Research Laboratory
Washington, DC 20375

Dr. John W. Rockway
Comm. Technology Prog. Off.
Code 8105
Naval Ocean Systems Center
San Diego, CA 92152

Dr. Barry P. Shay
Joint Program Office,
ODUSD(P)
The Pentagon, Rm 40825
Washington, DC 20301

Dr. Sydney R. Parker
Professor, Electrical Engineering
Code 62PX
Naval Postgraduate School
Monterey, CA 93940

Dr. George B. Wright
Office of Naval Research
Code 427
Arlington, VA 22217

OTHER GOVERNMENT AGENCIES

Dr. Ronald E. Kagarise
Director
Division of Materials Research
National Science Foundation
1800 G Street
Washington, DC 20550

Director
Division of Electrical, Computer
and Systems Engineering
National Science Foundation
Washington, DC 20550

Dr. Desn L. Mitchell
Section Head
Condensed Matter Sciences Section
Division of Materials Research
National Science Foundation
1800 G Street, N. W.
Washington, DC 20550

Judson C. French, Director
Center for Electronics and Electrical
Engineering
8358 Metrology Building
National Bureau of Standards
Washington, DC 20234

NON-GOVERNMENT AGENCIES

Director
Columbia Radiation Laboratory
Columbia University
538 West 120th Street
New York, NY 10027

Director
Coordinated Science Laboratory
University of Illinois
Urbana, IL 61801

Associate Director of Materials
and Electronics Research
Division of Applied Sciences
McKay Laboratory 107
Harvard University
Cambridge, MA 02138

Director
Electronics Research Center
University of Texas
P. O. Box 7728
Austin, TX 78712

Director
Electronics Research Laboratory
University of California
Berkeley, CA 94720

Director
Electronic Sciences Laboratory
University of Southern California
Los Angeles, CA 90007

Director
Microwave Research Institute
Polytechnic Institute of New York
333 Jay Street
Brooklyn, NY 11201

Director
Research Laboratory of Electronics
Massachusetts Institute of Technology
Cambridge, MA 02139

Director
Stanford Electronics Laboratory
Stanford University
Stanford, CA 94305

Director
Edward L. Ginzton Laboratory
Stanford University
Stanford, CA 94305

Dr. Leeter Eetmen
School of Electrical Engineering
Cornell University
316 Phillips Hall
Ithaca, NY 14850

Dr. Carlton Welter
Electro Science Laboratory
The Ohio State University
1320 Kinnear Road
Columbus, OH 43212

Dr. Richard Seeks
Dept. of Electrical Engineering
Texas Tech University
Lubbock, TX 79409

Director
School of Electrical Engineering
Georgia Institute of Technology
Atlanta, GA 30332

Dr. John F. Welkup
Dept. of Electrical Engineering
Texas Tech University
Lubbock, TX 79409

Mrs. Renete D'Arcangelo
Editorial Office
130 Pierce Hall
Division of Applied Sciences
31 Oxford Street
Cambridge, MA 02138

**DAT
FILM**